NUMERICAL MODELING OF SALT TECTONICS AT RIFTED CONTINENTAL MARGINS

by

Janice Allen

Submitted in partial fulfilment of the requirements
for the degree of Doctor of Philosophy

at

Dalhousie University
Halifax, Nova Scotia
June 2016

Table of Contents

List of Tables

List of Figures

Abstract

This thesis applies finite element numerical modeling to a range of projects investigating salt tectonics at rifted continental margins. Both two-dimensional and fully three-dimensional models are used. The first project demonstrates that incorrect density scaling in physical analogue models of salt tectonics leads to: 1) overestimated buoyancy force and 2) underestimated pressure gradient and sediment strength. Numerical models (2D) show a shift in salt structures, from diapir-minibasin pairs to expulsion rollover, when density scaling errors are corrected. The second and third projects use 2D nested models, which allow for dynamic evolution of the continental margin scale system while providing high resolution visualization of salt basins, to study the interactions among syn-rift salt deposition and deformation, post-salt sedimentation, and ongoing rifting tectonics. This work makes the important advancement of allowing salt basin geometry to evolve dynamically. The second project considers intermediate width margins, and shows that the timing of salt deposition relative to rifting (early syn-rift vs late syn-rift salt) leads to distinct patterns of salt distribution and deformation. Key features of salt tectonics at the Central Red Sea are captured using a layered salt succession deposited in the mid to late syn-rift period. The third project considers wide continental margins, developed from weak continental crust. In addition to studying syn-rift salt tectonics, the impact of sedimentation on the style of rifting is investigated. A comparison is made to the central and northern Nova Scotia margin. The final project presents preliminary results from a fully 3D numerical modeling study of the formation of minibasins through uneven sediment loading over salt. This work compares the evolution of 2D-equivalent and fully 3D model designs, exploring the importance of studying even simple salt tectonic systems using a fully 3D approach.

List of Abbreviations and Symbols Used

Abbreviation/Symbol	Description
LS	Large Scale
SS	Small Scale
ϕ	Internal angle of friction for clastic sediments
L^m	Length measurement in the model
L^n	Length measurement in nature
t	Time
ρ	Density
g	Acceleration due to gravity
η	Viscosity
t^m	Time measurement in the model
t^n	Time measurement in nature
$\rho_s{}^m$	Density of salt in the model
$\rho_s{}^n$	Density of salt in nature
g^m	Acceleration due to gravity in the model
g^n	Acceleration due to gravity in nature
η^m	Viscosity measurement in the model
η^n	Viscosity measurement in nature
v	Velocity
v^m	Velocity measurement in the model
v^n	Velocity measurement in nature
σ_Y	Clastic sediment yield strength
ρ_d	Clastic sediment density
$\sigma_Y{}^m$	Clastic sediment yield strength in the model
$\sigma_Y{}^n$	Clastic sediment yield strength in nature
σ_{zz}	Buoyancy force per unit area
$\sigma_{zz}{}^m$	Buoyancy force per unit area in the model
$\sigma_{zz}{}^n$	Buoyancy force per unit area in nature

ΔP	Horizontal pressure gradient
σ'_{ij}	Deviatoric stress tensor
x_i	Spatial coordinate
P	Pressure (mean stress)
v_i	Velocity component
$\dot{\varepsilon}_{ij}$	Strain rate tensor
h or $h(x)$	Height above base of the model
h_1, h_2, h_3	Specific elevations above the base of the model
W, W_1, W_2	Gaussian widths
$v_{prograde}$	Progradation velocity
ALE	Arbitrary Lagrangian Eulerian
J'_2	Second invariant of the deviatoric stress
P_f	Hydrostatic pore fluid pressure
ρ_g, ρ_{grain}	Grain density for compacting clastic sediments
ρ_f, ρ_{fluid}	Pore fluid density for compacting clastic sediments
n_o	Surface porosity for compacting clastic sediments
c	Compaction coefficient for compacting clastic sediments
z	Depth below sediment surface
AP or AP-1	Analogue Properties
NPL	Natural Properties with Low sediment density
NPH	Natural Properties with High sediment density
NPN	Natural Properties with Neutral sediment density
NPC	Natural Properties with Compacting sediment density
APS	Analogue Properties with corrected sediment Strength
APB	Analogue Properties with corrected Bouyancy
NPHW	Natural Properties with High sediment density and Water effects
APM	Analogue Properties Marine

P'	Effective pressure
ρ_w	Density of water
PDSM	polydimethylsiloxane
T	Temperature
$K, K(T)$	Thermal conductivity
A	Radioactive heat production per unit volume
	Or
	Pre-exponential scaling factor
α	Volumetric thermal expansivity
WQz	Wet Wuartzite
DMD	Dry Maryland Diabase
WOl	Wet Olivine
f	Scaling factor
$\dot{I}_2'$	Second invariant of the deviatoric strain rate tensor
n	Power law exponent
Q	Activation energy
V	Activation volume
	Or
	Volume
R	Universal gas constant
ϕ_{eff}	Effective internal angle of friction
C	Cohesion
C_p	Specific heat
λ	Wavelength
RS or R	Right Side
LS or L	Left Side
AC	Aggrading Clastic sediment
ACV	Aggrading Clastic sediment Variant
ES	Early syn-rift Salt

LS	Late syn-rift Salt
NS	Nova Scotia
ECMA	East Coast Magnetic Anomaly
OCT	Ocean Continent Transition
SMART	Scotian MARgin Transects
NSC	Nova Scotia Central margin
NSNE	Nova Scotia North Eastern margin
PKL	Pre-Kinematic Layer

Chapter 1: Introduction

1.1 Background on Salt Tectonics

The deposition and deformation of evaporites plays an important role in the development of many rifted continental margins around the world (Fig. 1.1). Evaporites are found along many rifted margins, and have a unique influence on the structural and thermal evolution of surrounding rocks. Halite flows more readily than most sedimentary rocks, and is modeled in this work as having a linear viscous rheology. Strictly speaking, this flow law applies to halite deforming by pressure solution (Carter *et al*., 1993; *Keken et al*., 1993), however in places we have extended this simplification to model salt comprising either pure halite or halite containing stronger evaporites or clastic sediments. Over geologic time, halite flows like a fluid, forming complex structures internally and in overlying rocks. In contrast, most sedimentary rocks deform in a brittle manner. Halite also has a higher thermal conductivity than most sedimentary rocks, and as such alters the thermal regime in surrounding rocks. In this thesis halite is often used to represent evaporites more generally (though in some cases we do consider mixed evaporite successions). Unless otherwise noted, 'salt' here refers to halite.

Salt tectonics, the deformation of salt and surrounding rocks, significantly impacts the evolution of many rifted margins and as such the study of salt tectonics is important to our understanding of the evolution of rifted margins. Because of its influence on the structural and thermal evolution of surrounding rocks, salt tectonics is also of interest to

the petroleum industry, as salt influences the maturation of oil and gas, as well as the development of traps.

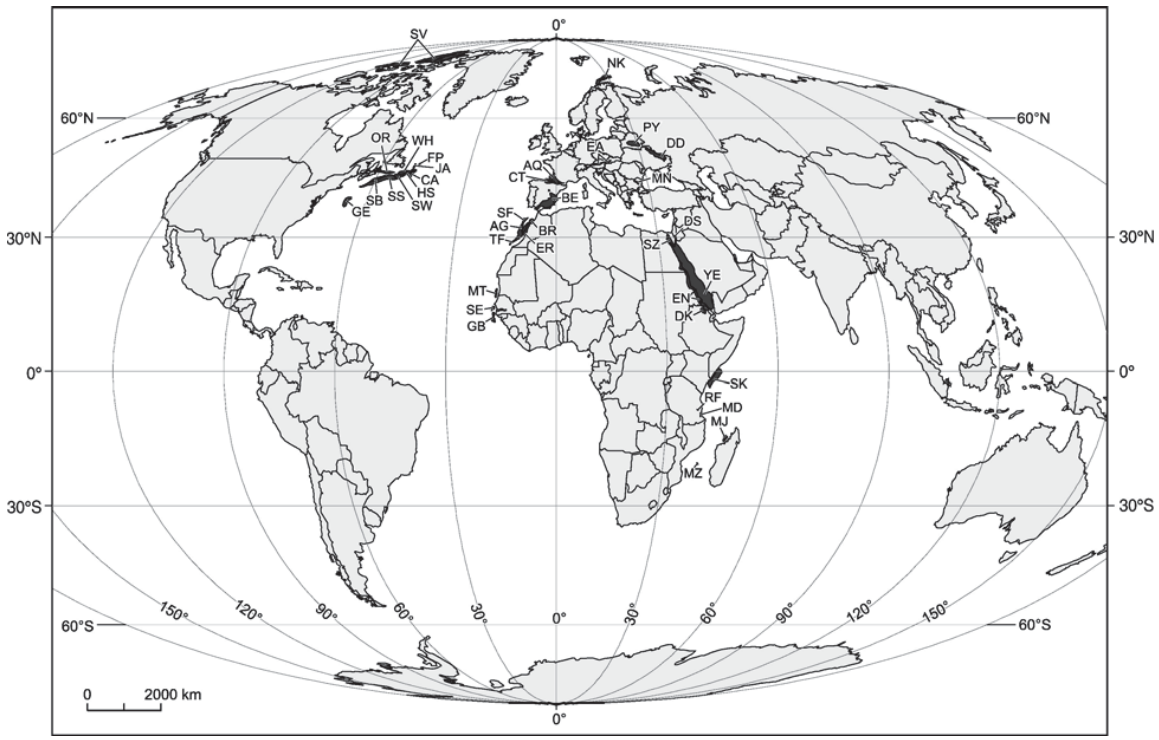

Figure 1.1, from *Hudec and Jackson*, 2007 (Figure 2). Some examples of known syn-rift salt basins around the world. Salt is shown in black.

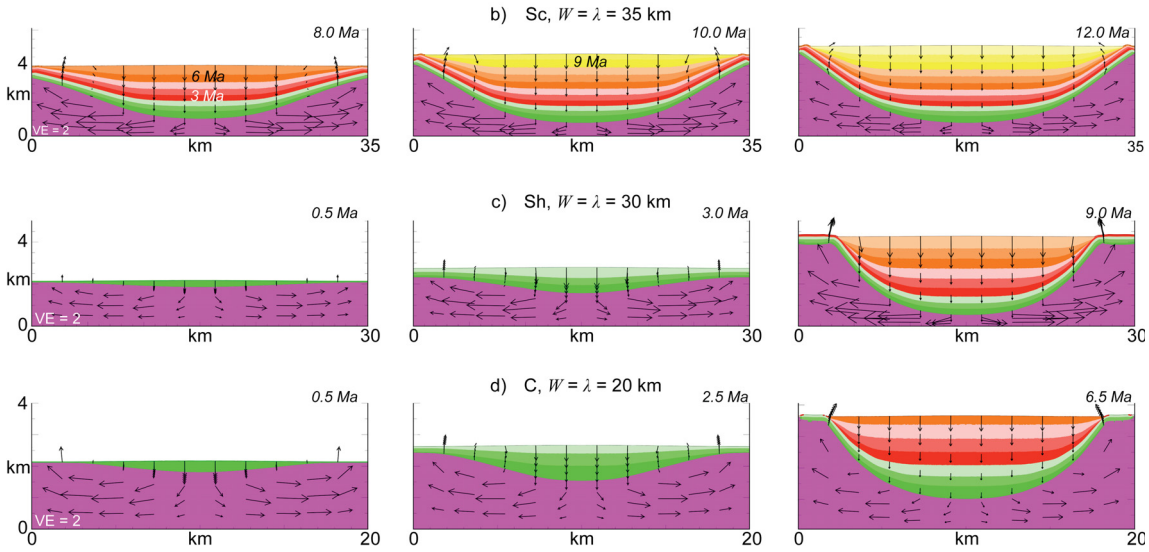

Figure 1.2, from *Goteti et al*. (Figure 6). Numerical modeling output showing minibasin formation through uneven sedimentation, for three sediment compaction profiles.

Large scale movement of salt can take place in response to gravity alone, termed gravity gliding, to pressure gradients in the overburden, referred to as gravity spreading, or to a combination of the two (e.g. *Brun and Fort*, 2001; *Mourgues and Cobbold*, 2006; *Fort et al*., 2004). Under the influence of gravity alone, salt will flow down an incline; if the base of a salt body is sloped, salt will flow under the force of its own weight. Overlying sediment applies a differential pressure to salt whenever this sediment is of uneven thickness (or density). Salt will flow from an area of higher pressure (under heavier or thicker sediment) to one of lower pressure (under lighter or thinner sediment). This process is explored by *Gemmer et al*. (2005); an example of salt flow in response to uneven sedimentation can be seen in Figure 1.2, from *Goteti et al*. (2012). Salt flowing in response to differential pressure or to gravity alone can deform by either Couette flow

(shearing of the salt, with velocity increasing linearly from the base to top of salt), Pouseiulle flow (squishing of the salt, with a curved velocity profile reaching a maximum at the vertical centre of the salt), or a combination thereof (e.g. *Gemmer et al*., 2005), depending on the magnitude of the pressure difference experience by the salt body. Significant quantities of salt can be translated tens of kilometers from the original place of deposition (e.g. *Kendell*, 2012) (Figure 1.3).

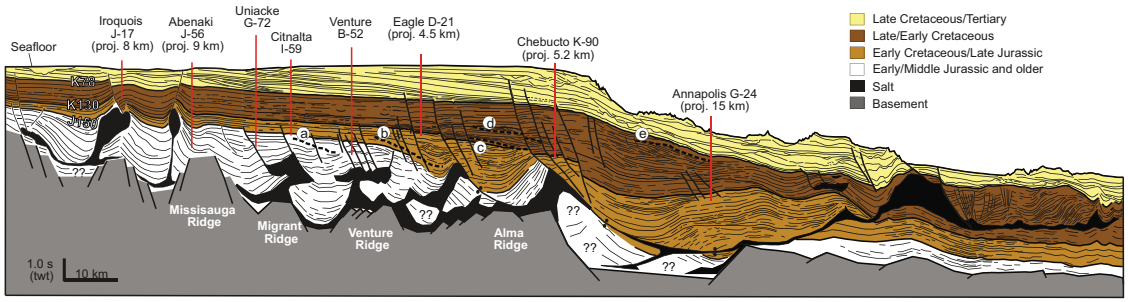

Figure 1.3, from *Kendell*, 2012 (Figure 4). Line drawing from seismic data through the Sable Subbasin, offshore Nova Scotia, showing salt (in black), highly deformed and having travelled a considerable distance from its original place of deposition.

Another aspect of the study of salt tectonics has been to focus on the processes that lead to the deformation of salt. In this way, previous studies have, for example, examined the relative importance of margin tilt (which slopes the base of the salt body, inducing gravity gliding), overburden type and rate of deposition (which impacts differential pressure, encouraging gravity spreading), and viscosity of the salt (which determines how readily the salt will flow) in determining what types of salt tectonics structures will evolve in a given system (*Goteti et al*., 2013). In this thesis, two papers explore the relationships between the ongoing rifting process, sedimentation after salt deposition, and the distribution and deformation of salt. In this way, the present work explores salt

tectonics in the context of the external processes occurring at the time of salt deposition and deformation.

1.2 Approaches to Studying Salt Tectonics

Salt tectonics has been studied extensively in natural systems, particularly through the use of seismic and well log data (e.g. *Rowan et al*., 2014; *Fort et al*., 2004; *Hudec et al*., 2008; *Adam and Krezseck*, 2012; *Kendell*, 2012). Following from this type of work, research of salt tectonics has branched to include numerical (e.g. *Chemia et al*., 2008; *Albertz et al*., 2010; *Albertz and Beaumont*, 2010; *Longoni et al*., 2010; *Burchardt, et al*., 2011; *Goteti et al*., 2012) and physical analogue (e.g., *Costa and Vendeville*, 2002; *Del Vintisette* et al., 2005; *Bonini,* 2003; *Ge et al*., 1997; *Baikpour et al*., 2010; *McClay et al*., 2003) modeling. Conceptual (e.g. *Rowan*, 2014) and analytical (e.g. *Gemmer et al*., 2005) approaches have also been applied to understanding the deposition and particularly the deformation of salt. Evaporites have been studied at young (e.g. *Ligi et al*., 2012; *Mitchell et al*., 2010; *Augustin et al*., 2014, studying the Red Sea) and old (e.g. *Mohriak and Leroy*, 2012; *Karner et al*., 1997, studying the South Atlantic margin) rifted margins around the world. Modeling of evaporite deposition and deformation ranges in scale from individual structures a few kilometers wide (e.g. *Goteti et al*., 2012; *Koupriantchik et al*., 2005; *Brun and Mauduit*, 2008), to regional-scale analyses capturing an entire rifting margin or margin pair (e.g. *Adam and Krezseck*., 2012; *Vendeville,* 2005; *Huismans and Beaumont*, 2011). Sample output from a numerical modeling study that examined formation of individual minibasin through uneven sedimentation is shown in Figure 1.2 (*Goteti et al*., 2012). Figure 1.4 shows example output from a physical

analogue model designed to study salt tectonics along the Nova Scotia margin, offshore Canada (from *Adam and Krezseck*). This type of model is one approach used to describe, characterize, and attempt to explain the wide range of salt-related deformation styles/products observed in natural analogues. For example, *Hudec et al*. (2008) explore a range of formation mechanisms for minibasins (Figure 1.5).

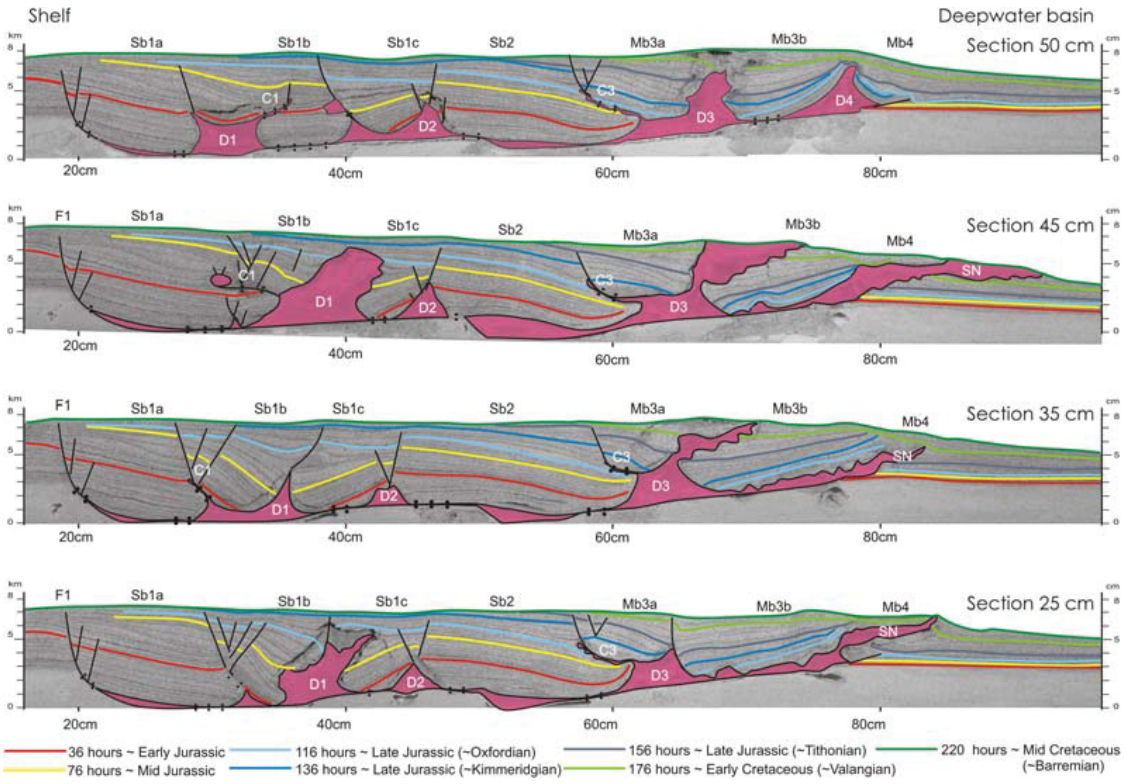

Figure 1.4, from *Adam and Krezseck* (Figure 6). Sections from a regional scale physical analogue experiment studying the margin offshore Nova Scotia, showing along strike variation in the development of salt tectonics.

Numerical experiments are easily repeatable; the same model can be re-run many times with variations on the inputs, allowing an exploration of the impacts of individual parameters. Numerical modeling has tackled a number of questions in salt tectonics, including the impact of basement geometry on salt flow (*Albertz et al*., 2010, *Albertz and*

Beaumont, 2010), the relative importance of sedimentation, margin tilt, and salt viscosity (Goteti et al., 2013), the details of diapir formation (e.g. *Longoni et al*., 2011; *Chemia et al*., 2008). Until recently, numerical models of salt tectonics have been limited to 2D analyses. Two-dimensional numerical modeling studies of salt tectonics continue to be informative; 2D software used to model salt tectonics is well established and captures a range of physically realistic behavior.

Salt tectonics has also been studied extensively using physical analogue models. This approach has successfully reproduced features such as passive and active diapir formation, fold and thrust belts, salt rollers, and extensional faults (e.g., Costa and *Vendeville*, 2002; *Del Vintisette et al.*, 2005; *Bonini*, 2003; *Ge et al*., 1997; *Baikpour et al*., 2010; *McClay et al*., 2003). These models have contributed to our understanding of the development of salt tectonics features, but have also had some limitations. In particular, proper scaling (of length, time, density, force, pressure/stress) is an ongoing limitation of physical analogue models. This error in scaling has been noted previously, but the importance of the error, in terms of its impact on the development of salt tectonics in physical analogue models, has been debated (*Brun and Fort*, 2011; *Warsitzka et al.*, 2011). Physical analogue models of salt tectonic systems have successfully reproduced many features seen in nature, leading some researchers to believe the scaling errors are not significant.

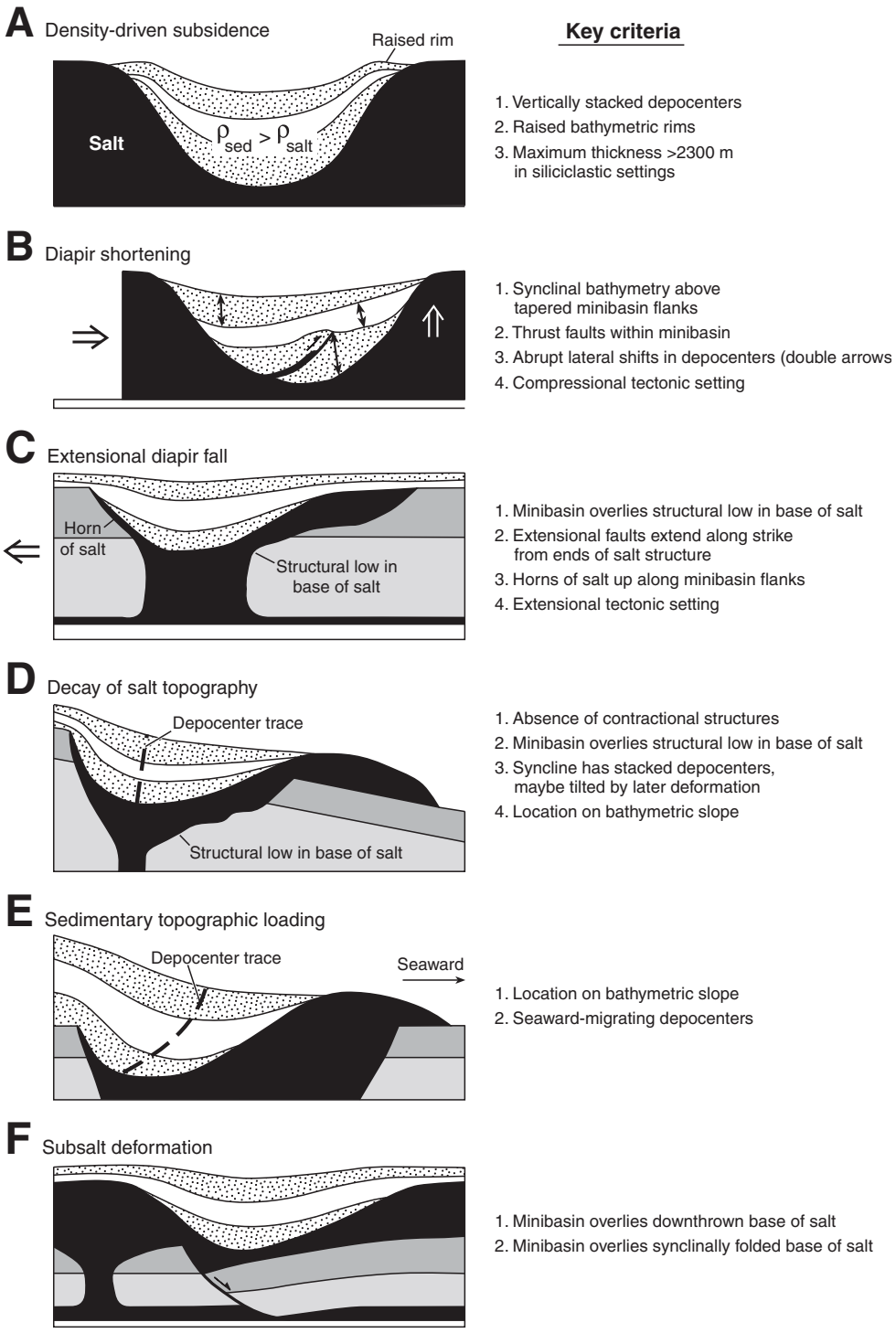

Figure 1.5, from *Hudec et al*., 2008 (Figure 26). Several mechanisms for minibasin formation, and the suggested criteria for distinguishing between them.

Both physical analogue and numerical modeling approaches have inherent advantages and disadvantages. Compared to numerical modeling, perhaps the most notable advantage of physical models is that they are 3-dimensional. Physical models can capture the distinctly three-dimensional nature of salt deformation. Until recently, this has been a limitation of numerical modeling of salt tectonics. Reproducing physical experiments exactly can be challenging, and the apparatus is such that often only a single experiment can be run at a time. Some properties of natural systems are not yet easily reproduced in physical experiments, including pore fluid pressure – although some effort has been made to mimic pore fluid pressure with compressed air (*Mourgues and Cobbold*, 2006; *Cobbold and Castro*, 1999) - and strain softening/hardening. Some previous studies have presented preliminary analyses of salt tectonics using 3D numerical modeling approaches (e.g. *Ismael-Zadeh et al*., 2004; *Koupriantchik et al*., 2005; *Longoni et al*., 2011; *Longoni et al*., 2010; *Massimi et al*., 2007). This previous work has tackled simple problems in salt tectonics, sometimes with the assumption of a viscous sedimentary overburden.

1.3 Methods

This work includes 2D and 3D numerical modeling of salt tectonics. In both cases, finite element numerical modeling software was used. All projects used software developed and/or augmented within the student's extended research group. The 2D software, Sopale Nested (*Fullsack*, 1995; *Beaumont et al*., 2009), was well established before the present work was undertaken, having been used to study a variety of problems in geodynamics (e.g. *Albertz et al*., 2010; *Albertz and Beaumont*, 2010; *Goteti et al*., 2013,

Goteti et al., 2012), rifted continental margins (e.g. *Huismans and Beaumont*, 2011; *Huismans and Beaumont*, 2008), offset rift basins (*Chenin and Beaumont*, 2013), pressurized sedimentary rock systems (*Ings and Beaumont*, 2010), and channel flow in high pressure and ultra-high pressure metamorphic settings (e.g. *Butler et al.*, 2013; *Butler et al*., 2011). The first three projects in this thesis used the Arbitrary Eulerian-Lagrangian software Sopale and Sopale Nested, which allows for large deformation of the model, by tracking material properties on a cloud of Lagrangian particles, while performing mechanical and thermal calculations on the Eulerian cells. This flexibility is necessary in the study of salt tectonics, where complex structures form as salt and the surrounding rocks are highly deformed. Fully 3D numerical modeling in this thesis uses the software DOUAR, which was developed within the student's extended research group (*Braun et al*., 2008). DOUAR has previously been used to study, for example, oblique convergence in mountain building systems (*Whipp et al*., 2014), crustal extension in three dimensions (*Allken et al*., 2012, 2011), and the formation of a critical wedge in a small orogen (*Braun and Yamato*, 2010). However, at the onset of this project DOUAR lacked certain functionality that was necessary for the study of salt tectonics. Consequently, several new features were added to the DOUAR code, by the student and members of her supervisory committee, to adapt DOUAR so it could be used to effectively study salt tectonics. These adaptations were necessary before the present work could be completed, and are described in this thesis.

The first paper used previously existing features of Sopale to evaluate the impact of incorrect scaling in physical analogue models of salt tectonics. The models in this paper

are designed to approximate physical analogue models, with a flat model base that does not consider isostasy, and a simple, pre-defined salt basin geometry. Numerical modeling is uniquely positioned to tackle the question of how significant these errors are, as the same model design can be run with incorrect and corrected density values. The repeatability of these numerical models allowed for a careful examination of the impacts of errors in density scaling.

Sopale has recently been upgraded to include the option of a nested model, where a high resolution small scale (SS) model is embedded within a lower resolution large scale (LS) model. This adaptation allows high resolution visualization of deformation over a subset of the model, while retaining a large model domain over which dynamic processes operate. In the context of salt tectonics, this has allowed a more realistic study of the development of salt tectonics along rifted margins. Papers 2 and 3 use a nested model in which the SS model shows the development of salt basins and the deposition and deformation of salt at a high resolution, while the salt basins themselves evolve dynamically, in direct response to the process of continental rifting. The shape and position of salt basins along the margin is not, as it was in previous studies (e.g. *Albertz et a*l., 2010; *Albertz and Beaumont*, 2010; *Goteti et al*., 2013; *Goteti et al*., 2012), predetermined, but rather evolves dynamically. High resolution imaging of the salt basins is critical, as salt tectonics structures vary significantly over short length scales. The large model domain is necessary to capture the scale of deformation that occurs during continental rifting, a process that directly impacts salt basin formation. Running the entire model at a resolution necessary to view salt tectonics features is neither

necessary nor feasible; hence the nested code is important to effectively study these systems with a reasonable computational time.

The fourth project in this thesis uses fully 3D numerical modeling to study the development of minibasins, a salt tectonic structure that has received attention in recent years. Several new features were added to the software, DOUAR, so it could capture a realistic representation of salt deformation. These adaptations are described in more detail in the supplementary material for Chapter 5. As mentioned previously, salt flows readily and forms complex structures. Consequently, numerical modeling software used to study salt tectonics must accommodate large deformations. To facilitate this, DOUAR was adapted so that fewer internal surfaces needed to be tracked. Previously, DOUAR has relied on internal surfaces to mark the interface between different materials (such as salt and overlying sediment). These surfaces tended to become warped and tangled with one another after substantial deformation, limiting run length. We have added the option to track material properties on the cloud of Lagrangian particles, reducing the reliance on internal surfaces and improving run length. Before this work, DOUAR could model linear viscous or frictional plastic materials, which we use to represent salt and sediment, but did not capture compacting density for clastic sediments. This is important to salt tectonics, as the deformation of salt is driven in part by differential pressure from overlying sediment, and this pressure is directly dependent on the sediment density. We have added the ability for materials to have a compacting density with depth, allowing us to model sedimentary overburden with a realistic density profile. Prior to this work, sedimentation in DOAUR was limited to a flat aggradation profile. A range of new

sedimentation geometries were added, to better reflect sedimentation conditions typical of salt tectonics system. The geometry of sediment overlying salt is important, as this contributes to differential pressure, which influences salt deformation. We also added pore fluid pressure to the mechanical calculations, to better represent submarine conditions. At the time of this thesis, pore fluid pressure was taken as hydrostatic, though adjustments, for example to allow overpressure, may be made in the future. Several of these additions had additional steps not listed here; for a full description of the alterations, refer to the supplementary material in Chapter 5. The results presented in Chapter 5 are preliminary, and demonstrate the potential of the modifications made to DOUAR, and pointing to the possibility of fully 3D numerical modeling of salt tectonics in the near future. Some work remains before reliable models of minibasin formation through uneven sedimentation can be produced using this software.

1.4 Key Contributions

This thesis addresses a number of previously outstanding questions in the field of salt tectonics. The first paper (Chapter 2) clarifies the errors in density scaling of materials commonly used in physical analogue models of salt tectonics systems, and demonstrates the impact of these errors. Prior to this work, there was no direct exploration of the impacts of these scaling errors on the evolution of salt tectonics systems. The second and third papers (Chapters 3 and 4) expand our understanding the development of salt tectonics, by exploring the deposition and deformation of salt in the context of an actively rifting margin pair system. Previous numerical modeling studies of salt tectonics had pre-defined the shape and size of salt basins at the time of deposition, whereas the

analyses presented here allow salt basin geometry to evolve dynamically, in response to the rifting process and sediment and salt deposition. This is a more realistic representation of nature, and has allowed, for the first time, numerical modeling to explore the impact of the timing of salt deposition relative to rifting on the distribution and deformation of salt at rifted margins. The fourth project demonstrates the potential of fully 3D numerical modeling of salt tectonic structures, in which realistic sediment properties are used. Salt deformation is inherently three-dimensional, and previous numerical modeling of salt tectonics has largely been limited to 2D. Some previous work has been published on the deformation of salt using 3D numerical modeling, but previous studies have generally not captured the frictional-plastic deformation and compacting density of the overburden. These features are critical to accurately modeling salt tectonics, and as such, the present study constitutes a substantial advance in this field.

1.5 Structure of the Thesis

The work is presented as a series of papers, with overarching introduction, methods, and discussion/conclusions sections. The introduction section outlines a justification for and a summary of the impacts of the present work. The methods section gives an overview of the numerical modeling methods used, assumptions/limitations used, and the reasoning behind these choices. Some required modifications made to existing software are also mentioned in this section. Four research papers comprise the thesis work, and are presented in the order in which they were completed. The four papers tackle different questions in salt tectonics, but all relate to the study of salt deposition and deformation at rifted continental margins. The first paper considers the impact of density scaling errors

in physical analogue models of salt tectonics at the scale of an individual salt basin. The second and third papers study syn-rift salt tectonics as it relates to ongoing rifting and post-salt sedimentation, under different crustal strength regimes. These two papers consider a much larger, continental margin scale domain. The third paper also examines more broadly the impact of sedimentation on a wide rifted continental margin. The fourth paper presents one of the first attempts at fully three-dimensional numerical modeling of salt tectonics with realistic sedimentary overburden. The discussion/conclusions section summarizes the main findings of this work, places this work in the context of ongoing research in the field of salt tectonics, and suggests opportunities for further research building on this work.

This research takes advantage of recent advances in numerical modeling capabilities, and in the fourth project pushes this capability to fully 3D modeling. The second and third projects use a nested approach, allowing high resolution visualization of salt deformation while incorporating the dynamics of the full margin pair. The first project uses models designed to be comparable with physical analogue experiments. Given that the move to fully 3D numerical modeling is new, the capacity to produce fully 3D models with fine resolution, both in time and in space, is still evolving. Fully 3D models with relatively small overall spatial and temporal dimensions, such as the single minibasins models in this thesis, make a useful contribution, using the capacity of current hardware and software.

Chapter 2: Impact of Inconsistent Density Scaling on Physical Analogue Models of Continental Margin Scale Salt Tectonics

Janice Allen[1] and Christopher Beaumont[2]

1) Department of Earth Sciences, Dalhousie University, 1459 Oxford Street, Halifax,

N.S., Canada, B3H 4R2

2) Department of Oceanography, Dalhousie University, 1355 Oxford Street, Halifax,

N.S., Canada, B3H 4R2

2.1 Preface

This chapter is based on the paper 'Impact of Inconsistent Density Scaling on Physical Analogue Models of Continental Margin Scale Salt Tectonics', by Janice Allen and Chris Beaumont, published in the Journal of Geophysical Research: Solid Earth (Allen and Beaumont, 2012). The paper has not been modified substantially from the published version, though it has been reformatted to suit the thesis. The copyright agreement form for this chapter can be found in Appendix A. Janice Allen ran the models in this paper (with supervision), wrote the manuscript and prepared the figures, edited the manuscript with input from the co-author, and prepared the manuscript for publication. Chris Beaumont had a leading role in the design of the models in this project, and provided supervision on all aspects of the work.

2.2 Abstract

The influence of inaccuracies in density scaling on the structural evolution of physical analogue experiments of salt systems has been debated, and is here investigated considering a gravity spreading example. Plane strain finite element numerical analysis was used to systematically evaluate the impact of changes in density scaling on buoyancy force, sediment strength, and pressure gradient. A range of densities typical of natural systems (including compacting sediment) and physical analogue experiments was included. A fundamental shift in the structure of the salt-sediment system, from diapir-minibasin pairs to expulsion rollover, was observed when sediment and salt densities were altered from values typical of physical experiments (1600 and 990 kg/m^3) to those most often found in nature (1900-2300 and 2150 kg/m^3). Experiments equivalent to physical analogue models but with reduced sediment density showed diapir-minibasin pair geometry, persisting to sediment densities of ~1300 kg/m^3. Salt burial by pre-kinematic sediments was found to suppress diapir formation for thicknesses greater than ~750 m (0.75 cm at the laboratory scale). The relative importance of disproportionately high buoyancy force, low sediment strength, and pressure gradient in physical experiments was investigated by isolating each of these scaling errors in turn. Buoyancy was found to be most influential in the development of diapir-minibasin pairs versus expulsion rollover geometry. Finally, we demonstrate that dry physical analogue experiments with sediment density reduced to ~1140 kg/m^3 (achievable through mixing

with hollow glass beads) would provide a reasonable approximation of submarine salt systems in nature (including water load and hydrostatic pore fluid pressure).

2.3 Introduction

Physical analogue models have been used extensively to study the deformation of salt under various applied loads and deformation constraints [e.g., *Costa and Vendeville*, 2002; *Del Ventisette et al*., 2005, 2006; *Bonini*, 2003; *Ge et al.*, 1997; *Baikpour et al.*, 2010; *Brun and Mauduit*, 2009], and in particular as influenced by pressure gradients induced by sedimentation [e.g., *Rowan and Vendeville*, 2006; *Maillard et al*., 2003; *McClay et al*., 2003; *Vendeville and Cobbold*, 1987]. These models have the distinct advantage that they can produce fully three-dimensional results. The technique of physical analogue modeling has successfully recreated observed structures such as extensional faulting, diapirism, and fold-and-thrust belts [e.g., *Costa and Vendeville*, 2002; *Del Vintisette et al*., 2005; *Bonini*, 2003; *Ge et al*., 1997; *Baikpour et al*., 2010; *McClay et al*., 2003]. Combinations of physical and numerical models have also been used to investigate aspects of salt tectonics, e.g., *Schultz-Ela et al*., [1993], who studied the mechanics of active diapirism. One limitation of the physical analogue models, however, lies in the availability of suitable materials with properties which can fulfill the requirements of dynamic scaling. Factors that require further investigation include viscous non-linearity and temperature dependence of halite (or more generally evaporite) rheology, the effect of pore fluid pressures [*Mourgues and Cobbold*, 2006; *Cobbold and Castro*, 1999], isostasy, and the impact of basin evolution in a submarine versus subaerial setting [*Gemmer et al.*, 2005]. In particular, this paper examines the importance of

density scaling in gravity spreading experiments.

Analogue models commonly use viscous materials, such as silicone elastomer, to represent salt (rocksalt, halite), and sand or other granular materials, which have a frictional-plastic rheology, to represent siliciclastic sediments, such as shale and sandstones. It is argued that the elastomer is appropriate as an analogue to salt because, although intrinsically viscoelastic, it has a linear viscous behaviour at the strain rates normally encountered in the physical experiments. Silicone, polymethylsiloxane polymer PDMS (SGM-36), has also been commonly used to model ductile sequences in the upper crust. The polymer has a Newtonian linear viscous behaviour at low strain rates, a density of 970 kg/m^3 [*Kuo*, 1999], (also quoted as varying from 950-990 kg/m^3), [*Ge et al*., 1997; *Krezsek et al*., 2007] a yield strength of 4 Pa and a viscosity of 5x10^4 Pa s [*Weijermars and Schmeling*, 1986; *Weijermars et al.,* 1993]. Although this polymer is commonly used to model salt, it is also considered by some to be an appropriate analogue material for overpressured shales from surface to ~6 km depth [*Cohen and McClay*, 1996]. The behaviour of sand has also been investigated and it has been shown to have properties that depend on packing, and to undergo limited strain hardening and softening [e.g., *Lohrmann et al*., 2003], which will affect localization of model faults. However, it can be argued that natural sediments have equivalent properties that also lead to faulting [*Marone*, 1998].

If we accept that sand and silicone have appropriate rheological properties which can be scaled to natural conditions, one potential problem remains in that the densities of sifted

silica sand and silicone do not have the required dynamical similarity to the natural prototype in sedimentary basins. The frictional strength of the sediment also depends on its density, placing an independent requirement on the scaled sediment density, not just the density difference between the sediment and the salt. As recently as 2011, it has been argued that the density scaling in analogue models is acceptable [*Brun and Fort*, 2011; *Warsitzka et al.*, 2011] but little has been done to test this assertion.

Given the difficulty of finding analogue materials with the appropriate densities we use a series of numerical model experiments with simple geometries to examine the impact of the densities of salt and overburden in salt tectonics. With this approach, it is possible to vary the density of salt and sedimentary rock to examine, for a given configuration, the resulting deformation styles for material properties consistent with both natural systems and physical analogue models. In recent years, there has been a tendency to consider differential pressure as the primary driving force behind continental margin salt tectonics [e.g., *Dooley et al*., 2007; *Vendeville*, 2005; *McClay et al*., 2003]; by comparison, the impact of buoyancy forces has been downgraded. It has previously been demonstrated that both buoyancy and lateral pressure gradients influence the structural evolution of salt systems [*Ings et al*., 2005]. In addition to investigating the scaling of physical analogue salt models, the results we present build on this analysis, providing insight into the relative importance of lateral differential pressure and vertical buoyancy forces in driving salt tectonics. Finally, consideration is given to the importance of water load and pore fluid pressure in the natural system equivalent experiments, for submarine systems, and the results are compared with a physical analogue equivalent experiment in which the

sediment density has been reduced to provide an appropriately scaled density difference between sediment and salt.

After a short discussion on scaling and an outline of the numerical method used, experiment design and results are presented for two areas of focus: the impact of varying densities from natural to physical analogue model equivalent values; and isolating the effects of buoyancy, pressure gradient, and sediment strength. The discussion and conclusions sections encompass all aspects of this study.

2.4 Scaling of Physical Analogue Models of Salt Tectonics Systems to a Dry, Subaerial Natural System

The following is a description of typical scaling between a natural system and physical analogue experiments, including select natural and scaled parameters and calculated scaling ratios. In the following, the superscripts 'n' and 'm' are used to denote measurements in nature and in physical analogue ('model') experiments, respectively. Note that throughout g, the acceleration due to gravity, and ϕ, the internal angle of friction for clastic sediments, are not scaled. The section concludes by highlighting three scaling inaccuracies which arise from the scaling errors introduced by densities of typical salt and sand analogue materials.

Length scaling was chosen such that 1 km in nature equates to 1 cm in physical analogue experiments, particularly when considering a thickness of sediment or salt. The ratio of lengths in nature, L^n, to those in physical experiments, L^m, is thus:

$$\frac{L^m}{L^n} = \frac{10^{-2} m}{10^3 m} = 10^{-5} \tag{2.1}$$

Note that in the numerical analyses presented here, for simplicity, length dimensions were selected to match natural values for all experiments (L^m/L^n=1).

Time scaling can be determined as follows:

$$t \propto \frac{\rho_s g L}{\eta} \tag{2.2}$$

$$\frac{t^m}{t^n} = \frac{{\rho_s}^m g^m L^m}{\eta^m}\left(\frac{\eta^n}{{\rho_s}^n g^n L^n}\right) = \frac{\eta^n}{\eta^m}\left(\frac{{\rho_s}^m}{{\rho_s}^n}\right)\left(\frac{g^m}{g^n}\right)\left(\frac{L^m}{L^n}\right)$$

where t is time, η and ρ_s are viscosity and density of the salt or salt analogue material (silicone), and g is the acceleration due to gravity. This can be simplified because the natural value of gravity is retained, implying a scaling equal to one, and assuming length is scaled correctly.

$$\frac{t^m}{t^n} = \frac{\eta^n}{\eta^m}\left(\frac{\rho^m}{\rho^n}\right) \tag{2.3}$$

Velocity, v, scales according to:

$$v \propto \frac{L}{t} \tag{2.4}$$

$$\frac{v^m}{v^n} = \frac{L^m}{L^n}\left(\frac{t^n}{t^m}\right) = \frac{L^m}{L^n}\left(\frac{\eta^n}{\eta^m}\right)\left(\frac{{\rho_s}^m}{{\rho_s}^n}\right)$$

Note that in the numerical experiments presented here progradation velocity (the rate at which the prograding sediment profile was moved across the model domain, and the only imposed velocity) was selected to match nature in all cases.

Sediment yield strength, σ_Y, is proportional to the density of the sediment, ρ_d, length (depth), the acceleration due to gravity, and the internal angle of friction of the sediment, ϕ.

$$\sigma_Y \propto \rho_d g L \sin\phi \tag{2.5}$$

The effect of cohesion will be addressed in future work, but is considered to be less significant than the factors addressed here. Assuming the scaling for g is one and ϕ also has the natural value, sediment yield strength scales according to the length scaling and the density of the sediment.

$$\frac{\sigma_Y^m}{\sigma_Y^n} = \frac{{\rho_d}^m}{{\rho_d}^n}\left(\frac{L^m}{L^n}\right)$$

The buoyancy force per unit area, σ_{zz} acting to displace salt vertically though an overlying layer of sediment is proportional to the difference in densities of the two materials.

$$\sigma_{zz} \propto \frac{(\rho_d - \rho_s)}{\rho_s} L g \tag{2.6}$$

Assuming g is not scaled:

$$\frac{\sigma_{zz}^m}{\sigma_{zz}^n} = \frac{\left(\rho_d^m - \rho_s^m\right)}{\rho_s^m}\left(\frac{\rho_s^n}{\left(\rho_d^n - \rho_s^n\right)}\right)\frac{L^m}{L^n}$$

The horizontal pressure gradient experienced by salt under a layer of sediment of varying thickness is given by:

$$\frac{\Delta P}{L} = \frac{\rho_d g \Delta L}{L} \tag{2.7}$$

Assuming gravity is not scaled, the horizontal pressure gradient scales as the sediment density over length.

$$\left(\frac{\Delta P}{L}\right)^m \Big/ \left(\frac{\Delta P}{L}\right)^n = \frac{\rho_d^m}{\rho_d^n}\left(\frac{L^n}{L^m}\right)$$

Table 2.1 summarizes the above analysis, highlighting the differences between scaling ratios calculated using correctly-scaled analogue densities and densities of common analogue materials. Natural densities of 2300 kg/m^3 and 2150 kg/m^3 [*Hudec et al.*, 2009] have been assumed for clastic sediments and salt. It can be seen that densities of sediment and salt analogues often used in physical experiments of salt tectonics result in an underestimation of the sediment yield strength and cause the buoyancy and pressure gradient forces to be disproportionately large and small, respectively. The magnitude of these inaccuracies will vary according to the properties (e.g. sediment density) of the natural prototype. The values in Table 2.1 therefore represent examples, not the full range, of inaccuracies.

Table 2.1: Scaling Ratios Between Physical Models and Dry or Submarine Natural Systems

Scaling Parameter	Scaling Ratios (model/nature)		
	Compared to dry natural system		Compared to submarine natural system
	With correctly-scaled analogue densities	With currently-used analogue densities (ρ_d = 1600 kg/m^3; ρ_s = 990 kg/m^3)	With modified analogue densities (ρ_d = 1300 kg/m^3; ρ_s = 1150 kg/m^3)
Length, L (10^{-5})	1.0	1.0	1.0
Time, t (10^{-9})	1.0	0.46	0.46
Velocity, v (10^{-14})	1.0	0.46	0.46
sediment strength, σ_y (10^{-5})	1.0	**0.70**	**1.0**
buoyancy, σ_z (10^{-5})	1.0	**8.8**	**1.0**
pressure gradient, ΔP (10^{-5})	1.0	**0.70**	**1.0**

2.5 Numerical Methods

Evolution of the models was calculated using a 2D plane-strain finite element software, Sopale [*Fullsack*, 1995]. Only mechanical calculations were performed, as described below. An Arbitrary Lagrangian Eulerian (ALE) method for creeping flows [*Fullsack*, 1995; *Willett*, 1999], in which the Eulerian grid stretched vertically to adapt to the changing material domain, was used to calculate the velocity field, stress, strain rate, and deformation resulting from the applied pressure gradient. A Lagrangian grid and passive tracking particles are advected according to the velocity field and used to re-grid the material properties. The equilibrium force balance (Equation 2.9) was solved for incompressible (Equation 10), gravitationally-driven flow of frictional-plastic sediment overlying viscous salt.

$$\frac{\partial \sigma'_{ij}}{\partial x_i} - \frac{\partial P}{\partial x_j} + \rho g = 0 \qquad i,j = 1,2 \tag{2.9}$$

$$\frac{\partial v_i}{\partial x_i} = 0 \qquad i,j = 1,2 \tag{2.10}$$

where σ'_{ij} is the deviatoric stress tensor, x_i are the spatial coordinates, P pressure (mean stress), v_i a component of velocity and the strain rate tensor is:

$$\dot{\varepsilon}_{ij} = \frac{1}{2}\left(\frac{\partial v_i}{\partial x_j} + \frac{\partial v_j}{\partial x_i} \right) \tag{2.11}$$

All models presented here have boundary conditions specifying zero horizontal velocities on the vertical model boundaries and at the base of the model. Deformation is therefore driven solely by the gravitational force caused by the model geometry and the prograding sediments.

In all models presented here, progradation of sediment is accomplished by filling all unoccupied space below a curve at each time step with new sediment. The curve is defined by a half-Gaussian function, such that the model bathymetry, *h(x)* is given by:

$$h(x) = \begin{cases} h_1 & x < x_1 \\ h_2 + (h_1 - h_2)\exp\left(-\dfrac{(x - x_1)^2}{W^2}\right) & x \geq x_1 \end{cases} \tag{2.12}$$

where h_1 and h_2 are the landward and seaward elevations, respectively, and W is the Gaussian width such that $L=2W$ is the approximate width of the progradation profile. The progradation profile is translated laterally at velocity $v_{prograde}$. Material is neither added nor removed where the current model surface is above the progradation profile. We use the terminology, bathymetry, and landward and seaward because these are appropriate terms for the natural system. However, it is important to remember that water loading, as in a submarine system, is seldom used in analogue experiments and is therefore omitted in our models, except for NPHW which is discussed later.

Water loading in NPHW is represented as a boundary load applied normal to the upper surface of the model. The hydrostatic water pressure increases both the solid and fluid pressures in the finite element model.

We accepted a prototype with linear viscous salt (halite), with viscosity of 10^{18} Pa s [*van Keken et al.,* 1993*; Goteti et al.,*in press]. This allowed us to focus on the mechanical scaling, without considering the associated thermal scaling, which is necessary for power-

law creep, and which is normally ignored in laboratory analogue salt tectonic models. The choice of a linear flow law for the salt is also consistent with the linear flow law for silicone used in the laboratory experiments. Sediments, other than salt, were modeled as frictional-plastic materials such that their yield, σ_Y, is pressure dependent and obeys the Drucker-Prager yield criterion:

$$\sigma_Y = \left(J_2'\right)^{1/2} = \left(P - P_f\right)\sin\phi \tag{2.13}$$

where $J_2' = \frac{1}{2}\sigma_{ij}'\sigma_{ij}'$ is the second invariant of the deviatoric stress, P is the mean stress, P_f is the hydrostatic pore fluid pressure (if included), ϕ is the internal angle of friction, and σ_{ij}' is the deviatoric stress tensor. In this analysis $\phi = 30°$ in all the models (Table 2.1).

When compacting prograding sediments were applied, these had a grain density, ρ_g, of 2640 kg/m^3, pore fluid density, ρ_f, of 1000 kg/m^3, surface porosity, n_o, of 0.52, and compaction coefficient, c, of 4.7x10^{-4} m^{-1}. These values have been shown to provide a good fit to average siliciclastic sediment properties in the northern Gulf of Mexico [*Hudec et al*., 2009]. For each time step the kinematic compaction model calculates the sediment density as a function of depth, z, according to Equation 2.14. The density increases as a function of depth by expulsion of pore fluid and the corresponding volume was reduced by vertical contraction equal to the incremental volume of the expelled pore fluid. This calculation is separate from the finite element solution which remains incompressible (Equation 10).

$$\rho_d(z) = \rho_g - \left(\rho_g - \rho_f\right)n_o e^{-cz} \tag{2.14}$$

2.6 Results

2.6.1 Natural Versus Analogue Experiment Densities

All of the model experiments were performed at the scale of the natural prototype using prototype material properties except for the analogue model equivalents, which used sand and silicone densities. Following *Krezsek et al*. [2007], we used 990 kg/m^3 for the silicone density. Using lower values, e.g., 970 kg/m^3, would marginally increase the buoyancy forces. Models computed at the laboratory scale would give equivalent results, but scaled according to equations 1-7. Initial model geometry and material properties are shown in Figure 2.1. The sediment load is shown at an advanced progradation position, for clarity. All models initially had a horizontal, rectangular cross-section 2 km thick salt basin constrained on either end by sedimentary rocks. This geometry was chosen for simplicity, but tapered salt basins could also be used [*Albertz and Beaumont*, 2010]. A smooth prograding deltaic sedimentary wedge was simulated by moving a half-Gaussian curve seaward at a constant rate of 0.3 cm/yr, and filling all unoccupied space under the curve with sediment at each time step. A time step of 10^4 yr was used for all model runs; this choice obeys the CFL criterion, a requirement for stable material advection, condition for all models [*Press et al*., 1986, p.627]. The wedge height varies from 3 km above the initial salt/sediment surface in the shelf region, landward of the continental slope, to 200 m below this surface seaward of the slope. The prograding sediment wedge was initially placed landward of the salt basin, so that progradation would reproduce progressive advance of a delta onto the salt. This sedimentation model is not intended to correspond to the natural system in detail, but could be easily reproduced in a laboratory

experiment.

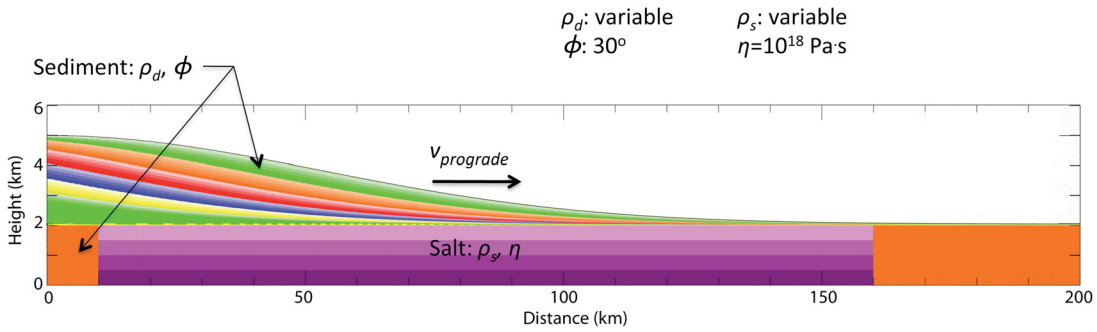

Figure 2.1: Model geometry and material properties. Here ρ_d and ρ_s are sediment and salt density, ϕ is the internal angle of friction of the sediment, η is salt viscosity, and $v_{prograde}$ is the progradation rate. The position of the sediment is shown as having prograded over the salt, for clarity. In all experiments, the sedimentary wedge was initially placed to the left of the salt basin.

In keeping with most analogue laboratory models isostatic compensation and thermal subsidence of the underlying lithosphere were not considered; the base of the model was treated as a rigid substratum. These simplifications and those noted above produce 2D numerical experiments corresponding to the most basic physical analogue models in which sediment progrades at a uniform rate over a pre-existing uniform salt layer, and in which deformation does not vary in the along strike direction, perpendicular to the direction of progradation [e.g., *Vendeville,* 2005].

Five model experiments examining the impact of sediment and salt densities are summarized below. In Model AP (Analogue Properties) densities correspond to the physical analogue models (salt, 990 kg/m^3 and sediment 1600 kg/m^3). Models NPL, NPH, NPN, (Natural Properties with Low, High, and Neutral density sediment) and NPC (Natural Properties with Compacting sediment) include material properties that are similar to natural systems, including salt density of 2150 kg/m^3. In NPL the sediment

density is 1900 kg/m^3, chosen to represent near surface, uncompacted sediment, whereas in NPH it is 2300 kg/m^3, consistent with moderately compacted clastic sediment [*Hudec et al*., 2009; *Velde*, 1996; *Baldwin and Butler*, 1985; *Sclater and Christie*, 1980]. Model NPN has sediment density 2150 kg/m^3, equal to that of salt, and was chosen to isolate the effects of differential pressure, by eliminating the buoyancy force between the salt and sediment. In model NPC sediment compacts vertically according to a kinematically specified Athy type [*Athy*, 1930] compaction curve (equation 14).

In addition, a sensitivity analysis was conducted considering separately the influence of density contrast between sediment and salt and initial thickness of sediment cover on structural evolution. First, the original analogue system properties outlined above were used, and sediment density was reduced for successive runs. Second, a uniform layer of sediment was placed on top of the salt before progradation of sediments across the model; sediment thickness was increased for successive model runs. Model parameters are summarized in Table 2.2.

Table 2.2: Model Parameters

Experiment identification	NPN	NPH	NPL	NPC	AP-1	APB	APS	NPHW	APM
Salt properties									
Density, ρ_s (kg/m^3)	2150	2150	2150	2150	990	1450	1540	2150	1300
Viscosity,η (Pa.s)	10^{18}	10^{18}	10^{18}	10^{18}	10^{18}	10^{18}	10^{18}	10^{18}	10^{18}
Sediment properties									
Density, ρ_d (kg/m^3)	2150	2300	1900		1600	1600	2150	2300	1150
Grain density, ρ_g (kg/m^3)				2640					
Surface porosity, n_o				0.52					
Pore fluid density, ρ_f (kg/m^3)	0	0	0	1000	0	0	0	0	0
Compaction coefficient, c	30	30	30	$4.7*10^{-4}$	30	30	30	30	30
Cohesion, C (MPa)									
Internal angle of friction, ϕ (^{o})									
Progradation rate (cm/a)	0.3	0.3	0.3	0.3	0.3	0.3	0.3	0.3	0.3
Thickness of pre-kinematic sediment cover (m)	50	50	50	50	50	50	50	50	50

Figures 2.2-2.6 show the evolution of each of the first five models, as a series of panels. Salt is shown as four initially horizontal layers in different shades of magenta, which allows the internal deformation of the salt to be visualized. All of these layers have the same properties. Sediments bounding the salt basin are orange and prograding sediments are colour coded according to chronostratigraphic age, each shade corresponding to 1.0 Ma of evolution (colour changes represent 5.0 Ma).

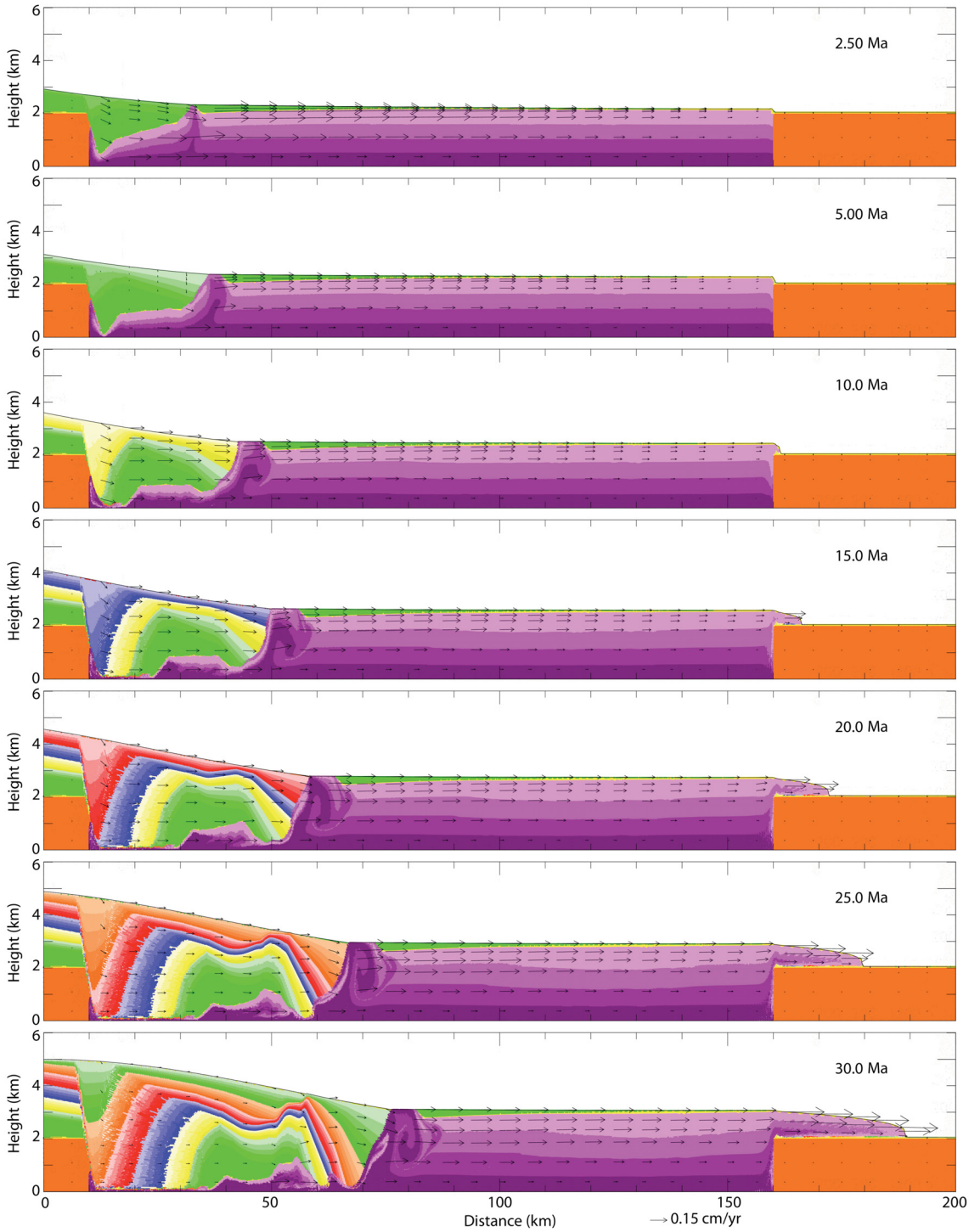

Figure 2.2: Experiment Natural Properties, Neutral (NPN), representative of nature with neutrally buoyant sediment ($\rho_d = \rho_s = 2150$ kg/m^3). Salt is magenta, pre-kinematic sediment is orange, prograding sediment has graded colouration. Vertical exaggeration 8:1. Prograding sediments form an expulsion rollover; salt is expelled laterally, thickens, and forms a nappe over the distal sediment buttress.

2.6.1.1 Experiments with Densities Representative of Natural Systems

Each of the natural system properties experiments becomes gravitationally unstable during sediment progradation and develops a linked system in which extension below the model continental slope is balanced by shortening at the toe of the corresponding model slope. Details of the evolving geometry vary among the experiments. In the most simple example, NPL (Figure 2.3), this linked system is expressed by the development of a listric normal fault and rollover structure against the boundary of the basin paired with a counter-regional expulsion rollover which develops as salt is expelled laterally from beneath the prograding sediments. In NPN (Figure 2.2) there is subsidiary faulting within the rollover structure and in NPH several faults develop. In all cases shortening seaward of the progradation profile produces regional thickening of the salt body and subsequent development of a salt nappe over the distal bounding sediment block. Folding can be seen within the salt nappe, most clearly between differently coloured salt layers. In proximity to the expulsion rollover, the salt develops a rotational flow geometry, in response to lateral squeezing of salt from beneath the prograding sediment. Overall, there is a simple and understandable progression of salt-tectonic styles in which deformation increases with the density of the prograding sediment.

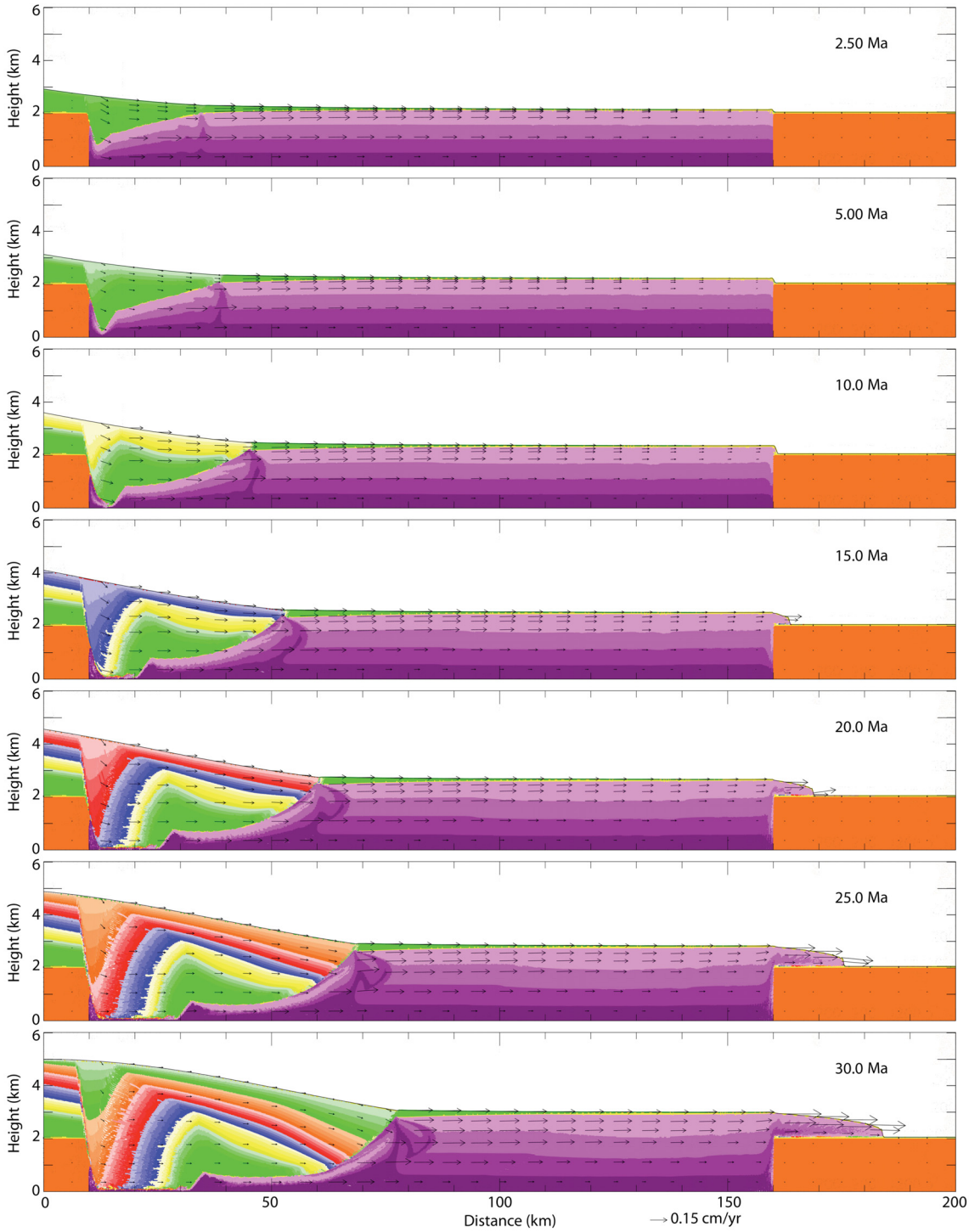

Figure 2.3: Experiment Natural Properties, Low (NPL), representative of nature with low density sediment (ρ_d = 1900 kg/m^3; ρ_s = 2150 kg/m^3). Salt is magenta, pre-kinematic sediment is orange, prograding sediment has graded colouration. Vertical exaggeration 8:1. Prograding sediments form an expulsion rollover with shallow dip angle. Salt is expelled laterally, thickens, and forms a nappe over the distal sediment buttress.

2.6.1.1.1 Experiment NPN: Nature Equivalent, with Neutrally Buoyant Sediment

Experiment NPN, with sediment density constant and equal to that of salt (Figure 2.2), develops a quasi-Poiseuille flow in the salt beneath the sediment during early progradation. Lateral movement of the salt ahead of the prograding sediment is accommodated through a laterally decaying Couette flow of the salt (together with a thin carapace of sediment) which is responsible for thickening the salt. By 10 Ma the paired rollovers that develop from listric normal faulting and lateral salt expulsion form a large sedimentary depocenter that has an anticlinal turtle-like structure with a trapped basal salt pillow. The basal salt near the proximal edge of the salt basin becomes very thin, however, it does not weld, as can be seen by the continued basal slip throughout the experiment. From this point on salt both ahead of the prograding sediments and trapped beneath them exhibits Couette flow. Between 10 and 30 Ma the system advances seaward by continued rollover on the normal fault, slip on the thin basal salt layer and salt expulsion from the footwall of the counter-regional rollover. This increases the size of the depocenter and the anticlinal structure, and extends the zone of apparent sediment welding seaward. From 20 Ma there is subsidiary normal sense deformation within the anticline above the salt pillow. Thickening of the salt body is evident as early as 2.5 Ma, and a nascent salt nappe develops by 10 Ma. As expected, no buoyancy-driven diapirs develop and salt is only exposed at the surface adjacent to the base of the slope. Note that the salt has risen to the same level as sediment to the right, as expected given that they have the same densities. Internal rotational flow in the salt is clearly evident adjacent to the seaward expulsion rollover.

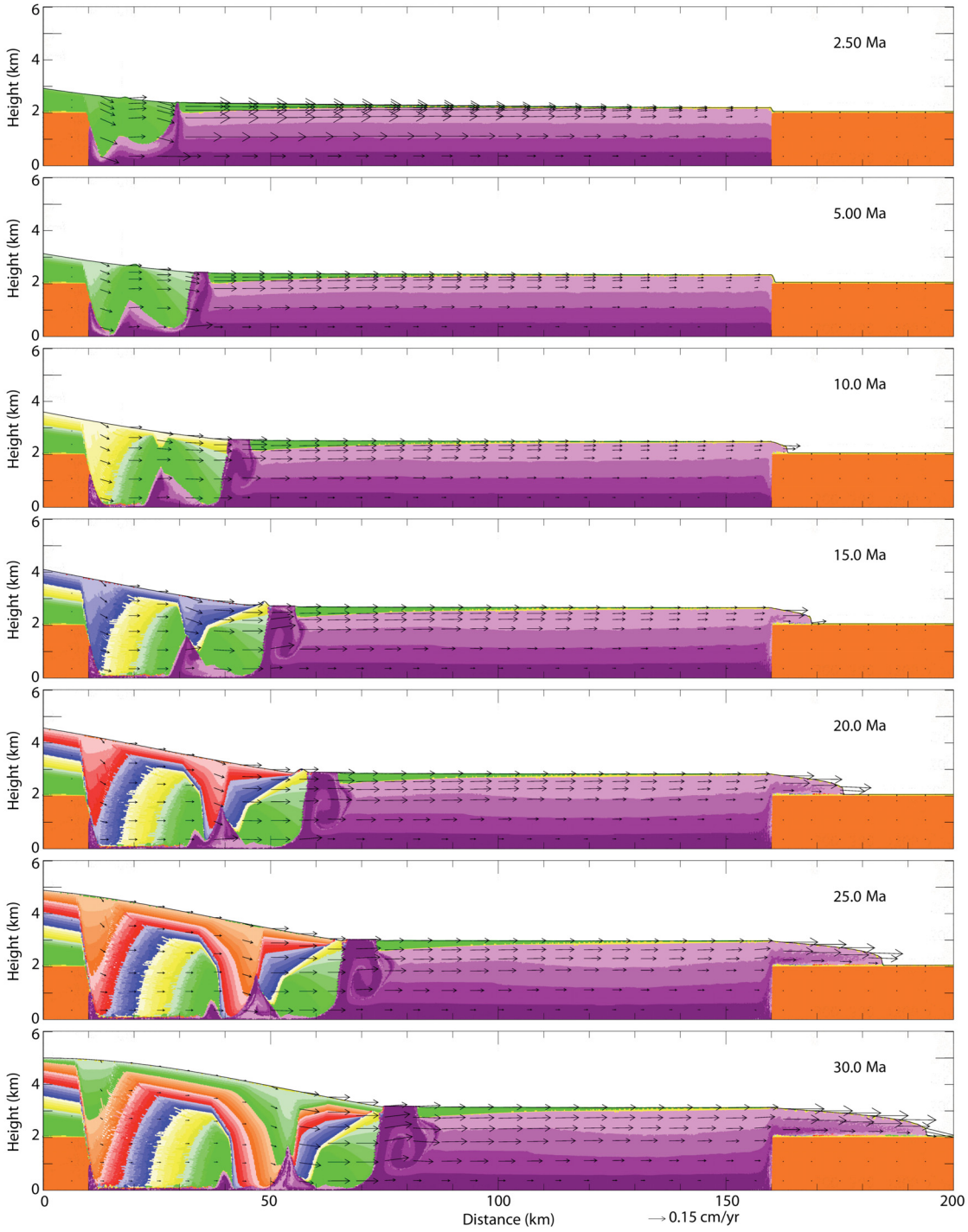

Figure 2.4: Experiment Natural Properties, High (NPH), representative of nature with high density sediment (ρ_d = 2300 kg/m^3; ρ_s = 2150 kg/m^3). Salt is magenta, pre-kinematic sediment is orange, prograding sediment has graded colouration. Vertical exaggeration 8:1. Prograding sediments form an expulsion rollover with steep dip angle and experience both regional and counter-regional faulting. Salt is expelled laterally, thickens, and forms a nappe over the distal sediment buttress.

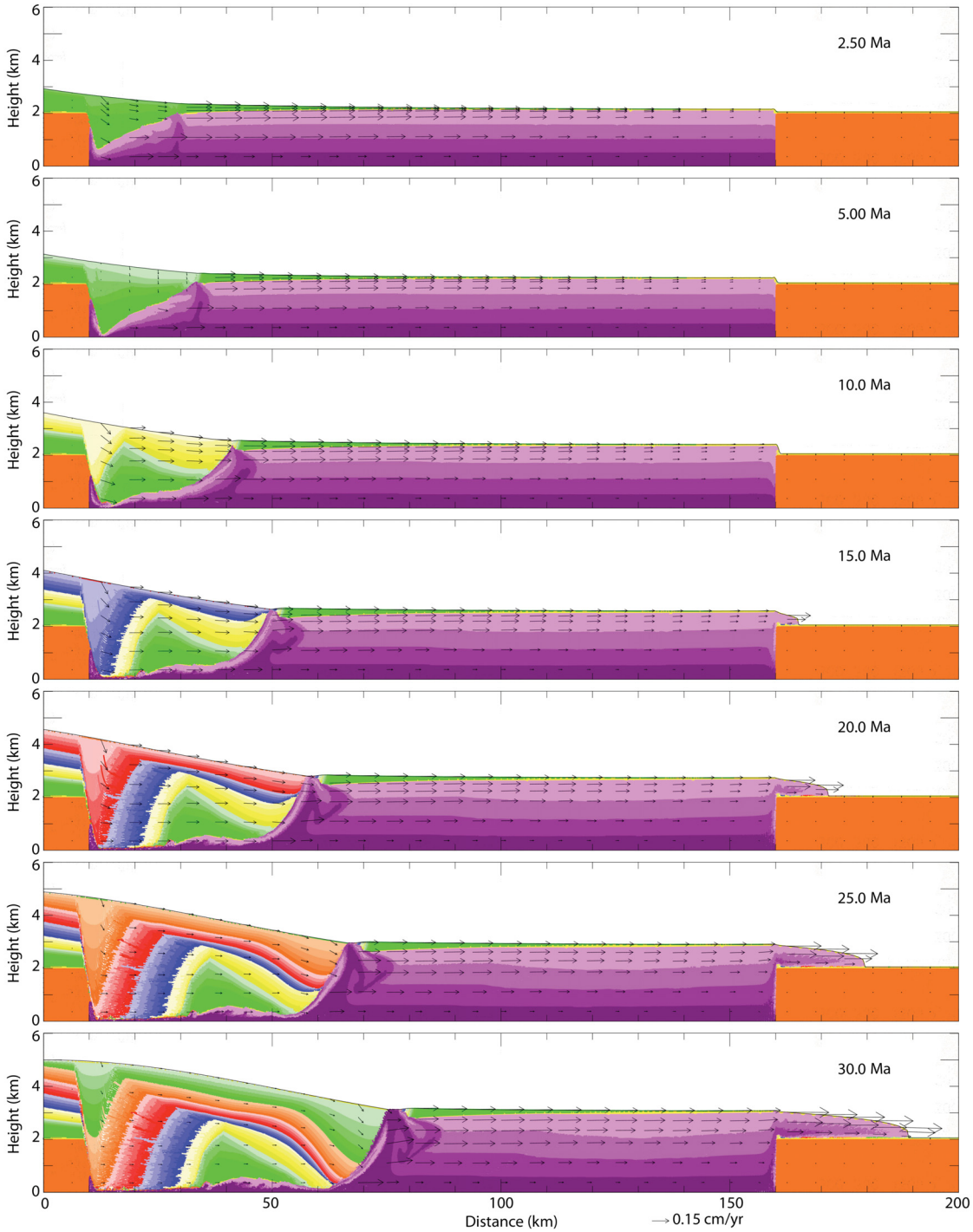

Figure 2.5: Experiment Natural Properties, Compacting NPC, representative of nature with compacting sediment. Salt is magenta, pre-kinematic sediment is orange, prograding sediment has graded colouration. Vertical exaggeration 8:1. Prograding sediments form an expulsion rollover with moderate dip angle and experience both regional and counter-regional faulting. Salt is expelled laterally, thickens, and forms a nappe over the distal sediment buttress.

2.6.1.1.2 Experiment NPL: Nature Equivalent, with Low Density Sediment

In NPL (Figure 2.3), the sediment, density 1900 kg/m^3, is less dense than the salt and represents a stable stratification with no upward salt buoyancy. As in experiment NPN (Figure 2.2), early flow in the salt is characterized by Poiseuille flow beneath the prograding sediments and Couette flow seaward of the slope. The velocities are, however, smaller than in NPN, owing to the lower sediment density. Salt expulsion is less vigorous; the seaward expulsion rollover and extreme thinning of the basal salt begin to develop at 15 Ma and mature later, between 20 and 30 Ma. In other respects NPN and NPL are similar, except that NPL has no salt exposed at the surface and there is no faulting within the anticline.

2.6.1.1.3 Model NPH: Nature Equivalent, with High Density Sediment

The results of experiment NPH, with sediment density constant at 2300 kg/m^3, more dense than salt, are shown in Figure 2.4. Magnitudes of both Poiseuille and Couette flow in the salt are larger in this experiment, owing to the larger pressure gradient, and the whole system is more mobile than in all other experiments with natural system equivalent densities. Here extension involves the formation of several listric normal faults. Formation of paired listric normal and expulsion rollovers between lateral positions 10 and 30 km begins before 5 Ma. Adjacent to the landward edge of the basin, beds rotate to dip landward in response to movement along the listric normal fault that forms at the basin edge. Between 20 and 30 km, initially an expulsion rollover causes successive beds

in this region to dip seaward, but subsequent movement along a normal fault bisects the anticlinal depocenter (at 15 Ma) and results in a landward dip of the beds between 30 and 50 km at this time. The salt pillow trapped beneath the associated anticlinal structure migrates seaward as the sediment detaches above the salt and translates seaward. By 20 Ma a counter-regional normal fault has formed at 40 km above the salt pillow and this structure and its landward counterpart become the main extensional structures. Thickening of the salt seaward of the progradation profile results in the formation of a salt nappe by 10 Ma. As in NPN salt is exposed at the surface at the toe of the slope.

2.6.1.1.4 Experiment NPC: Compacting Sediment

Figure 2.5 shows the results of experiment NPC, with natural system equivalent densities and compacting prograding sediments. This experiment evolved similarly to the others with natural system equivalent densities. Early in the model evolution salt moved with a Poiseuille flow under the prograding sediments and a Couette flow ahead of them. An expulsion rollover developed by 10 Ma. Between 15 and 30 Ma the expulsion rollover propagated seaward. A salt nappe forms between 10 and 15 Ma. The overall evolution is intermediate to experiments NPL and NPN.

2.6.1.2 Experiment AP-1: Analogue Experiment Equivalent Densities

The results of experiment AP-1, with analogue experiment equivalent sediment and salt densities of 1600 kg/m^3 and 990 kg/m^3, the highest density contrast of all experiments presented, is shown in Figure 2.6. The evolution is distinctly different from the natural system equivalent experiments in that AP-1 develops a series of 2D minibasins and diapirs (strictly salt walls), instead of an expulsion rollover. By 0.5 Ma salt has locally pierced the overlying prograding sediments, and by 2.5 Ma three diapir-minibasin pairs have formed. Nearly all salt in this region is expelled from beneath the sinking minibasins and into the emerging diapirs. The large topographic relief of the diapirs allows the low density salt (silicone equivalent) to spread laterally above the sand forming wide diapir tops that coalesce to form a canopy (Figure 2.6: 5,15 Ma). This is certainly assisted by squeezing of the diapirs. The canopy flows downslope assisted by loading by prograding sediments. Thin sediment seaward of the base of the slope is folded and disaggregated, and the disrupted regions become the focus of shortening. Even small pieces of this thin overburden sink rapidly to the base of the salt layer. The bases of the minibasins, although apparently welded against the bottom of the salt basin, continue to detach and translate the diapir-minibasin province seaward as the landward bounding rollover structure continues to develop. Figure 2.7 highlights the development of diapir-minibasin pairs in this experiment. In this figure the colour sequence showing the chronostratigraphy of prograding sediments has been altered to show structural features in more detail; all prograding sediment has the same material properties. During minibasin formation sediment layers initial dip landward, but rotated to dip seaward as

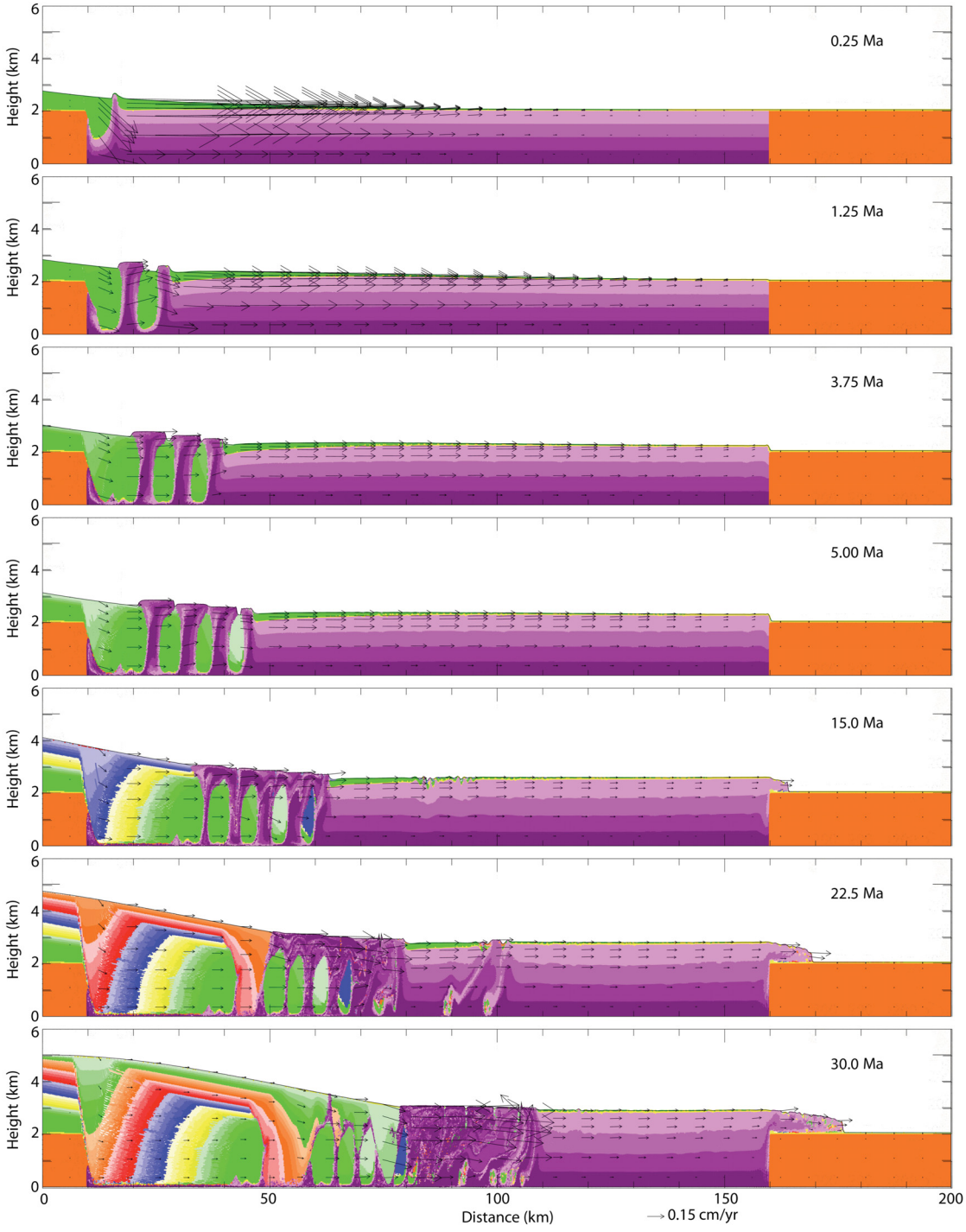

Figure 2.6: Experiment Analogue Properties (AP1), representative of physical analogue experiments with densities (ρ_d = 1600 kg/m^3; ρ_s = 990 kg/m^3) which overestimate buoyancy and underestimate sediment strength and pressure gradient. Salt is magenta, pre-kinematic sediment is orange, prograding sediment has graded colouration. Vertical exaggeration 8:1. Diapir minibasin pairs form in response to progradation and migrate seaward. Salt moves vertically through diapirs, coalesces into a canopy, and flows into the main salt body. Salt thickening and nappe formation is also observed.

salt was expelled preferentially from beneath the distal region of the minibasin. Lateral movement of salt ahead of the prograding sediments was dominated by Couette flow. By 10 Ma squeezing of the diapirs causes salt to be conducted vertically and expelled at the surface as sheets that coalesce into a canopy. Diapir and minibasin formation continue until 15 Ma, at which point thickening of the salt body seaward of the progradation profile prevents further sedimentation at the toe of the slope. A salt nappe also forms at this time, over the distal syn-depositional sediment block. Between 15 and 30 Ma continued squeezing of the diapirs evacuates nearly all salt to the surface, where it flows down slope and reintegrates with the autochthonous salt body.

2.6.1.3 Influence of Reduced Density Contrast and Thickness of Initial Cover

In addition to the experiments outlined above, two additional tests were performed to determine the sensitivity of structural style (diapir-minibasin pairs versus expulsion rollover) to variations in density contrast between the sediment and salt and initial thickness of sediment cover. These experiments used densities, geometry, and progradation rate as in AP-1, except as noted. For a salt density of 990 kg/m^3, it was found that diapirs and minibasins formed for sediment densities greater than 1300 kg/m^3 (density contrasts of approximately 300 kg/m^3 or greater), while at lower sediment densities an expulsion rollover formed.

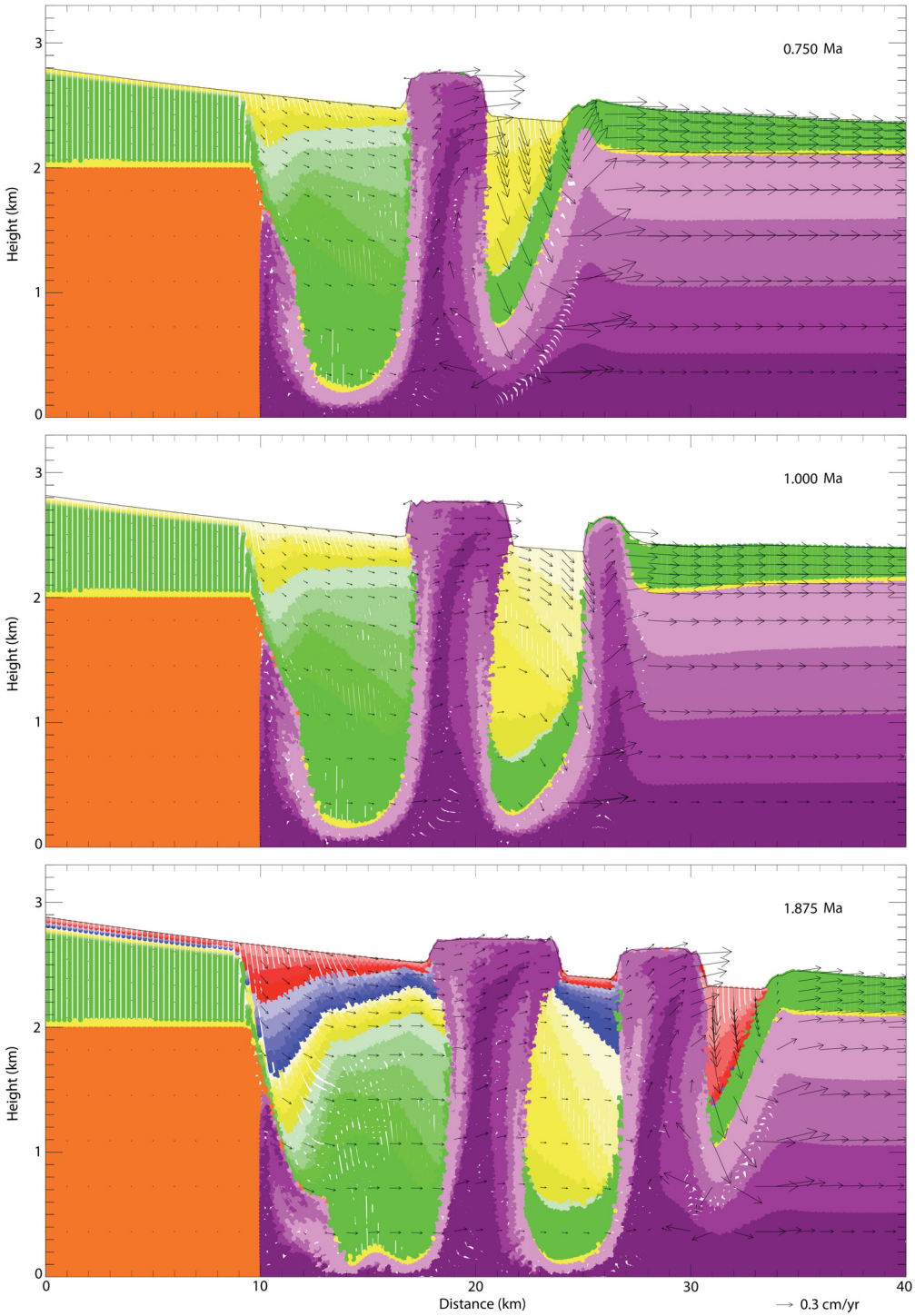

Figure 2.7: Detail of dipair and minibasin formation, for experiment AP1, with densities representative of physical analogue experiments (ρ_d = 1600 kg/m^3; ρ_s = 990 kg/m^3). Salt is magenta, pre-kinematic sediment is orange, prograding sediment has graded colouration. Vertical exaggeration 8:1.

The addition of a layer of uniform-thickness sediment over the entire model domain, before the onset of progradation, served to reduce the tendency for diapirs and minibasins to form. For sediment and salt densities of 1600 kg/m^3 and 990 kg/m^3, initial sediment cover thicknesses of 750m or more suppressed diapir and minibasin formation. This can be ascribed to the finite strength of the overburden which is larger than the buoyancy force that develops at the salt-sediment interface [*Schultz-Ela et al*., 1993].

2.6.2 Isolating the Impact of Buoyancy, Sediment Strength, and Pressure Gradient

The above experiments demonstrate the difference in structural evolution resulting from a change of sediment and salt densities from values typical of nature to those often used in physical experiments, but do not isolate the separate effects on the buoyancy force and sediment strength. To isolate the impact of a disproportionately large buoyancy force, the experiment APS (representative of analogue experiments but with corrected sediment strength) set sediment density equal to 2150 kg/m^3 (an intermediate value of the nature-equivalent range), and salt density equal to 1540 kg/m^3. This preserved the analogue experiment density difference between sediment and salt at 610 kg/m^3, as in experiment AP-1, but corrected for the decreased sediment strength associated with typical analogue experiment sand density of 1600 kg/m^3. Conversely, to isolate the impact of decreased sediment strength, in experiment APB (representative of analogue experiments but with corrected buoyancy) the absolute density of sediment was held at the analogue equivalent value of 1600 kg/m^3, and the salt density was increased to 1450 kg/m^3, to give a density difference of 150 kg/m^3, more representative of nature. Table 2.3 outlines the four experiments considered in this aspect of the analysis.

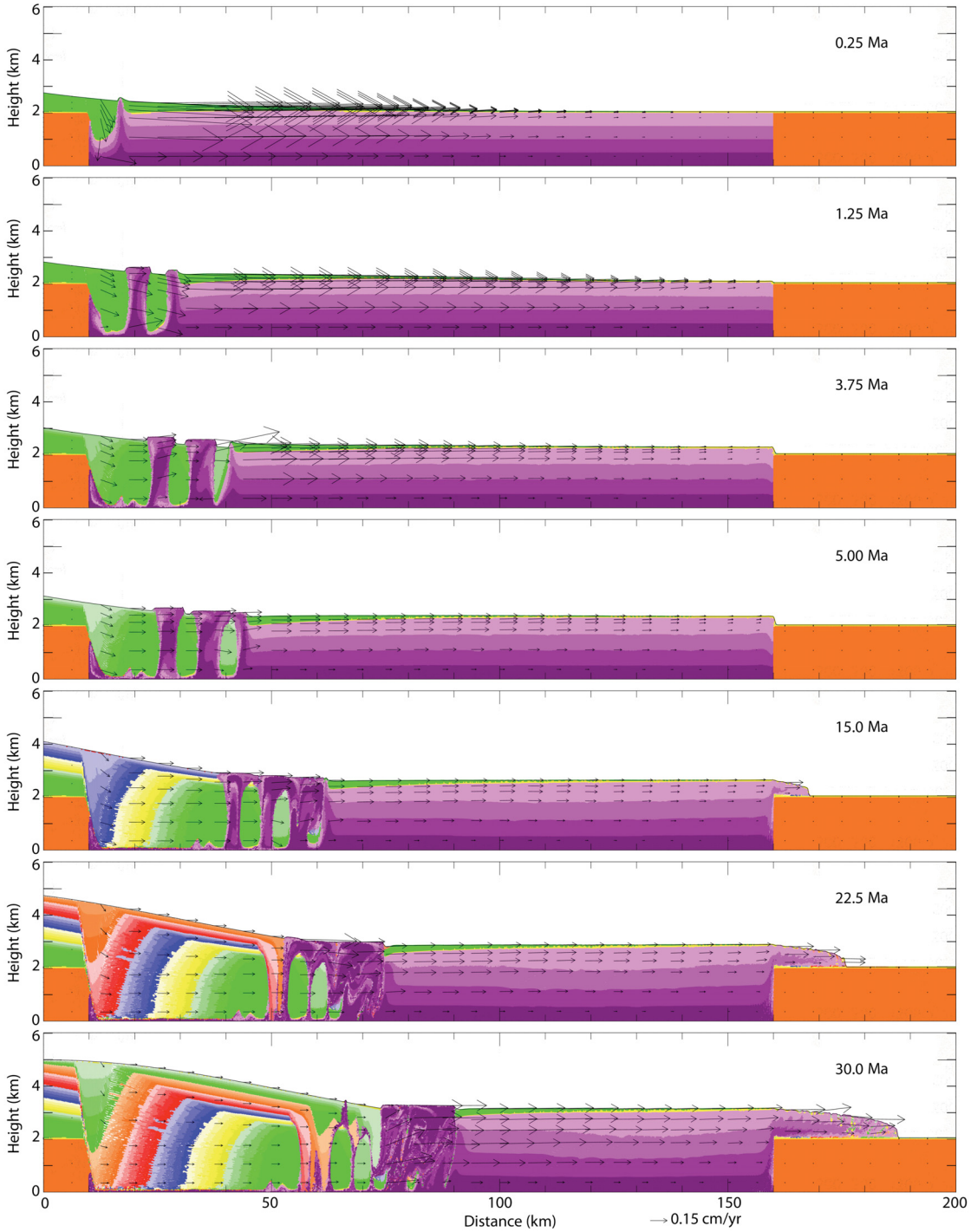

Figure 2.8: Experiment Analogue Properties, Strength corrected (APS), with physical analogue experiment densities corrected for low sediment strength and pressure gradient while maintaining disproportionately high buoyancy (ρ_d = 2150 kg/m^3; ρ_s = 1540 kg/m^3). Salt is magenta, pre-kinematic sediment is orange, prograding sediment has graded colouration. Vertical exaggeration 8:1. Diapir minibasin pairs (three, compared to four for experiment AP1) form in response to progradation and migrate seaward. Salt moves vertically through diapirs, coalesces into a canopy, and flows into the main salt body. Salt thickening and nappe formation is also observed.

The results of experiments APS and APB (Figures 2.8 and 2.9) are shown in the same manner as the previous models. Experiment APS, which isolates the effect of high buoyancy force in the analogue-equivalent experiments, develops a diapir-minibasin style geometry, though with fewer of these structures than were observed for the original analogue-equivalent experiment AP1. In contrast, experiment APB, which isolated the impact of disproportionately low sediment strength and pressure gradient when using analogue-equivalent densities, developed the paired normal fault and expulsion rollover system similar to those seen in experiments NPN, NPL, NPH, and NPC (Figure 2.2, 2.3, 2.4, and 2.5, respectively), with nature-equivalent densities. Successive sediment beds rotate to a relatively steeply-dipping final orientation, thereby forming the primary anticlinal structure, and by 30 Ma a normal fault develops within the anticline above the salt pillow (Figure 2.9).

Overall, experiment APB (Figure 2.9) is similar to NPH (Figure 2.4), which has the same salt-sediment density difference, 150 kg/m^3. However, the sediment density is lower, 1600 versus 2300 kg/m^3 and this likely accounts for differences in the evolution of the expulsion rollover. In the NP series of models (Figures 2.2-2.5), the relatively high density sediment develops a differential pressure that is sufficient to expel salt from beneath the expulsion rollover efficiently, so that little is trapped as diapirs or pillows. By contrast, experiment APB develops a series of asymmetric minibasins, starting at ~10 Ma, near the seaward edge of the prograding sediment wedge, against the main body of the salt. We interpret this behaviour to reflect the lower pressure gradient and reduced

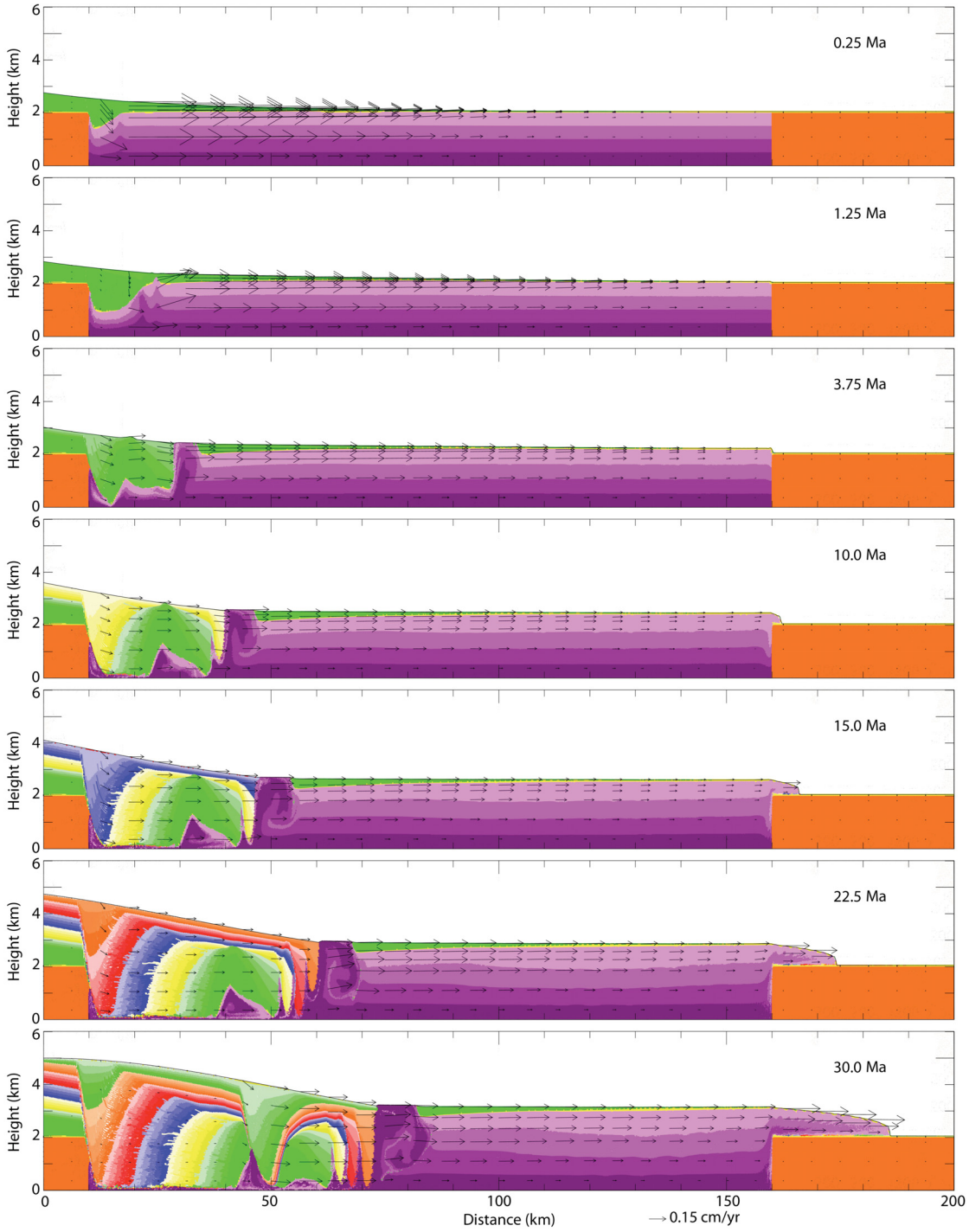

Figure 2.9: Experiment Analogue Properties, Buoyancy corrected (APB), with physical analogue experiment densities altered to correct disproportionately high buoyancy while maintaining underestimated sediment strength and pressure gradient (ρ_d = 1600 kg/m^3; ρ_s = 1450 kg/m^3). Salt is magenta, pre-kinematic sediment is orange, prograding sediment has graded colouration. Vertical exaggeration 8:1. Prograding sediments form an expulsion rollover with steep dip angle and undergo regional faulting. Salt is expelled laterally, thickens, and forms a nappe over the distal sediment buttress.

expulsion rate, such that sediment progrades faster than salt expulsion and the prograding sediment sinks rapidly into the thick salt to form a minibasin before the salt can be expelled. This process occurs in incremental steps such that salt is episodically trapped as pillows between each of the minibasins.

Table 2.3: Experimental Design Investigating Relative Importance of Buoyancy Force and Sediment Strength/Pressure Gradient on Structural Evolution Resulting from Changes in Salt and Sediment Density

	Buoyancy Force Disproportionately Large →	**Buoyancy Force Correction**
Sediment Strength/Pressure Gradient Disproportionately Small	Analogue Experiment Equivalent Values AP-1 $\rho_s = 990$ kg/m^3 $\rho_d = 1600$ kg/m^3	Isolated Impact of Sediment Strength APB $\rho_s = 1450$ kg/m^3 $\rho_d = 1600$ kg/m^3
↓		
Sediment Strength/Pressure Gradient Correction	Isolated Impact of Buoyancy APS $\rho_s = 1540$ kg/m^3 $\rho_d = 2150$ kg/m^3	Nature-Equivalent Values NPH $\rho_s = 2150$ kg/m^3 $\rho_d = 2300$ kg/m^3

It appears that inaccuracies in the scaling of the buoyancy force are most influential in determining the style of structural evolution and, in particular, are responsible for the development of minibasin-diapir systems in APS and AP-1, whereas none develop in the models with natural scaling. However, the differential pressure is also important and low density sediment, as in APB, leads to less efficient salt expulsion than in models with natural scaling.

2.7 Discussion

2.7.1 Behavior of the Models

In all experiments the prograding sedimentary wedge created a horizontal pressure gradient within the underlying salt. Failure and gravitational spreading were accommodated by a zone of extension at the landward edge of the slope and a zone of contraction seaward of the toe of the slope. Extension was accommodated by the formation of normal faults in the sedimentary overburden. Contraction created features included thickening of the distal salt body, formation of a salt nappe at the seaward edge of the salt basin, and squeezing of diapirs, where these had formed. This general behaviour can be attributed to the horizontal differential pressure exerted by the prograding sediments.

Buoyancy also influenced salt movement, particularly in cases where the prograding sediment was more dense than the underlying salt. The magnitude of the density difference between salt and overlying sediment determined the rate at which sediment sank into the salt. For the natural system equivalent experiments this was manifest as differences in the dip angle of sedimentary layers within an expulsion rollover (denser sediment produced more steeply-dipping beds). In the analogue model equivalent experiments AP-1 and APS, the density contrast, 610 kg/m^3, was sufficiently large to allow formation of rapidly-sinking minibasins and associated diapirs.

Both Poiseuille and Couette flow were observed within the salt. Stability of a frictional-plastic overburden overlying a viscous substratum, and the resultant flow regime within

the viscous layer, has previously been analyzed [*Lehner*, 1977, 2000; *Last*, 1988; *Vendeville and Jackson*, 1992; *Gemmer et al*., 2004]. Poiseuille flow occurred when a horizontal pressure gradient was imposed by lateral variation in the thickness of the sedimentary overburden, and the overburden remained stable. Couette, or shear, flow occurred either when sedimentary overburden was moving laterally above the salt, imposing a horizontal velocity at the salt surface, or when the horizontally flowing salt body had a free upper surface with no sedimentary cover. Poiseuille flow is most easily observed beneath the prograding sediments in the early evolution (up to 10 Ma) of experiments NPL (Figure 2.3) and NPN (Figure 2.2), since in these cases sinking of sediment into the salt and salt expulsion occurred relatively slowly. Couette flow was observed seaward of the progradation profile in all experiments. In this region, salt was bounded by a no-slip surface at the base of the model and a free surface at the top of the salt. The magnitude of velocity vectors decreased towards the distal end of the salt basin, were lateral movement was impeded by the syn-depositional sedimentary buffer, resulting in thickening of the salt body.

The four natural system equivalent experiments applied similar horizontal differential pressure to the salt (variations were due to differences in sediment density; geometry of the prograding sediment remained constant). The effects of buoyancy, however, differed among these experiments, as the ratio of density of overburden to salt was varied. All natural system equivalent experiments (NPN, NPL, NPH, and NPC, Figures 2.2-2.5) produced similar structural styles. Landward of the top of the slope, extension was accommodated by a series of regional and in some cases counter-regional normal faults.

An expulsion rollover formed beneath the slope, with bedding layers rotating downward as salt was expelled from beneath the deposited sediments, resulting in dip angles higher than those at the time of deposition. Seaward of the toe of slope contraction was accommodated by thickening of the salt body. In each case, when the top of salt elevation had increased by approximately 600 m a salt nappe formed over the distal syn-depositional sediment block. The influence of differing sediment density was observed in the dip angle of successive beds within the expulsion rollover, with lower density sediments producing expulsion rollovers with lower dip angles, and vice versa. Experiment NPC (Figure 2.5) produced an expulsion rollover with dip angle between that of NPL and NPH. The relative instability of experiments NPH, NPN, and NPL, as demonstrated by magnitude of velocity within the salt under prograding sediment, was generally found to agree with predicted relative instability, mobility, calculated according to *Gemmer et al*. [2004].

2.7.2 Buoyancy

The effect of buoyancy forces was much more pronounced in the analogue model equivalent experiments, owing to the higher density difference between sedimentary overburden and salt, compared to the natural system equivalent experiments. The analogue properties experiment AP-1, with high density difference between sediment and salt, produced a profoundly different style of salt and sediment deformation than did the experiments with natural system equivalent densities. The high difference in density between sedimentary overburden and salt resulted in rapid sinking of the prograding

sediments, and the production of minibasins and diapirs at the toe of the progradation profile. No diapirs formed in the dry natural system equivalent models because these models did not develop plastic Rayleigh-Taylor instabilities, the equivalent of viscous Rayleigh-Taylor instabilities, but in which one or more of the materials has a finite yield strength. Experiment APS, with modified analogue equivalent densities which corrected the low sediment strength and pressure gradient, developed similarly to AP-1. Experiment APB, with analogue equivalent densities modified to correct for the disproportionately high buoyancy force, developed an expulsion rollover, similarly to experiments NPH, NPL, NPN, and NPC.

2.7.3 Differential Pressure and Sediment Strength

In addition to enhanced buoyancy forces in the analogue property models, all models with low density overburden, AP-1, APM, and APB, and NPHW exert lower absolute and horizontal differential pressures, and have reduced sediment strength by comparison with the natural property models. These factors reduced the efficiency of salt expulsion but the effect was less important than that of buoyancy.

Density differences intermediate between nature and physical experiment typical values were also considered, as was as the impact of initial thickness of sediment cover. It was found that a change in the structural evolution of salt and overlying sediment, from diapir-minibasin pairs to an expulsion rollover, occurred when the salt-overburden density difference was reduced below 300 kg/m^3. At these lower density differences the

growth of plastic Rayleigh-Taylor instabilities does not proceed quickly enough for diapirs and minibasins to form at a given location before the accumulated thickness of sediment cover suppresses vertical movement of salt. With sediment and salt densities of 1600 kg/m^3 and 990 kg/m^3, the same as for experiment AP-1, an initial sediment cover of thickness 750 m or greater resulted in suppression of diapir and minibasin formation. At thicknesses greater than or equal to 750 m the buoyancy force induced by the density inversion does not become sufficient to overcome the strength of the frictional-plastic sediment overburden.

2.7.4 Comparison with Physical Models

This analysis compares 2D numerical models with 3D analogue models, however care was taken to select for comparison analogue models which generally had little variation in structure in the along strike direction.

The structural features produced in the analogue equivalent experiments presented here have certain similarities to previously published physical experiments. Active development of diapiric ridges in response to horizontal differential pressure in gravity spreading experiments was observed by *Vendeville* [2005] and *Rowan and Vendeville* [2006]. Vendeville observed both active and reactive diapirism when successively longer tapered wedges of high density sediment were placed over an initially horizontal silicone substratum, simulating progradation. In this analysis the silicone had a free surface ahead of the prograding sediment. Thickening and formation of a nappe were observed in this

region, as continued progradation progressively expelled silicone laterally from beneath the applied sand. In this experiment prograding sediment was instantaneously placed over the silicone layer, resulting in faulting of the sediment and initially active diapir growth at several locations along the full length of the sediment wedge. *Rowan and Vendeville* [2006] formed minibasins and induced passive diapirism by applying an uneven pre-kinematic sediment layer (0.0 to 0.3 cm thick), allowing the model to equilibrate, and then adding subsequent syn-kinematic layers to the height of the resultant silicone ridges. *Loncke et al.* [2010] approximated two-dimensional plan form geometry in their gravity spreading experiment, by including a trough in the pre-kinematic salt basement geometry, oriented radially with respect to a lobate progradation front. They observed the formation of roughly linear diapiric ridges, perpendicular to the direction of applied horizontal differential pressure.

While active diapirism was observed early in the evolution of all experiments presented here which simulated the buoyancy force typical of physical analogue experiments, laboratory experiments that simulate gravity gliding and spreading often develop diapirs or diapiric ridges in response to faulting [e.g. *McClay et al.*, 2003; *Brun and Fort*, 2004], and active diapirism is less common. The way in which prograding sedimentation is simulated in physical experiments, typically through the application of distinct sand wedges, each of which is emplaced quickly, much faster than in nature, favours faulting and reactive diapirism. The use of a slowly moving progradation profile in the numerical analyses presented here facilitates active diapirism, and more closely simulates continuous, progressive sedimentation,. It should also be noted that the progradation

profile we use does not limit the volume of sediment available to fill bathymetric lows at any given time step, further encouraging minibasin development. Another factor which influences the development of diapir-minibasin pairs is the thickness of pre-kinematic sediment cover over salt. Our analyses show that at thicknesses greater than ~ 750 m (0.75 cm at the laboratory scale) the finite frictional strength of the sediment cover is sufficient to suppress active diapir formation, even in models like AP-1. Many physical experiments which produce only reactive diapirism, involve a pre-kinematic sand cover over silicone of thickness greater than 0.75 cm [e.g., *Del Ventisette et al*., 2005; *Brun and Fort*, 2004]. Note that sediment was assigned zero cohesion in the numerical experiments presented here. *Lohrmann et al*. [2003] reported that sands used for analogue experiments typically have an effective cohesion on the order of 50-100 Pa, equivalent to 5-10 MPa at the natural scale, which would provide an additional force to counter diapir formation.

Recently, *Brun and Fort* [2011, Appendix 2] comment on the scaling used in analogue models, "The density contrast between silicone putty and sand ($\Delta\rho$ = 1.4) is slightly higher than might be expected between salt and sediments in nature ($\Delta\rho$ =1.05 to 1.18) according to *Weijermars et al*. [1993]. However, as pointed out by *Weijermars et al*. [1993] and *Vendeville and Jackson* [1992], this disparity is acceptable because the density contrast between salt and sediments is not the primary factor responsible for the rise of diapirs". We suggest that there are circumstances where buoyancy has a strong effect on diapirism, as shown in the model experiments presented here. The view that

buoyancy is not important may result from an over emphasis on horizontal differential pressure as the major driving force in salt tectonics.

2.7.5 Consideration of Sub-marine versus Sub-aerial Setting and Pore Fluid Pressure: A Possible Remedy for Scaling Errors in Physical Analogue Experiments

2.7.5.1 Scaling to a Submarine Natural System

The results presented above point to scaling discrepancies between analogue models and their natural prototypes (Table 2.1, column 3) and this has consequences, as shown by the results of the numerical models. In the absence of materials that scale correctly, we suggest an alternative approach that helps reconcile the analogue and natural systems, namely; that the dry analogue models be compared with truly submarine natural systems. That is, we propose that dry analogue experiments, with reduced sediment density, can be scaled to represent natural submarine salt tectonics. In a submarine setting the buoyancy force at the seabed, between the water and sediment is approximately proportional to 1300 kg/m^3 (~ 2300 - 1000 kg/m^3) and that acting between sediment and the salt is 150 kg/m^3 (~2300 - 2150 kg/m^3), where we have assumed the sediment density is 2300 kg/m^3 for illustrative purposes. We have also used a nominal density of water of 1000 kg/m^3, but the calculations are easily done for sea water, density 1030 kg/m^3; the points we make are valid for both cases. The scaling of the buoyancy forces in analogue experiments can be made approximately correct by using dry (no water loading) analogue models with sediment density 1300 kg/m^3 and silicone density 1150 kg/m^3. These choices reproduce the natural submarine density differences. The equivalent conclusion is reached by

assuming that in the natural submarine system the sediment and salt act with their reduced densities owing to the buoyancy of the water.

Similarly, the horizontal differential pressure exerted by prograding sediment in a submarine setting is also approximately proportional to its reduced density, 1300 kg/m^3 (~ 2300 - 1000 kg/m^3), which likewise can be reproduced by sediment with density 1300 kg/m^3. Moreover, flow of submarine salt occurs in proportion to its reduced density, 1150 kg/m^3 (2150 - 1000 kg/m^3), which would be equal to silicone of density 1150 kg/m^3, flowing subaerially.

Finally, the strength of hydrostatically pressured sediment can be reproduced as follows. If hydrostatic pore fluid of pressure P_f is included in the model design, sediment yield strength, σ_Y is given by:

$$\begin{aligned} \sigma_Y &= P' \sin\phi \\ \sigma_Y &= \left(P - P_f\right)\sin\phi \\ \sigma_Y &= gL\left(\rho_d - \rho_w\right)\sin\phi \end{aligned} \tag{15}$$

where P' is the effective pressure acting within the sediment and ρ_w is the density of water and we have used the lithostatic pressure as an approximation of the mean stress. By inspection, the yield strength is equal to that of dry sediment with density 1300 kg/m^3, so that if sediment with this density can be made, the dry analogue model will be approximately equivalent to the submarine natural system.

Under these circumstances the dry analogue laboratory model would be correctly scaled

to a simple submarine natural system in which other factors, like sediment compaction, are ignored. In practice, sediment densities equal to that of silicone have been achieved by mixing sand with hollow ceramic microspheres [*Rossi and Storti*, 2003; *Dooley et al*., 2009], so a density in the range 1000 - 1300 kg/m^3) could easily be achieved. Silicone with density of 1140 kg/m^3 was used by *Storti et al*., 2007], while others have been achieved similar silicone densities by mixing lower densities silicones, such as PDMS (SGM-36), with inert higher-density particles [eg. *Marues*, 2008; *Bialas et al*., 2011]. The scaling (Equations 4-7) has been recalculated using the reduced, effective densities of the natural sediment and salt, 1300 and 1150 kg/m^3 (Table 2.1, column 3).

2.7.5.2 Tests of Models Scaled for Submarine Conditions

Two experiments were conducted to test the proposed scaling of dry analogue models for submarine salt tectonics (including both water load and hydrostatic pore fluid pressure). First, experiment NPHW used salt and sediment densities of 2150 and 2300 kg/m^3, the same as for experiment NPH, but added water (density 1000 kg/m^3) to a depth greater than the prograding sediments, as well as hydrostatic pore fluid pressure in the sediment. It was assumed that the salt was impermeable and dry, except for fluid inclusions, and therefore there is no pore fluid effect in the salt. Thus NPHW is a submarine equivalent of NPH and has properties that correspond to simplified submarine natural systems. The second experiment, APM, set sediment and salt densities to 1300 and 1150 kg/m^3, with the density difference between sediment and salt corrected to a value more representative of nature by reducing sediment density and increasing salt density, with respect to the

earlier AP models. This model corresponds quite well to an equivalent submarine experiment. Here, the effect of water loading and hydrostatic fluid pressure are not included (APM is a 'dry' model), and sediment and salt act with their densities reduced by an amount equal to the density of water. NPHW and APM are respectively models corresponding to a simplified natural submarine prototype, and the 'dry' correctly density scaled analogue equivalent.

The results (Figures 2.10 and 2.11) show reasonable agreement between NPHW and APM. In both cases, salt breached the sedimentary overburden at approximately 2.5 Ma. For NPHW a single diapir-minibasin pair formed at this location between 2.5 and 7.5 Ma. Subsequent vertical movement of salt within the diapir was limited, and a salt canopy over the adjoining minibasin formed 10-15 Ma later than in experiment AP-1. A salt nappe formed in both experiments, and traveled between 20 and 25 km beyond the distal edge of the original salt basin. For both NPHW and APM a series of late-stage minibasins formed near the front of the prograding sediment wedge, beginning at 10 Ma. In the case of APM (Figure 2.11) the minibasins formed against the main body of salt, whereas in NPHW minibasin formation occurred against the landward edge of the single diapir formed earlier in the experiment. These late-stage minibasins are similar to those in APB and evolve in the same way, as prograding sediment progressively sinks into accommodation space created as the salt moves laterally under differential pressure, similar to the 'sedimentary topographic loading' mechanism of minibasin formation explained by Hudec et al. [*Hudec et al.,* 2009]. They similarly occur in models with low differential pressure resulting from a low density of the overburden (1300 kg/m^3 in APM)

or a corresponding low density difference between the overburden and water (an effective density of 2300-1000 kg/m^3 in NPHW).

A third experiment was conducted, corresponding to the best approximation to the submarine natural prototype that can be achieved in dry analogue models without adjusting the density of the PDMS (SGM-36) silicone. This experiment had sediment and salt densities of 1140 kgm^3 and 990 kg/m^3. Here the assumption is that the density of silicone cannot be increased and therefore the sediment density is chosen to preserve the natural difference between sediment and salt densities, 150 kg/m^3. This experiment developed similarly to APM.

2.7.6 Scaled Models for Submarine Salt Tectonics

A promising direction for improving the scaling of analogue models is to design them to reproduce submarine conditions. If the density of sand used in physical analogue experiments is reduced by mixing with hollow ceramic microspheres, a range of densities can be produced such that the density difference between sand and silicone approximates natural conditions. The density difference between silicone and air, which influences the rate at which silicone with a free surface flows under the influence of gravity, like the distal salt nappe, is similar to that between salt and water, and can be adjusted by mixing the silicone with inert higher density particles. This is also true for the differential pressure, which for submarine conditions scales with the density difference between overburden and water. Lastly, the reduction in sediment strength resulting from the low

density of sand compared to sedimentary rocks in nature (1300 kg/m^3 versus ~2300 kg/m^3) is equivalent to the strength reduction in the natural system associated with introducing hydrostatic pore fluid pressure throughout the sedimentary overburden. Under these conditions, scaled dry analogue models can reasonably reproduce their natural, hydrostatically pressured submarine equivalents. These conditions produce density scaling for submarine salt tectonic analogue experiments which is as accurate as possible within the limitations imposed by partial density stripping, that is, reducing the absolute densities of materials but preserving the density differences at interfaces between them. Comparison of models NPHW (Figure 2.10) and APM (Figure 2.11) provides one example of these limitations. Of course, scaled density variations with compaction are more difficult to reproduce, as are pore-fluid overpressures [*Mourgues and Cobbold,* 2006].

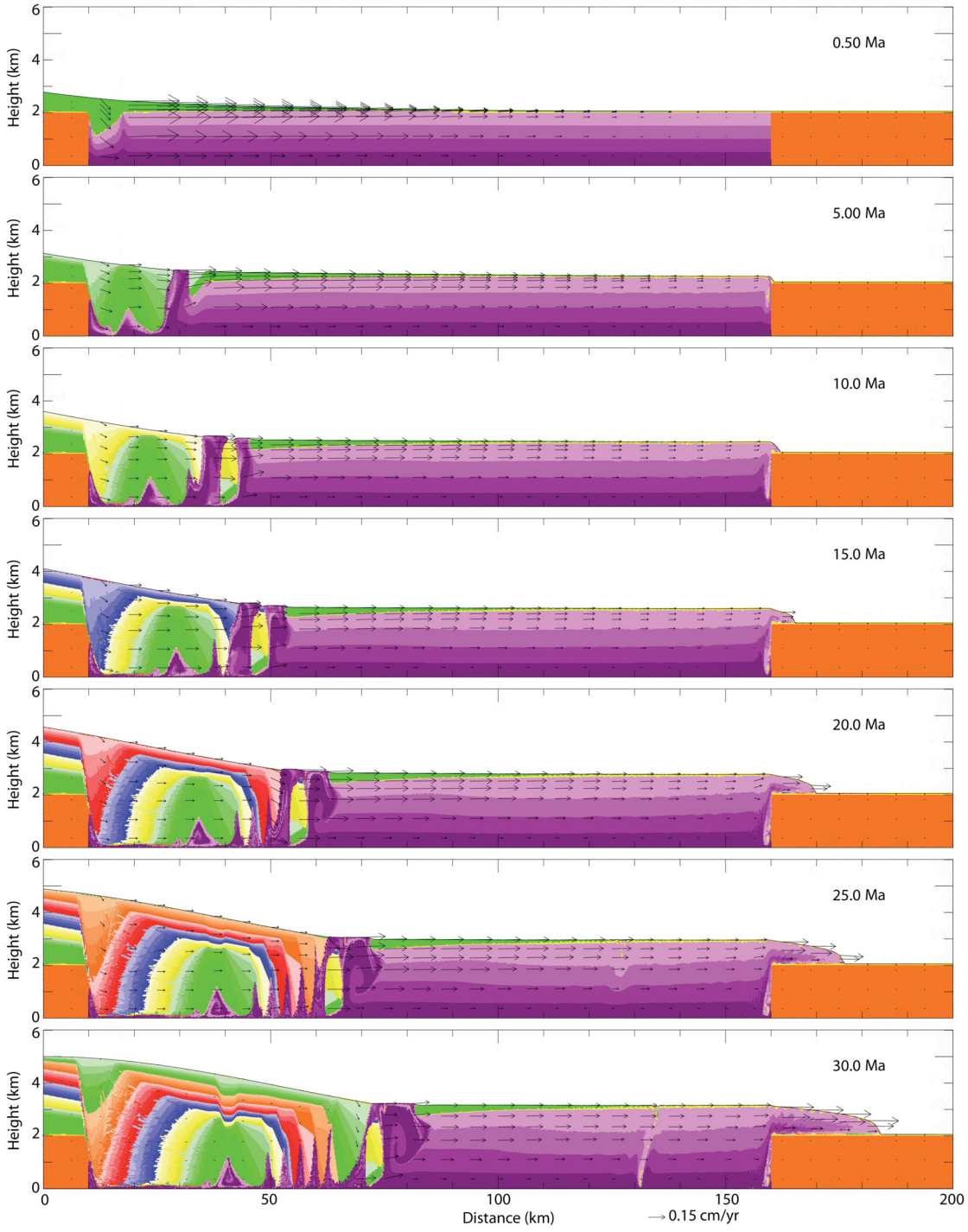

Figure 2.10: Experiment Natural Properties, High density, with Water (NPHW), representative of submarine natural system (ρ_d = 2300 kg/m^3; ρ_s = 2150 kg/m^3, with water load and hydrostatic pore fluid pressure). Salt is magenta, pre-kinematic sediment is orange, prograding sediment has graded colouration. Vertical exaggeration 8:1. A single diapir minibasin pair forms. Subsequent progradation results in an expulsion rollover with steep dip angle. Salt is expelled laterally and thickens; the salt nappe flows at a slower rate over the distance sediment buttress, compared to experiment NPH.

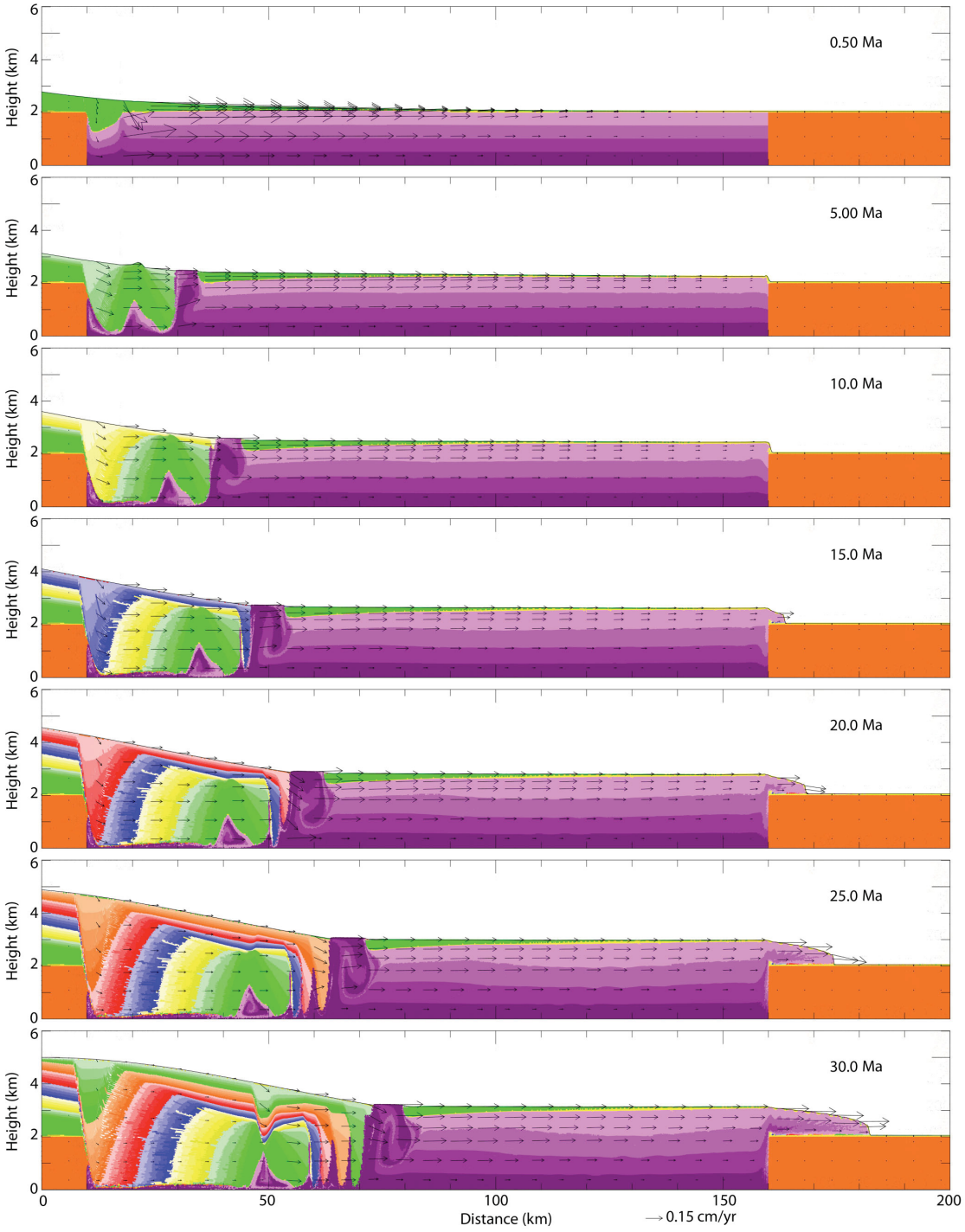

Figure 2.11: Experiment Analogue Properties, Modified (APM), representative of physical analogue experiments with reduced sediment density (ρ_d = 1300 kg/m^3; ρ_s = 1150 kg/m^3), considered to be analogous to a submarine natural system. Salt is magenta, pre-kinematic sediment is orange, prograding sediment has graded colouration. Vertical exaggeration 8:1. Prograding sediments form an expulsion rollover with steep dip angle. Salt is expelled laterally, thickens, and forms a nappe over the distal sediment buttress.

2.8 Conclusions

1. Densities of sedimentary rock and salt analogue materials typically used in physical analogue experiments of salt tectonics systems result in three scaling inaccuracies, when compared with nature:
    a. Buoyancy is overestimated owing to the excessively high ratio of density difference between sedimentary overburden and salt divided by the density of salt;
    b. Pressure gradient and sediment strength are underestimated, owing to the lower density of sand compared to sedimentary rock;
    c. Time is underestimated (progresses more quickly) in the physical experiments compared to nature, owing to the lower density of silicone compared to salt.
2. All else being held equal, a change in salt and sediment density from values typically encountered in nature to those often used in physical analogue experiments results in a fundamental shift in the structural evolution of a gravity spreading salt tectonics system, from expulsion rollover to diapir-minibasin pairs.
3. The overestimated buoyancy force in physical analogue experiments has more impact on the overall style of system evolution than do the underestimated sediment strength and pressure gradient. Considering physical analogue equivalent experiments, the formation of diapir-minibasin pairs persists for sediment densities as low as ~1300 kg/m^3 (~300 kg/m^3 more dense than the salt analogue) and for initial sediment cover thicknesses up to roughly 750 m (0.75 cm at the laboratory scale). The later may explain in part why the extent of

diapirism observed in our experiments is not often seen in physical analogue models, as initial cover thicknesses > 1 cm are often applied.

4. The way in which prograding sediments are applied is probably also partially responsible for the infrequency with which active diapirism is observed in physical analogue experiments, compared to the range of conditions under which it is observed in our numerical analysis. It is common in physical experiments to apply prograding sediments rapidly in distinct wedges and not to subsequently 'top up' areas of subsidence; this pattern favours faulting and the formation of reactive diapirs.
5. If the density of sand is reduced to ~1300 kg/m^3, as has been demonstrated possible by mixing with hollow ceramic microspheres [*Dooley et al.*, 2009], and the density of silicone is ~1150 kg/m^3 (possibly increased by mixing with higher density inert particles), dry physical analogue experiments are a reasonable representation of submarine gravity-driven salt tectonics systems.
6. We recommend that physical experiments that are directly comparable with these numerical analyses be undertaken.

2.9 Acknowledgements

This work was funded in part by NSERC. JA acknowledges an NSERC graduate scholarship. CB was also supported by the Canada Research Chair in Geodynamics. We acknowledge helpful discussions with Steven Ings and Mark Deptuck, and thank Mark Deptuck for a review of an earlier version of the paper. We thank Bruno Vendeville, an anonymous reviewer, and the associate editor for constructive comments.

2.10 References

Albertz, M., C. Beaumont, J.W. Shimeld, S.J. Ings, and S. Gradmann (2010), An investigation of salt tectonic structural styles in the Scotian Basin, offshore Atlantic Canada: 1: Comparison of observations with geometrically simple numerical models, *Tectonics*, *29*, TC4017, doi:10.1029/2009TC002539.

Albertz, M., and C. Beaumont (2010), An investigation of salt tectonic structural styles in the Scotian Basin, offshore Atlantic Canada: 2. Comparison of observations with geometrically complex numerical models, Tectonics, 29, TC4018, 2010, doi:10.1029/2009TC002540.

Athy, L.F. (1930), Density, porosity, and compaction of sedimentary rocks, *American Association of Petroleum Geologists Bulletin*, *14*, 1-22.

Baldwin, B., and C.O. Bulter (1985), Compaction curves, *American Association of Petroleum Geologist Bulletin, 69*, 622-623.

Baikpour, S., G. Zulauf, A. Sebti, H. Kheirolah, and C. Dieti (2010), Analogue and geophysical modelling of the Garmsar Salt Nappe, Iran: constraints on the evolution of the Alborz Mountains, *Geophysical Journal International*, *182*(2), 599-612, doi: 10.1111/j.1365-246X.2010.04656.8.

Bialas, R.W., Funiciello, F., and C. Faccanna (2011), Subduction and exhumation of continental crust: insights from laboratory models, *Geophysical Journal International, 184*, 43-64, doi: 10.1111/j.1365-246X.2010.04824.x.

Bonini, M. (2003), Detachment folding, fold amplification, and diapirism in thrust wedge experiments, *Tectonics*, *22*(6), 1065-1076, doi: 0.1029/2004JB003552.

Brun, J.P., and X. Fort (2004), Compressional salt tectonics (Angolan margin), *Tectonophysics*, *382*, 129-150, doi: 10.1016/j.tecto.2003.11.014.

Brun, J.P., and X. Fort (2011), Salt tectonics at passive margins: Geology versus models, *Marine and Petroleum Geology*, *28*, 1123-1145, doi: 0.1016/j.marpetgeo.2011.03.004.

Brun, J.P., and T.P.O. Mauduit (2009), Salt rollers: Structure and kinematics from analogue modelling, *Marine and Petroleum Geology*, *26*(2), 249-258, doi: 10.1016/j.marpetgeo.2008.02.002.

Cobbold, P.R., and L. Castro (1999), Fluid pressure and effective stress in sandbox models, *Tectonophysics*, *301*, 1-19, doi: 10.1016/S0040-1951(98)00215-7.

Cohen, H.A., and K. McClay (1996), Sedimentation and shale tectonics of the northwestern Niger Delta front, *Marine and Petroleum Geology*, *13*(3), 313-328, doi:

10.1016/0264-8172(95)00067-4.

Costa, E., and B.C. Vendeville (2002), Experimental insights on the geometry and kinematics of fold-and-thrust belts above weak, viscous evaporitic decollement, *Journal of Structural Geology*, *24*(11), 1729-1739, doi: 10.1016/S0191-8141(01)00169-9.

Del Ventisette, C., D. Montanari, M. Bonini, and F. Sani (2005), Positive fault inversion triggering 'intrusive diapirism': an analogue modeling perspective, *Terra Nova*, *17*, 478-485, doi: 0.1111/j.1365-3121.2005.00637.x.

Del Ventisette, C., D. Montanari, F. Sani, and M. Bonini (2006), Basin inversion and fault reactivation in laboratory experiments, *Journal of Structural Geology*, *28*, 2067-2083, doi: 10.1016/j.jsg.2006.07.012.

Dooley, T.P., M.P.A. Jackson, and M.R. Hudec (2007), Initiation and growth of salt-based thrust belts on passive margins: results from physical models, *Basin Research*, *19*(1), 165-177, doi: 0.1111/j.1365-2117.2007.00317.x.

Dooley, T.P., M.P.A. Jackson, and M.R. Hudec (2009), Inflation and deflation of deeply buried salt stocks during lateral shortening, *Journal of Structural Geology*, *31*, 582-600, doi: 10.1016/j.jsg.2009.03.013.

Fullsack, P. (1995), An arbitrary Lagrangian-Eulerian formulation for creeping flows and its application in tectonic models, *Geophysical Journal International*, *120*(1), 1-23.

Ge, H.X., M.P.A. Jackson, and B.C. Vendeville (1997), Kinematics and dynamics of salt tectonics driven by progradation, *American Association of Petroleum Geologists Bulletin*, *81*(3), 398-423.

Gemmer, L., C. Beaumont, and S.J. Ings (2005), Dynamic modelling of passive margin salt tectonics: effects of water loading, sediment properties and sedimentation patterns, *Basin Research*, *17*, 383-402.

Gemmer, L., S.J. Ings, S. Medvedev, and C. Beaumont (2004), Salt tectonics driven by differential sediment loading: stability analysis and finite-element experiments, *Basin Research*, *16*, 188-218, doi: 10.1111/j.1365-2117.2004.00229.x.

Goteti, R., S. J. Ings, and C. Beaumont (in press), Development of Salt Minibasins Initiated by Sedimentary Topographic Relief, Earth and Planetary Science Letters.

Hudec, M.R., M.P.A Jackson, and D.D. Schultz-Ela (2009), The paradox of minibasin subsidence into salt: Clues to the evolution of crustal basins, *Geological Society of America Bulletin*, *121*(1-2), 201-221.

Kuo, A.C.M. (1999), *Polymer Data Handbook*, Oxford University Press, p. 57-73.

Krezsek, C., Adam, J., and D. Grujic (2007), Mechanics of fault and expulsion rollover systems developed on passive margins detached on salt: insights from analogue modelling and optical strain monitoring, *Geological Society, London, Special Publications, 292*: 103-121, doi: 10.1144/SP292.6.

Lohrmann, J., N. Kukowski, J. Adam, and O. Oncken (2003), The impact of analogue material properties on the geometry, kinematics, and dynamics of convergent sand wedges, *Journal of Structural Geology*, *25*, 1691–1711, doi: 10.1016/S0191-8141(03)00005-1.

Loncke, L., B.C. Vendeville, V. Gaullier, and J. Mascle (2010), Respective contributions of tectonics and gravity-driven processes on the structural pattern in the Eastern Nile deep-sea fan: insights from physical experiments, *Basin Research*, *22*(5), 765-782, doi: 10.1111/j.1365-2117.2009.00436.x.

Maillard, A., V. Gaullier, B.C. Vendeville, and F. Odonne (2003), Influence of differential compaction above basement steps on salt tectonics in the Ligurian-Provencal Basin, northwest Mediterranean, *Marine and Petroleum Geology*, *20*(1), 13-27, doi: 10.1016/S0264-8172(03)00022-9.

Marone, C. (2003), Laboratory-derived friction laws and their application to seismic faulting, *Annual Review Earth and Planetary Science Letters*, *26*, 643-696, doi: 10.1146/annurev.earth.26.1.643.

Marues, F.O. (2008), Thrust initiation and propagation during shortening of a 2-layer model lithosphere, *Journal of Structural Geology, 30*(1), 29-38, doi: 10.1016/jsg.2007.09.005.

McClay, K., T. Dooley, and G. Zamora (2003), Analogue models of delta systems above ductile substrates, in, *Subsurface Sediment Mobilization*, *Geological Society Special Publication*, *216*, edited by P. Van Rensbergen, R.R. Hillis, A.J. Maltman, and C.K.Morley, 411-428, doi: 10.1144/GSL.SP.2003.216.01.27.

Mourgues, R. and P.R. Cobbold (2006), Sandbox experiments on gravitational sliding and gliding in the presence of fluid overpressures, *Journal of Structural Geology*, *28*, 887-901, doi: 10.1016/j.jsg.2005.12.013.

Press, W.H., B.P. Flannery, S.A. Teukolsky, and W.T. Vetterling (1986), *Numerical Recipes*, Cambridge Univeristy Press, Cambridge.

Rossi, D., and F. Storti (2003), New artificial granular materials for analogue laboratory experiments: aluminum and siliceous microspheres, *Journal of Structural Geology, 25*(11), 1893-1899, doi: 10.1016/S0191-8141(03)00041-5.

Rowan, M.G., and B.C. Vendeville (2006), Foldbelts with early salt withdrawal and diapirism: Physical models and examples from the northern Gulf of Mexico and the

Flinders Ranges, Australia, *Marine and Petroleum Geology*, *23*(9-10), 871-891, doi: 10.1016/j.marpetgeo.2006.08.003.

Sclater, J.G., and P.A.F. Christie (1980), Continental stretching: An explanation of the post-mid-Cretaceous subsidence of the central North Sea basin, *Journal of Geophysical Research*, *85*, 3711-3739, doi: 10.1029/JB085iB07p03711.

Schultz-Ela, D.D., M.P.A. Jackson and B.C. Vendeville (1993), Mechanics of salt diapirism, *Tectonophysics, 228*, 275-312.

Storti, F., Soto Marin, R., Rossetti, F., and A.M. Casas Sainz (2007), Evolution of experimental thrust wedges accreted from along-strike tapered, silicone-floored multilayers, *Journal of the Geological Society*, *164*(1), 73-86, doi: 10.1144/0016-76492005-186.

van Keken, P.E., C.J. Spiers, A.P., van den Berg, and E.J. Muyzert, E.J. (1993), The effective viscosity of rocksalt: implementation of steady-state creep laws in numerical models of salt diapirism. *Tectonophysics, 225*, 457-476.

Velde, B. (1996), Compaction trends of clay-rich deep sea sediment, *Marine Geology*, *133*, 193-201, doi: 10.1016/0025-3227(96)00020-5.

Vendeville, B. (2005), Salt tectonics driven by progradation: Part I - Mechanics and kinematics, *American Association of Petroleum Geologists Bulletin*, *89*(8), 1071-1079, doi: 10.1306/03310503063.

Vendeville, B., and P.R. Cobbold (1987), Synsedimentary gravitational sliding and listric normal growth faults – insights from scaled physical models, *Comptes Rendus de L Academeie Des Sciences Serie II*, *305*(16), 1313-1319.

Warsitzka, M., Kley, J., Jahne, F., and N. Kukowski (IN PRESS), Salt diapirism driven by differential loading – some insights from analogue modelling, *Tectonophysics*, doi: 10.1016/j.tecto.2011.11.018.

Weijermars, R. H., and H. Schmeling (1986), Scaling of Newtonian and non-Newtonian fluid-dynamics without inertia for quantitative modeling of rock flow due to gravity (including the concept of rheological similarity), *Physics of the Earth and Planetary Interiors*, *43*(4), 316-330, doi: 10.1016/0031-9201(86)90021-X.

Weijermars, R., M.P.A. Jackson, and B. Vendeville (1993), Rheological and tectonic modeling of salt provinces, *Tectonophysics*, *217*, 143-174, doi: 10.1016/0040-1951(93)90208-2.

Chapter 3: Continental Margin Syn-Rift Salt Tectonics at Intermediate Width Margins

Janice Allen[1] and Christopher Beaumont[2]

1) Dalhousie University, Department of Earth Sciences, 1355 Oxford St., Halifax, NS,

Canada, B3H 4R2, janice.allen@gmail.com;

2) Dalhousie University, Department of Oceanography, Halifax, Nova Scotia, Canada

3.1 Preface

This chapter is based on the paper 'Continental Margin Syn-Rift Salt Tectonics at Intermediate Width Margins', by Janice Allen and Chris Beaumont, published in the Basin Research (Allen and Beaumont, 2015). The paper has not been modified substantially from the published version, though it has been reformatted to suit the thesis. The copyright agreement form for this chapter can be found in Appendix A. Janice Allen designed and ran the models in this paper (with supervision), interpreted results, wrote the manuscript and prepared the figures, edited the manuscript with input from the co-author, and prepared the manuscript for publication. Chris Beaumont provided input and oversight on all aspects of the work.

3.2 Abstract

This paper examines interactions among syn-rift continental margin extension, evaporites, particularly rocksalt (halite), deposited in the overlying sedimentary basins, and clastic sediment loading. We present dynamically evolving 2D numerical models that combine syn-rift lithospheric extension, with salt (viscous halite, 10^{18} - 10^{19} Pa s) and clastic (frictional-plastic) sediment deposition to investigate how salt is distributed and subsequently mobilized during syn-rift extension. Example results are shown, contrasting salt deposition in the early, mid and late syn-rift phases of a single lithospheric extension model. The lithospheric model is chosen to give depth-dependent extension and intermediate width margins with proximal grabens and a hyperextended distal region. The models exhibit diachronous migration of extension toward the rift axis and this is reflected in the faulting of overlying sediments. The models illustrate the roles of timing of salt deposition, relative to rifting and subsequent sedimentation, in defining the location and deformation of syn-rift salt, with post-salt sediment progradation in some models. Late deposition of salt leads to increased lateral extent of the original salt body and decreased variation in salt thickness. Seaward flow of salt increases with later deposition; early syn-rift salt is deposited and trapped in the grabens, while mid and late syn-rift salt tends to flow towards the distal margin or even over the oceanic crust. Prograding clastic post-salt sediments drive more substantial seaward movement of mid and late syn-rift salt. A numerical model of the Red Sea with evaporite deposition during the mid to late syn-rift period, preceded and followed by aggrading and prograding clastic sediment, shows reasonable agreement with observations from the central Red Sea.

3.3 Introduction

Many rifted continental margins are strongly influenced by the deposition and deformation of evaporites owing to the inherent weakness of the rocksalt (halite) component. Evaporites are commonly deposited during the process of continental rifting, which involves lithospheric extension, the formation of the rifted margin, and the development of near-isolated basins in which seawater evaporates and 'salt' is precipitated. Considerable effort has been directed to understanding the controls on the precipitation and deformation of evaporites, generally termed 'salt tectonics' (which we will use here unless we need to distinguish halite (rocksalt) from other evaporites) (*Ge et al*., 1997; *Hudec and Jackson*, 2007; *Hudec et al*., 2009; *Warren,* 2010, *Warren,* 2006), in part owing to the importance of this topic to the petroleum industry. Previous studies have largely focused on salt tectonics of rifted margins after continental breakup, when rifting and lithospheric extension are finished. Less attention has been paid to the interaction between salt deposited during rifting, 'syn-rift salt', and crustal deformation that accompanies rifting. The latter is, however, important because syn-rift salt deposition is common and the syn-rift tectonics may have a profound impact on the mobilization of the salt and the ensuing salt tectonics. For example, in cases where salt has already been strongly deformed by the underlying crustal tectonics, which partitions the salt into grabens separated by horsts, the effect of gravity gliding and/or spreading (e.g. *Fort and Brun,* 2012) may be less important than for post-rift salt deposited on a regionally smooth surface. The goal of this study is to develop dynamically evolving numerical models of the coupled lithospheric extension-salt tectonic system and to use these models to study

the interaction among rifting tectonics, sedimentation, and the deposition and deformation of salt and more generally evaporites.

Rifted continental margins form as a result of the extension, stretching and thinning of the lithosphere prior to continental breakup and ocean floor spreading. Several conceptual mechanisms have been proposed to explain this process, including pure shear (*McKenzie*, 1978), simple shear (*Wernicke*, 1981, 1985), and combinations thereof (*Lister et al*., 1986, 1991). Numerical modeling has been used to study the evolution of rifted margins, including the development of wide versus narrow rifts (*Buck*, 1991; *Hopper and Buck*, 1996; *Buck et al*., 1999; *Huismans and Beaumont*, 2011, 2014.) and symmetric versus asymmetric rifts (*Nagel and Buck*, 2004, 2007; *Huismans and Beaumont*, 2005). The style of rifting has been shown to be influenced by the overall composition of the mantle lithosphere (e.g. *Gueydan et al*., 2008) and crust (*Nagel and Buck*, 2004; *Lavier and Manatschal*, 2006; *Van Avendonk et al*., 2009; *Huismans and Beaumont*, 2011). In general, it has been shown that strong crust and/or lithospheric mantle promotes narrow rifting, while weak or hot mantle lithosphere and crust promotes wide rifting. There is less consensus as to the controls on symmetric versus asymmetric modes of rifting. Numerical modeling has also shed light on the controls leading to particular styles of deformation during rifting, such as large-offset low angle normal faults (*Hopper and Buck,* 1998; *Buck*, 1993; *Lavier and Buck*, 2002; *Lavier et al*., 1999), channel flow of viscous layers within the crust (*Hopper and Buck*,1996; *Jammes et al*., 2010, *Huismans and Beaumont*, 2008), offset rift basins (*Chenin and Beaumont,* 2013; *Braun and Beaumont*, 1989), and core complexes (e.g. *Lavier et al*., 1999; *Choi et al*., 2013).

Physical analogue models have also been used to study the overall style of rifting. These have suggested that cold, strong lithosphere leads to a narrow mode of rifting, and that hot, weak lithosphere promotes wide rifting (*Brun*, 1998; *Tire*l *et al*., 2006). *Sokoutis et al*. (2007) studied the importance of weak heterogeneities in the crust and lithospheric mantle, in favouring localized and distributed rifting, respectively.

Factors controlling the deformation of salt have been studied independently of margin-scale tectonics, by both numerical (e.g. *Chemia et al*., 2008; *Albertz et al*., 2010; *Albertz and Beaumont*, 2010; *Longoni et al*., 2010; *Burchardt, et al*., 2011; *Goteti et al.*, 2012) and physical analogue (e.g. *Ge et al.*, 1997; *Costa and Vendeville*, 2002; *Bonini*, 2003; *Del Ventisette et al*., 2004, 2005; *Brun and Mauduit*, 2009; *Baikpour et al.*, 2010) modelling methods. For example, in previous numerical experiments by *Goteti et al*. (2012, 2013), a geometrically defined salt basin was deformed by uneven sediment loading, tilt of the model, or some combination thereof. Analogue models of salt tectonics at rifted margins have focused on the role of gravity gliding as a means of mobilizing salt, with gravity spreading generally considered less important (*Brun and Fort*, 2011; *Adam et al*., 2012a), though the formation of particular structures, such as minibasins, has required differential loading by sediments (e.g. *Adam et al*., 2012b).

The importance of timing of salt deposition relative to ongoing rifting, in determining deformation and mobilization of salt, has recently been highlighted by *Rowan* (2014). Using the rifting model of *Peron-Pinvidic and Manatschal* (2009, 2013) as a conceptual template for the crustal tectonics, Rowan outlines unique characteristics of salt bodies

deposited in the pre-rift, syn-stretching, syn-thinning, and syn-exhumation phases of rifting.

A major challenge for the numerical modelling has been to achieve sufficient resolution such that the interaction of crustal deformation with salt and clastic sedimentation can be resolved in models that necessarily include extension of the whole of the lithosphere. We believe we have overcome this difficulty by developing and using subscale (nested) high-resolution models for the crust and sediment, as we explain below.

In this paper we present numerical models that superimpose the deposition and deformation of salt on the regional tectonic setting of the syn-rift extension of conjugate rifted margins. The analyses presented here improve on previous work, in that they allow salt basin geometry to be dynamically defined by the ongoing process of continental stretching and break up. We first consider simple models with and without syn-rift clastic sedimentation to demonstrate styles of margin evolution (without salt deposition). Next we present models with salt deposition in the early, mid and late syn-rift phases, similar to the syn-thinning, syn-stretching, and syn-exhumation phases discussed by *Rowan* (2014). In some models, clastic sedimentation continues after salt is deposited, providing an additional driving force for the deformation of salt. The resultant salt structures evolve directly from the interactions among the rifting process, ongoing clastic sedimentation, and physical properties of the salt itself. Lastly, we consider the natural example of coupled rifting and the salt/evaporite tectonics system at the Red Sea.

To keep things simple, this work considers only one type of lithosphere, with an intermediate crust composition, displaying characteristics between the Type I and Type II/III margins of *Huismans and Beaumont* (2011, sub.). This is also similar to the rheology used by *Lavier and Manatschal* (2006), whose numerical models have a strong gabbroic lower continental crust.

3.4 Methods

3.4.1 Numerical Methods

A 2D Arbitrary-Lagrangian-Eulerian (ALE) finite element model (Sopale Nested, *Fullsack* 1995; *Beaumont et al.*, 2009) was used in this analysis. Sopale Nested solves thermo-mechanically coupled, incompressible viscous-plastic creeping (Stokes) flows (Equations 3.1-3.3). Note that compaction of sediments is handled separately (see section 3.3.2).

$$\frac{\partial \sigma_{ij}}{\partial x_i} - \frac{\partial P}{\partial x_j} + \rho g = 0 \qquad i,j = 1,2, \tag{3.1}$$

$$\frac{\partial v_i}{\partial x_i} = 0 \quad i=1,2, \tag{3.2}$$

$$\rho c_p \left(\frac{\partial T}{\partial t} + v_i \frac{\partial T}{\partial x_i} \right) = K(T) \frac{\partial}{\partial x_i} \frac{\partial T}{\partial x_i} + A + v_2 \alpha g T \rho \qquad i=1,2, \tag{3.3}$$

Where σ_{ij} is the deviatoric stress tensor, x_i are the spatial coordinates, P pressure (mean stress), ρ density, g gravitational acceleration, and v_i a component of velocity. Equation 3 is the energy balance in which c_p specific heat, T temperature, t time, K thermal conductivity (which is temperature dependent in the mantle), A radioactive heat

production per unit volume, and α volumetric thermal expansivity. The last term is the temperature correction for adiabatic heating when material moves vertically at velocity v_2. The mechanical and thermal systems are coupled through the temperature-dependent lithospheric viscosity and density and are solved sequentially during each model time step. The model design (Figure 3.1) includes a layered crust, lithospheric mantle and sublithospheric mantle, each with thermally-activated power-law viscous (Equation 3.4), and brittle (frictional-plastic) (Equation 5) rheologies.

3.4.2. Material Properties

The rheological properties of the lithosphere are based on 'Wet' Quartzite (WQz) (*Gleason and Tullis*, 1995) (upper crust and sediments), Dry Maryland Diabase (DMD) (*Mackwell et al.*, 1998) (lower crust), and 'Wet' Olivine (WOl) (*Karato and Wu*, 1993) (mantle lithosphere and sublithospheric mantle). When the state of stress is below plastic yield Sopale Nested uses the above laboratory-derived flow laws for dislocation creep to calculate the effective viscosity, η, using the following power-law expression:

$$\eta = f A^{-1/n} (\dot{I}_2')^{(1-n)/2n} \exp\left[\frac{Q + VP}{nRT}\right] \tag{3.4}$$

where A is the pre-exponential scaling factor, $\dot{I}_2'$ is the second invariant of the deviatoric strain rate tensor ($\frac{1}{2}\dot{\varepsilon}_{ij}'\dot{\varepsilon}_{ij}'$), n is the power law exponent, Q is the activation energy, V is the activation volume, which makes the viscosity dependent on pressure, P, T is the absolute temperature, R is the universal gas constant, $\dot{\varepsilon}_{ij}'$ is the deviatoric strain rate

tensor, and *f* is a scaling factor chosen to represent materials that are viscously weaker or stronger than the reference flow law (*Butler et al*., 2014). A complete list of material properties, including densities, used in the models is given in Table 3.1. Salt (specifically halite) is treated as a linear viscous material with a viscosity of either 10^{18} or 10^{19} Pa s . While this is a simplification that strictly applies to halite deforming by pressure solution (*Carter et al*., 1993; *Keken et al*., 1993), we believe it covers the range of effective viscosities to be expected for salt comprising halite or halite containing some amount of other stronger evaporites. Mixed lithologies remains a complex problem and our current models do not have sufficient resolution to model halite mixed with other evaporites. However, in the models for the Red Sea we do consider layers of other evaporites that have a finite yield strength.

Materials deforming by brittle failure (including clastic sediments and finite-strength evaporites), obey the pressure dependent plastic Drucker-Prager yield criterion:

$$\sigma_y = (J_2^{/})^{1/2} = C\cos\phi_{eff} + P\,Sin\phi_{eff} \qquad (3.5)$$

where $J_2^{/} = \frac{1}{2}\sigma_{ij}^{/}\sigma_{ij}^{/}$ is the second invariant of the deviatoric stress, C is the cohesion, and $\sigma_{ij}^{/}$ is the deviatoric stress tensor. ϕ_{eff} the effective internal angle of friction varies, ϕ_{eff} = 15–2°, where the initial value, 15°, includes the effect of hydrostatic pore fluid pressure, and the final value, 2°, represents a fully strain-softened material. The reduction in strength is achieved by linearly decreasing ϕ_{eff} over the range of strain ε = 0.5–1.5**.**

We use the Boussinesq approximation (*Schubert et al.*, 2001) in the calculations. Densities are not adjusted for compressibility when materials are buried at depth, however, density does change as a result of thermal expansion, with thermal expansivity values given in Table 3.1. Quoted densities (Table 3.1) are STP values.

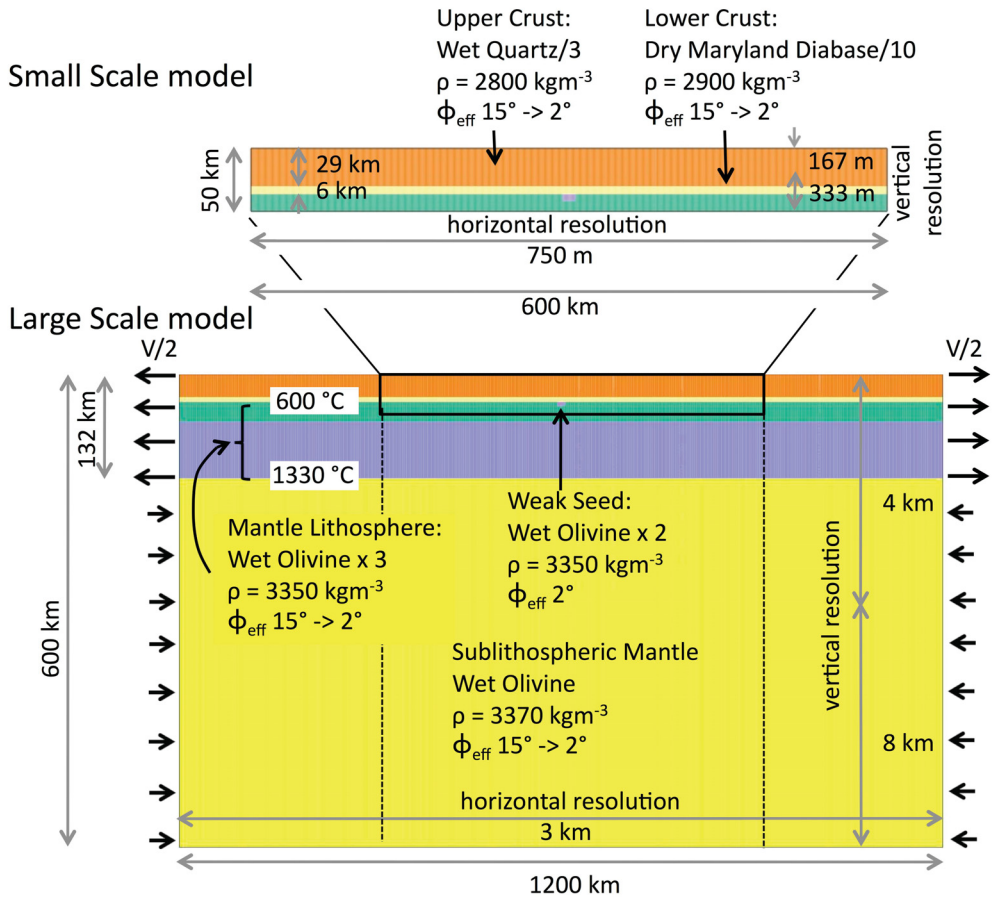

Fig. 1

Figure 3.1: Model design, showing initial geometry and rheological layering. The small-scale (SS) model is embedded in the large-scale (LS) model. See text and Table 1 for description of material properties; ρ and ϕ_{eff} are density and internal angle of friction. A boundary velocity, V/2, is applied to the lithosphere at either side of the model, such that the total rifting velocity, V = 1.0 cm a^{-1}. Base and sides are free slip boundaries. Basal heat flux, 22 mWm^{-2}, and crustal radioactive heat production, 0.95 μWm^{-3}, give base crust and lithosphere temperatures of 600 and 1330 °C. Side boundaries are insulated. Mantle weak seed serves to localize initial deformation. All models include water loading.

3.5 Model Design

The models in this work comprise the upper 600 km of the mantle and continental lithosphere (Figure 3.1) and contain two overlapping regions, a large scale (LS) domain model (1200 km horizontally by 600 km vertically, 400 x 140 elements) and an embedded small scale (SS) sub-domain model (300-900 km horizontally and 0-40 km vertically, 800 x 240 elements). Elements in the small-scale model are 750m wide by 167 m deep. This arrangement achieves a higher-resolution SS solution by solving the problem sequentially for each time step, first for the LS domain and then for the high-resolution SS domain using boundary conditions derived from the LS solution. The LS domain has a stress free upper surface, and free slip side and basal boundary conditions. The SS domain has a stress-free upper surface and velocity boundary conditions specified by interpolating the LS velocities on its other boundaries.

Table 3.1: Rheological and thermal properties of model materials.

Material and Rheology	Mechanical Properties				Thermal Properties		
	ρ (kg/m^{-3})	C (MPa)	η (Pa s)	Φ (°), Strain range	K (Wm^{-1}K^{-1}), Temperature range (°C)	C_p Specific heat (J Kg^{-1} K^{-1})	A_c (μW m^{-3})
Clastic sediments, WQz/3	variably compact	10		15–2, 0.5–1.5	2.25	750	0.0
Salt (halite)	2150	NA	10^{18} or 10^{19}	NA	5.858	750	0.0
Mixed evaporites	2300	10		15–2	2.25	750	0.0
Continental Upper Crust, WQz/3	2800	10		15–2, 0.5–1.5	2.25	750	0.95
Continental Lower Crust, DMD/10	2900	10		15–2, 0.5–1.5	2.25	750	0.95
Oceanic Crust, DMD/10	2900	10		15–2, 0.5–1.5	2.25	750	0.0
Continental Mantle Lithosphere, WOlx3	3350	2		15 – 2, 0.5 – 1.5	5.0 – 3.0, 0 - 777	750	0.0

Material and Rheology	Mechanical Properties				Thermal Properties		
	ρ (kg/m^{-3})	C (MPa)	η (Pa s)	Φ (^{o}), Strain range	K (Wm^{-1}K^{-1}), Temperature range (°C)	C_p Specific heat (J Kg^{-1} K^{-1})	A_c (μW m^{-3})
Oceanic Mantle Lithosphere, WOlx3	3350	2		10–2, 0.5–1.5	5.0 – 3.0, 0 - 777	750	0.0

Additional properties: the pre-exponential scaling factor, A, power law exponent, n, activation energy, Q, and activation volume, V, are 8.57x10^{-28} Pa^{-n} s, 4.0, 223 kJ mol^{-1}, and 0 m^3 mol^{-1} for WQz, 5.78x10^{-27} Pa^{-n} s, 4.7, 485 kJ mol^{-1}, and 0 m^3 mol^{-1} for DMD, and 1.76x10^{-14} Pa^{-n} s, 3.0, 430 kJ mol^{-1} and 1.2x10^{-5} m^3 mol^{-1} for WOl.

3.5.1. Initial Configureuration

Material properties of the crust, lithosphere, and sublithospheric mantle are assigned based on initially horizontal subdivisions. The continental crust comprises an upper (orange) layer of wet quartzite rheology scaled by f = 1/3, and a lower (sand colour) layer of dry Maryland diabase rheology scaled by f = 1/10. The upper and lower crust are 29 km and 6 km thick, respectively. The mantle lithosphere, extending from 35 to 132 km and shown in green (upper) and blue (lower), has a rheology based on the wet olivine flow law, scaled by a factor of f = 3 (Figure 3.1). Sublithospheric mantle (yellow) has a wet olivine flow law with scaling factor of f = 1. The f-scaling factors were chosen to create an upper crust that is slightly weaker than the Gleason and Tullis (1995) WQz flow law, a lower crust of gabbroic to granulite composition, and a partly dehydrated mantle lithosphere (Beaumont *et al*., 2006; Butler *et al.*, 2014). A small (12 km wide by 5 km thick) weak seed (wet olivine rheology with reduced internal angle of friction, ϕ_{eff} = 2°) is positioned in the uppermost mantle lithosphere, and serves to focus deformation during the initial stages of rifting.

The system is initially in a thermal steady state, with a laterally uniform temperature field, a uniform basal heat flux (q = 22 mWm^{-2}), and insulated side boundaries (q = 0). The crust has uniform radiogenic heat production, A_c = 0.95 μWm^{-3}. Initial temperatures at the Moho and the base of the lithosphere are 600 °C and 1330 °C, respectively. The lithospheric and sublithospheric mantle have temperature-dependant thermal conductivities consistent with an olivine-dominated composition. The thermal conductivity of the mantle lithosphere, $K_{ml}(T)$

decreases linearly from 5.0 to 3.0 $Wm^{-1}K^{-1}$ over a temperature range T = 0 – 777 °C. The conductivity of the sublithospheric mantle, $K_{slm}(T)$ increases linearly from 3.0 to 40.0 $Wm^{-1}K^{-1}$ over a temperature range T = 1323 - 1353 °C to achieve heat transport in the sublithospheric mantle equal to that of marginal convection and an adiabatic gradient of 0.4 °C km^{-1}. Thermal properties are summarized in Table 3.1.

Lithospheric extension at total rate V =1 cm a^{-1} is driven by side boundary conditions where horizontal velocities, ± V/2 are applied to the entire lithosphere on each side (Figure 3.1). Water loading is applied such that the water surface is at depth = 1 km before and after salt deposition; during salt deposition the water surface is maintained at 500 m above the top of salt surface. This depth was chosen to be consistent with a conceptual evaporation-seepage model of an isolated salt basin and associated drawdown of its surface, in which the long-term averaged water depth is 500 m and the water surface in the basin is 500 m below sea level.

3.5.2 Sedimentation

Sedimentation is applied by filling all unoccupied space between the surface of the model and a defined bathymetric profile with sediments at each time step. Two definitions of the bathymetric profile are used in these experiments. Salt is deposited through simple aggradation, with a horizontal bathymetric profile with stationary vertical position h_{salt}. Salt thickness therefore increases as accommodation space is generated through ongoing rifting

and thermal subsidence. In places where the existing sediments or salt are higher than the aggradation profile they are not removed. Clastic sediments are deposited according to either an aggradational profile with vertical position h_o, or a bathymetric profile, $h(x)$, defined by two half Gaussian curves (Equation 6), representing deltaic progradation across both continental margins as they develop.

$$h(x) = \begin{cases} h_1 & x < x_1 \\ h_2 + (h_1 - h_2)\exp\left(-\dfrac{(x - x_1)^2}{W_1^2}\right) + (h_3 - h_2)\exp\left(-\dfrac{(x - x_2)^2}{W_2^2}\right) & x_1 \le x \le x_2 \\ h_3 & x > x_2 \end{cases} \qquad [6]$$

Here h_1 and h_3 are the sediment surface positions landward of the progradation profile at the left and right margins, h_2 is the sediment surface position seaward of the progradation profiles, and W_1 and W_2 are the Gaussian half widths at each margin. All h values are depths measured below the initial model surface. Each progradation profile is translated seaward across its respective margin, such that the positions of x_1 and x_2 move in opposite directions with velocity $v_{prograde}$.

Clastic sediments in the models presented here are compactable. For each time step the compaction model calculates the sediment density for each horizontal location as a function of depth, z, according to Equation 7. When new sediment is added the density distribution as a function of depth increases (Equation 7) and this increase is assumed to be by expulsion of

pore fluid. The corresponding volume as a function of depth is reduced by vertical contraction equal to the incremental volume of the expelled pore fluid at that depth.

$$\rho_d(z) = \rho_g - \left(\rho_g - \rho_f\right) n_o e^{-cz} \tag{7}$$

The sediments have a grain density, ρ_g, of 2640 kg m^{-3}, pore fluid density, ρ_f, of 1000 kg m^{-3}, surface porosity, n_o, of 0.52, and compaction coefficient, c, of 4.7x10^{-4} m^{-1}. These values have been shown to provide a good fit to average siliciclastic sediment properties in the northern Gulf of Mexico (*Hudec et al*., 2009). This compaction calculation is separate from the finite element solution, which remains incompressible (Equations 2). Salt is considered not to compact.

3.5.3 Experiment Design

The experiments presented here comprise four sets of models. Models 1E and 1F are designed to show end member rifted margins in which the rift basin either has no sedimentation (Model 1E, E= Empty) or is kept close to full by a simple model of syn-rift sedimentation (Model 1F, F=Full) (Table 3.2). Both of these models have water loading, as do the other models described here. These models provide background examples for the settings in which both salt and clastics may be deposited. Model Sets 2, 3, and 4 respectively deposit salt in the early, mid, and late syn-rift phases. In particular, Model Set 4 deposits salt in the latest syn-rift period, over thick sag basin sediments. Final model results are shown for both 10^{18} and 10^{19} Pa s viscosity salt. Each model set contains experiments with no sedimentation after salt deposition, and with prograding clastic sediments after salt deposition. In all of these models the properties of the lithosphere remain the same. Table 3.2

outlines the design parameters of the models with times given in Ma (millions of years) since the start of the model calculation.

3.5.3.1 Model Set 1: Rifting with and without Deposition of Clastic Sediments

Model 1E (Figure 3.2) illustrates rifting of the two-layer, intermediate strength continental crust used for all models in this paper, in the absence of sedimentation. The continental crust and uppermost mantle deform in a relatively brittle manner, with thinning of the upper continental crust achieved through shearing in the models, which we interpret as faulting (Figure 3.2[1]). Deformation localizes at about 10 Ma, followed by rupture of the lower continental crust and upper lithospheric mantle by 13.5 Ma (Figure 3.2[2]), and rupture of the lower lithospheric mantle by 19-20 Ma (Figure 3.2[3]). There is some ductile decoupling of the upper and lower continental crust, but the lower crust remains coupled to and is advected away from the rift axis with the lithospheric mantle. Final separation of the upper continental crust at 26 Ma is followed by ocean-floor spreading (Figure 3.2[4]). The model therefore undergoes the same two-stage breakup as the Type I and III models (*Huismans and Beaumont*, 2011, 2014). The resultant margins are mildly asymmetric, with widths between 100 and 150 km. In the final configuration (Figure 3.2d-f) continental upper/mid crust is underlain by lower crust in the proximal margin, and continental mantle lithosphere in the mid-margin, but is underplated by material corresponding to oceanic crust in the distal margin (Figure 3.2[5]). Extension is clearly depth-dependent, with the lower part of the lithosphere separating before the upper crust, which is hyper-extended and completely decoupled from the underlying lithosphere in the distal margin. The model produces a rough bathymetry

Table 3.2: Experiment design, showing timing and depth for sedimentation profiles for Model Sets 1-4

Model Set 1: Rifting With and Without Deposition of Clastic Sediments						
Model Name	Description	Clastic Sedimentation				
		Start (Ma)	End (Ma)	h_1 (km)	$h_1 = h_2$ (km)	h_3 (km)
Model 1E	Base model					
Model 1F	Base model with clastic sediments	0	27	2.0		
		27	NA		1.0	5.0

Model Sets 2-4: Impact of Timing of Salt Deposition Relative to rifting, and the Role of Subsequent Sedimentation						
Model Name	Description	Pre-salt aggradation	Salt Deposition		Post-salt progradation	
		h_1 (km)	Start, End (Ma)	h_1 (km)	$h_1=h_2$ (km)	h_3 (km)
Model 2A	Early syn-rift salt, no sedimentation	1.25	10.5-12	1.25		
Model 2B	Early syn-rift salt, with progradation	1.25	10.5-12	1.25	1.0	5.0
Model 3A	Mid syn-rift salt, no sedimentation	3.0	15-19	3.0		
Model 3B	Mid syn-rift salt, with progradation	3.0	15-19	3.0	1.0	5.0
Model 4A	Late syn-rift salt, no sedimentation	3.0	23-24	2.5		
Model 4B	Late syn-rift salt, with progradation	3.0	23-24	2.5	1.0	5.0

Note: All *h* values are depths measured below the initial model surface.

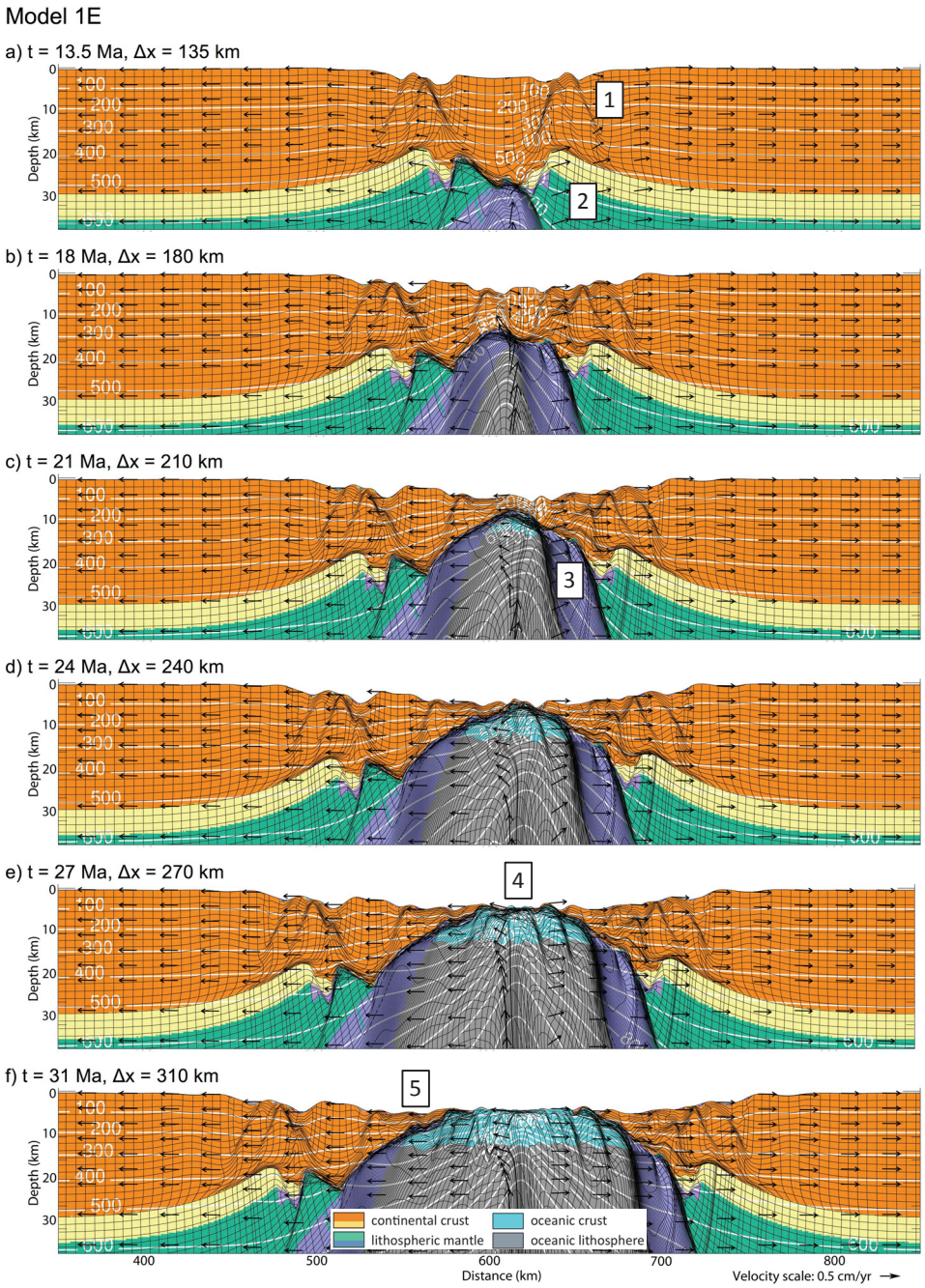

Fig. 2

Figure 3.2: Model 1E, intermediate crust reference model with no sedimentation, but including water loading. Successive panels show model evolution with model time, t, and current total extension, Δx. White isotherms are contoured at 100 °C intervals with the model surface at 0 °C. Velocity is shown by the black arrows. Deformation of the model can be seen in bending of the originally horizontal and vertical Lagrangian mesh (black lines). Continental crust thins primarily through faulting [1]. Lithospheric mantle and lower crust rupture before upper crust, and advect away from the rift axis [2,3]. Upper continental crust separates later, at ~27 Ma [4], and is underlain by lower lithospheric mantle or material equivalent to oceanic crust [5]. Vertical exaggeration 4:1.

with distinct, separate graben basins in the proximal margins and smoother, deeper regions in the distal margin. The model results are not very sensitive to rifting velocity. For faster rifting, up to 2 cm a^{-1}, rifting processes develop at slightly smaller levels of extension and the distal margin upper continental crust is not as thin.

The effective strain rate (square root of the 2^{nd} invariant of strain rate) (Figure 3.3) illustrates the diachronous nature of stretching of the upper/mid continental crust in this model. Thinning of the upper/mid continental crust by faulting is initially focused at a pair of horst and graben structures on either side of the rift axis (Figure 3.3 [1]), then migrates towards the rift axis during the period 14 to 27 Ma. After ~ 15 Ma, active deformation of the upper crust is localized in a region above the rift axis (Figure 3.3 [2]), and crust in more proximal regions of the margin experiences only minor ongoing stretching/thinning. Decoupling of the upper and lower continental crust (Figure 3.3[3]) is less significant after 18 Ma. After final breakup of the continental crust, at ~ 27 Ma, additional deformation is isolated to the upwelling oceanic mantle and the oceanic rift axis (Figure 3.3[4]).

Model 1F (Figures 3.4 and 3.5) has the same starting configuration at Model 1E, but includes deposition of a thick succession of aggrading clastic sediments throughout the rifting process, followed by prograding clastic sediments in the post-rift phase. Clastic sediments (Figure 3.4) are given rainbow colors (Figure 3.4, key) for each 5 Ma interval, with shades within each color band changing every 1 Ma. The additional load applied by the sediments isostatically amplifies the depths of the deeper basins in the early to mid

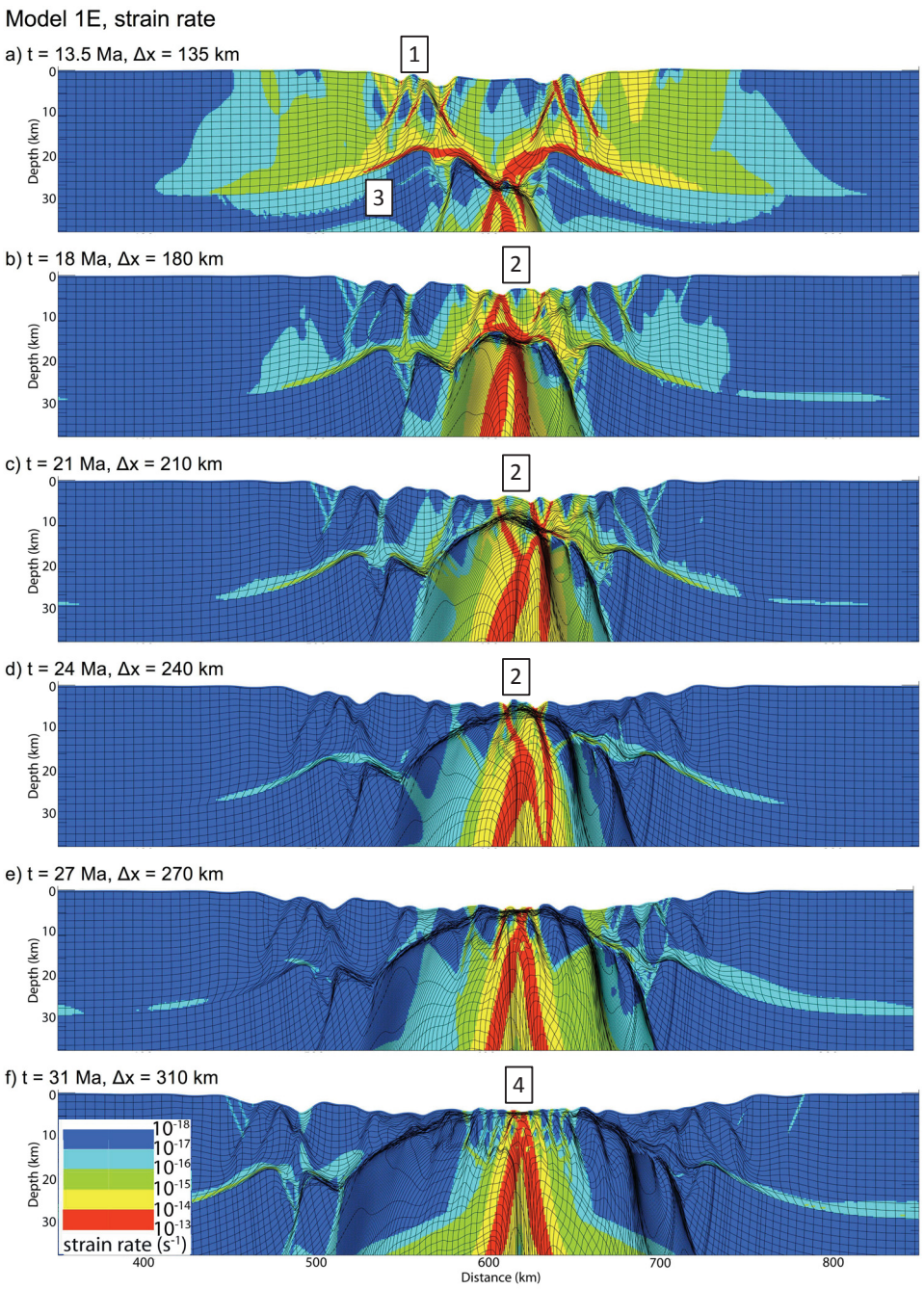

Fig. 3

Figure 3.3: Model 1E, intermediate crust reference model with no sedimentation. Successive panels show effective strain rate, s^{-1} (square root 2nd invariant of strain rate, coloured according to logarithmic scale), with model time, t, and current total extension, Δx. Early deformation is focused on fault-bounded graben in the proximal margins [1]. Deformation subsequently migrates towards the rift axis [2]. Some decoupling occurs between upper and lower continental crust, early in the model evolution [3]. After breakup of the upper crust, deformation is restricted to the developing oceanic crust [4]. Vertical exaggeration 4:1.

syn-rift phases (Figure 3.4[1]). Deposition of sediments has a negative feedback effect on the stretching of the crust and leads to a more diffuse style of deformation (Figure 3.5[1]). However, the breakup of upper continental crust occurs at approximately the same time, 27 Ma (Figure 3.4[2]), as in Model 1E. The overall width of the margin pair is similar in Models 1E and 1F, however the two margins are more symmetric in Model 1F, with sedimentation (Figure 3.4[3]). Temperatures of the upper continental crust are higher in Model 1F, compared to Model 1E, owing to thermal blanketing by the sediments (Figure 3.4[4]). This is particularly pronounced in the distal margin, where upper crust temperatures range from about 0 to 400°C in Model 1F (Figure 3.4[4]), compared to 0 to 250 °C in Model 1E (Figure 3.2). The difference in temperature probably accounts for the differing rifting styles.

The simple aggradational style of sedimentation throughout the evolution of Model 1F, with a constant h_0 = 2 km, results in thick sag-basin style successions (Figure 3.4[5]), and highlights the diachronous deformation which is similar to that experienced by the continental upper crust. In the early syn-rift period sediments are deposited in fault-bounded grabens (Figure 3.4[1]), and deformation of sediments is largely constrained to slip along these faults. As rifting continues, crustal thinning creates accommodation space over the rift axis, such that between 18 and 27 Ma progressively younger sediments are deposited in successively more distal parts of the margin (Figure 3.4[5]. Deformation of these sediments is localized near the rift axis (Figure 3.4; Figure 3.5c-f). The resultant sedimentary succession is faulted throughout much of its thickness, which is shown by the total strain (Figure 3.6e[2]), though only faults in the distal part of the margin were

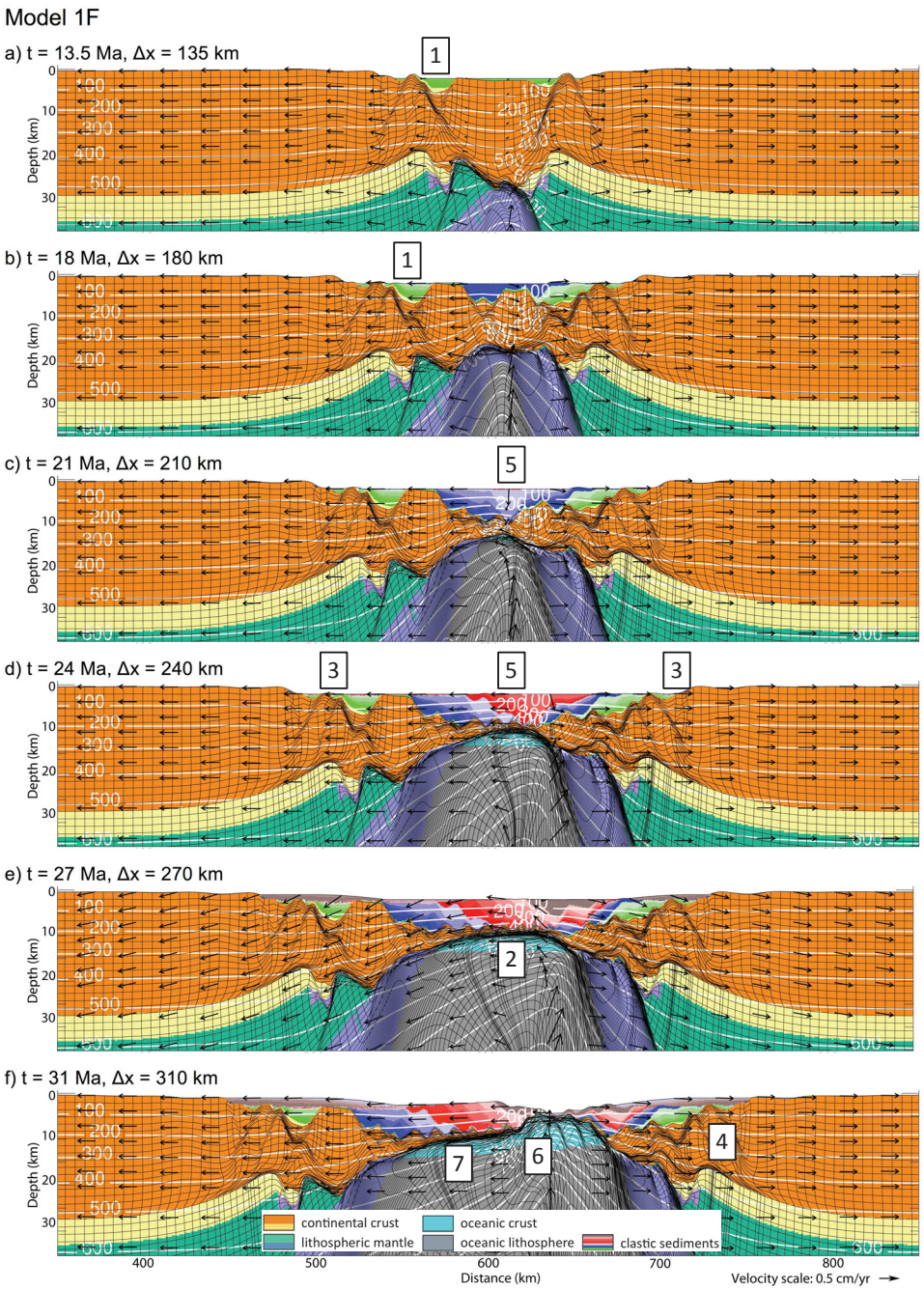

Fig. 4

Figure 3.4: Model 1F, intermediate crust with sag basin type aggrading sediments followed by sediment progradation, and including water loading. Successive panels show model evolution with model time, t, and current total extension, Δx. See Fig. 2 caption for notation. Isostatic adjustment leads to deeper proximal basins with sedimentation [1]. Sediment deposition at the rift axis forms a thick, seaward-younging succession over the mid-to-distal margins [2,5]. Sedimentation leads to a more symmetric margin pair [3], likely resulting from higher temperatures in the upper crust [4], but produces a wider region of hyper-extended upper crust [7]. Isostatic adjustment of the sag basins and adjacent oceanic crust forms a basement high that impedes seaward flow of sediment [6]. Vertical exaggeration 4:1.

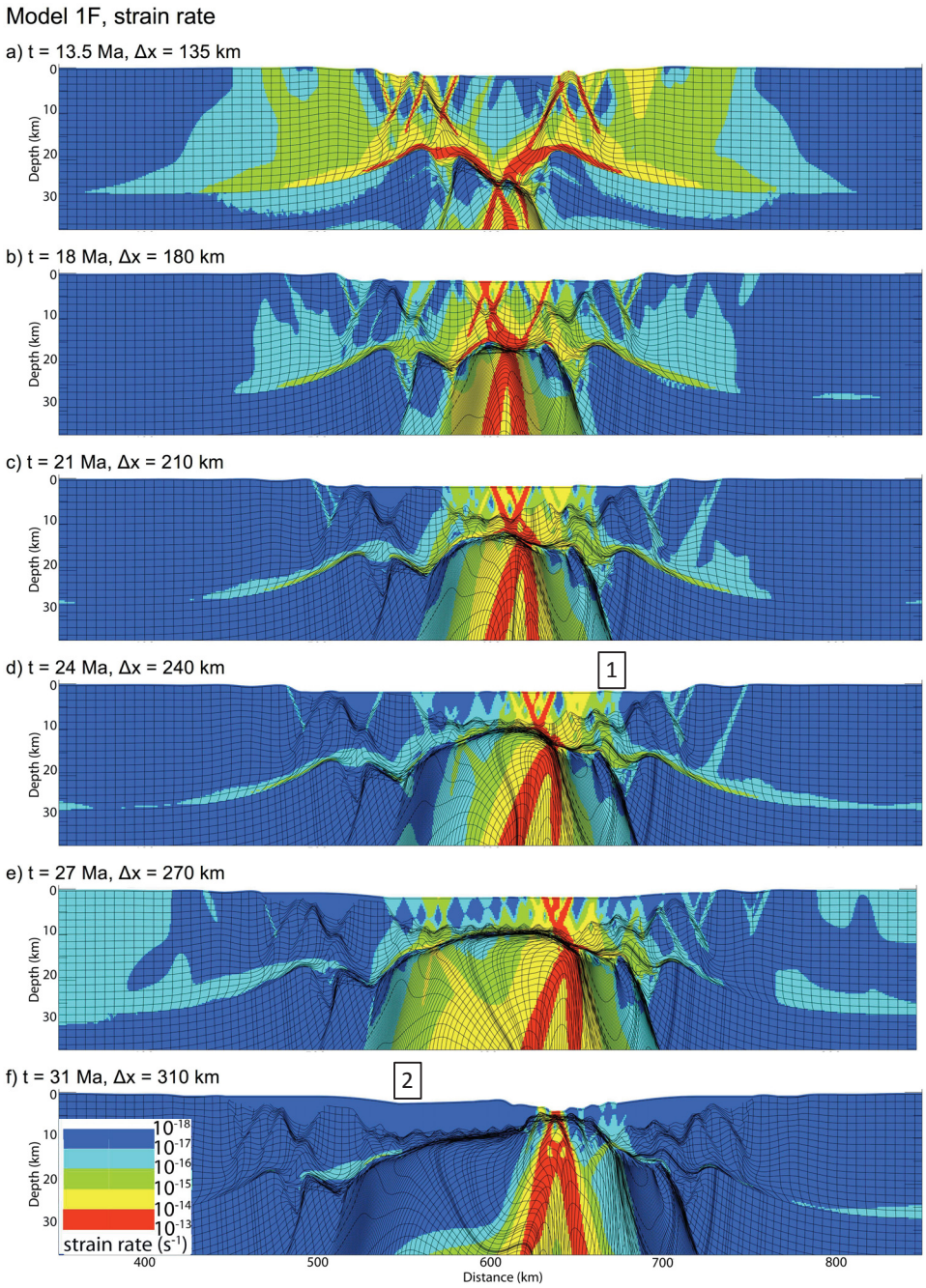

Fig. 5

Figure 3.5: Model 1F, intermediate crust with sag basin type aggrading sediments followed by sediment progradation. Successive panels show effective strain rate, s^{-1} (square root 2nd invariant of strain rate, coloured according to logarithmic scale) with model time, t, and current total extension, Δx. Sedimentation leads to a more diffuse style of deformation [1]. Deformation migrates from the proximal basin towards the distal margin. After breakup of continental crust, deformation is restricted to the emerging oceanic crust; prograding sediment deposited at the proximal and mid margin at this time is not faulted [2]. Strain rate does not include compaction of sediments. Vertical exaggeration 4:1.

active at any one point in time. This can be seen clearly in the incremental strain plots (Figure 3.6 left/right, b, d), where incremental strain is the difference in accumulated total strain between successive points (0.5 Ma increments) in the model evolution. Here incremental strain is only large at the rift axis (Figure 3.6[1]. The mid region of the margins experiences a small amount of thermal subsidence, resulting in deposition of a thin layer of young, undeformed sediments over older, faulted sediments (Figure 3.6[3]). Starting at 27 Ma, sediments prograde over the proximal to mid regions of each margin (Figure 3.4e, f; Figure 3.6c[4]). These sediments are not deformed by faults (Figure 3.5[2] and Figure 3.6d[4]) because crustal extension has been replaced by ocean-floor spreading and is no longer active in these and other regions in the model where prograding sediments are deposited.

3.6 Model Sets 2-4: Impact of Timing of Salt Deposition Relative to Rifting, and the Role of Post-Salt Sedimentation

In this section we explore the impact of timing of salt deposition relative to ongoing rifting, as well as the influence of sedimentation after salt deposition, on the distribution and deformation of salt. Model Sets 2, 3 and 4 respectively deposit salt in the early, mid, and latest syn-rift periods. Each set contains a model with no sedimentation after salt deposition, which isolates the impact of timing of salt deposition relative to the rifting process, on the location and geometry of initial salt bodies. Also in each set is a model with prograding clastic sediments following salt deposition, which illustrates the relative importance of the timing of salt deposition and post-salt sedimentation on the development of salt tectonics.

3.6.1 Early Syn-rift Salt Deposition

Models 2A and 2B deposit salt in the early syn-rift period, from 10.5 to 12 Ma, with Model 2B also including prograding clastic sediments after salt deposition (Figures 3.7 and 3.8). Owing to the early syn-rift timing of deposition, salt in these models is initially mostly confined to a pair of fault-bounded grabens on either side of the rift axis (Figure 3.7[1]), with a thin layer over the intervening horst block. Salt is deposited either directly on the continental crust or over a thin layer of clastic sediment, and as such the geometry of the initial salt bodies directly reflects the ongoing deformation of the crust. The thick salt bodies are generally narrow, isolated, and restricted by the steep walls of the proximal grabens, particularly at the left margin (Figure 3.7[2]). Initial salt thickness varies considerably across the basins, reaching a maximum of 3.5 and 1.8 km on the left and right hand margins. This discrepancy is due to the asymmetric nature of the margin development, with upwelling of the asthenospheric mantle and formation of oceanic crust more prominent on the right margin, leading to reduced basin subsidence in this region. Internal deformation of the salt is evident, with flow generally downwards at the edges of the grabens and upwards towards the centre of the salt body (Figure 3.7[3] and Figure 3.8[1]). Deposition of salt in Model Set 2 has a feedback effect that influences the geometry of the evolving rift basins. In Model 2A the proximal basin on the left hand margin reaches a depth of nearly 3.8 km by 21 Ma (Figure 3.7b[3]), compared to under 3 km for Model 1E (Figure 3.2), with no sedimentation, and roughly 5 km for Model 1F (Figure 3.4), with the thick sedimentation succession. In Model 2A the base of the same

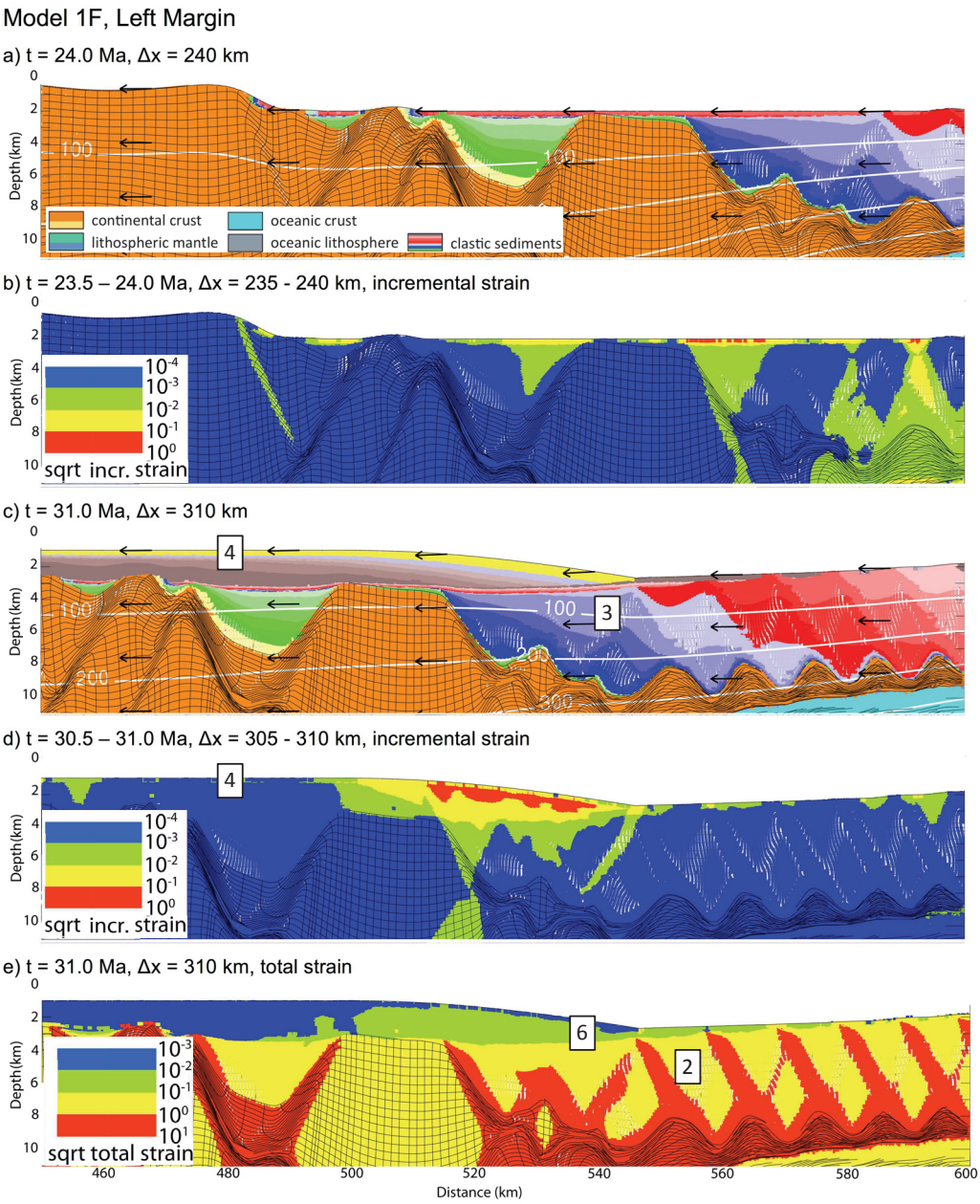

Fig. 6 left

Figure 3.6 left/right: Model 1F, intermediate crust with sag basin type aggrading sediments followed by sediment progradation, and including water loading. a) and c) show model geometry at time, t, and extension, Δx. See Fig. 2 caption for notation. b) and d) show incremental effective strain (square root of second invariant of incremental strain, coloured according to a logarithmic scale) for the time interval and incremental extension shown. e) shows geometry and total cumulative effective strain. Active deformation of sediments shifts towards the rift axis over time[1]; the resultant sediment package is faulted throughout it's lateral extent, but only faults near the current distal margin are active at any time [2]. Sediment deposited at the mid margin late in the rifting process is not faulted [3,4,6]. Oceanic crust forms a bathymetric high that impedes sediment deposition [5]. Note in this case the strains for the sediments include the effects of compaction of the prograding sediments. Vertical exaggeration 4:1.

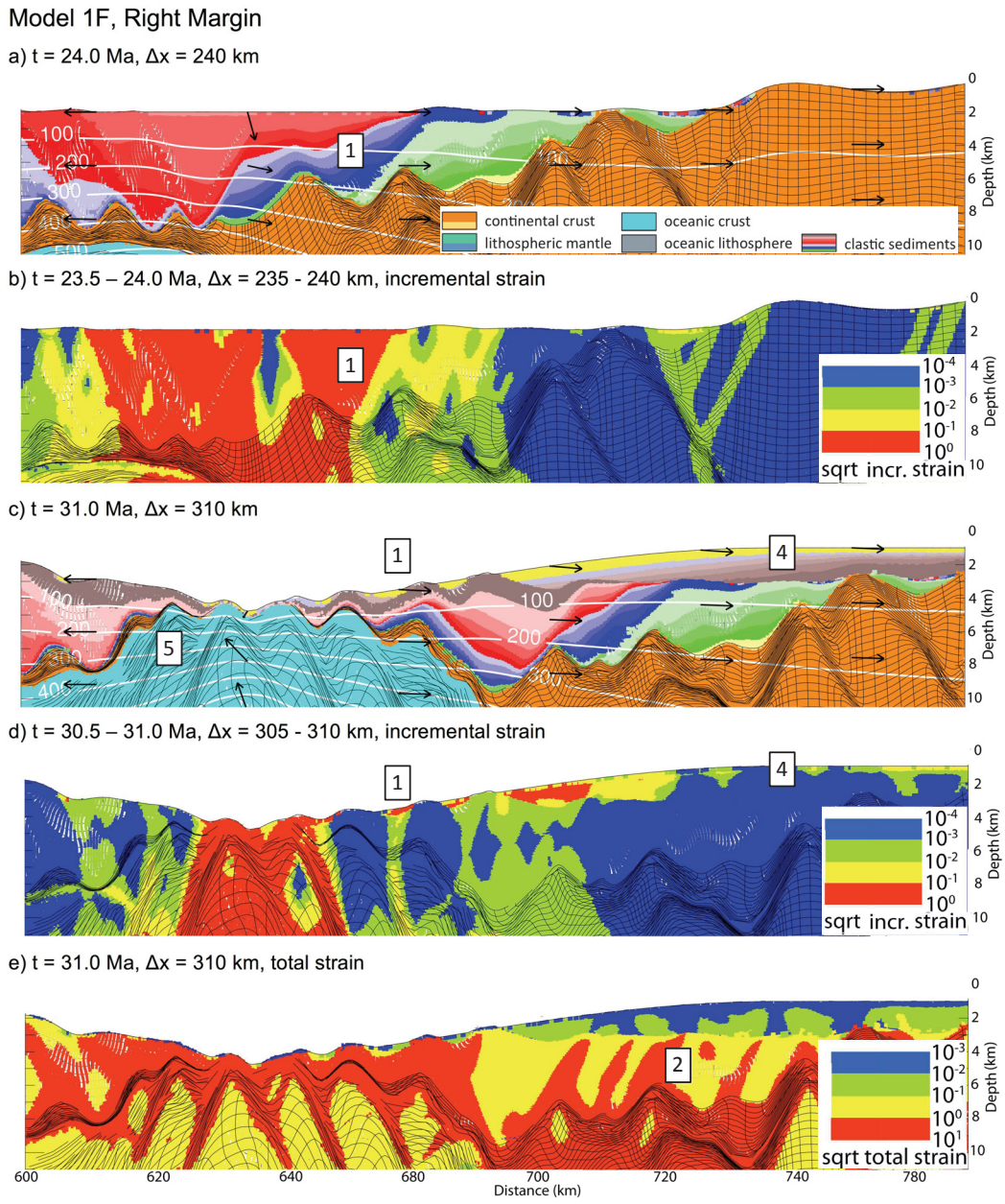

Fig. 6 right

Figure 3.6 left/right: Model 1F, intermediate crust with sag basin type aggrading sediments followed by sediment progradation, and including water loading. a) and c) show model geometry at time, t, and extension, Δx. See Fig. 2 caption for notation. b) and d) show incremental effective strain (square root of second invariant of incremental strain, coloured according to a logarithmic scale) for the time interval and incremental extension shown. e) shows geometry and total cumulative effective strain. Active deformation of sediments shifts towards the rift axis over time[1]; the resultant sediment package is faulted throughout it's lateral extent, but only faults near the current distal margin are active at any time [2]. Sediment deposited at the mid margin late in the rifting process is not faulted [3,4,6]. Oceanic crust forms a bathymetric high that impedes sediment deposition [5]. Note in this case the strains for the sediments include the effects of compaction of the prograding sediments. Vertical exaggeration 4:1.

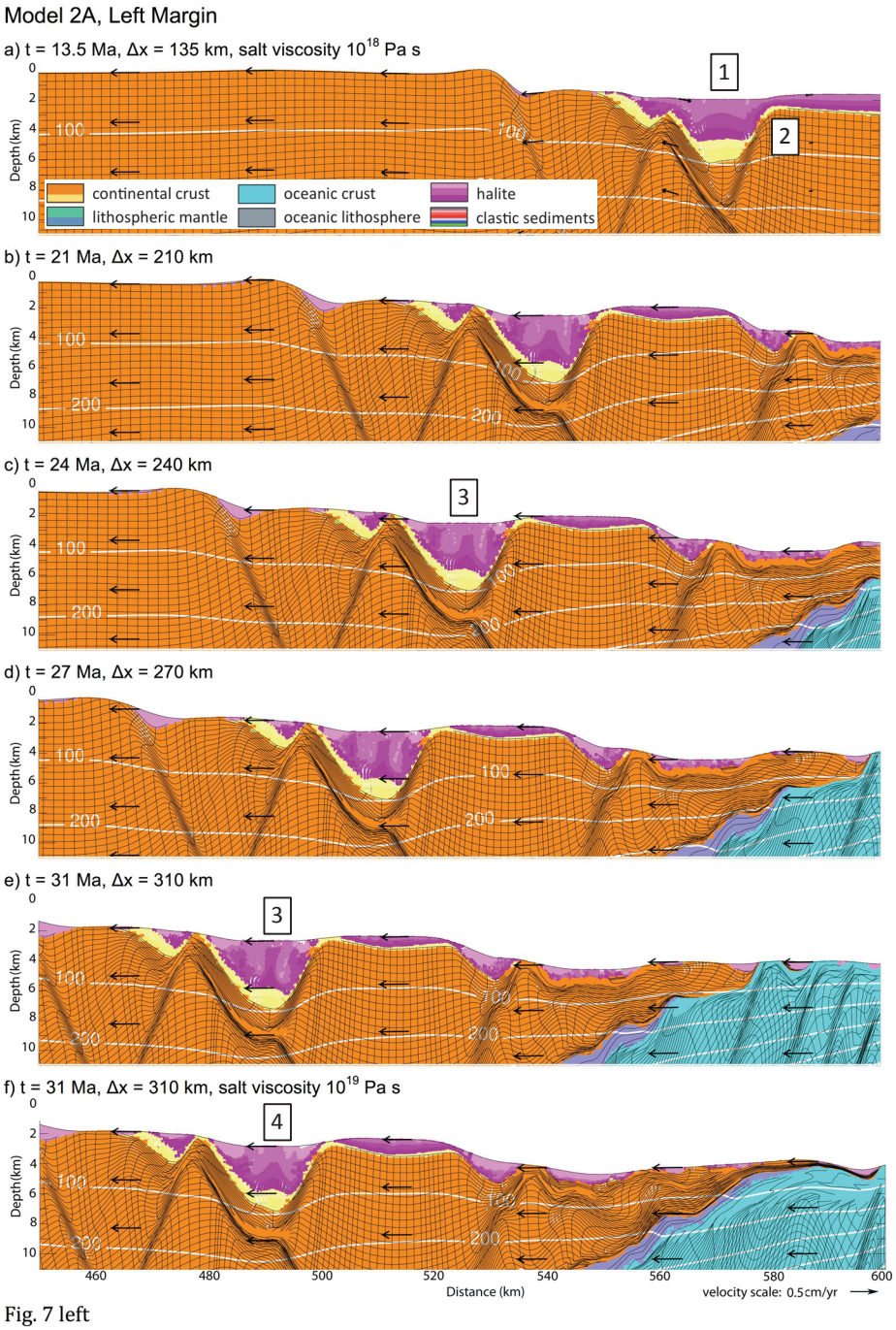

Fig. 7 left

Figure 3.7 left/right: Model 2A, early syn-rift salt deposition with no post-salt sedimentation, for the left and right hand margins. a)-e) show model evolution for salt viscosity 10^{18} Pa s; f) shows final configuration for salt viscosity 10^{19} Pa s. See Fig. 2 caption for notation. Salt deposition is focused in a pair of fault-bounded graben in the proximal margin [1], and produces thick, narrow salt bodies [2], particularly at the left margin. Internal deformation of salt is evident. Salt flows down at the basin edges and up in the centre of the salt body [3]; this deformation is less pronounced for salt viscosity 10^{19} Pa s [4]. Vertical exaggeration 4:1.

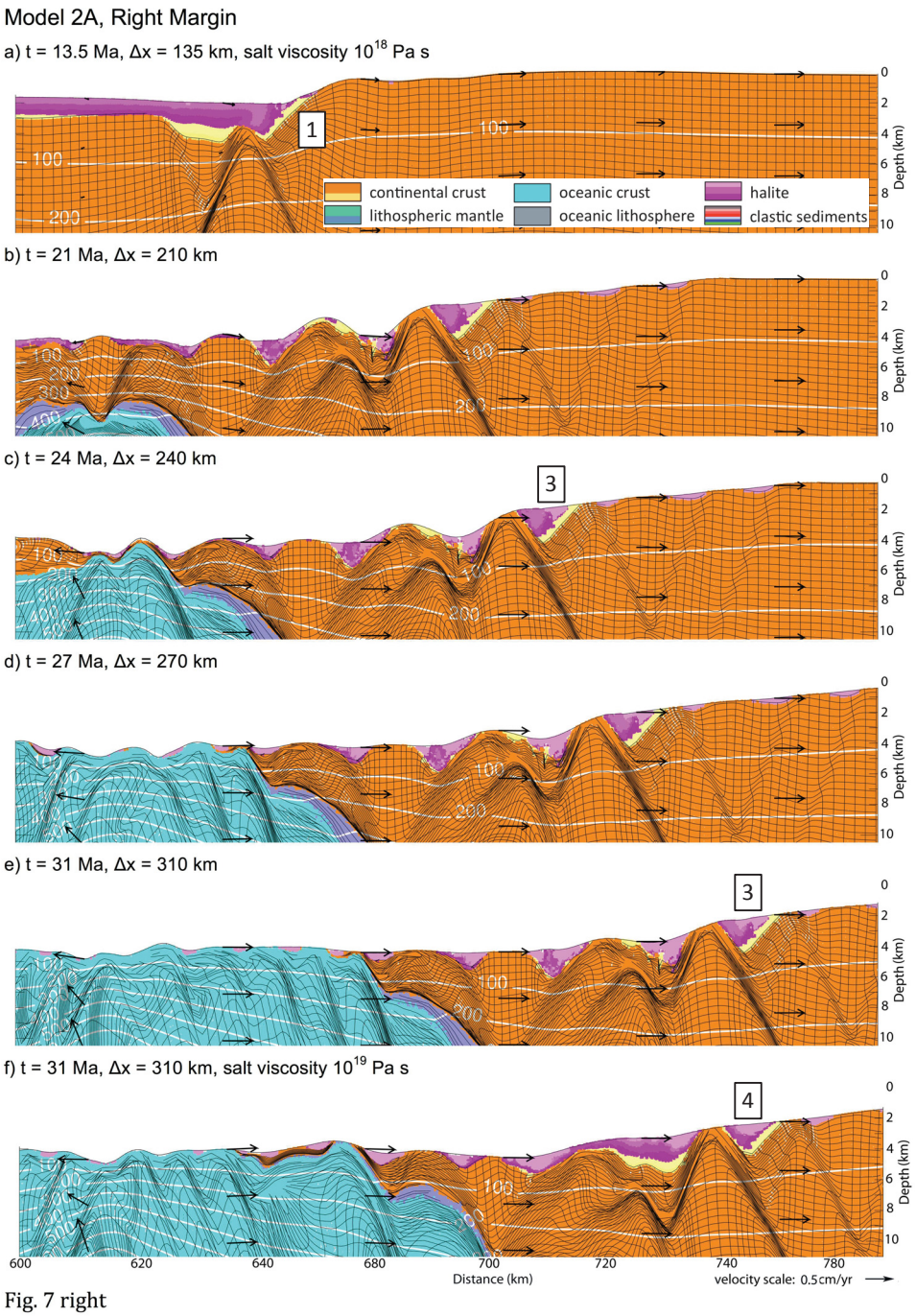

Fig. 7 right

Figure 3.7 left/right: Model 2A, early syn-rift salt deposition with no post-salt sedimentation, for the left and right hand margins. a)-e) show model evolution for salt viscosity 10^{18} Pa s; f) shows final configuration for salt viscosity 10^{19} Pa s. See Fig. 2 caption for notation. Salt deposition is focused in a pair of fault-bounded graben in the proximal margin [1], and produces thick, narrow salt bodies [2], particularly at the left margin. Internal deformation of salt is evident. Salt flows down at the basin edges and up in the centre of the salt body [3]; this deformation is less pronounced for salt viscosity 10^{19} Pa s [4]. Vertical exaggeration 4:1.

basin reaches ~ 100 °C when filled with salt, compared with 0 °C for Model 1E and 150 °C for Model 1F.

The prograding sediments, Model 2B, result in significantly more deformation of the salt than in Model 2A. In the left proximal graben loading by the prograding sediment forms an expulsion rollover, in which salt is initially expelled and thickened (Figure 3.8[2]) and later develops into a diapir (Figure 3.8[3]). Vertical flow of salt into the diapir at the left margin can be seen, with older salt over younger salt at the top of the diapir (Figure 3.8[3]). Similarly, salt is expelled from the most proximal graben in the right margin (Figure 3.8[4]), some of which flows over the barrier into the next graben. It is then further expelled seaward by sediment loading, which halves its initial 2km thickness. It then forms a small diapir (Figure 3.8[5]). In this case passive diapirism does not persist as the model evolves, owing to rapid burial by clastic sediments (Figure 3.8[6]). In the distal margin, what was initially a continuous layer of salt becomes disaggregated as the underlying crust extends, leaving isolated small pockets of salt (Figure 3.8[7]).

In the corresponding model with salt viscosity 10^{19} Pa s (Figure 3.8f left, right), salt deformation is less pronounced. When there is no sedimentation after salt deposition internal deformation can still be seen, though to a lesser extent than in the case with 10^{18} Pa s salt viscosity (Figure 3.7[4]). Under the influence of prograding sediments, a less well-developed expulsion rollover forms at the left margin, with a thickened salt body at the seaward edge of the proximal basin, but without forming a diapir (Figure 3.8[8]). Lateral movement of salt between sub-basins on the right margin is correspondingly less

efficient for salt with viscosity 10^{19} Pa s, leading to reduced salt thickness in the most seaward proximal basin on the right margin (Figure 3.8[9]). Prograding sediments do not lead to diapirism at the right margin, for the case with 10^{19} Pa s salt viscosity. The effect of the 10^{19} versus 10^{18} Pa s salt is more muted in Model 2A, in the absence of sediment progradation, because without a prograding wedge providing differential pressure, salt is only mobilized by the thick-skinned crustal deformation and salt of both viscosities responds in a similar way.

3.6.2 Mid Syn-rift Salt Deposition

Model Set 3 (Figures 3.9 and 3.10) shows the results of salt deposition in the mid syn-rift period, from 15 to 19 Ma. Before salt is deposited, clastic sediments aggrade to 2 km below sea level. Model 3A has no sedimentation after salt, while Model 3B includes clastic progradation. In these models because salt is deposited later it is located not only in the proximal basins, but also in a region across the rift axis, where subsidence resulting from additional crustal thinning has created new accommodation space (Figure 3.9[1]). The salt basins in Model Set 3 are generally wider than those of Model Set 2 owing to the later salt deposition, which has allowed rifting to be more advanced with a correspondingly wider region of accommodation space available for salt over the ridge axis (Figures 3.9 and 3.10). Salt in the proximal basins reaches a maximum initial thickness of 4 km at the right hand margin, and approximately 1 km on the left hand margin. The discrepancy is due to the asymmetric nature of margin development, with

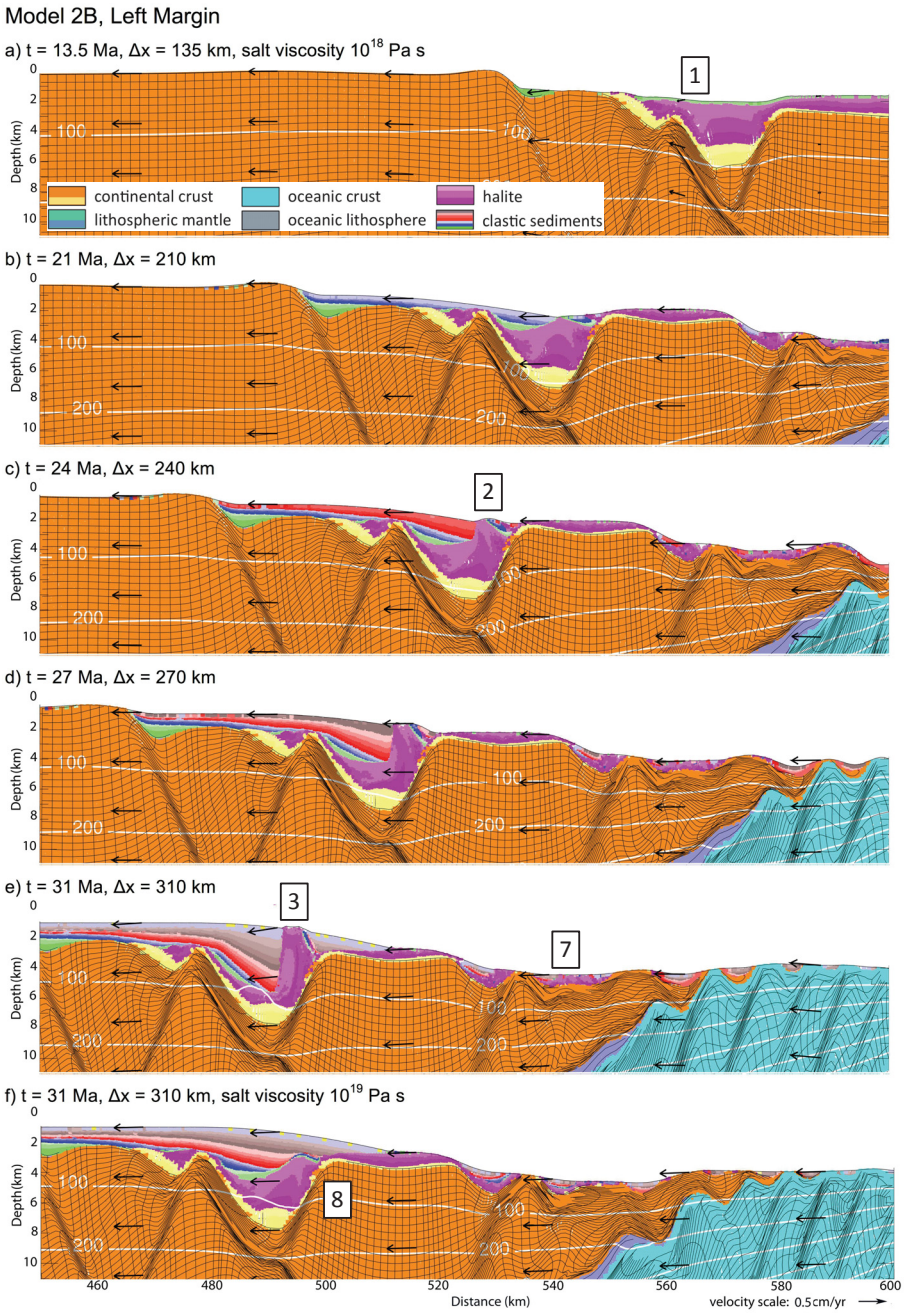

Fig. 8 left

Figure 3.8 left/right: Model 2B, early syn-rift salt deposition with post-salt sediment progradation, for the left and right hand margins. a)-e) show model evolution for salt viscosity 10^{18} Pa s; f) shows final configuration for salt viscosity 10^{19} Pa s. See Fig. 2 caption for . Prograding sediment leads to more highly deformed salt, including development of expulsion rollovers [2] and diapirs [3,5] that either grow passively [3] or are buried by rapid sedimentation [6]. Internal deformation of salt occurs at basin edges in the early model evolution [1], and within diapirs [3]. Salt flows between sub-basins [4]. Salt deposited over the horst block distends and becomes disaggregated [7]. Similar, though less pronounced, deformation occurs with salt viscosity 10^{19} Pa s; development of diapirs [8] and flow of salt between sub-basins [9] is suppressed. Vertical exaggeration 4:1.

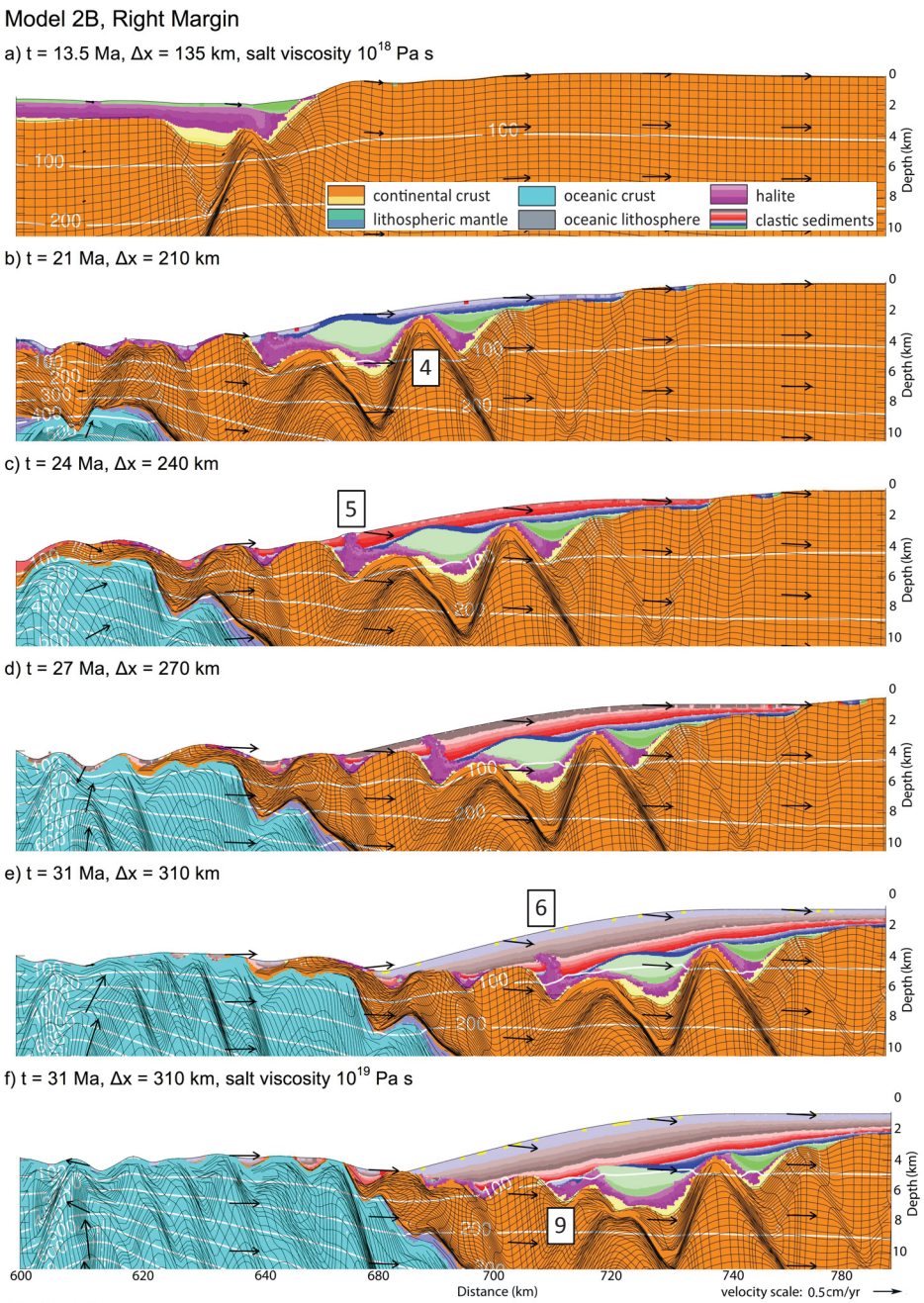

Fig. 8 right

Figure 3.8 left/right: Model 2B, early syn-rift salt deposition with post-salt sediment progradation, for the left and right hand margins. a)-e) show model evolution for salt viscosity 10^{18} Pa s; f) shows final configuration for salt viscosity 10^{19} Pa s. See Fig. 2 caption for . Prograding sediment leads to more highly deformed salt, including development of expulsion rollovers [2] and diapirs [3,5] that either grow passively [3] or are buried by rapid sedimentation [6]. Internal deformation of salt occurs at basin edges in the early model evolution [1], and within diapirs [3]. Salt flows between sub-basins [4]. Salt deposited over the horst block distends and becomes disaggregated [7]. Similar, though less pronounced, deformation occurs with salt viscosity 10^{19} Pa s; development of diapirs [8] and flow of salt between sub-basins [9] is suppressed. Vertical exaggeration 4:1.

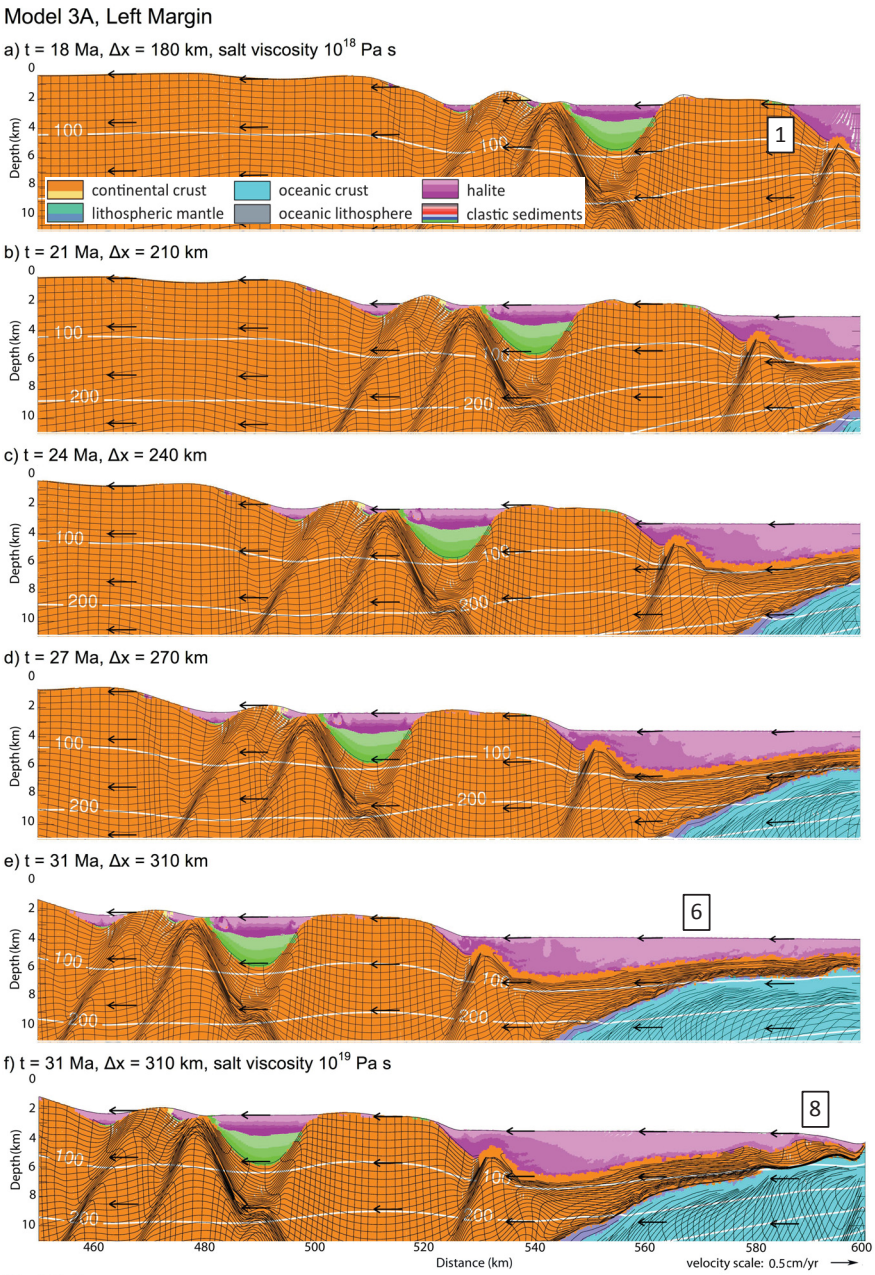

Fig. 9 left

Figure 3.9 left/right: Model 3A, mid syn-rift salt deposition with no post-salt sedimentation, for the left and right hand margins. a)-e) show model evolution for salt viscosity 10^{18} Pa s; f) shows final configuration for salt viscosity 10^{19} Pa s. See Fig. 2 caption for notation. Salt is deposited both in proximal basins and across the rift axis [1]. Thicker salt deposition and a smoother base of salt surface facilitate lateral movement of salt [2]. Salt flows readily between sub-basins, with older salt flowing over younger salt [3]. Salt deposited over the rift axis stretches and thins, producing escarpments [4], maintaining a nearly uniform salt layer over thinned continental and oceanic crust to 27 Ma model evolution [5], and distributing salt across the mid and distal margins [6]. Salt viscosity 10^{19} Pa s leads to a more distinct pattern of older salt flowing over younger salt [7] and more pronounced salt escarpments [8]. Vertical exaggeration 4:1.

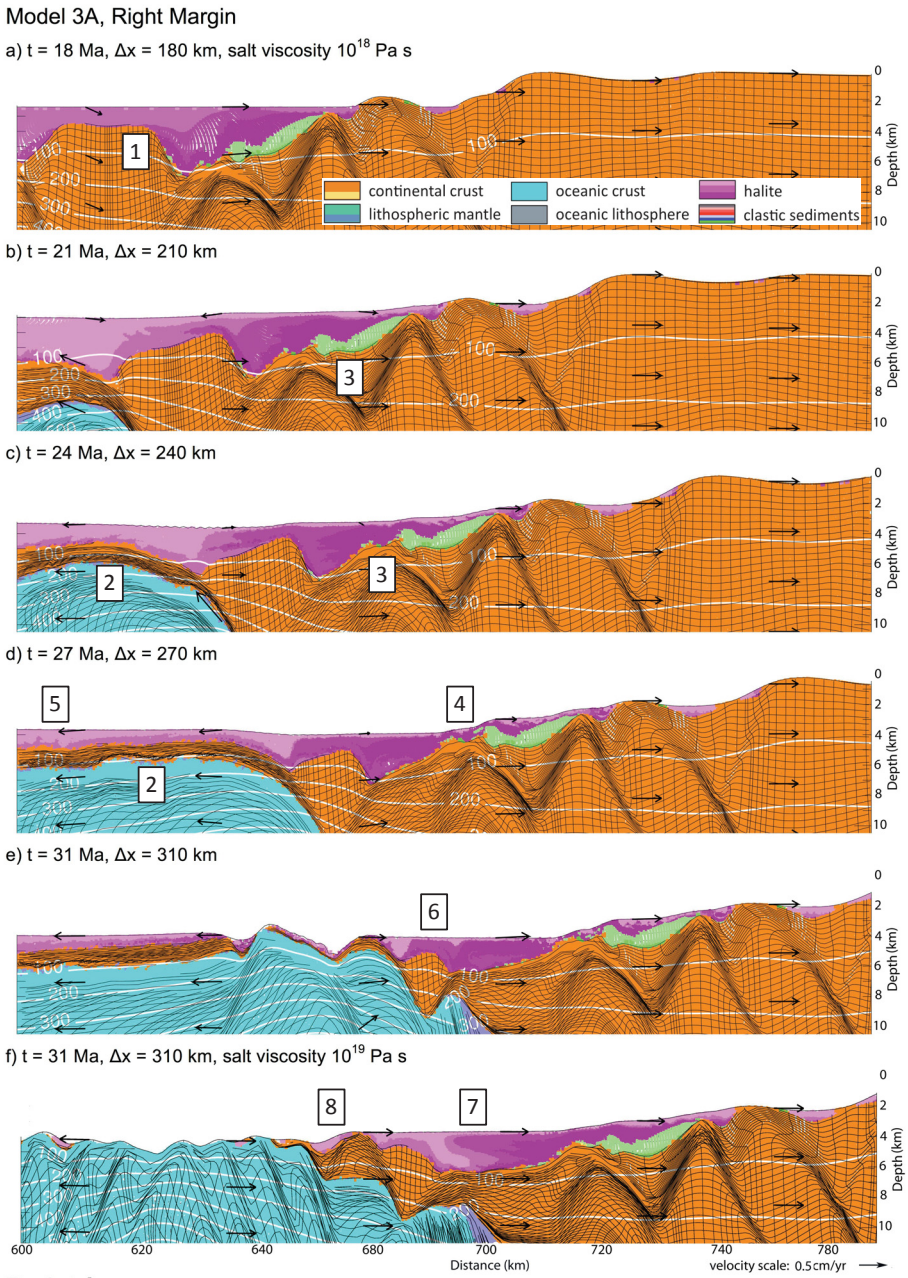

Fig. 9 right

Figure 3.9 left/right: Model 3A, mid syn-rift salt deposition with no post-salt sedimentation, for the left and right hand margins. a)-e) show model evolution for salt viscosity 10^{18} Pa s; f) shows final configuration for salt viscosity 10^{19} Pa s. See Fig. 2 caption for notation. Salt is deposited both in proximal basins and across the rift axis [1]. Thicker salt deposition and a smoother base of salt surface facilitate lateral movement of salt [2]. Salt flows readily between sub-basins, with older salt flowing over younger salt [3]. Salt deposited over the rift axis stretches and thins, producing escarpments [4], maintaining a nearly uniform salt layer over thinned continental and oceanic crust to 27 Ma model evolution [5], and distributing salt across the mid and distal margins [6]. Salt viscosity 10^{19} Pa s leads to a more distinct pattern of older salt flowing over younger salt [7] and more pronounced salt escarpments [8]. Vertical exaggeration 4:1.

crustal thinning and subsidence focused at the right margin during the mid syn-rift period. Initial salt thickness over the rift axis is 3.5 to 4 km.

Salt deposited in the mid syn-rift period is more likely to experience lateral flow, compared to salt deposited in the early syn-rift period, owing to the wider region of thicker deposition and the smoother basal salt surface in the distal margin during the later stages of rifting (Figure 3.9[2]). The later timing of salt deposition favours lateral movement of salt both by creating accommodation space over the rift axis which does not have a seaward barrier to salt flow, and by reducing the height of barriers to seaward flow in the grabens, by infill with clastic sediments before salt deposition. The second effect is most noticeable at the right margin between 18 and 24 Ma (Figure 3.9[3]), where salt is able to flow between two sub-basins created in response to upwelling and crustal thinning in this region. This combined seaward gravitationally-induced flow and extension of the salt by thick-skinned crustal extension reduces the initially uniform height of the top of the salt layer and produces salt escarpments where salt thins over underlying basement and clastic sediments (Figure 3.9[4]). The mobility of the 10^{18} Pa s salt, as seen in the region over the rift axis, is remarkable. Even though salt deposition ends at 19 Ma it continues to extend and flow seaward over the rift axis such that as late as 27 Ma there is still a nearly uniform layer bridging the oceanic crust (Figure 3.9[5]). Thus, salt deposited over the rift axis thins and flows seaward in response to continued thinning of the continental crust, such that even in the absence of prograding sediments this salt spans the mid and distal sections of both margins (Figure 3.9[6]).

The addition of prograding sediments (Figure 3.10) further mobilizes the salt, facilitating both seaward flow of salt and the development of more complex salt tectonics structures where the sediments load the salt. On both margins, differential pressure induced by prograding sediments leads to thickened salt bodies at the distal end of basins, such as between 24 and 31 Ma (Figure 3.10[1]). Large amounts of salt expulsion can be seen on the right margin, with older salt flowing over younger salt in the form of a tongue (Figure 3.10[2]). An expulsion rollover and subsequent diapir form in the graben on the left margin (Figure 3.10[3]). This salt remains trapped in the grabens but there is seaward flow of salt in the distal margin resulting in the formation of one major salt escarpment (Figure 3/10[4]).

Results from equivalent models with salt viscosity of 10^{18} and 10^{19} Pa s (Figures 3.9e, f and 3.10e, f) show how higher viscosity salt retards flow. In Model 3A 10^{19} Pa s (Figure 3.9f) salt ruptures much earlier in the model evolution, very little salt flows onto the most distal margin, and almost none flows onto oceanic crust. Salt over the mid-margin shows a more distinct pattern of older salt flowing over younger salt at 31 Ma (Figure 3.9[7]). Salt escarpments in the distal margin are also more pronounced for the case with 10^{19} Pa s salt (Figure 3.9[8]). For Model 3B (Figure 3.10f), more of the 10^{19} Pa s salt remains trapped beneath the prograding sediments at the right mid-margin (Figure 3.10[5]), and expelled salt forms a much thicker tongue (Figure 3.10[6]). The diapir formed in the proximal basin on the left margin is narrower (Figure 3.10[7]).

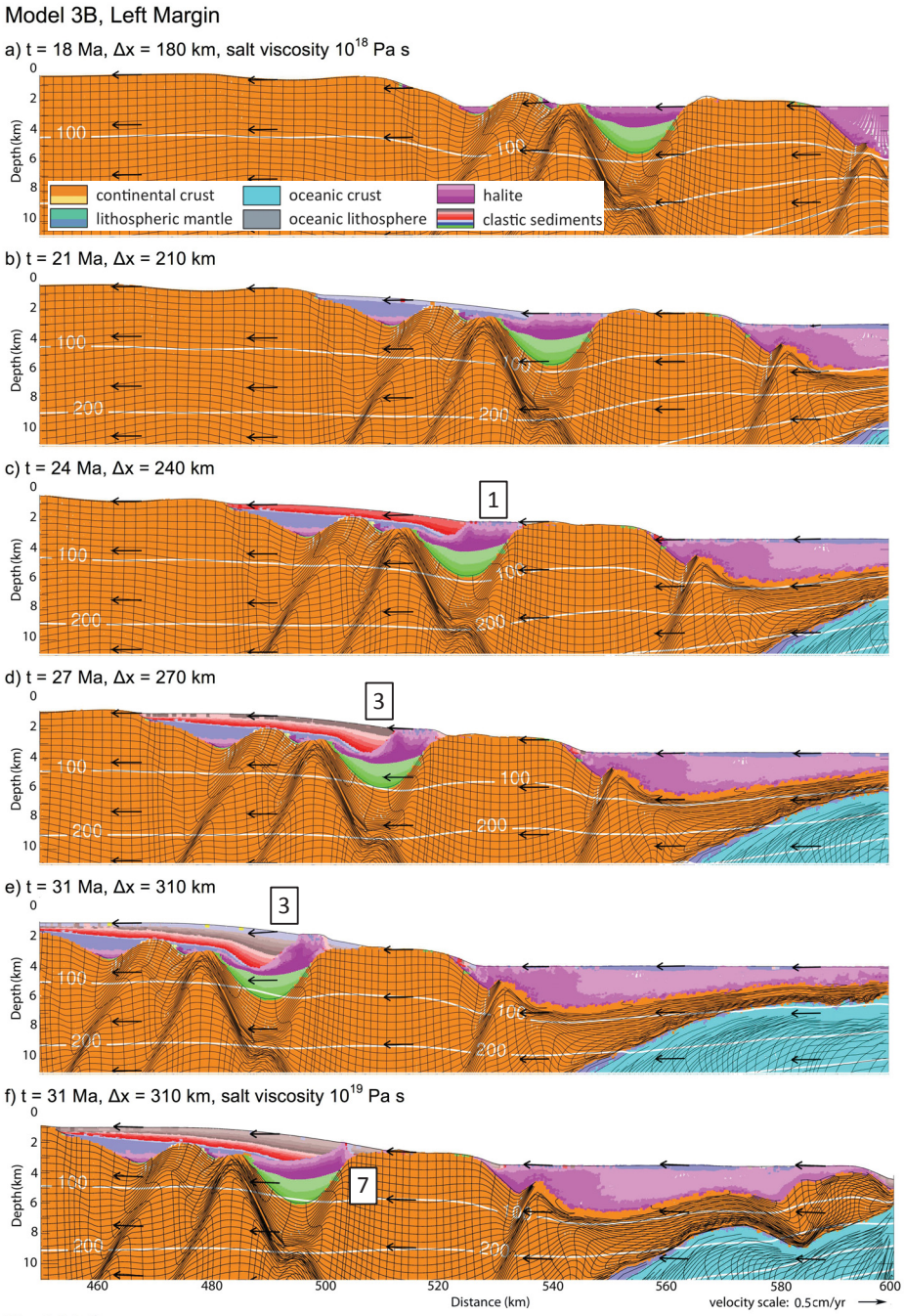

Fig. 10 left

Figure 3.10 left/right: Model 3B, mid syn-rift salt deposition with post-salt sediment progradation, for the left and right hand margins. a)-e) show model evolution for salt viscosity 10^{18} Pa s; f) shows final configuration for salt viscosity 10^{19} Pa s. See Fig. 2 caption for notation. Prograding sediments drive seaward movement of salt and the development of more complex salt tectonic structures, including: thickened salt bodies [1], a salt tongue with older salt flowing over younger salt [2], expulsion rollover and diapir [3], and a salt escarpment [4]. Salt viscosity 10^{19} Pa s leads to more salt trapped beneath prograding sediments [5], a thicker salt tongue [6], and a narrower diapir [7]. Vertical exaggeration 4:1.

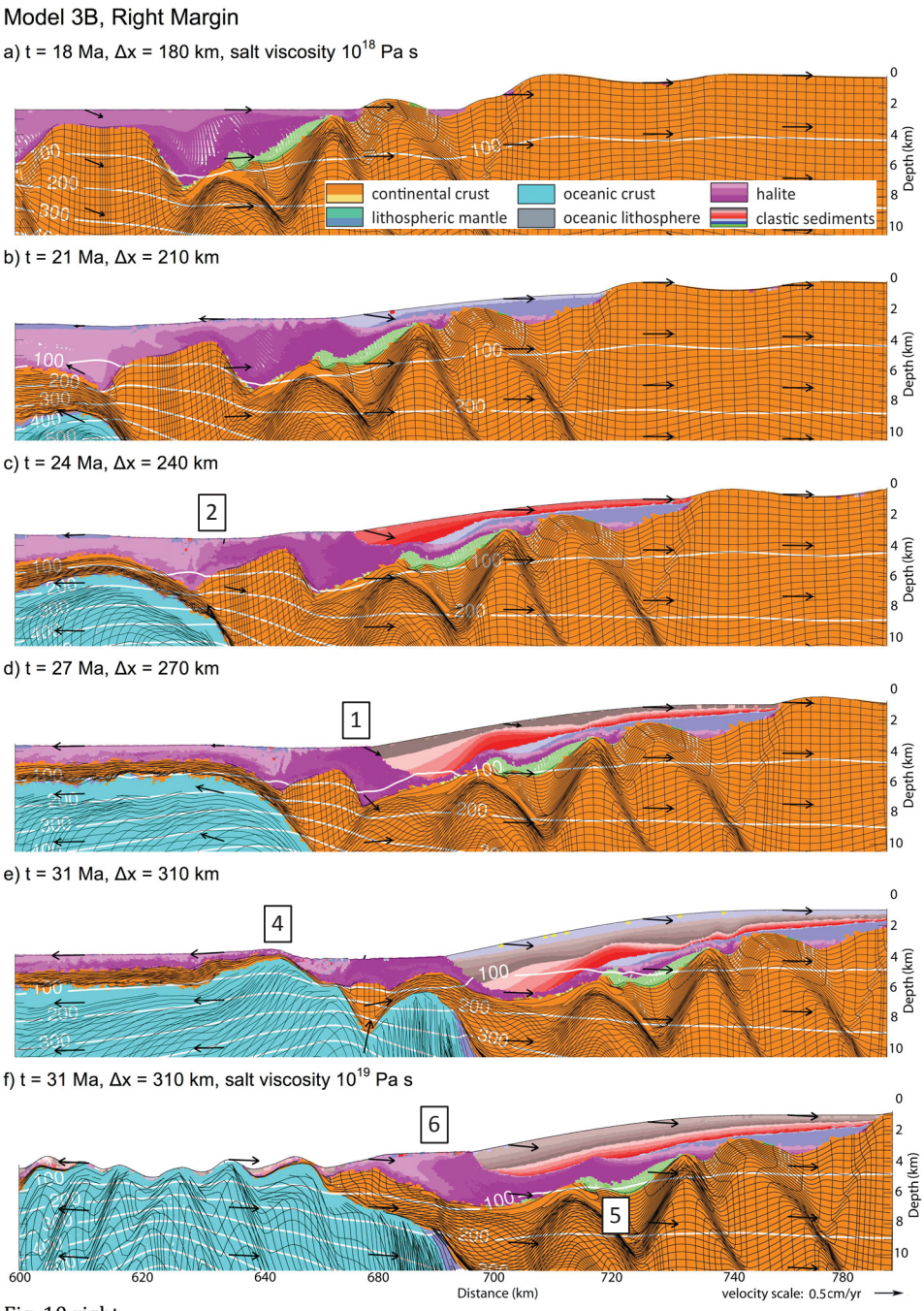

Fig. 10 right

Figure 3.10 left/right: Model 3B, mid syn-rift salt deposition with post-salt sediment progradation, for the left and right hand margins. a)-e) show model evolution for salt viscosity 10^{18} Pa s; f) shows final configuration for salt viscosity 10^{19} Pa s. See Fig. 2 caption for notation. Prograding sediments drive seaward movement of salt and the development of more complex salt tectonic structures, including: thickened salt bodies [1], a salt tongue with older salt flowing over younger salt [2], expulsion rollover and diapir [3], and a salt escarpment [4]. Salt viscosity 10^{19} Pa s leads to more salt trapped beneath prograding sediments [5], a thicker salt tongue [6], and a narrower diapir [7]. Vertical exaggeration 4:1.

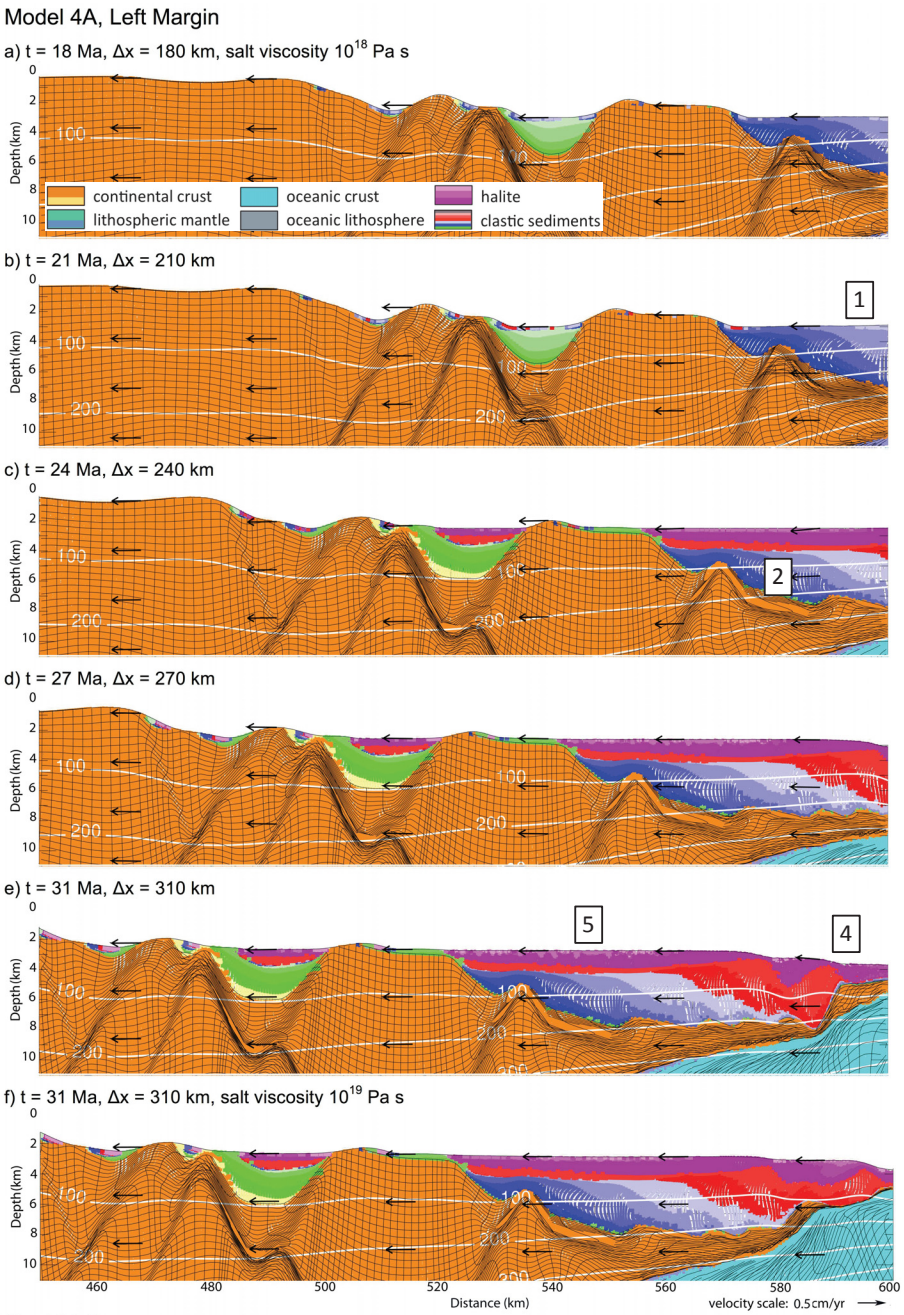

Fig. 11 left

Figure 3.11 left/right: Model 4A, late syn-rift salt deposition with no post-salt sedimentation, for the left and right hand margins. a)-e) show model evolution for salt viscosity 10^{18} Pa s; f) shows final configuration for salt viscosity 10^{19} Pa s. See Fig. 2 caption for notation. Salt is deposited as a broad, continuous layer over a thick succession of syn-rift clastic sediments [1], producing a smooth base of salt surface [2]. Initial salt thickness is relatively uniform across the rift axis, except where rapid thinning of the continental crust produces accommodation space filled by salt [3]. Where salt is thick, it freely flows towards the distal margin, producing escarpments [4]; lateral flow and drawdown is not significant where salt is thin[5] or is trapped in basins formed by syn-rift sediment [6]. Vertical exaggeration 4:1.

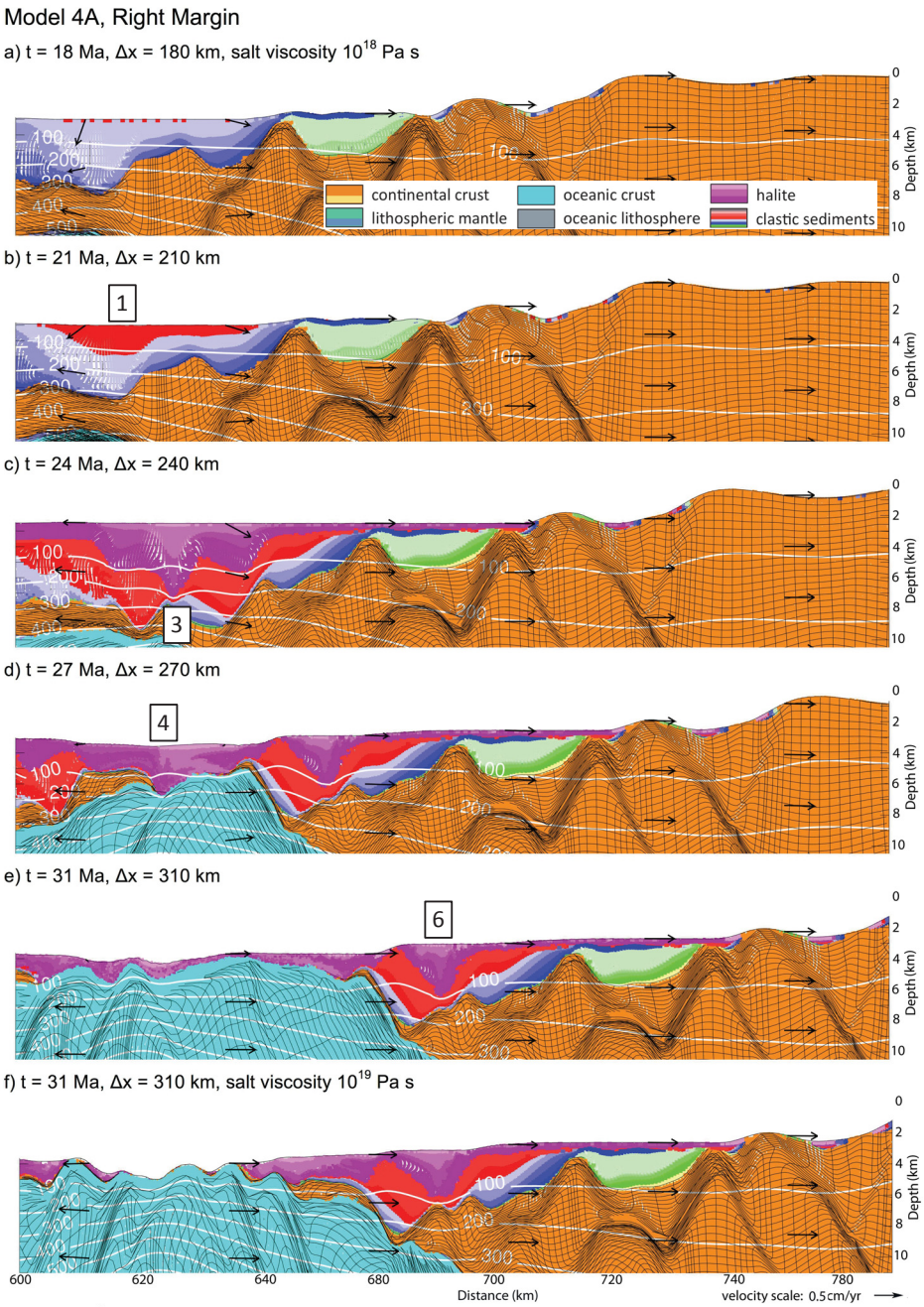

Fig. 11 right

Figure 3.11 left/right: Model 4A, late syn-rift salt deposition with no post-salt sedimentation, for the left and right hand margins. a)-e) show model evolution for salt viscosity 10^{18} Pa s; f) shows final configuration for salt viscosity 10^{19} Pa s. See Fig. 2 caption for notation. Salt is deposited as a broad, continuous layer over a thick succession of syn-rift clastic sediments [1], producing a smooth base of salt surface [2]. Initial salt thickness is relatively uniform across the rift axis, except where rapid thinning of the continental crust produces accommodation space filled by salt [3]. Where salt is thick, it freely flows towards the distal margin, producing escarpments [4]; lateral flow and drawdown is not significant where salt is thin[5] or is trapped in basins formed by syn-rift sediment [6]. Vertical exaggeration 4:1.

3.6.3 Late Syn-rift Salt Deposition

In Model Set 4 (Figures 3.11 and 3.12) salt is deposited during the latest syn-rift phase, from 23 to 24 Ma. Pre-salt sedimentation is a thick succession of aggrading clastic sediments (Figure 3.11[1], Figure 3.12[1]), similar to Model 1F. In Model 4A there is no sedimentation after salt deposition, whereas in Model 4B there are prograding clastics. Extensive sedimentation before salt deposition leads to a smoother base of salt surface in Model Set 4 (Figure 3.11[2]). Initial salt thickness is relatively uniform across the margin, at ~ 2 km, except directly over the rift axis, where rapid thinning of the continental crust generates accommodation space that is quickly filled with salt (Figure 3.11[3]). With the exception of the proximal horst blocks in both margins, salt is deposited in a broad, largely continuous body extending across the rift.

The late syn-rift salt at the rift axis is thick and it experiences little resistance to extension and lateral flow during crustal breakup and ocean floor spreading, as can be seen from the distributed thin salt and the drawdown effect on the salt surface, creating escarpments (Figure 3.11[4], Figure 3.12[2]). The lateral flow and drawdown is not significant in the mid-margin, where salt is thin (Figure 3.11[5]), or where the salt is trapped in rift basins largely filled with pre-salt clastic sediments (Figure 3.11[6]). The addition of prograding sediments, in Model 4B (Figure 3.12), serves to mobilize, expel and thicken salt deposited in the mid-margin regions (Figure 3.12[3]), but in contrast to the earlier models the salt in the proximal grabens, which is now thinner than in previous models, is rapidly buried with little deformation (Figure 3.12[4]). At the right margin pre-salt sediments impede salt expulsion (Figure 3.12[5]), but with further progradation more salt would

flow onto the oceanic crust. Overall, salt tectonics in the proximal margins is less well developed than in Model Sets 2 and 3, owing to reduced salt deposition because less accommodation space is available here during salt deposition.

Salt with viscosity 10^{19} Pa s (Figures 3.11f and 3.12f) has reduced lateral flow, particularly in the distal margins where it ruptures after a small amount of flow onto the oceanic crust (Figure 3.12[6]). Correspondingly, salt escarpments are less pronounced in cases with 10^{19} Pa s salt, except where the salt layer has broken above the oceanic crust. In addition, more salt remains trapped under the prograding sediment wedge at the mid-margin (Figure 3.12[7]).

3.7 Summary and Discussion

We have presented results of numerical models designed to improve our understanding of syn-rift salt tectonics by investigating the interactions among lithospheric extension and breakup, salt deposition, and clastic sedimentation. We include models with no sediments (Figures 3.2 and 3.3), with clastic sediments (Figures 3.4 and 3.6), and with syn-rift salt, with and without clastic overburden (Figures 3.7-3.12). The scope was purposely limited to models of a single type of lithosphere in order to focus on the salt-tectonic style in relation to timing of salt deposition relative to rifting and subsequent sedimentation. Lithospheric properties were chosen to represent an intermediate style, between the strong (Type I) and weak crust (Type II) models (*Huismans and Beaumont*, 2011, 2014), in which lower crust remains attached to the mantle, as in Type III (*Huismans and*

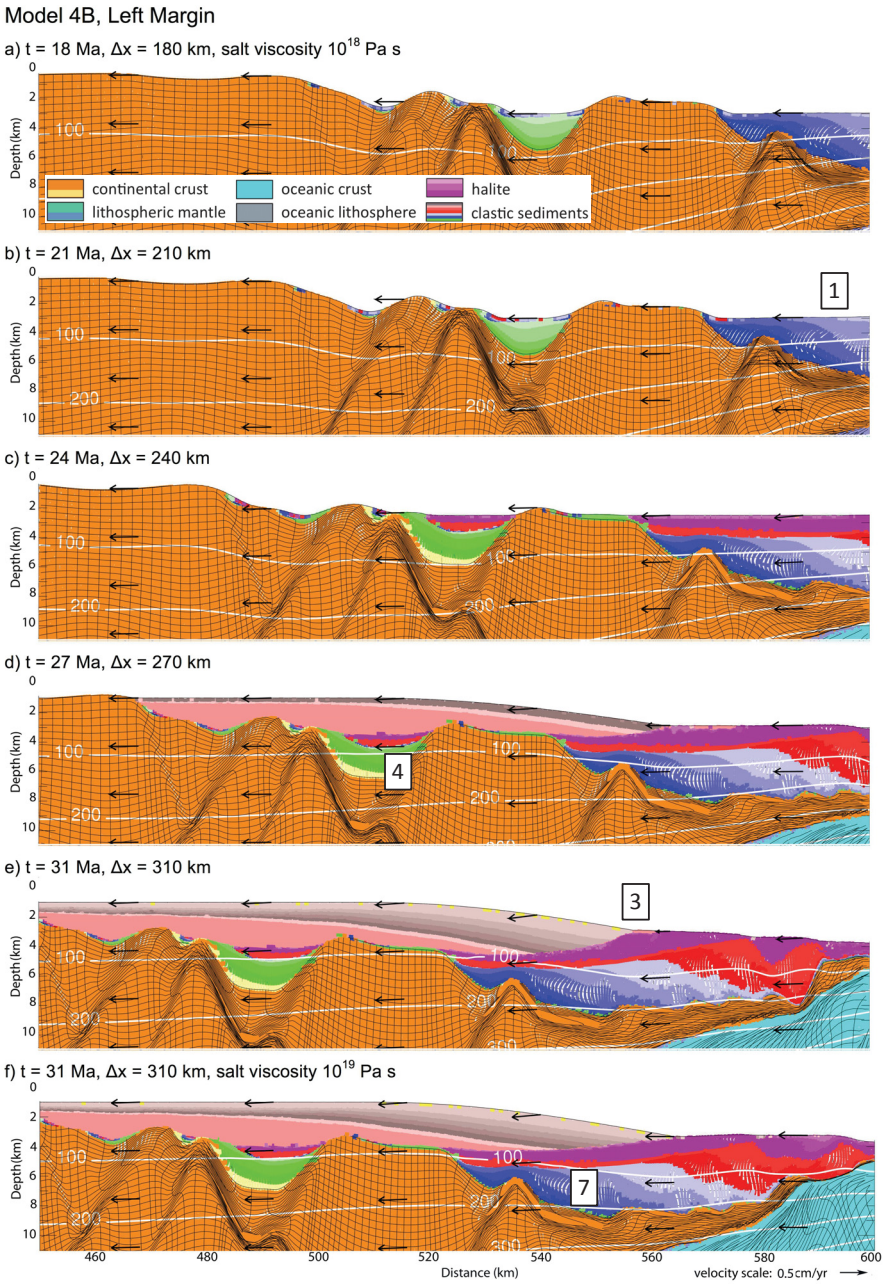

Fig. 12 left

Figure 3.12 left/right: Model 4B, late syn-rift salt deposition with post-salt sediment progradation, for the left and right hand margins. a)-e) show model evolution for salt viscosity 10^{18} Pa s; f) shows final configuration for salt viscosity 10^{19} Pa s. See Fig. 2 caption for notation. Salt is deposited as a continuous layer across the rift axis, over thick syn-rift sediment [1]. Salt drawdown forms escarpments [2]. Prograding sediments drive lateral flow and thickening of salt at the mid-margin [3]. Thin salt in the proximal basins experiences little deformation [4]. Salt flows across the distal margin and over oceanic crust, except where impeded by syn-rift sediments [5]. Salt viscosity 10^{19} Pa s impedes lateral flow of salt; the salt layer ruptures earlier and little salt flows over oceanic crust [6]. More salt is trapped under the prograding wedge with 10^{19} Pa s salt viscosity [7]. Vertical exaggeration 4:1.

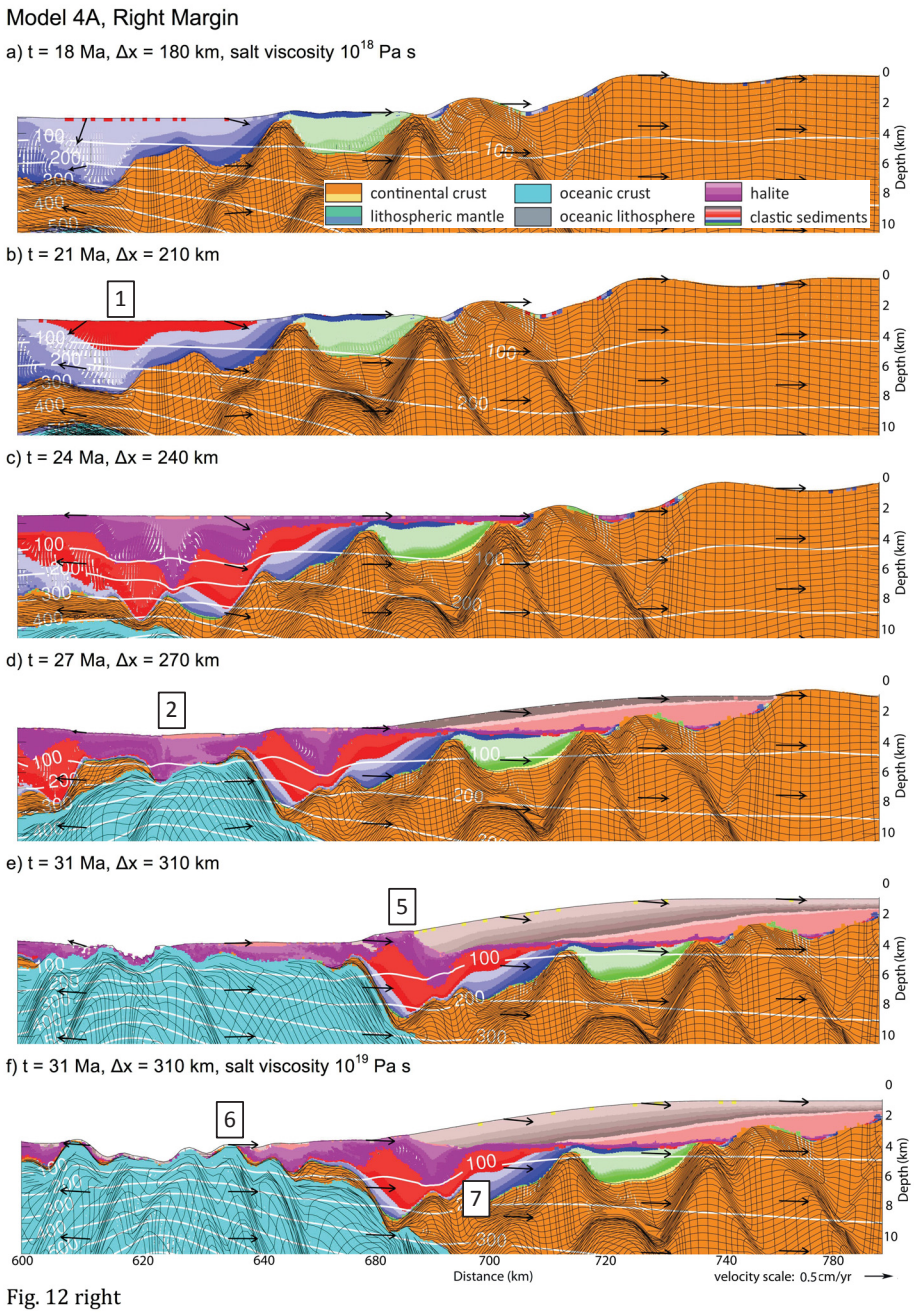

Fig. 12 right

Figure 3.12 left/right: Model 4B, late syn-rift salt deposition with post-salt sediment progradation, for the left and right hand margins. a)-e) show model evolution for salt viscosity 10^{18} Pa s; f) shows final configuration for salt viscosity 10^{19} Pa s. See Fig. 2 caption for notation. Salt is deposited as a continuous layer across the rift axis, over thick syn-rift sediment [1]. Salt drawdown forms escarpments [2]. Prograding sediments drive lateral flow and thickening of salt at the mid-margin [3]. Thin salt in the proximal basins experiences little deformation [4]. Salt flows across the distal margin and over oceanic crust, except where impeded by syn-rift sediments [5]. Salt viscosity 10^{19} Pa s impedes lateral flow of salt; the salt layer ruptures earlier and little salt flows over oceanic crust [6]. More salt is trapped under the prograding wedge with 10^{19} Pa s salt viscosity [7]. Vertical exaggeration 4:1.

Beaumont, 2014). These properties lead to a brittle, faulted style of thinning of the upper continental crust, producing graben basins in the early syn-rift phase. The conjugate margins are asymmetric, with margin widths between 100 and 150 km. Thermal subsidence is minor, owing to the narrow region of continental crust underlain by upwelled lithospheric mantle and the short rifting interval (13 to 31 Ma) for lithospheric cooling to develop. Of course, the width of the margins, duration of the syn-rift period, and location, geometry, and continuity of rift basins will vary depending on crustal rheology and the resultant rifting style. We will address the implications of narrow and wide margins for the associated salt tectonics in future work.

The results demonstrate that clastic sediment alone has important feedbacks on the style of continental extension and breakup, even for the relatively strong crust used in this paper. By comparison with Model 1E, the water-loaded reference case, sedimentation in Model 1F not only isostatically amplifies basin subsidence but the sediment loading enhances offset on the basin-bounding faults and the associated basins are deeper (cf. Figure 3.4[1]). Deposition of thick clastic sediments throughout rifting in Model 1F also imparts a more symmetric margin geometry, compared to Model 1E, by reducing the feedback impact of upper crust thickness and hence strength variations during extension. However, the overall dimensions of the rift system and duration of rifting are similar in both models. Thus, in our models, deposition of thick sediments does not favour a narrower rifting mode, as indicated by *Bialas and Buck* (2009). Nor does the deposition of sediments prolong rifting as suggested by *Corti et al*. (2010, 2013). Sediment cover, both salt and clastics, insulates the upper crust during rifting, resulting in higher

temperatures of the thinned upper continental crust, particularly at the distal margin during in the mid- and late syn-rift phases, thereby promoting wider hyperextended regions (cf. Figure 3.2f and Figure 3.4[7]).

The lithospheric model presented here shows clear evidence of diachronous stretching. Thinning of the upper crust is mostly accomplished through faulting which is initially partitioned between two fault-bounded grabens (Figures 3.3[1]). As rifting continues, deformation of the upper crust migrates towards the rift axis and the faults in the early proximal grabens are abandoned. By the late syn-rift period thinning of the upper crust is restricted to the most distal margins (Figure 3.3[2]). When sediments are deposited during rifting, as in Model 1F (Figures 3.5 and 3.6), they display the same pattern of a shifting locus of deformation, from the proximal to distal regions of the margin, as rifting proceeds. The resultant sediment package is faulted throughout its lateral extent, but only the sediments near the current distal part of the margin are actively deforming (Figure 3.6[2]). The diachroneity means that faults through sediment in the more distal part of the margin will have been active more recently than those through sediments in the proximal and mid-margin regions.

Our models (e.g. 1F, Figures 3.4 and 3.6) experience a small amount of thermal subsidence at the mid-margin, resulting in a thin layer of sediment at this location in the mid- to late syn-rift period. These sag basin sediments at the mid-margin are not cut by faults even though the underlying sediments are faulted (Figure 3.6[3,6]). This is because diachronous stretching of the crust has migrated in the interim to the rift axis. It therefore

appears that the observed pattern of faulted early syn-rift sag basin sediments overlain by undeformed late syn-rift sediments (e.g. *Karner and Gamboa*, 2007; *Karner and Driscoll*, 1999) can be explained by the diachronous extension of the margin, even though these authors did not favour this explanation. Formation of undeformed syn-rift sag basins is also consistent with mid-margin syn-rift thermal subsidence that occurs once extension has migrated to the distal margin, as noted by *Huismans and Beaumont* (2014).

The early, mid, and late syn-rift salt deposition models, shown schematically in Figure 3.13, demonstrate that distinct salt tectonic styles evolve as a consequence of the timing of deposition of salt relative to rifting of the continental crust. There is also reasonable agreement with the conceptual models for salt deposition syn-rift salt tectonics presented by *Rowan* (2014), although his models are based on syn-stretching, syn-thinning, and syn-exhumation phases of rifting (*Peron-Pinvidic and Manatschal*, 2009) which differ from our rifting models. In our early syn-rift models (Models 2A and 2B, Figures 3.7 and 3.8) salt is deposited in proximal basins, and initial autochthonous salt bodies have a thick narrow geometry, owing to the limited pre-salt sedimentation (Figure 3.13a). In the absence of subsequent sedimentation, deformation of salt in our models is mainly restricted to downward flow along the footwall of basin-bounding faults (Figure 3.7a, b left). As suggested by *Rowan* (2014), salt remains largely confined to the proximal region as rifting continues, though under the influence of differential pressure induced by prograding sedimentation some salt is able to flow over basement highs between fault-bounded basins (Figure 3.8a, b right). Vertical movement of salt is also observed at basin boundaries (Figure 3.8[2], [3]) leading to passive diapirism, as suggested by *Rowan*

(2014), as a consequence of salt expulsion by sediment loading (Figure 3.13a), but in one case this ceased when the diapir was rapidly buried by prograding sediments (Figure 3.8[6]; Figure 3.13a).

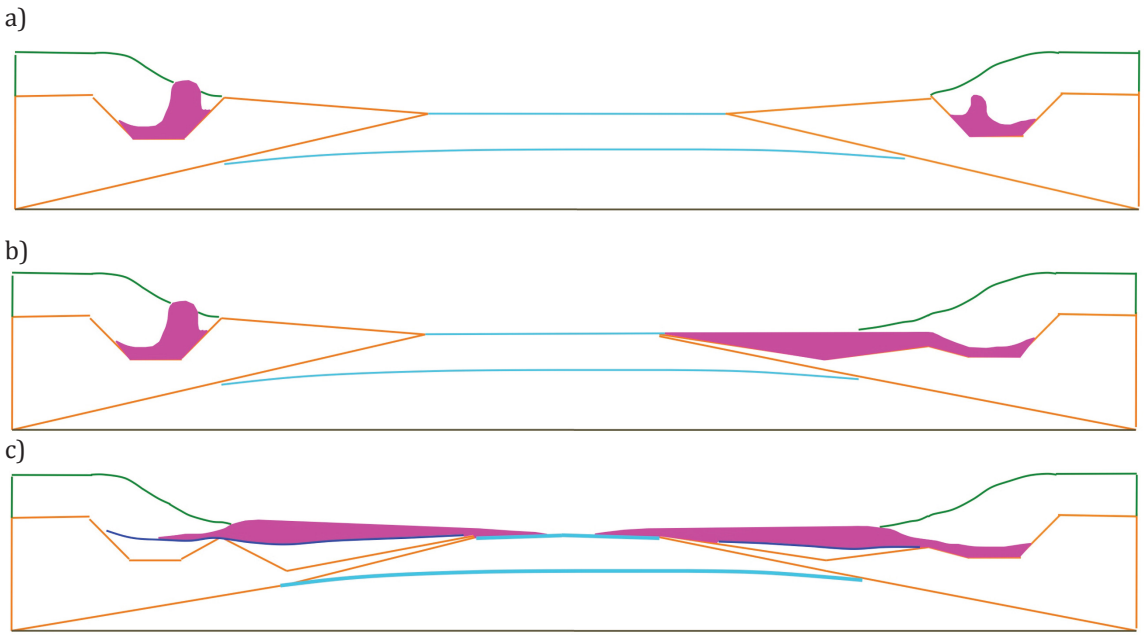

Fig. 13

Figure 3.13: Schematic diagram of final distribution of salt deposited in the a) early, b) mid, and c) late syn-rift periods. Early syn-rift salt (a) remains largely confined to fault-bounded graben in the proximal margin. Mid syn-rift salt (b) is distributed across the proximal to mid margin, and may extend over the distal margin as rifting continues. Late syn-rift salt (c) is predominantly found in the mid to distal margin, and may extend over oceanic crust.

Our mid-syn-rift salt models (3A and 3B, Figures 3.9 and 3.10) are characterized by salt deposited in the proximal grabens and across a broad region spanning the rift axis (Figure 3.13b). Salt at the rift axis both extends and flows seaward though gravity gliding, assisted by gravity spreading for Model 3B (Figure 3.10b-e right) driven by post-salt prograding sediments. Mobilization of salt by thick-skinned, crustal, deformation, as suggested by Rowan (2014) for syn-thinning salt, is present (Model 3A, Figure 3.9b-e right) but confined to the distal margin because extension has already migrated to the rift

axis, resulting in little movement along faults underlying salt in the mid and proximal margin. This shift in locus of crustal deformation, from the proximal to distal margin, will probably proceed more slowly for other crustal compositions, such that thick-skinned deformation of mid-syn-rift salt may be more important for a weaker or hotter continental crust.

Prograding sediments serve to expel mid-syn-rift salt toward the distal margin, whereas significant salt remains in the mid-margin in the absence of post-salt sedimentation (Figures 3.9 and 3.10). In contrast to *Rowan*'s (2014) description of syn-thinning salt, our results show that appreciable mid-syn-rift salt may be deposited in proximal basins (Figure 3.9) and remain there, forming diapirs following sediment progradation (Figure 10[3]). This will clearly depend on the crustal rifting style and the available accommodation. *Rowan*'s (2014) description may apply to a weaker crust with shallower proximal grabens that have less accommodation. Gaps along strike in natural basement highs between grabens can also assist salt flow around the basement highs, whereas gaps do not occur in our 2D models.

In our models, and as indicated by *Rowan* (2014), by the latest syn-rift phase thinning of the continental crust is largely complete and residual extension is confined to the most distal margin, so mobilization of salt occurs by thin-skinned, not thick-skinned, deformation. Our late syn-rift models (4A and 4B, Figures 3.11 and 3.12) deposit salt broadly across both margins. Except where crust continues to extend (Figure 3.11[3]), the base of salt surface is smoothed by a thick succession of previously deposited sediments,

facilitating seaward salt flow. Thick salt flows seaward by extension and gravity gliding, assisted by gravity spreading where prograding sediments follow salt deposition (Figures 3.11 and 3.12). However, thinner salt in the mid and proximal margin is less mobile; under sediment progradation, salt deposited at the mid margin thickens, but resists flow to the distal margin (Figure 12[3]).

Unlike our earlier salt tectonic models (eg. *Albertz et al*., 2010; *Goteti et al*., 2013), the results presented here provide an improved integrated physical understanding of the development of salt tectonics at rifted margins by not prescribing the salt basin geometry but, instead, allowing it to evolve in a self-consistent manner during extension of the crust, and by considering the interactions among salt deposition, rifting and ongoing sedimentation. This analysis, therefore, offers insight into the relative importance of rifting, timing of salt deposition and sedimentation, in driving salt tectonics at rifted continental margins for particular cases. Additional work is, however, required to investigate a more comprehensive range of sedimentation styles on salt deformation, and to extend the present work to strong and weak continental crust compositions that lead to respectively narrow and wide rifted margins.

3.8 The Red Sea: A Natural Example of Syn-rift Salt Tectonics

The Red Sea is in the late syn-rift to early post-rift phase of breakup, hosts an incipient oceanic ridge, and contains thick evaporite deposits, making it the ideal location to study the interaction between continental rifting and salt tectonics in a

young syn-rift setting. It also provides an opportunity to address the role of non-halite evaporites, as we explain below. However, despite being ideal, the paucity of suitable data in the public domain means that our comparison with models must be regarded as preliminary. Opening of the Red Sea proceeded from south to north; oceanic crust in the southern Red Sea forms a continuous axial trough and is ~ 5 million years old (e.g. *Ligi et al*., 2012; *Bonatti*, 1985; *Cochran*, 1983), while the central Red Sea is characterized by segments with a focused axial trough containing 2-3 Ma-old oceanic crust (*Bonatti*, 1985; *Chu and Gordon*, 1998; *Cochran and Martinez*, 1988; *Searle and Ross*, 1975), separated by regions with a more diffuse axial depression where oceanic crust is not exposed (*Ligi et al*., 2012; *Mitchell et al.,* 2010; *Augustin et al*., 2014). Here we use 'Ma-old' and 'Ma ago' to mean time measured backward from the present to avoid confusion with model time 'Ma' measured from the start of extension.

Syn-rift sedimentation in the Red Sea consists of open marine and shallow marine deposits, including a thick evaporite succession (eg. *Bosworth et al*., 2005), and can be categorized as pre-evaporite, mixed evaporite, halite, mixed evaporite, and post-evaporite packages. The pre-evaporite package consists primarily of sandstone, shale, and various carbonate facies (*Bosworth et al*., 2005). The earliest confirmed syn-rift strata in the central Red Sea are 21-24 Ma-old in age (*Scott and Govean*, 1985; *Hughes and Filatoff*, 1995). Between 14 and 5 Ma-ago, the Red Sea and Gulf of Suez were isolated from the Gulf of Aden, desiccated, and a thick evaporite package

was deposited (e.g. *Ligi et al*., 2012; *Bosworth et al*., 2005). The evaporite succession consists of two assemblages: massive halite, and a mixed evaporite composed of anhydrite, shale, and sandstone, with occasional halite and limestone (*Izzeldin,* 1987), which was deposited both before and after the halite. This distinction is important, as halite can be considered to deform according to a linear viscous flow law, while the mixed evaporite package almost certainly has a finite strength. Early evaporite deposition consisted of the mixed evaporite package. Massive halite deposition was widespread throughout the Red Sea at 10 Ma-ago, corresponding with a significant drop in sea level (*Haq et al.*, 1987). Deposition switched again to mixed evaporites, indicating a shallow marine environment, before 5.3 Ma-ago, though the timing of this change is debated (e.g. *Richardson and Arthur*, 1988). Evaporite deposition ceased at about 5.3 Ma-ago. The post-evaporite package consists mainly of clastic material derived from the uplifted rift shoulders. This material is largely trapped in near-shore minibasins formed by mobilization of halite; very little sediment has been transported to the axial trough. (*Bosworth et al*., 2005). A thin layer of hemipelagic sediments, ranging in thickness from 0.2 to 0.6 km, and thinner towards the rift axis, overlies the salt (*Ligi et al*., 2012), and likely prevented large scale dissolution of the salt, resulting in the relatively smooth salt surface observed today (*Mitchell et al*., 2010).

Salt tectonics developed quickly in the Red Sea. Evaporite deposition ceased 5 Ma-ago, and in that time complex autochthonous and allochthonous evaporite structures have formed (*Augustin et al*., 2014). Evaporites were originally deposited

as a continuous body across the two margins, and then separated in places when oceanic crust reached the seabed (e.g. *Mohriak and Leroy*, 2012; *Orszag-Sperber et al.*, 1998), possibly aided by dissolution of salt through exposure to hydrothermal fluids (*Mitchell et al.*, 2010). Maximum original thickness of the total evaporite package is estimated at between 2 and 7 km (*Ligi et al.*, 2012, *Mitchell et al.*, 2010,). The thickness of the massive halite layer is less well constrained, though Bosworth *et al.* (2005) assume this to be 300 m at the present, for areas far from salt walls/ridges. We take this to represent a residual thickness considerably less than the original average. Evaporites display a gravity-driven basinward movement, with extensional features in the proximal margins and contraction features in the distal margins (*Rowan*, 2014). In the central and southern Red Sea, thick salt walls and diapirs are separated by the incipient oceanic ridge. In the central Red Sea evaporite lenses, submarine namakiers (Figure 3.15c), are advancing towards the rift axis through gravity gliding, flowing around protruding elements of the continental crust. The namakiers mainly flow where the crust has low rugosity, whereas the exposed oceanic crust has higher rugosity (*Augustin et al.*, 2014, Figure 3.4). Evaporites are present over the oceanic crust, as evidenced by magnetic anomalies under the leading edge of the salt (*Mitchell et al.*, 2010). The rapid development of salt tectonics in the Red Sea is interpreted to be driven by extensional tectonics, generating margin tilt and producing basement steps, and by prograding sedimentation over salt. The relative importance of these two factors is not well understood.

Our model (Model RS) incorporates the five main phases of syn-rift sedimentation inferred for the Red Sea. Both Pre- and Post-evaporite sediment packages (Table 3.3) are composed of compacting frictional-plastic clastic sediments, deposited in respective aggradational and progradational settings. The mixed evaporite package, Evaporite-1 and Evaporite-3, is also modeled as frictional plastic, to capture the finite strength of this layered succession of evaporite and clastic sediments, but has a higher initial density and, like the halite, does not compact (Table 3.1). Evaporite-2, halite, is modeled as a linearly viscous material with viscosity 10^{19} Pa s. We use the same properties for the lithosphere as in the earlier models because the model results, e.g Model 1E, F (Figures 3.3 and 3.4) have a similar overall geometry to the Red Sea (Figures 3.14 and 3.15), although the proximal grabens may be overemphasized. As is clear from Figure 3.15c (also see *Augustin et al*., 2014, Figure 4c) the salt flow regime is three dimensional near the rift axis with oceanic crust exposed in the deeps and salt covering the rift axis elsewhere. Our 2D model cannot reproduce this complexity. We therefore consider the present configuration of the central Red Sea to represent a time ~3 Ma after breakup of the continental crust, which *Augustin et al*., (2014) interpret to be relatively uniform along strike, not segmented by 'nodes'. Crustal breakup happens in our Model RS, at 27 Ma model time (where Ma is the model evolution time) and define the sedimentation history relative to this point. Pre-evaporite sediments are deposited to 17 Ma model evolution (13 Ma-ago). Evaporite-1, mixed evaporites, is deposited from 17-20 Ma model evolution (13-10 Ma-ago). Evaporite-2, halite, is deposited from 20 to 24 Ma model evolution (10 - 6 Ma-ago), followed by Evaporite-3, mixed evaporites.

Evaporite deposition ceases and post-evaporite sedimentation begins at 25 Ma (5 M- ago).

Our model (Model RS) (Figure 3.14) captures many of the features characterizing the central Red Sea (Figure 3.15). In particular, we compare our model with those segments of the central Red Sea where a localized axial trough has formed, but note there are other segments where the oceanic crust is not exposed (Figure 3.15c). Halite is deposited as a continuous layer between the margins, predominantly in a region over the rift axis, in the mid syn-rift period (Figure 3.14 [1]); this agrees with previous interpretations (*Mohriak and Leroy*, 2012; *Orszag-Sperber et al.*, 1998; *Augustin et al.*, 2014). Halite deposition is preceded and followed by mixed evaporites (Figure 3.14 [2]). Maximum initial thickness of the halite layer is ~ 3.5 km (Figure 3.14 [3]). Original thickness for the full evaporite package (including halite and mixed evaporites) is 3-5 km (Figure 3.14 [4]), which falls within the range of suggested original salt thicknesses (*Ligi et al.*, 2012; *Mitchell et al.*, 2010). Evaporite-3 deposited over halite ruptures by 27 Ma model evolution (Figure 3.14 [5]), exposing halite at the seafloor. A portion of halite is subsequently expelled from under Evaporite-3, flowing seaward and increasing the halite thickness over the rift axis (Figure 3.14 [6]). Evaporite-2, halite, at the rift axis then stretches and thins, ultimately rupturing at ~ 33 Ma model evolution (Figure 3.14 [6,7]). This produces a seaward-thinning halite profile in the most distal margin, consistent with previous interpretation (*Ligi et al.*, 2012). Some halite is trapped in the mid margin, beneath Evaporite-3 (Figure 3.14 [8]).

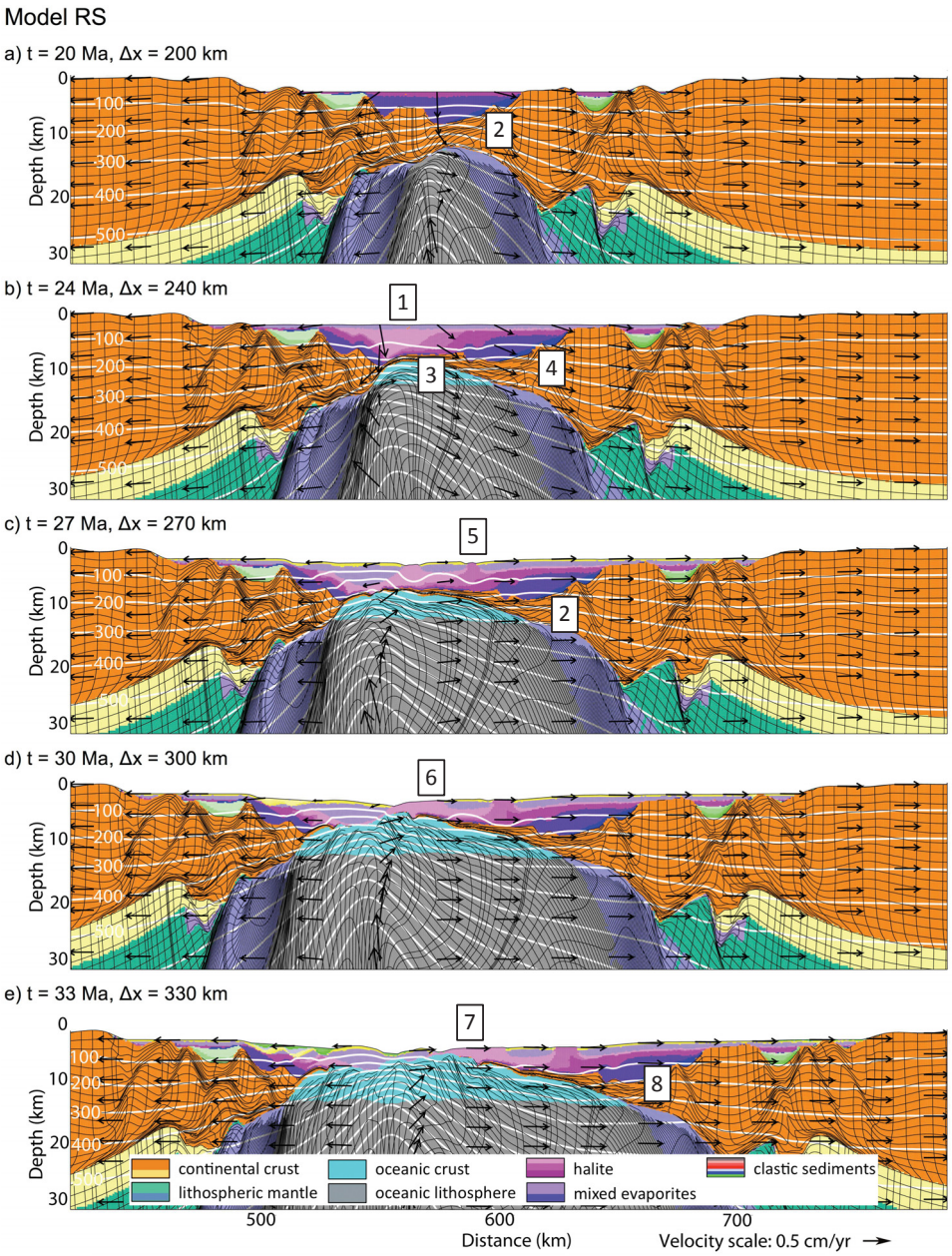

Fig. 14

Figure 3.14: Model RS, model of evolution of the central Red Sea with mid to late syn-rift salt deposition and water loading. Salt (halite) viscosity is 10^{19} Pa s. Successive panels show model evolution with model time, t, and current total extension, Δx. See Fig. 2 caption for notation. Halite is deposited as a continuous layer across the rift axis [1], in the mid syn-rift period, preceded and followed by mixed evaporite deposition [2]. Maximum initial thickness of the halite [3] and total evaporite package [4] are 3.5 and 3-5 km. Mixed evaporite over halite ruptures, exposing halite at the seafloor [5]. Halite is expelled from beneath overlying mixed evaporite, increasing halite thickness at the rift axis [6]. Halite at the rift axis subsequently thins and ruptures [6,7], producing a seaward-thinning profile [7]. Some halite is trapped beneath mixed evaporite at the mid margin [8]. Vertical exaggeration 4:1.

Table 3.3: Sedimentation characteristics for Model RS, of the Central Red Sea

Sediment Name	Rheology	Start (Ma)	End (Ma)	h_1=h_2 (km)	h_3 (km)	A (m)	λ (km)
Pre-Evaporite	Frictional-plastic clastics	0	17	3.0			
Evaporite-1	Mixed evaporites	17	20	3.0			
Evaporite-2	Halite	20	24	2.5			
Evaporite-3	Mixed evaporites	24	25	2.2		25	20
Post-Evaporite	Frictional-plastic clastics	25	25.1	2.0			
		25.1	NA	2.0	5.0		

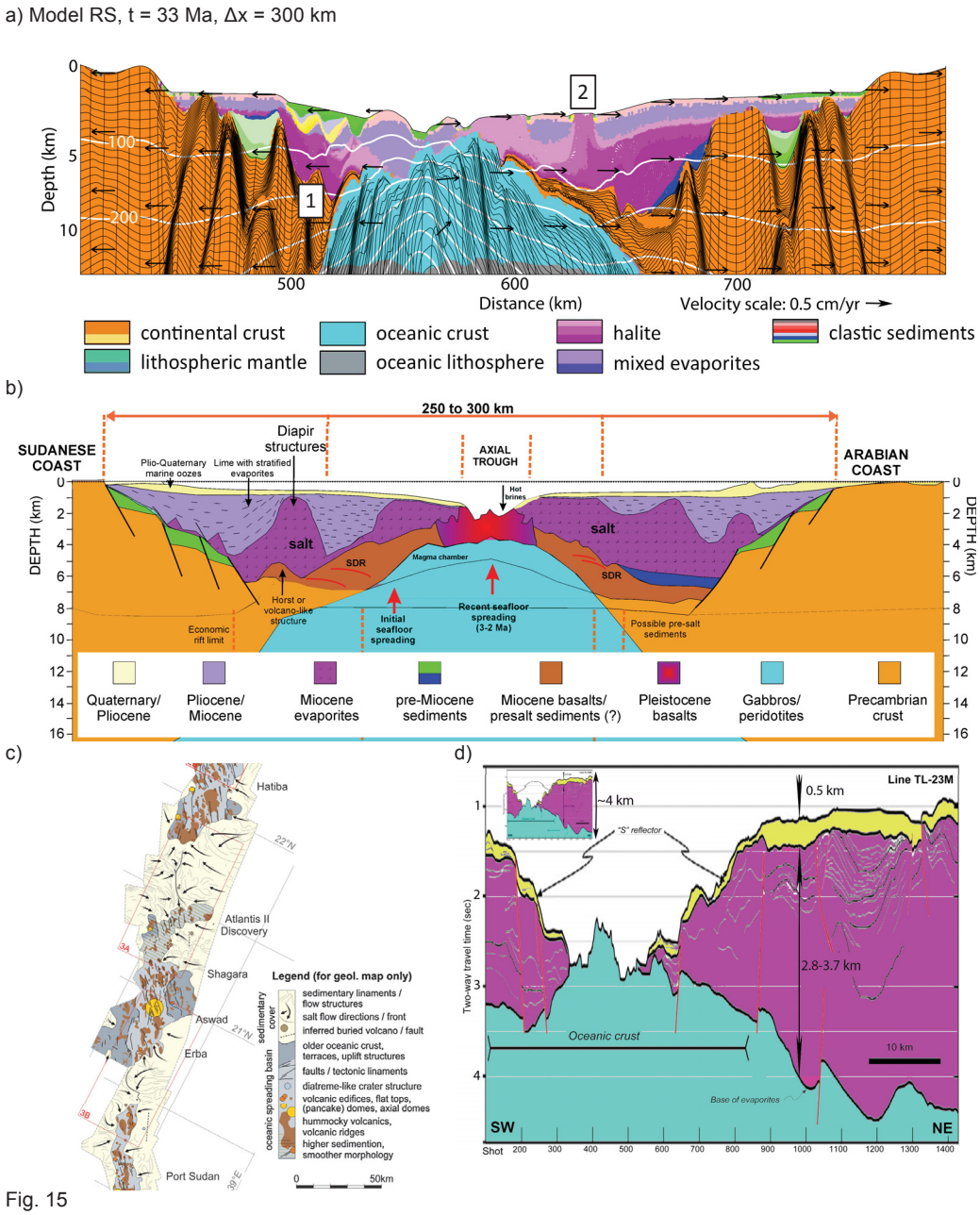

Fig. 15

Figure 3.15: Comparison of: a) Model RS at 33 Ma model evolution with; b) diagram of cross section of the southern Red Sea (after *Mohriak and Leroy*, 2012), and; d) line drawing interpretation of seismic reflection profile across the axial trough, central Red Sea (after *Ligi et al.*, 2012). Small inset in d) shows the Ligi et al. (2012) section at the same scale as the panels above. Vertical exaggeration 12:1. Note it would be equally valid to reverse the polarity of panel a. Panel c) shows regions of the central Red Sea where oceanic crust is exposed and others covered by namakiers (after *Augustin et al.*, 2014). In a) Evaporite-1 and Evaporite-2 (halite) have the same shades of magenta colouration to match b) in which pre-halite evaporites are not distinguished from halite (salt). Evaporite-3 in a) and corresponding evaporite in b) are shown in lavender. See Fig. 2 caption for notation. In a) halite flows between sub-basins [1], and produces a diapir [2]. Note the significant width of oceanic crust beneath the sediments.

The presence of halite at the mid margin agrees with the diagrammatic interpretation offered by *Mohriak and Leroy* (2012), though we note that their interpretation (Figure 3.15b) is meant to represent the southern Red Sea. Those parts of the central Red Sea where oceanic crust is exposed represent a similar, albeit younger by 2-3 Ma, stage of evolution to the southern Red Sea, and hence may be expected to host similar evaporite features. Model RS at 30 Ma (Figure 3.15a) represents an averaged case, with a small amount of residual salt over the rift axis, and is therefore intermediate between Figure 15b and regions with namakiers (Figure 3.15c).

At the mid margin on the left side of Model RS halite flows between sub-basins (Figure 3.15 [1]). At the right distal margin halite breaches the overlying Evaporite-3 (mixed evaporite) and forms a diapir (Figure 3.15 [2]). By 30 Ma model time (Figure 3.14d), equivalent to the present day configuration for the central Red Sea, Evaporite-2 (halite) thickness is highly variable, ranging from less than 0.5 km in the proximal to mid region of the left margin, to a maximum of 4.5 km at the diapir on the right margin. The highly variable halite thickness, including very thin halite far from diapirs/salt walls, is consistent with the interpretation of Bosworth *et al.* (2005). Halite over the most distal left margin and oceanic crust at this location is ~1.5-2.0 km thick; the total evaporite package at the most distal right margin is ~ 3.0 km thick.

We characterize evaporite deposition in the central Red Sea as mid to late syn-rift, by comparison with our syn-rift salt deposition models. In comparing our Red Sea model against our syn-rift salt models, we focus on deposition of Evaporite-2, halite. The timing of halite deposition relative to rifting in Model RS falls between the halite deposition windows for our mid and late syn-rift models. The original geometry of halite in Model RS most closely resembles our mid syn-rift models. As Model RS evolves, halite flows seaward, onto thinned continental crust and emerging oceanic crust, similarly to Model Set 4. This characterization of halite deposition in the central Red Sea as mid to late syn-rift agrees well with Rowan's suggestion of the northern Red Sea, which lags the central Red Sea in rifting by a few million years, is an example of syn-thinning salt.

Lastly, it is important to note that the lithospheric rifting models we use are suited to magma-poor margins, because we do not consider the impact on rifting of decompression melting or magma injection into the crust. Under these circumstances, the models do not apply to the southern Red Sea-Afar Triangle region where magmatism is important (e.g. *Ebinger et al.*, 2010). We believe the models do apply to the central Red Sea to the degree that magmatism within the extending syn-rift continental crust is less dominant. Our model results are generally consistent with observations, which can be interpreted to indicate either that magmatism is subordinate in the central Red Sea, or that magmatism in the form of dyke injection is prevalent but did not affect the style of rifting. The latter explanation is plausible because the shear zones in our models are weak owing to strain softening, which mimics the effect of fluid pressure from dykes when they are first

injected. Moreover, the model crust (Figure 3.15) is also hot, particularly in the oceanic part where temperatures reach 600 °C. This implies that intermittent injection of thin dykes would need to occur sufficiently often to augment the crustal temperature for there to be a feedback effect that significantly weakens the crust owing to heating.

3.9 Conclusions

We have used 2D numerical models to examine the effects of underlying crustal extension on the mobilization of overlying syn-rift salt (evaporites) and the subsequent salt tectonics. The models include generic examples, where the timing of salt deposition is varied in relation to rifting, and one for the specific natural example of the Red Sea. For the intermediate crust presented in this paper, which results in brittle deformation of the upper crust and some decoupling between the upper and lower crust, the following conclusions can be drawn regarding the interactions among the dynamically evolving rifted margin, sedimentation, and the deposition and deformation of salt.

1. Diachronous stretching initially focuses thinning of the upper continental crust in the proximal margin but this migrates to the distal margin in the mid to late syn-rift phases, preferentially creating accommodation space at the most distal margin, and leading to sag basin deposits that young seaward (Figures 3.2-3.6).
2. The sag basin deposits also reflect the diachronous stretching and deformation in that they are cut by a series of abandoned seaward-dipping normal faults, with faults in the distal region having most recently been active. Owing to diachronous

stretching, faults through sag basin deposits do not extend to the uppermost, youngest, layers of the syn-rift sediments, and do not cut overlying post-rift sediments (Figure 3.6).

3. Salt deposition during the early, mid-, and late syn-rift periods leads to distinct patterns of salt distribution and deformation (Figure 3.13). Early syn-rift salt is largely confined to fault-bounded grabens in the proximal margins. Mid- and late syn-rift salt is deposited as a continuous layer across the conjugate margin pair, and extends and flows readily over the distal margin or, particularly for late syn-rift salt, onto the oceanic crust. Late syn-rift salt may be deposited as a broad layer of relatively uniform thickness over thick sag basin sediments.
4. In all cases, and as noted in previous studies, the addition of prograding sediments after salt deposition leads to an increased tendency for lateral salt expulsion and flow, and the development of more complex salt tectonic structures. For early syn-rift salt, progradation produced expulsion rollovers and diapirs in the proximal margin grabens. Mid syn-rift salt developed thickened salt bodies, diapirs, and salt tongues with older salt flowing over younger, at the mid margin. Sediments prograding over late syn-rift salt resulted in increased lateral flow of salt from the mid margin, thickened salt at the distal margin, and an increased tendency for salt to flow over the oceanic crust.
5. Our characterization of early, mid and late syn-rift salt shows reasonable agreement with Rowan's (2014) description of salt deposition in the syn-stretching, syn-thinning, and syn-exhumation periods.

6. Model RS (Red Sea), which deposits an evaporite package consisting of halite and mixed evaporites during the mid- to late syn-rift period, captures several characteristic features of salt tectonics at the central/southern Red Sea, including: initial halite and total evaporite thickness; seaward flow of halite and development of diapir/salt wall and minibasins pairs at the distal margin; and seaward-thinning halite that extends over the oceanic crust (Figures 3.14 and 3.15).

3.10 Acknowledgments

This work was funded in part by NSERC and by the Killam Trusts. J.A. acknowledges an NSERC graduate scholarship and a Killam pre-doctoral award. C.B. was funded by an NSERC Discovery Grant and by the Canada Research Chair in Geodynamics. We thank Mark Deptuck for helpful discussion surrounding salt basin geometry. We also acknowledge Mark Deptuck, Steven Ings, David Whipp, and Nick Culshaw for constructive comments on an earlier version of this work. Numerical models used the software SOPALE-Nested, developed from SOPALE by D. Guptill and members of the Dalhousie Geodynamics Group. SOPALE was originally developed at Dalhousie University by P. Fullsack. We thank the reviewers, Dave Waltham and Tim Dooley, and the editor, Cindy Ebinger, for their assistance in fine-tuning this paper, particularly in regards to improving readability for a broad audience.

3.11 References

Adam, J., Ge, Z. & Sanchez, M. (2012a) Salt-structural styles and kinematic evolution of the Jequitinhonha deepwater fold belt, central Brazil passive margin. *Marine and Petroleum Geology*, 37, 101-120, doi: 10.1016/j.marpetgeo.2012.04.010.

Adam, J., Ge, Z. & Sanchez, M. (2012b) Post-rift salt tectonic evolution and key control factors of the Jequitinhonha deepwater fold belt, central Brazil passive margin: Insights from scaled physical experiments. *Marine and Petroleum Geology*, 37, 70-100, doi: 10.1016/j.marpetgeo.2012.06.008.

Albertz, M. & Beaumont, C. (2010) An investigation of salt tectonic structural styles in the Scotian Basin, offshore Atlantic Canada: 2. Comparison of observations with geometrically complex numerical models. *Tectonics*, 29, TC4018, doi: 10.1029/2009TC002540.

Albertz, M., Beaumont, C., Shimeld, J.W., Ings, S.J. & Gradmann, S. (2010) An investigation of salt tectonic structural styles in the Scotian Basin, offshore Atlantic Canada: 1: Comparison of observations with geometrically simple numerical models. *Tectonics*, 29, TC4017, doi:10.1029/2009TC002539.

Augustin, N., Devey, C.W., Van Der Zwan, F.M., Feldens, P., Tominaga, M., Bantan, R.A., AND Kwasnitschka T. (2014) The rifting to spreading transition in the Red Sea. *Earth and Planetary Science Letters*, 395, 217-230. doi: 10.1016/j.epsl.2014.03.047.

Baikpour, S., Zulauf, G., Sebti, A., Kheirolah, H. & Dieti, C. (2010) Analogue and geophysical modelling of the Garmsar Salt Nappe, Iran: constraints on the evolution of the Alborz Mountains. *Geophysical Journal International*, 182(2), 599-612, doi: 10.1111/j.1365-246X.2010.04656.8.

Beaumont, C. & Ings, S.J. (2012) Effect of depleted continental lithosphere counterflow and inherited crustal weakness on rifting of the continental lithosphere: General results. *Journal of Geophysical Research – Solid Earth*, 177, B08407, doi: 10.1029/2012JB009203.

Beaumont, C., Jamieson, R.A., Butler, J.P. & Warren, C.J. (2009) Crustal structure: A key constraint on the mechanism of ultra-high-pressure rock exhumation. *Earth and Planetary Science Letters*, 287(1-2), 116-129, doi: 10.1016/j.epsl.2009.08.001.

Beaumont, C., Nguyen, M.H., Jamieson R.A. & Ellis, S. (2006) Channel flow, ductile extrusion and exhumation on continental collision zones. *Geological Society Special Publication*. 268, 91-145, doi: 0.1144/GSL.SP.2006.268.01.05.

Bialas, R.W. & Buck, W.R. (2009) How sediment promotes narrow rifting: Application to the Gulf of California. *Tectonics*, 28, TC4014, doi:10.1029/2008TC002394 .

Bonatti, E. (1985) Punctiform initiation of seafloor spreading in the Red-Sea during transition from a continental to an oceanic rift. *Nature*, 316(6023), 33-37, doi: 10.1038/316033a0.

Bonini, M. (2003) Detachment folding, fold amplification, and diapirism in thrust wedge experiments. *Tectonics*, 22(6), 1065-1076, doi: 0.1029/2004JB003552.

Bosworth, W., Huchon, P. & McClay, K. (2005) The Red Sea and Gulf of Aden basins. *Journal of African Earth Sciences*, 43(1-3), 334-378, doi: 10.1016/j.jafrearsci.2005.07.020.

Braun, J. & Beaumont, C. (1989) Dynamical models of the role of crustal shear zones in asymmetric continental extension. *Earth and Planetary Science Letters*, 93(3-4), 405-423, doi: 10.1016/0012-821X(89)90039-3.

Brun, J.P. (1998) Narrow rifts versus wide rifts: inferences for the mechanics of rifting from laboratory experiments, *Philosophical Transactions of the Royal Society of London*, 357, 695-712, doi: 10.1098/rsta.1999.0349.

Brun, J.P. & Fort, X. (2011) Salt tectonics at passive margins: Geology versus models. *Marine and Petroleum Geology*, 28(6), 1123-1145, doi: 10.1016/j.marpetgeo.2011.03.004.

Brun, J.P. & Mauduit, T.P.O. (2009) Salt rollers: Structure and kinematics from analogue modeling. *Marine and Petroleum Geology*, 26(2), 249-258, doi: 10.1016/j.marpetgeo.2008.02.002.

Buck, W. R. (1991) Modes of continental lithospheric extension, J. *Geophysical Research*, 96(B12), 20,161–20,178.

Buck, W. R., (1993) Effect of lithospheric thickness on the formation of high- and low-angle normal faults. *Geology*, 21, 933–936, doi: 10.1130/0091-7613(1993)021.

Buck, W.R., Lavier, L.L. & oliakov, A.N.B. (1999) How to make a rift wide. *Philosophical Transactions of the Royal Society of London*, 357, 671-693. doi: 10.1098/rsta.1999.0348.

Burchardt, S., Koyi, H. & Sschemling, H. (2011) Strain pattern within and around denser blocks sinking within Newtonian salt structures. *Journal of Structural Geology*, 33(2), 145-153, doi: 10.1016/j.jsg.2010.11.007.

Butler, J.P., Beaumont, C. & Jamieson, R.A. (2014) The Alps 2: Controls on crustal subduction and (ultra) high-pressure rock exhumation in Alpine-type orogens, *Journal of Geophysical Research*.

Carter, N.L., Handin, J., Russell, J.E. & Horseman, S.T. (1993) Rheology of rock salt. *Journal of Structural Geology*, 15, 1257-1271.

Chenin, P. & Beaumont, C. (2013) Influence of offset weak zones in the development of rift basins: activation and abandonment during continental extension and breakup. *Journal of Geophysical Research*, 118(4), 1698-1720, doi 10.1002/jgrb.50138.

Chemia, Z., Koyi, H. & SCchmeling, H. (2008) Numerical modeling of rise and fall of a dense layer in salt diapirs. *Geophysical Journal International*, 172(2), 798-816, doi: 10.1111/j.1365-246X.2007.03661.x.

Choi, E., Buck, W.R., Lavier, L.L. & Petersen, K.D. (2013) Using core complex geometry to constrain fault strength. *Geophysical Research Letters*, 40*(*15), 3863 – 3867, doi: 10.1002/grl.50732.

Chu, D.Z. & Gordon, R.G. (1998) Current plate motions across the Red Sea. *Geophysical Journal International*, 135(2), 313-328, doi: 10.1046/j.1365-246X.1998.00658.x.

Cochran, J.R. (1983) A model for the development of the Red Sea. *American Association of Petroleum Geologists Bulletin,* 67, 41-69.

Cochran, J.R. & Martinez, F. (1988) Evidence from the northern Red-Sea on the transition from continental to oceanic rifting. *Tectonophysics*, 153(1-4), 25-53, doi: 10.1016/0040-1951(88)90006-6.

Corti, G., Ranalli, G., Muluget, G., Agostini, A., Sani, F. & Zugu, A. (2010) Control of the rheological structure of the lithosphere on the inward migration of tectonics activity during continental rifting. *Tectonophysics*, *490*, 165-172, doi: 10.1016/j.tecto.2010.05.004.

Corti, G., Ranalli, G., Agostini, A. & Sokoutis, D. (2013) Inward migration of faulting during continental rifting: Effects of pre-existing lithospheric structure and extension rate. *Tectonophysics*. 594, 137-148, doi: 10.1016/j.tecto.2013.03.028.

Costa E. & Vendeville, B.C. (2002) Experimental insights on the geometry and kinematics of fold-and-thrust belts above weak, viscous evaporitic decollement. *Journal of Structural Geology*, 24(11), 1729-1739, doi: 10.1016/S0191-8141(01)00169-9.

Del Ventisette, C., Monanari, D., Sani, F. & Bonini, M. (2004) Basin inversion and fault reactivation in laboratory experiments. *Journal of Structural Geology*, 28(11), 2067-2083, doi: 10.1016/j.jsg.2006.07.012.

Del Ventisette, C., Montanari, D., Bonini, M. & Sani, F. (2005) Positive fault inversion triggering 'intrusive diapirism': an analogue modeling perspective. *Terra Nova*, 17, 478-485, doi: 0.1111/j.1365-3121.2005.00637.x.

Ebinger, C., Ayele, A., Keir, D., Rowland, J., Yirgu, G., Wright, T., Belachew, M. & Hamlings, I. (2010) Length and timescales of rift faulting and magma intrusion: The Afar rifting cycle from 2005 to present. *Annual Reviews of Earth and Planetary Science,* 38, 439–66, doi: 10.1146/annurev-earth-040809-152333.

Fort, X. & Brun, J.P. (2012) Kinematics of regional salt flow in the northern Gulf of Mexico. *Geological Society, London, Special Publications,* 363, 265-287, doi: 10.1144/SP363.12.

Fullsack, P. (1995) An arbitrary Lagrangian-Eulerian formulation for creeping flows and its application in tectonic models. *Geophysical Journal International*, 12*0*(1), 1-23.

Gawthorpe, R.L., Sharp, I., Underhill, J.R. & Gupta, S. (1997) Linked sequence stratigraphic and structural evolution of propagating normal faults. *Geology*, 25(9), 795-798, doi: 10.1130/0091-7613(1997)025.

Ge, H.X., Jackson, M.P.A. & Vendeville, B.C. (1997) Kinematics and dynamics of salt tectonics driven by progradation. *American Association of Petroleum Geologists Bulletin*, 81(3), 398-423.

Gleason, G.C. & Tullis, J. (1995) A flow law for dislocation creep of quartz aggregates determined with the molten-salt cell. *Tectonophysics*, 247(1-4), 1-23, doi: 10.1016/0040-1951(95)00011-B.

Goteti, R., Ings, S.J. & Beaumont, C. (2012) Development of salt minibasins initiated by sedimentary topographic relief. *Earth and Planetary Science Letters*, 339, 103-116, doi: 10.1016/j.epsl.2012.04.045.

Goteti, R., Beaumont, C. & Ings, S.J. (2013) Factors controlling early stage salt tectonics at rifted continental margins and their thermal consequences. *Journal of Geophysical Research – Solid Earth*, 118(6), 3190-3220, doi: 10.1002/jgrb.50201.

Gueydan, F., Morency, C. & Brun, J.P. (2008) Continental rifting as a function of lithosphere mantl strength. *Tectonophysic*s, 460, 83-93. doi:10.1016/j.tecto.2008.08.012.

Haq, B.U., Hardenbol, J. & Vail, P.R. (1987) Chronology of fluctuating sea levels since the Triassic. *Science*, 235(4793), 1156-1167, doi: 10.1126/science.235.4793.1156.

Hempton, M.R. (1987) Constraints on Arabian plate motion and extensional history of the Red-Sea. *Tectonics*, 6(6), 687-&, doi: 10.1029/TC006i006p00687.

Hofmann, C., Courillot, V., Feraud, G., Rochette, P., Yirgu, G., Ketefo, E. & Pik, R. (1997) Timing of the Ethiopian flood basalt event and implications for plume birth and global change. *Nature*, 389(6653), 838-841.

Hopper, J.R. & Buck, W.R. (1996) The effect of lower crustal flow on continental extension and passive margin formation. *Journal of Geophysical Research*, 101(B9), 175-194, doi: 0.1029/96JB01644.

Hopper, J.R. & Buck, W.R. (1998) Styles of extensional decoupling. *Geology*, 26(8), 699-702, doi: 10.1130/0091-7613(1998)026.

Hudec, M.R. & Jackson, M.P.A. (2007. Terra Infirma: Understanding salt tectonics, *Earth Science Reviews*, 82(1-2), 1-28, doi 10.1016/j.earscirev.2007.01.001.

Hudec, M.R., Jackson, M.P.A. & Schultz-Ela, D.D. (2009) The paradox of minibasin subsidence into salt: Clues to the evolution of crustal basins. *Geological Society of America Bulletin, 121*(1-2), 201-221, doi: 10.1130/B26275.1.

Hughes, G.W. & Beydoun, Z.R. (1992) the Red-Sea Fule of Aden – biostratigraphy, lithostratigraphy and paleoenvironments. *Journal of Petroleum Geology*, 15(2), 135-156, doi: 10.1111/j.1747-5457.1992.tb00959.x.

Hughes, G.W. & Filatoff, J. (1995) New biostratigraphic constraints on Saudi Arabian Red Sea pre- and syn- rift sequences. In: *Middle East Petroleum Geosciences, Geo '94 vol. 2* (Ed. by Al-Husseini, M.I.), pp 517-528. Gulf PetroLink, Bahrain.

Huismans, R. & Beaumont, C. (2005) Effect of plastic-viscous layering and strain softening on mode selection during lithospheric extension. *Journal of Geophysical Research – Solid Earth*, 110(B2), B02406, doi: 10.1029/2004JB003114.

Hsuimans, R. & Beaumont, C. (2008) Complex rifted continental margins explained by dynamical models of depth-dependent lithospheric extension. *Geology*, 36(2), 163-166, doi: 10.1130/G24231A.1.

Huismans, R. & Beaumont, C. (2011) Depth-dependent extension, two-stage breakup and cratonic underplating at rifted margins. *Nature*, 473(7345), 74-U85, doi: 10.1038/nature09988.

Huismans, R. & Beaumont, C. (2014) Rifted continental margins: The case for depth-dependent extension. *Earth and Planetary Science Letters,* 407, 148-162, doi:10.1016/j.eps1.2014.09.032.

Izzeldin, A.Y. (1987) Seismic, gravity and magnetic surveys in the central part of the Red Sea: Their interpretation and implications for the structure and evolution of the Red Sea. *Tectonophysics,* 143, 269-306.

Jammes, S., Manatschal, G. & Lavier, L. (2010) Interaction between prerift salt and detachment faulting in hyperextended rift systems: The example of the Parentis and Mauleon basins (Bay of Biscay and western Pyrenees). *American Association of Petroleum Geologists Bulleti*n, 94(7), 957-975, doi: 10.1306/12090909116.

Karner, G.D. & Driscoli, N.W. (1999) Tectonic and stratigraphic development of the West African and eastern Brazilian Margins: insights from quatitative basin modeling. In: *The Oil & Gas Habitats of the South Atlantic* (Ed. by Cameron, N.R., Bate, R.H. & Clure, V.S), Geological Society, London, Special Publications, 153, 11-40.

Karner, G.C. & Gamboa, L.A.P. (2007) Timing and origin of the South Atlantic pre-salt sag basins and their capping evaporites. *Geological Society, London, Special Publications*, 285, 15-35. Doi: 10.1144/SP285.2.

Karato, S. & Wu, P. (1993) Rheology of the upper mantle – a synthesis. *Science*, 260(5109), 771-778, doi: 10.1126/science.260.5109.771.

Keken, P.E., Spiers, C.T., Van Den Berg, A.P. & MUYZERT, E.J. (1993) The effective viscosity of rocksalt: implementation of steady-state creep laws in numerical models of salt diapirism. *Tectonophysics*, 225, 457-476.

Lavier, L. L., Buck, W.R. & Poliakov, A.N.B. (1999) Self-consistent rolling- hinge model for the evolution of large-offset low-angle normal faults. *Geology*, 27, 1127–1130, doi: 10.1130/0091-7613(1999)027.

Lavier, L. L. & Buck, W.R. (2002) Half graben versus large-offset low-angle normal fault: Importance of keeping cool during normal faulting. *Journal of Geophysical Research*, 107(B6), 2122, doi:10.1029/2001JB000513.

Lavier, L.L. & Manatschal, G. (2006) A mechanism to thin the continental lithosphere at magma-poor margins. *Nature,* 440(7082,: 324-328, doi: 10.1038/nature04608.

Ligi, M., Bonatti, E., Bortoluzzi, G., CiprianiI, A., Cocchi, L., Tontini, F.C., Carminate, E., Ottolini, L. & Schettino, A. (2012) Birth of an ocean in the Red Sea: Initial pangs. *Geochemistry Geophysics Geosystems*, 13, Q08009, doi: 10.1029/2012GC004155.

Lister, G.S., Etheridge, M.A. & Symonds, P.A. (1986) Detachment faulting and the evolution of passive continental margins. *Geology*, 14(3), 246-250, doi: 10.1130/0091-7613(1986)14.

ListerI, G.S., Etheridge, M.A. & SYmonds, P.A., (1991) Detachment models for the formation of passive continental margins. *Tectonics*, 10(5), 1038-1064, doi: 10.1029/90TC01007.

Longoni, M., Malossi, A.C.I. & VILLA, A. (2010) A robust and efficient conservative technique for simulating three-dimensional sedimentary basin dynamics. *Computers & Fluids*, 39(10), 1964-1976, doi: 10.1016/j.compfluid.2010.06.028.

Mackwell, S., Zimmerman, M. & Kohlstedt, D. (1998) High-temperature deformation of dry diabase with application to tectonics on Venus. *Journal of Geophysical. Research-Solid Earth*, 103, 975–984.

Mitchell, N.C., Ligi, M., Ferrante, V., Bonatti, E. & Rutter, E. (2010) Submarine salt flows in the central Red Sea. *Geological Society of America Bulletin*, 122(5-6), 701-713, doi: 10.1130/B26518.1.

McKenzie, D. (1978) Some remarks on the development of sedimentary basins. *Earth and Planetary Science Letters*, 40, 25-32, doi: 10.1016/0012-821X(78)90071-7.

Nagel, T.J. & Buck, W.R. (2004) Symmetric alternative to asymmetric rifting models. *Geology*. 32(11), 937-940, doi: 10.1130/G20785.1.

Nagel, T.J. & Buck, W.R. (2007) Control of rheological stratification on rifting geometry: a symmetric model resolving the upper plate paradox. *International Journal of Earth Sciences*, 96, 1047-1057, doi: 10.1007/s00531-007-0195-x.

Omar, G.I., Steckler, M.S., Buck, W.R. & Kohn, B.P. (1989) Fission-track analysis of basement apatites at the western margin of the Gulf-of-Suez rift, Egypt – evidence for synchroneity of uplift and subsidence. *Earth and Planetary Science Letters*, 94(3-4), 316-328, doi: 10.1016/0012-821X(89)90149-0.

Orszag-Sperber, F., Hardwood, G., Kendall, A. & Purser, B.H. (1998) A Review of the evaporites of the Red Sea – Gulf of Suez rift. In: *Sedimentation and Tectonics of Rift Basins: Red Sea – Gulf of Aden* (Ed. by Purser, B.H. & Bosence, D.W.J.). Chapman & Hall, London. 409-426.

Peron-Pinvidic, G. & Manatschal, G. (2009) The final rifting evolution at deep magma-poor passive margins from IberiaeNewfoundland: a new point of view. *International Journal of Earth Sciences*, 98, 1581-1597, doi: 10.1007/s00531-008-0337-9.

Peron-Pinvidic, G., Manatschal, G. & Osmundsen, P.T. (2013) Structural comparison of archetypal Atlantic rifted margins: A review of observations and concepts. *Marine and Petroleum Geology*, 43, 21-47, doi: 10.1016/j.marpetgeo.2013.02.002.

Richardson, M. & Arthur, M.A. (1988) The Gulf of Suez-Northern Red-Sea neogene rift – a quantitative basin analysis. *Marine and Petroleum Geology*, 5(3), 247-270, doi: 10.1016/0264-8172(88)90005-0.

Rowan, M.G. (2014) Passive-margin salt basins: hyperextension, evaporite deposition, and salt tectonics. *Basin Research*, *2*6, 154-182, doi: 10.1111/bre.12043.

Schubert, G., Turcotte, D. & Olson, P. (2001) *Mantle convection in the Earth and planets,* Cambridge University Press.

Scott, R.W. & Govean, F.M. (1985) Early depositional history of a rift basin – Miocene in Western Sinai. *Palaeogeography Palaeolimatology Palaeoecology*, 52(1-2), 143-158, doi: 10.1016/0031-0182(85)90035-5.

Searle, R.C. & Ross, D.A. (1975) Geophysical study of Red-Sea axial trough between 20.5degrees and 22degrees N. *Geophysical Journal of the Royal Astronomical Society*, 43(2), 555-572, doi: 10.1111/j.1365-246X.1975.tb00647.x.

Sokoutis, D., Corti, G., Bonini, M., Brun, J.P., Cloetingh, S., Maudiot, T. & Manetti, P. (2007) Modelling the extension of heterogeneous hot lithosphere. *Tectonophyics*, 444, 63-79, doi:10.1016/j.tecto.2007.08.012.

Tirel, C., Brun, J.P. & Sokoutis. D. (2006) Extension of thickened and hot lithospheres: Inferences from laboratory modeling. *Tectonics,* 25, TC1005, doi:10.1029/2005TC001804.

Van Avendonk, H.J.A., Lavier, L.L., Shillington, D.J. & Manatschal, G. (2009) Extension of continental crust at the margin of the eastern Grand Banks, Newfoundland. *Tectonophysics*, 468, 131-148, doi:10.1016/j.tecto.2008.05.030.

Warren, J.K. (2010) Evaporites through time: Tectonic, climatic and eustatic controls in marine and nonmarine deposits. *Earth-Science Reviews,* 98, 217–268, doi: 10.1016/j.earscirev.2009.11.004.

Warren, J. K. (2006) Evaporites: Sediments, Resources and Hydrocarbons. Springer, Berlin.

Wernicke, B. (1985) Low-angle normal faults in the basin and range province – nappe tectonics in an extending orogen. *Nature*, 291(5817), 645-648, doi: 10.1038/291645a0.

Wernicke, B. (1981) Uniform-sense normal simple shear of the continental lithosphere, *Canadian Journal of Earth Sciences*, 22(1), 108-125, doi: 10.1139/e85-009.

Winn, R.D., Crevello, P.D. & Bosworth, W. (2001) Lower Miocene Nukhul formation, Gebel el Zeit, Egypt: Model for structural control on early synrift strata and reservoirs, Gulf of Suez. *American Association of Petroleum Geologists Bulletin*, 85(10), 1871-1890.

Chapter 4: Feedback among syn-rift lithospheric extension, sedimentation and salt tectonics on wide, weak continental margins

Janice Allen[*], Christopher Beaumont[†], and Mark Deptuck[‡]

** Department of Earth Sciences, Dalhousie University, Halifax, N.S., Canada*
[†] Department of Oceanography, Dalhousie University, Halifax, N.S., Canada
[‡]1791 Barrington Street, 8th Floor, TD Centre, Halifax, NS, Canada

4.1 Preface

This chapter is based on a paper in preparation. The copyright agreement form for this chapter can be found in Appendix A. Janice Allen designed and ran the models in this paper (with supervision), interpreted results, wrote the majority of the manuscript and prepared most of the figures, edited the manuscript with input from the co-authors, and prepared the manuscript for publication. Mark Deptuck contributed to the text and figures of section 4.7, and provided editing on all sections of the paper. Chris Beaumont provided input and oversight on all aspects of the work, and contributed to the text of section 4.8.

4.2 Abstract

This paper uses numerical modeling to explore interactions among syn-rift lithospheric extension, salt deposition and deformation, and pre- and post-salt sedimentation, for wide rifted margins with weak continental crust. The impact of sedimentation on rifting is examined for both distributed, aggrading sediment and localized, deltaic-type prograding sediment. Distributed aggrading sediment loading enhances listric normal syn-rift faulting of the sediments and crust in the mid and distal margin. In contrast, localized prograding sedimentation initiates a positive feedback between sedimentation, faulting, and mid to lower crustal flow. This feedback causes localized crustal extension at the proximal margin, and leads to very thick sediments in deep proximal basins. The feedback is more pronounced when more sediment is deposited, and does not develop in models with stronger, narrower rifted margins. Early and late syn-rift salt deposition and mobilization is studied in conjunction with pre- and post-salt clastic sedimentation; later initiation of the post-salt prograding sediments leads to a less pronounced feedback with lower crustal flow, and a more significant advancement of the prograding wedge over the salt body. We compare our model results with the rifted Nova Scotia Atlantic margin, contrasting margin evolution and salt tectonics between the northeastern region, which experienced significant post-salt syn-rift sedimentation, and the central region, where less post-salt sediment was deposited. We show that the northeastern margin may have experienced enhanced proximal graben development owing to prograding sedimentation.

4.3 Introduction

Wide rifted margins, where thinned continental crust extends over hundreds of kilometers across the margin, are of significant scientific and economic importance. Considerable discussion has surrounded the formation of wide margins (e.g. *Unternehr et al.*, 2010; *Crosby et al*., 2011; *Huismans and Beaumont*, 2011; *von Nicolai et al.,* 2013), and the nature of both clastic sedimentation and evaporite (salt) deposition in this setting (e.g. *Burov and Cloetingh*, 1997; *Davison et al*., 2012; *Chen et al.,* 2013; *Rowan*, 2015). In particular, model results indicate that wide rifted margins develop where the mid and/or lower crust is viscously weak (e.g. *Huismans and Beaumont*, 2011, 2014). Deposition and deformation of syn-rift evaporites is important to the evolution of many rifted continental margins. Evaporites may be precipitated during the rifting process if (ephemerally) isolated basins containing hypersaline water experience arid conditions and widespread evaporation. The timing and location of rift basin development relative to the paleo-climate and/or latitude are important in this regard (*Olsen*, 1997; *Warren*, 2010). This paper explores the interactions between sedimentation and the evolution of wide rifted margins with weak crust, and investigates the importance of timing of evaporite (in our case salt, modeled as halite) deposition relative to rifting, on the development of syn-rift salt tectonics at these wide margin settings.

Rifted continental margins form through stretching, thinning, and breakup of continental lithosphere. This process has been explained geometrically using a number of mechanisms, including pure shear (*McKenzie*, 1978), simple shear (*Wernicke*, 1981,

1985), and combinations of the two that include sub-horizontal detachment within the lithosphere (*Lister et al*., 1986, 1991). More recently, the dynamics and style of continental rifting, including the structural features formed, has been studied using numerical models. In particular, these models demonstrate that margin width is strongly influenced by the material strength and temperature of the continental crust and/or lithospheric mantle, with strong and/or cold crust leading to narrow margins and weak and/or hot crust forming wide margins (*Nagel and Buck*, 2004; *Lavier and Manatschal*, 2006; *Gueydan et al*., 2008; *Van Avendonk et al*., 2009; *Huismans and Beaumont*, 2011, 2014). Physical analogue modeling analyses have also suggested that cold, strong lithosphere produces narrow rifts while hot, weak lithosphere forms wide rifts (*Brun*, 1998; *Tirel et al*., 2006).

The importance of timing of salt deposition relative to rifting is an emerging topic in the literature on rifted continental margins. In addition to the study of numerous natural systems, the mobilization and deformation of weak viscous evaporites ('salt tectonics') has been studied using numerical (e.g. *Chemia et al*., 2008; *Albertz et al*., 2010; *Albertz and Beaumont*, 2010; *Longoni et al*., 2010; *Burchardt, et al*., 2011; *Goteti et al.*, 2012) and physical analogue (e.g. *Ge et al.*, 1997; *Costa and Vendeville*, 2002; *Bonini*, 2003; *Del Ventisette et al*., 2004, 2005; *Brun and Mauduit*, 2009; *Baikpour et al.*, 2010) approaches. Timing of salt deposition relative to rifting is important in that it influences both the location of salt deposition and the subsequent mobilization of salt. Recent studies have considered the importance of timing of deposition of syn-rift salt in dictating both the location of salt across the margin and the style of salt tectonic structures that

develop (*Rowan*, 2014; *Allen and Beaumont*, 2015). A more comprehensive list of these previous studies is given in *Allen and Beaumont* (2015).

Some numerical and physical analogue experiments have explored the interactions between clastic sedimentation and the rifting process. These studies have suggested that sedimentation during rifting may favor the development of narrow margins (*Bialas and Buck*, 2009), and prolonged rifting (*Corti et al*., 2010, 2013). Specifically in regard to wide margins, previous studies have noted the development of deep sedimentary basins on margins with weak and/or hot continental crust (e.g. *Morley and Westaway*, 2006; *Clift*, 2015), and at hyper-extended margins (*Sun et al*., 2016).

This paper explores both the impact of sedimentation on the style of rifting, and the interaction among sedimentation, salt deposition, and the ensuing salt tectonics, at wide rifted margin settings. *Huismans and Beaumont* (2011, 2014) have shown that the style of rifting and resultant structural features of rifted margins is strongly influenced by continental crust strength. Separately, the importance of timing of salt deposition relative to rifting has also been introduced (e.g. *Rowan*, 2014; *Allen and Beaumont*, 2015). Here, we first explore interactions between distributed (aggrading) and localized (prograding) clastic sedimentation and the evolution of a wide rifted margin, and in particular the development of deep sedimentary basins through the positive feedback of sediment loading on mid- to lower crust flow. We then show that the location of syn-rift salt deposition and the style of subsequent salt tectonics are influenced by a combination of: 1) timing of salt deposition relative to the stage of rifting; 2) the style of continental

extension and breakup, as determined by continental crust strength, and; 3) the amount and distribution of pre- and post-salt clastic sedimentation. We discuss our results in the context of the central and northeastern Nova Scotian margin of Atlantic Canada, and explore how ongoing extensional deformation of the continental crust, coupled with different syn-rift sediment loading regimes, can account for differences in salt distribution and deformation, as well as the propensity to develop deep proximal basins along these two margin segments.

443 Methods

4.4.1 Numerical Methods

This work uses 2D thermo-mechanically coupled numerical models, computed using Sopale Nested [*Fullsack*, 1995; *Beaumont et al.,* 2009], an Arbitrary-Lagrangian-Eulerian (ALE) finite element software. Sopale Nested solves the incompressible viscous-plastic creeping (Stokes) flow equations, coupled to the heat equation (Equations 1-3);

$$\frac{\partial \sigma_{ij}}{\partial x_i} - \frac{\partial P}{\partial x_j} + \rho g = 0 \qquad i,j = 1,2, \tag{1}$$

$$\frac{\partial v_i}{\partial x_i} = 0 \quad i=1,2, \tag{2}$$

$$\rho c_p \left(\frac{\partial T}{\partial t} + v_i \frac{\partial T}{\partial x_i} \right) = K(T) \frac{\partial}{\partial x_i} \frac{\partial T}{\partial x_i} + A + v_2 \alpha g T \rho \qquad i=1,2, \tag{3}$$

where σ_{ij} is the deviatoric stress tensor, P pressure (mean stress), ρ density, g gravitational acceleration, and x_i are the spatial coordinates, v_i the components of

velocity. In equation 3, the energy balance, c_p is specific heat, T temperature, t time, K thermal conductivity (which is temperature dependent in the mantle), A_C crustal radioactive heat production per unit volume, and α volumetric thermal expansivity. The last term is the temperature correction for adiabatic heating when material moves vertically at velocity v_2. The mechanical and thermal systems are coupled through the temperature-dependence of the lithospheric viscosity and density, and are solved sequentially during each model time step. Compacting sediments are handled separately.

4.4.2 Material Properties

The model design is purposefully simple, with an initially uniformly layered crust, lithospheric mantle, and sublithospheric mantle (Fig. 4.1), each with thermally-activated power-law viscous (Equation 4), and brittle (frictional-plastic) (Equation 5) rheologies. Properties of the lithosphere are based on laboratory-derived flow laws for 'Wet' Quartzite (WQz) (*Gleason and Tullis*, 1995) (continental crust and clastic sediments) and 'Wet' Olivine (WOl) (*Karato and Wu*, 1993) (mantle lithosphere and sublithospheric mantle). Oceanic crust is based on Dry Maryland Diabase (DMD) (*Mackwell et al.*, 1998). When the state of stress is below plastic yield Sopale Nested uses these flow laws, expressed as a power-law equation (Equation 4) for dislocation creep to calculate the effective viscosity, η.

$$\eta = f A^{-1/n} (\dot{I}_2')^{(1-n)/2n} \exp\left[\frac{Q+VP}{nRT}\right] \qquad (4)$$

Here A is the pre-exponential scaling factor, $\dot{I}_2^{/}$ is the second invariant of the deviatoric strain rate tensor ($\frac{1}{2}\dot{\varepsilon}_{ij}^{/}\dot{\varepsilon}_{ij}^{/}$), n is the power law exponent, Q is the activation energy, V is the activation volume, which makes the viscosity dependent on pressure, P, T is the absolute temperature, R is the universal gas constant, and $\dot{\varepsilon}_{ij}^{/}$ is the deviatoric strain rate tensor. A scaling factor, f, is chosen to represent materials that are viscously weaker or stronger than the reference flow law (*Butler et al*., 2014). Material properties used in the models are given in Table 4.1.

Brittle deformation, including that of clastic sediments, that occurs when materials are at the yield stress σ_y, obeys the pressure-dependent plastic Drucker-Prager yield criterion:

$$\sigma_y = (J_2^{/})^{1/2} = P\,Sin\phi_{eff} + C\cos\phi_{eff} \qquad (5)$$

where $J_2^{/} = \frac{1}{2}\sigma_{ij}^{/}\sigma_{ij}^{/}$ is the second invariant of the deviatoric stress, C is the cohesion, and $\sigma_{ij}^{/}$ is the deviatoric stress tensor. Strain softening is included by varying the effective internal angle of friction, ϕ_{eff} = 15–2°, over a range of strain 0.5-1.5. The initial value, 15°, includes the effect of hydrostatic pore fluid pressure, and the final value, 2°, represents a fully strain-softened material.

STP densities of the materials used are given in Table 4.1. The continental crust has uniform properties except for a higher density lower crust, which was chosen to be consistent with the generally agreed interpretation that the continental crust has an increasingly intermediate, as opposed to felsic/acidic, composition with increasing depth. This choice also reduced the tendency for diapirism of the hot, weak lower crust in the

models. We use the Boussinesq approximation (*Schubert et al*., 2001) in the calculations. That is, densities are not adjusted for compressibility when materials are buried at depth. Density does, however, change as a result of thermal expansion, with thermal expansively values given in Table 4.1.

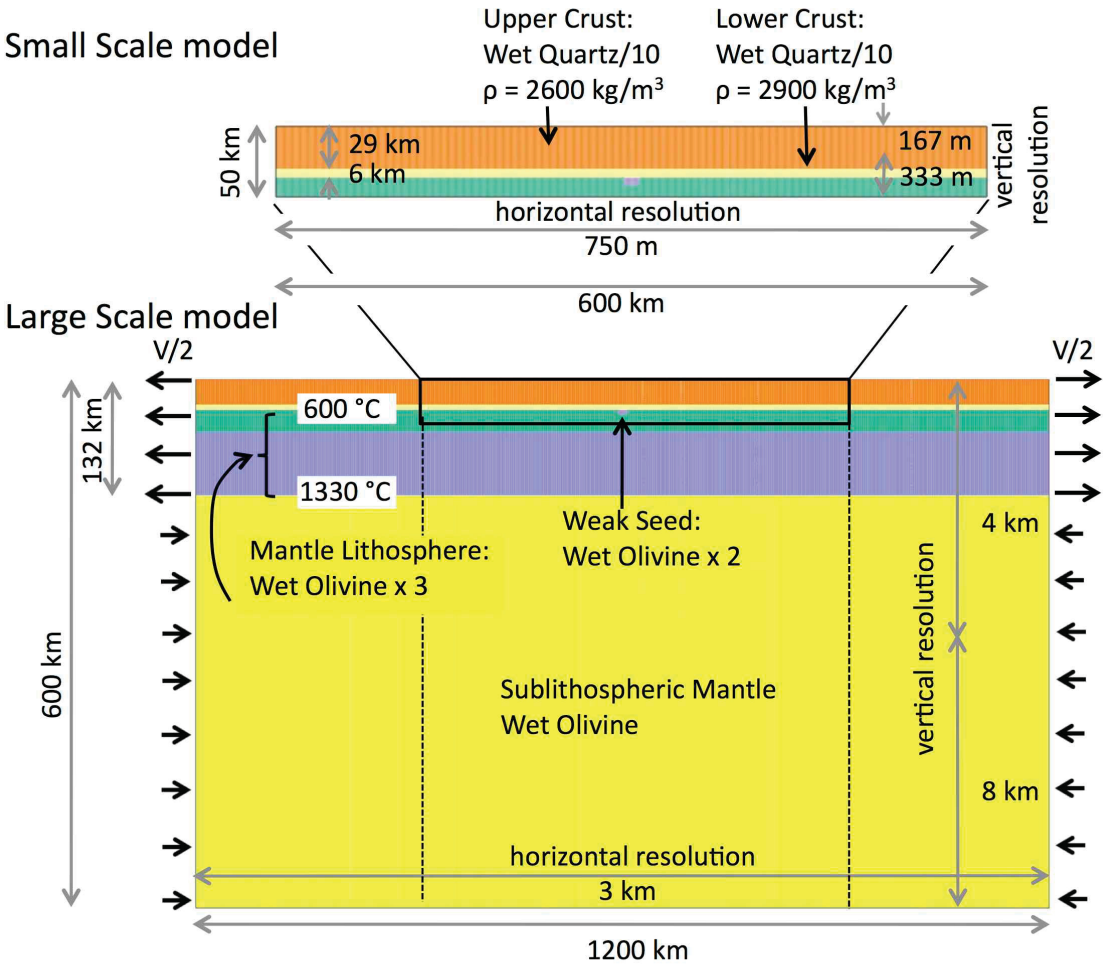

Fig. 1

Figure 4.1: initial model configuration, showing distribution of material properties, dimensions and finite element size for the large scale and small scale model, and velocity boundary conditions.

Table 4.1: Rheological and thermal properties of model materials.

Material and Rheology	Mechanical Properties				Thermal Properties		
	ρ (kg/m^{-3})	C (MPa)	η (Pa s)	Φ and Strain range (^{o})	K and Temp. range (°C)	C_p (J Kg^{-1} K^{-1})	A_c (μW m^{-3})
Clastic sediments, WQz/3	variably compact	10		15–2, 0.5–1.5	2.25	750	0.0
Salt (halite)	2150	NA	10^{18}	NA	5.858	750	0.0
Continental Upper Crust, WQz/10	2600	10		15–2, 0.5–1.5	2.25	750	0.95
Continental Lower Crust, WQz/10	2900	10		15–2, 0.5–1.5	2.25	750	0.95
Oceanic Crust, DMD/10	2900	10		15–2, 0.5–1.5	2.25	750	0.0
Continental Mantle Lithosphere, WOlx3	3350	2		15 – 2, 0.5 – 1.5	5.0 – 3.0, 0 - 777	750	0.0
Oceanic Mantle Lithosphere, WOlx3	3350	2		10–2, 0.5–1.5	5.0 – 3.0, 0 - 777	750	0.0
Sublithosphere mantle WOl	3370	2		15–2, 0.5–1.5	3.0 – 40, 1323 - 1353	750	0.0

Additional properties: the pre-exponential scaling factor, A, power law exponent, n, activation energy, Q, and activation volume, V, are 8.57x10^{-28} Pa^{-n} s, 4.0, 223 kJ mol^{-1}, and 0 m^3 mol^{-1} for WQz, 5.78x10^{-27} Pa^{-n} s, 4.7, 485 kJ mol^{-1}, and 0 m^3 mol^{-1} for DMD, and 1.76x10^{-14} Pa^{-n} s, 3.0, 430 kJ mol^{-1} and 1.2x10^{-5} m^3 mol^{-1} for WOl.

Salt (halite) is treated as a linear viscous material with a viscosity of 10^{18} Pa s. This simplification applies to halite deforming by pressure solution (*Carter et al*., 1993; *van Keken et al*., 1993), which we expect to be the high stress deformation mechanism in the models for halite. A higher value, 10^{19} Pa s may be more appropriate for salt comprising halite and other stronger evaporites. Our models do not have sufficient resolution to separately model halite layered with other evaporites.

4.4.3 Model Design

This work uses a nested (sub-gird) model design, that provides high resolution in the upper lithosphere and sediments, while covering a large enough area at low resolution to allow the model to calculate flow at the upper mantle scale (Fig. 4.1). The large scale (LS) domain extends from the surface of the model to 600 km depth, and is 1200 km wide. The small scale (SS) domain extends from the surface to 40 km depth, and from 300 to 900 km horizontally. Elements in the SS domain have a resolution of 167 m vertically by 750 m horizontally. At each time step, the model is solved first for the LS domain, then subsequently for the SS domain, using velocity boundary conditions from the LS domain solution for the sides and base of the SS domain. The LS domain has free slip vertical (side) and base boundary conditions. Both the LS and SS domains have a stress-free upper horizontal surface. Extension of the lithosphere is achieved by applying a horizontal velocity +/- $V/2$ to the side boundaries of the LS model domain, through the full depth of the lithosphere. Total extension rate is $V = 1.5$ cm a^{-1}. Volume and isostatic balance of the model domain is maintained by a weak inflow of sublithospheric material through the sides of the model (Fig. 4.1).

4.4.3.1 Initial configuration

Continental crust, mantle lithosphere, and sublithospheric mantle are originally defined in horizontal layers (Fig. 4.1). The sublithospheric mantle (yellow), extending from the base of the model to 132 km below the surface, follows a wet olivine flow law with scaling factor $f = 1$. Lithospheric mantle, shown in blue (lower) and green (upper) spans 132 to 35 km depth and has a wet olivine flow law scaled by $f = 3$. The continental crust, shown in sand (lower) and orange (upper) has a wet quartzite flow law with scaling factor $f = 1/10$ for the weak crust models used throughout this paper. This scaling factor was chosen to produce a wide margin pair with many of the characteristics of the Type II margins of *Huismans and Beaumont* (2011), while exploring the applicability of those characteristics to somewhat stronger weak crust in this study. A weak seed (wet olivine rheology with reduced internal angle of friction, $\phi_{eff} = 2°$), 12 km wide by 5 km thick, centered horizontally and positioned in the uppermost mantle lithosphere, focuses deformation in the early stages of rifting.

Initial configuration of our models includes a thermal steady state, with a laterally uniform temperature field, a uniform basal heat flux ($q = 22$ mWm^{-2}), and insulated side boundaries ($q = 0$). Temperatures at the Moho and the base of the lithosphere are 600 °C and 1330 °C, respectively. Continental crust has a uniform radiogenic heat production, $A_c = 0.95$ μWm^{-3}. Mantle lithosphere thermal conductivity, $K(T)$ decreases linearly from 5.0 to 3.0 Wm^{-1}K^{-1} over a temperature range $T = 0 – 777$ °C. Sublithospheric mantle thermal conductivity increases linearly from 3.0 to 40.0 Wm^{-1}K^{-1} over a temperature range $T = 1323$ - 1353 °C, so that heat transport in the sublithospheric mantle equals that

of marginal convection and an adiabatic gradient of 0.4 °C km^{-1}. Temperature-dependence of the thermal conductivities of the lithospheric and sublithospheric mantle is consistent with an olivine-dominated composition. Thermal properties are given in Table 4.1.

4.4.3.2 Water Load and Sedimentation

Water loading by the ocean is included in all of the models. For simplicity, we assume that sea level is 1 km below the original surface of the model. All space between sea level and the solid surface of the model is iteratively filled with water at each time step, until there is no additional isostatic subsidence.

When sedimentation is used, space between a specified bathymetric profile and the surface of the model is filled with sediment at each time step (water load is applied for the space between this bathymetric profile and sea level). Sediment filling is iterated until the specified bathymetric profile is filled, as the addition of sediment causes isostatic subsidence. Two types of bathymetric profiles are used: a horizontal profile rising at rage $v_{aggrade}$, representing aggrading sediment (including salt deposition), and a double half Gaussian profile (Equation 6) simulating sediments that prograde across each margin toward the centre of the model domain (moving in opposite directions), each with velocity $v_{prograde}$. Where the sediments or salt are above the bathymetric profile they are not removed.

$$h(x) = \begin{cases} d_1 & x < x_1 \\ d_2 - (d_1 - d_2)\exp\left(-\dfrac{(x - x_1)^2}{W_1^2}\right) - (d_3 - d_2)\exp\left(-\dfrac{(x - x_2)^2}{W_2^2}\right) & x_1 \le x \le x_2 \\ d_3 & x > x_2 \end{cases} \qquad [6]$$

In equation 6, *d(x)* is the depth of the bathymetric profile below the original surface position of the model, at horizontal position *x*, d_1 and d_3 are the positions of the profile on continents and continental shelves, and d_2 is its deepest position in the ocean. Value of these model parameters are given in Table 4.2, with time quoted in Ma (millions of years since the start of the model).

All clastic sediments in these models compact during burial; salt does not compact. Sediment density as a function of depth is calculated according to Equation 7, at each time step. Increases in density, when additional sediment is deposited and burial increases, are assumed to result from expulsion and loss of pore fluids. Corresponding decreases in volume are applied through vertical contraction of the sediment column, equal to the incremental volume of the expelled pore fluid, for a given depth, z.

$$\rho_d(z) = \rho_g - (\rho_g - \rho_f) n_o e^{-cz} \qquad (7)$$

Sediments have a grain density, ρ_g, of 2640 kg m^{-3}, pore fluid density, ρ_f, of 1000 kg m^{-3}, surface porosity, n_o, of 0.52, and compaction coefficient, *c*, of 4.7×10^{-4} m^{-1}. These values fit the average siliciclastic sediment properties in the northern Gulf of Mexico (*Hudec et al*., 2009). Water loading by the ocean is included in the models. For simplicity, we

assume that sea level is 1 km below the original surface of the model. All space between sea level and the solid surface of the model is filled with water at each time step.

Table 4.2 – Experiment design, showing type and duration of sedimentation for Model Sets 1-4

Model Sets 1,2: Impact of Sedimentation on Wide Margin Rifting

Model Name	Description	Clastic Sedimentation				
		Start (Ma)	End (Ma)	d_1 (km)	$d_1 = d_3$ (km)	D_2 (km)
Model 1	Base model					
Model 1-AF	Base model with aggrading sediment throughout	0	NA	3.5		
Model 1-AP	Base model with aggrading sediment for part of rifting	0	25	3.5		
Model 2-P1	More localized, prograding sediment	9	NA		1.0	1.0
Model 2-P2	Less localized, prograding sediment	9	NA		1.5	5.0

Model Set 3,4: Syn-rift Salt Tectonics, and Comparison with Nova Scotia Margin

Model Name	Description	Pre-salt aggradation	Salt Deposition		Post-salt progradation	
		h_1 (km)	Start, End (Ma)	d_1 (km)	$d_1=d_3$ (km)	D_2 (km)
Model 3-ES	Early syn-rift salt	3.5	12-13	1.8	1.0	5.0
Model 3-LS	Late syn-rift salt	3.5	32-34	1.8	1.0	5.0
Model 4-NSM	NS margin, more post-salt sedimentation	3.5	15-16	1.8	1.0	5.0
Model 4-NSL	NS margin, less post-salt sedimentation	3.5	15-16	1.8	1.8	5.0

Note: All *d* values are depths measured below the initial model surface.

4.4.4 Experiment Design

This work consists of three sets of models designed to explore the interaction among sedimentation, rifting, and salt tectonics, as well as a pair of models, Model Set 4, designed for comparison with the Nova Scotia margin. Model Set 1 shows the evolution of the weak crust base model used throughout this paper, with and without distributed, aggrading sediment. Model Set 2 shows the evolution of weak, intermediate and strong crust models with and without localized, prograding (deltaic) sediment at the proximal margin. Model Set 3 shows the impact of early versus late syn-rift salt deposition for the weak crust base model (Model Set 1, above). The two models used for comparison with the central and northeastern Nova Scotian margin have a similar early evolution, including timing of salt deposition relative to rifting, but differ in the location of salt deposition, and the amount of pre- and post-salt sedimentation. Model parameters are given in Table 4.2.

4.5 Interaction between Sedimentation and Margin Evolution

4.5.1 Model Set 1: Base Model Evolution With and Without Distributed, Aggrading Sediment

Model 1 is the weak continental crust base model used throughout this paper. It shows how the crust and uppermost mantle extend when there is only water loading but no sedimentation throughout rifting (Fig. 4.2). At the full extension rate of 1.5 cm a^{-1} the width of each conjugate margin increases progressively to ~450 km at final break up at 34 Ma (Fig. 4.2a, c, e). The crustal thickness profiles of the conjugates, shown by the distribution of materials (Fig. 4.2a, c, e) are similar and their taper angle is relatively

uniform except in the distal margin where there is some asymmetry (Fig. 4.2e). Equivalent panels (Fig. 4.2b, d, f) show the corresponding strain rate. Early in the rifting process there is notable decoupling between the lower crust and the continental mantle lithosphere (Fig. 4.2, seen in the sheared Lagrangian grid, the high strain rates at the base of the crust, and the large differential horizontal velocities in which the mantle lithosphere is translated much faster than the crust in the extending region [1]). This basal shearing begins early in the rifting process, persists after the lithospheric mantle ruptures, at about 10 Ma, and continues until final crustal break up, 24 Ma later. This style of extension, in which the crust decouples from the mantle and the mantle ruptures long before the crust (*Huismans and Beaumont*, 2011, 2014 Type II) leads to the exposure of the base of the crust at the distal margin to hot upwelling sublithospheric mantle which imposes a base of crust temperature up to 800-900 °C throughout most of the syn-rift evolution. This heating further weakens the lower crust, enhances the decoupling, and results in more rapid thinning of the lower crust than the upper crust, causing it to rupture by 25 Ma (Fig. 4.2c). The upper continental crust deforms through a series of conjugate shear zones, which are active simultaneously across both margins (Fig. 4.2b d), only waning at final breakup, 34 Ma after the onset of rifting (Fig. 4.2f). These shear zones are frictional-plastic near the surface but become viscous with a listric geometry in the mid-crust (Fig. 4.2). There is no preference for either set of conjugates, in keeping with the weak basal shear, therefore the model 'faults' dip equally in both directions. Extension on the shears is accommodated by the mid- and lower continental crust which deforms in a ductile manner, and flows laterally towards regions of thinned upper continental crust and then flows vertically in response to the pressure gradient (Fig.

4.2 [2]. The lower crust is more dense than the upper crust (Table 4.1) and resists upward flow. The overall style of the mid- to upper crustal deformation resembles boudinage with some boudins remaining relatively undeformed at the surface. Some deformation along listric shear zones in the continental crust continues at the proximal to mid margin, even after final breakup of the upper crust (Fig. 4.2f [3]), but most deformation is now focused at the rift axis in the nascent oceanic region. A slight asymmetry develops in the late syn-rift period (Fig. 4.2e [4]), as highly thinned upper continental crust approaches the point of rupture.

The equivalent model with added distributed, aggrading clastic sediment (Model 1-AF, aggrading full), alters the geometry of the margins, producing more abrupt changes in thickness of the continental crust (Fig. 4.3a-d [1] 4.4d). In this model, the surface of the sediment is horizontal and the thickest sediments accumulate where accommodation is greatest, above the rift axis. This model design was chosen as an end member with considerable sedimentation, to demonstrate how the style of evolution of the margin is impacted. Natural systems will fall between the end members presented here, with and without aggrading sedimentation. As sediment is added, the style of conjugate shearing in the crust changes (Fig. 4.3c) such that the most active shears locate at the rift axis (Fig. 4.3b, d). In Model 1-AF (Fig. 4.3, a-d), active shearing near the rift axis produces faults that dip toward the rift axis. Shearing persists for sufficient time that major offsets develop along the faults causing significant rotation of the hangingwall and producing heavily rotated syn-rift sediment above upper crustal fault blocks. Significant growth in the stratigraphic section is recorded across these faults. The listric shape of the shears

and their persistence combine to dissect the crust, producing the abrupt changes in crustal thickness in Model 1-AF in contrast to Model 1 (Fig. 4.4d).

Model 1-AF is an idealized end member that demonstrates the rift margin style when there is abundant aggrading sediment above the rift axis. Model 1- AP (aggrading partial) (Fig. 4.3 e,f) is a variant on this situation where sedimentation was shut off at 25 Ma, approximately 10 Ma before final breakup. This was done to approximate a more realistic case, where the accommodation space above the rift axis is not completely filled with sediment. The model retains some characteristics of Model 1-AF, for example the focused shearing at the rift axis and the abrupt changes in crustal thickness, but at the end of rifting the residual unfilled accommodation space above the rift axis and the overall necking of the crust on both sides of the rift axis are intermediate between Models 1 and 1-AF (Fig. 4.4d, e). Deformation of the thinned continental crust at the distal margin shows flow towards regions of thinned sedimentary overburden [2]. In all three cases final breakup is achieved at approximately 35 Ma and the margins have similar widths.

Model 1

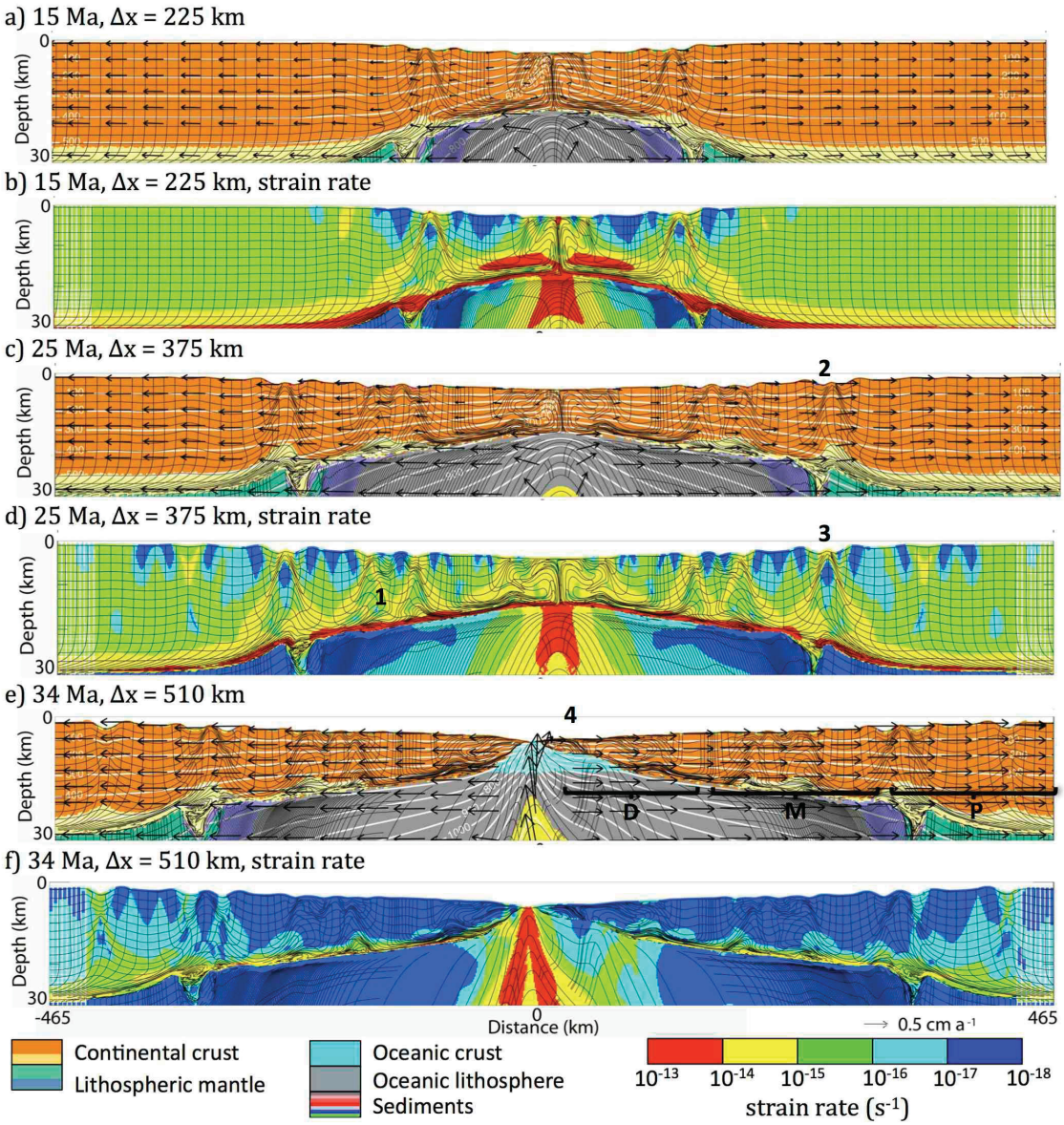

Figure 4.2: Model 1, base model with no sedimentation. Panels a), c), and e) show materials for successive points in the model evolution and velocity vectors (arrow),, and panels b), d), and f) show strain rate at the same times. In this and subsequent figures the Lagrangian grid (black) was initially horizontal and vertical, and progressively distorted throughout the model evolution. Thinning of the continental crust is distributed over several shear zones across the margin pair, with deformation occurring actively along much of the margin throughout the model evolution.

Model 1-AF

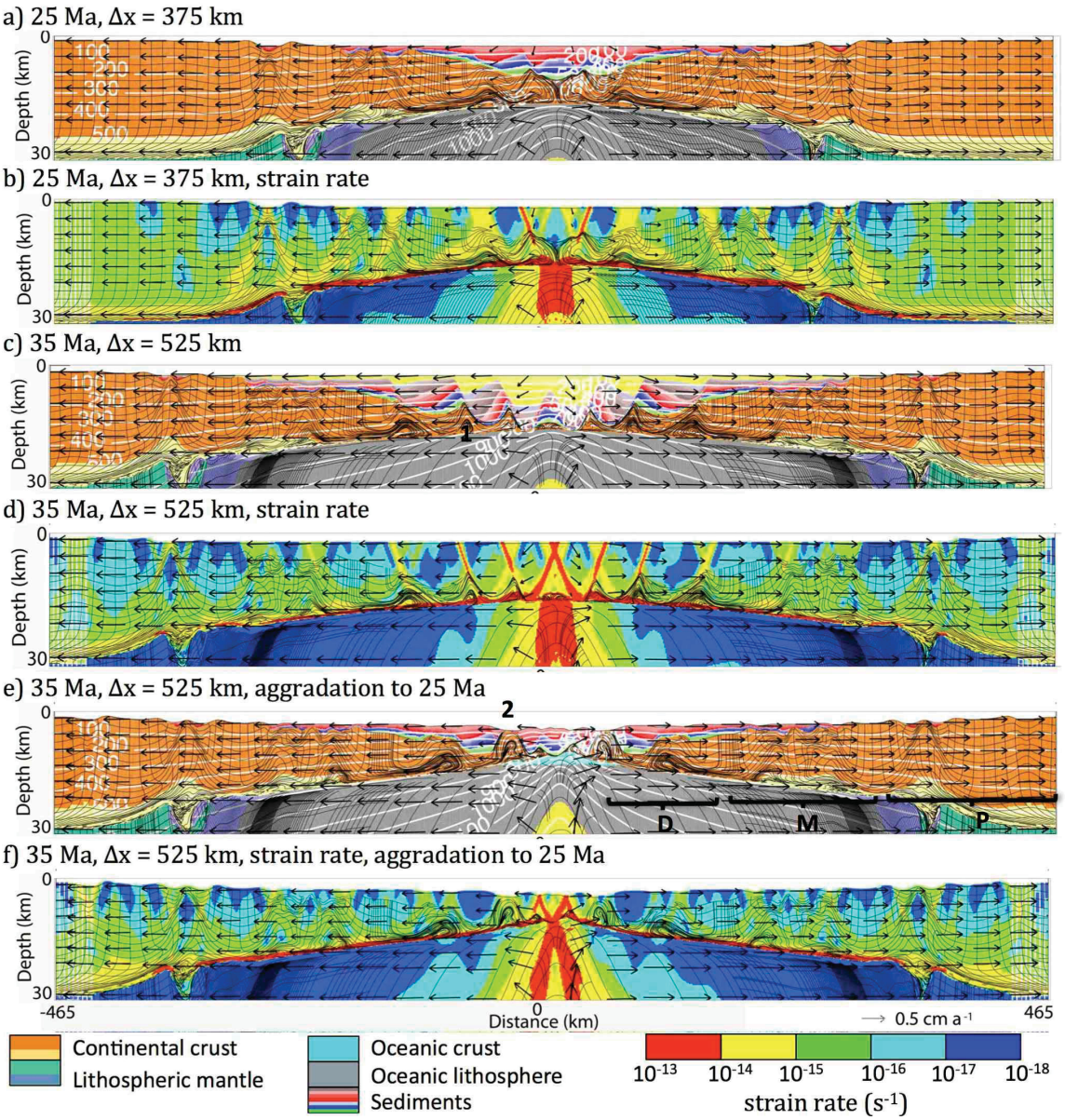

Figure 4.3: Model 1-AF, base model with aggrading sedimentation Panels a) and c) show materials for successive points in the model evolution, and panels b) and d) show strain rate at the same times. Panels e) and f) show material distribution and strain rate for Model 1-AP, in which aggradation stops part way through rifting. The addition of sediment results in more abrupt changes in continental crust thickness compared to the uniform taper of Model 1, the base model with no sedimentation (Fig. 2).

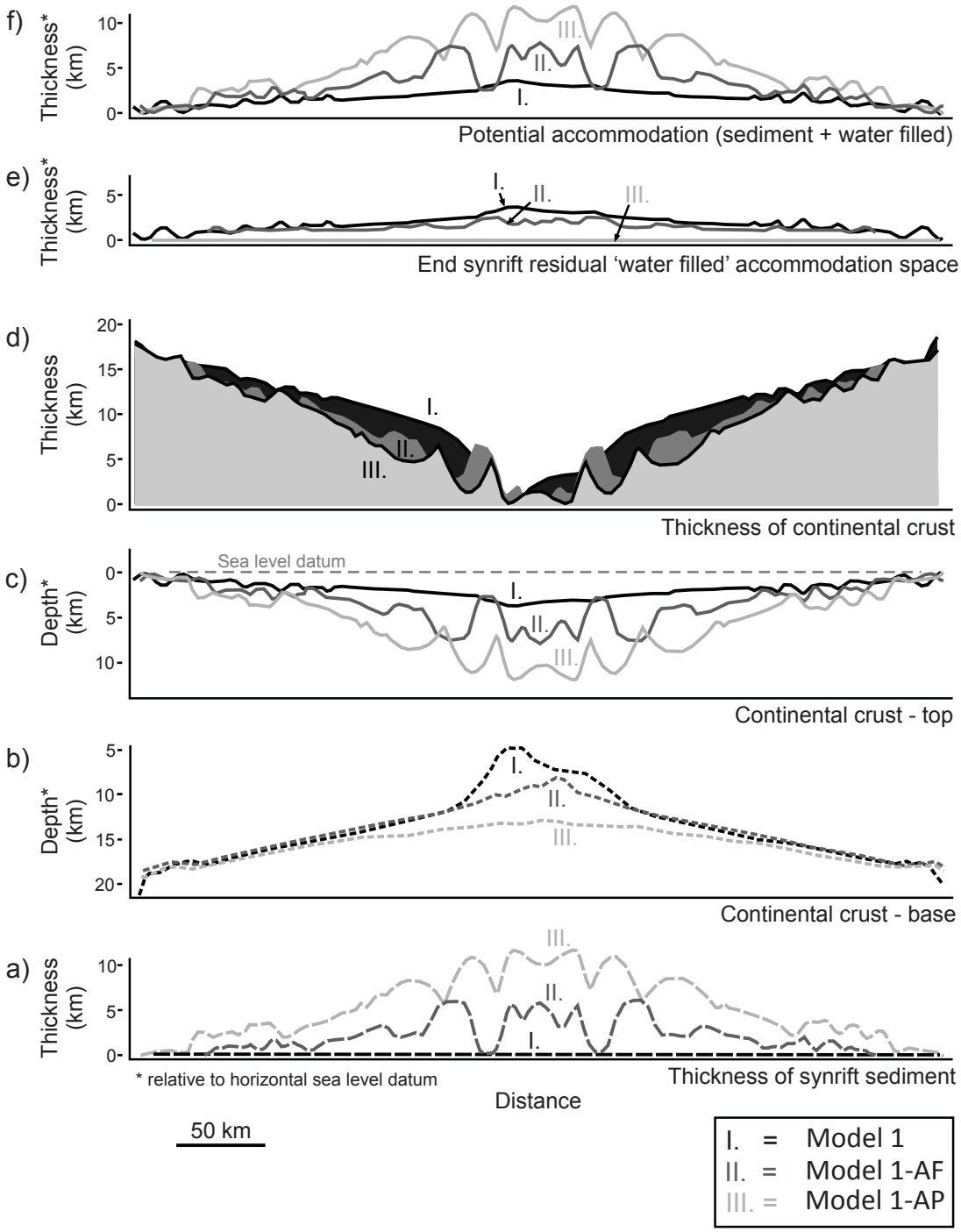

Figure 4.4: Comparison between Models 1, 1-AF, and 1-AP at the time of break-up of the upper continental crust, showing the impact of varying the thickness of aggrading synrift sediments across the rift axis (a) on the depth of the base of crust (b) and top of crust (c), and its resulting thickness (d). Increasing the thickness of synrift sediments causes both the top and bottom of the crust to subside, with enhanced shearing associated with the formation of rotated crustal blocks producing more abrupt crustal necking. e) Residual accommodation space at the end of rifting.

4.5.2 Model Set 2: Localized Sedimentation and Formation of Deep Proximal Basins

Models in the second set have prograding, deltaic-type sediment deposited at the proximal margin in the early to mid syn-rift period, and no sedimentation at the rift axis. This distribution was chosen to contrast with the regional aggradation in Model Set 1. In Model Set 2, both conjugate margins evolve in a similar manner, therefore results are shown for one conjugate margin only, to improve resolution of the images. Model 2-P1 (Fig. 4.5) has appreciable prograding sediment at the proximal margin. In contrast, Model 2-P2 (Fig. 4.6) has a lower progradation profile with its top 1 km lower than Model 2-P1 (Fig. 4.5). Note that for consistency and simplicity, sea level is not changed between the two models; this isolates the difference in sedimentation. Evolution of the proximal syn-rift basins in these two models is markedly different, with much deeper basins forming in response to the higher progradation profile. These models demonstrate the effect of sediment loading on the distribution and localization of deformation during rifting. The positive loading feedback is not just magnified isostatic adjustment. Instead, the sediment load, although relatively small in Model 2-P1 at 15 Ma (Fig. 4.5a,b), is sufficient to enhance shearing rates on the existing conjugate crustal shears below the proximal basin, thereby creating a localized horizontal velocity gradient across this basin and enhanced relative extension (Fig. 4.5a, b [1]). This feedback is expanded upon in the discussion, with reference to Fig. 4.13. In contrast to the first set of models, the sediment load also drives viscous flow at depth, which contributes to expelling weak mid-crust from beneath the basin [2]. The localized extension and lateral expulsion create grabens, and increase the basin accommodation space. When filled with sediment, the load is

magnified and, correspondingly, a positive feedback is generated. These effects can be seen by comparing Fig. 5 a, b with 5 c, d with a particular focus on the evolution of the basin after the deposition of the 'green' sediment. There has been significant shearing and flow in the crust, matched by new sediment ('blue to red') deposition in the basin. In addition, two new 'fault' bounded grabens have formed landward of the first basin (Fig. 4.5c, d [3]) and are evolving in a similar manner. Later in the syn-rift these additional grabens are now the deepest and contain up to 10 km of sediment (Fig. 4.5e [4]). Their bounding shears are now the most active (Fig. 4.5f [5]]. Despite the strong progradational character of the sediment delivery system, the overall pattern produced is a series of landward migrating depocenters.

The development of the proximal basins in Model 2-P1 (Fig. 4.5) can be contrasted with that of Model 2-P2 (Fig. 4.6), which shows only a minor positive feedback from the reduced sediment loading. In the latter case the proximal basins are similar to those that develop in Model 1 (Fig. 4.2), where there is only water loading. This result reinforces the interpretation that the sediment loading feedback loop plays a minor role in Model 2-P2.

The main effect of the sediment loading in Model 2-P1 is to modify the selection of the conjugate shears in the upper crust that control the extension. In Models 1 and 2-P2 conjugate shears that merge upward are selected beneath the proximal basins (Fig. 4.6 a-d), which results in exhumation of a horst structure in the middle of the basin but no

strong subsidence of the basin. In contrast, in Model 2-P1 the most active shears are those that bound the basin and merge downward (Fig. 4.5 c-f). Enhanced shearing on these conjugates leads to widening and subsidence of the basins and suppresses of the tendency for the horst structures to develop together with upward ductile flow in the mid-crust beneath the horsts.

In addition to the volume of sediment supplied during rifting, the extent to which proximal basins develop also depends on the strength of the crust. The positive loading feedback is diminished in models with strong and intermediate strength continental crust. Figure 7 shows weak, intermediate, and strong crust models without and with prograding sediment at the proximal margin. Model results are shown for the early to mid syn-rift period for each crust strength. Note that the model evolution is different for each, because these three models proceed through rifting at different rates. In each case, the top of the progradation profile is at sea level. Sedimentation drives the formation of deeper basins in all three models, but this result is most pronounced for the weak crust model. Very deep basins, containing up to 10 km of sediment [1], form at the proximal margin of the weak crust model, compared to basin depths of less than 2 km [2] for the similar model with no sedimentation. While the strong crust model produces a similarly thick sediment succession (~10 km) [3], the basin depth increases only slightly in response to sedimentation [4]. The model with intermediate strength crust similarly produces only marginally deeper basins with prograding sedimentation.

Model 2-P1

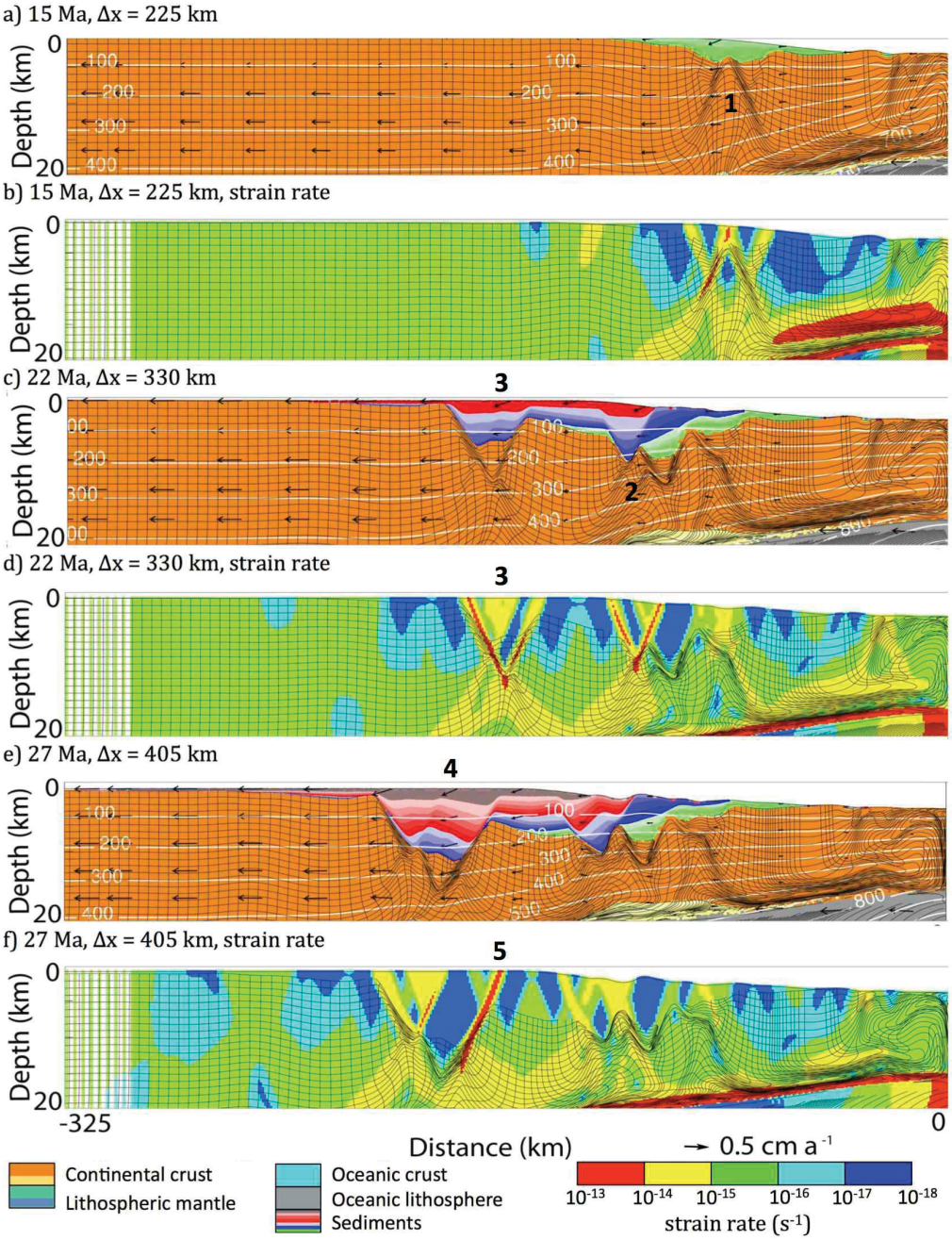

Figure 4.5: Model 2-P1, base model with considerable prograding sediment at the proximal margin. Panels a), c), and e) show materials for successive points in the model evolution, and panels b), d), and f) show strain rate at the same times. Substantial sediment accumulates in deep basins at the proximal margin. The left half of the margin pair is shown for simplicity; the corresponding right margin evolves similarly.

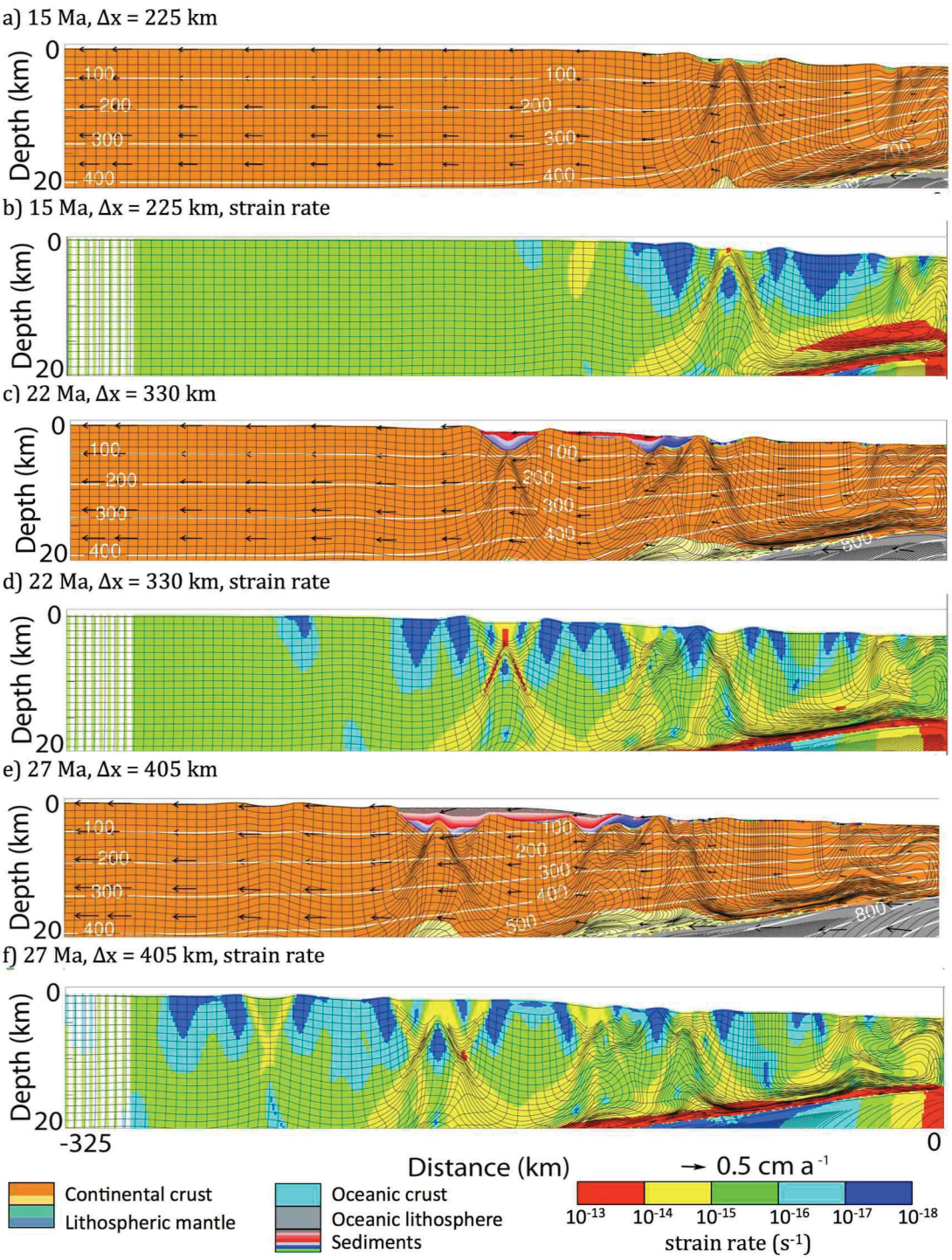

Figure 4.6: Model 2-P2, base model with prograding minimal sediment at the proximal margin. Panels a), c), and e) show materials for successive points in the model evolution, and panels b), d), and f) show strain rate at the same times. Sediment accumulates in proximal basins, which are much less deep than those of Figure 5. The left half of the margin pair is shown for simplicity; the corresponding right margin evolves similarly.

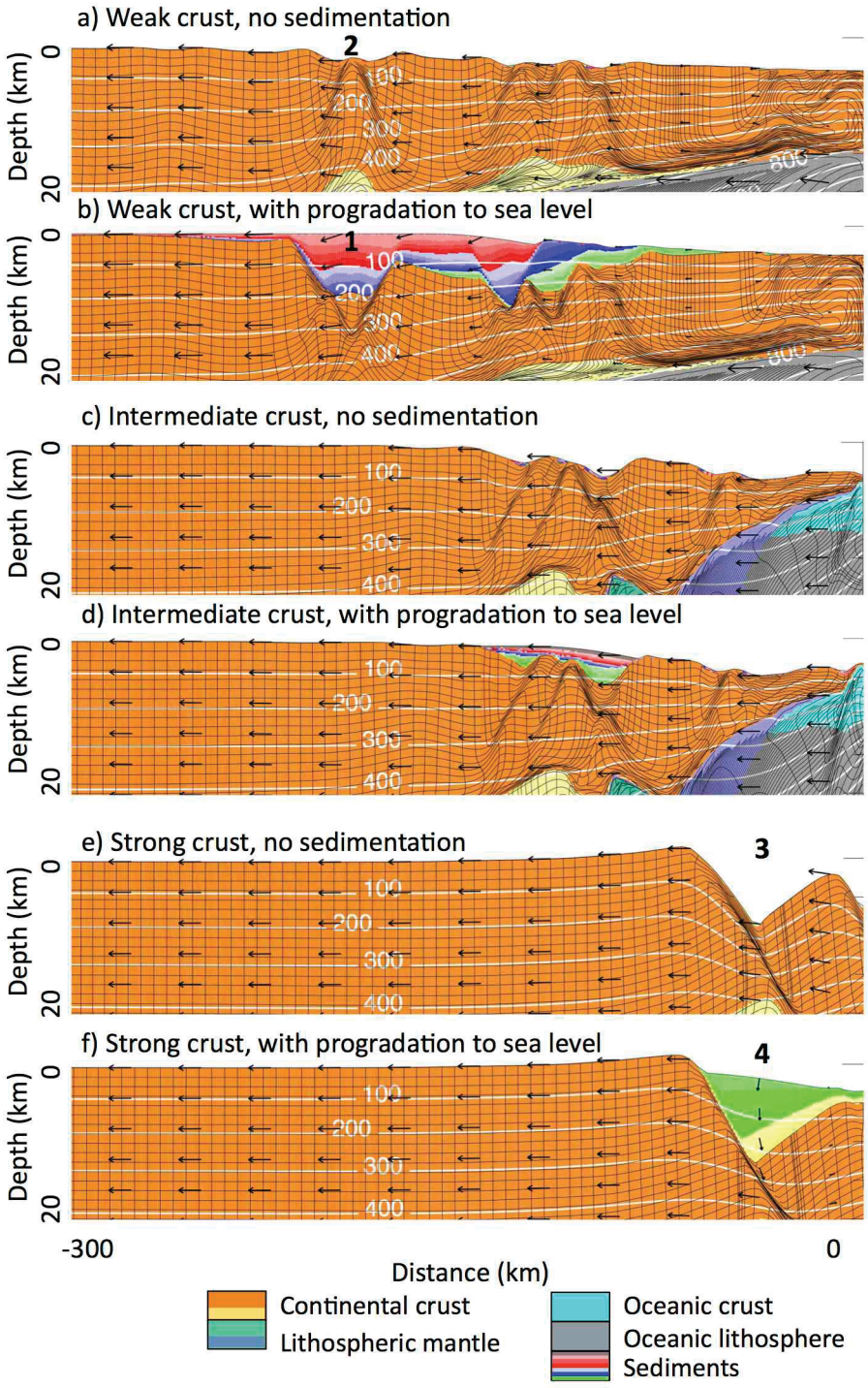

Figure 4.7: Weak (a and b), intermediate (c and d), and strong (e and f) crust models with and without prograding sedimentation at the proximal margin. Left half of model is shown; right half evolves similarly. In each case, the addition of sediment drives deepening of basins, compared to the comparable model without sedimentation. However, this effect is much more pronounced for the weak crust model than for the other two.

4.6 Syn-Rift Salt Tectonics at Wide Margins

4.6.1 Model Set 3: Early and Late Syn-Rift Salt Tectonics

Model Set 3 explores early and late syn-rift salt tectonics, using the weak crust base model (Model 1) presented above. In Model 3-ES (Early Salt) early syn-rift salt was deposited from 10-11 Ma (Fig. 4.8 L,R), and in Model 3-LS (Late Salt) late syn-rift salt was deposited from 32-34 Ma (Fig. 4.9 L,R). For Model 3-LS precursor clastic sediment fills accommodation space before salt deposition, following a horizontal aggrading profile. In both models salt is deposited as a continuous aggrading body, spanning the conjugate margins at the time of deposition (Fig. 4.8 and 9 [2]). There is, however, a contrast in salt deposition in the two models because the margin has extended more and become wide in Model 3-LS. As a result, late salt deposition leads to a broader distribution of salt across the margin in the late syn-rift and post-rift phases (Fig. 4.9). In Model-ES, early syn-rift salt is deposited directly onto the continental crust, both in the proximal basins that have developed by this time and over the mid margin. Initial salt thickness varies, reaching a maximum of ~ 3 km (Fig. 4.8 [1]). In Model 3-LA salt is deposited as a layer approximately 2 km thick, onto the smooth underlying sediments in the landwards parts of the model (Fig. 4.9 [1]), but in the listric-faulted distal regions nearer the rift axis salt is deposited in a series of stepped basins (Fig. 4.9 [2]). Some salt is also deposited in the proximal basins (Fig. 4.9). Continued movement along listric faults after late syn-rift salt was deposited increases the base of salt rugosity (Fig. 4.9L [3]). Late rifting also produces escarpments in the top salt surface and locally-ponded thickened salt bodies as salt flows into accommodation space created by faulting,

extension and thinning of underlying crust and sediments (Fig. 4.9 [3]). This style of salt tectonics reflects the way salt flows locally to adjust to extension of the underlying crust, which is similar to Model 1-AF (Fig. 4.3d). In contrast to the distal margin, there is little post-salt extension of the mid-margin in either model (Figs. 4.8 and 9) and therefore the salt remains largely undeformed.

Interaction among salt, post-salt sedimentation, and ongoing rifting shows some contrasts between the early and late syn-rift salt models. In both models, post-salt sedimentation comprises prograding, deltaic-type, clastic sediments on both conjugates. In Model 3-ES, designed to be like Model 2-P1 (Fig. 4.5), prograding post-salt sediment is trapped in proximal basins that develop and deepen in response to loading by the sediment (Fig. 4.8 [3]); this is an example of the positive feedback discussed above. Model 3-LS exhibits more interaction with post-salt sediment. The prograding wedge advances across each of the proximal margins, trapping some salt and expelling the rest laterally toward the mid margin (Fig. 4.9 [4]). The proximal basin, Fig. 4.9L, deepens in response to the load of prograding sediments, and a thick sedimentary succession is deposited. However, the feedback between sedimentation and crustal extension is much less pronounced here (Fig. 4.9L), compared to Model 3-ES (Fig. 4.8), and the earlier models, eg. Model 2-P1 (Fig. 4.5).

Model 3-ES (above) and Model 3-LS (below)

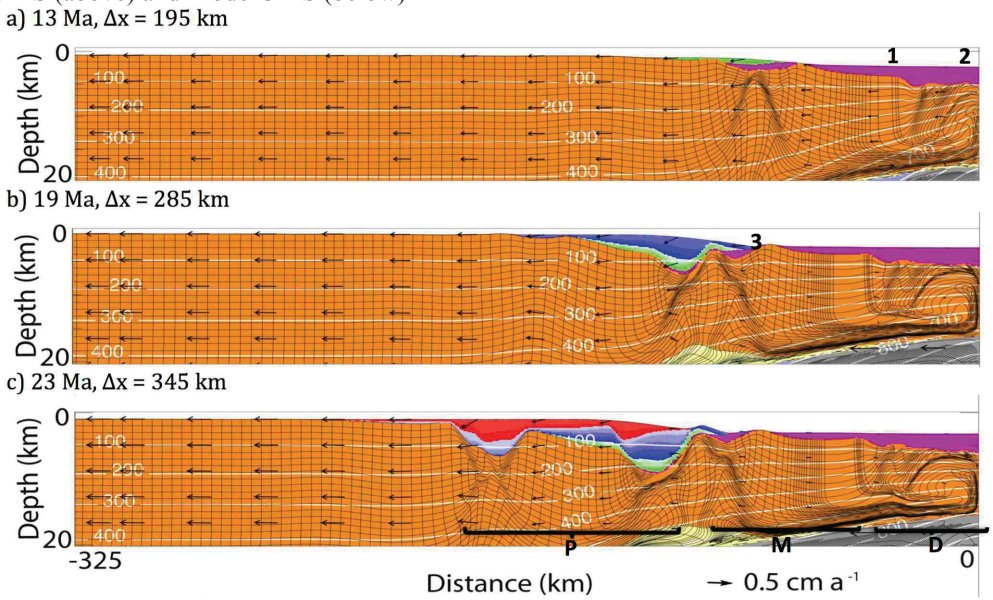

Figure 4.8 L: Model 3-ES, early syn-rift salt followed by sediment progradation. Panels a-c show successive times in model evolution. Salt is deposited onto continental crust, across the conjugate margins. Prograding sedimentat is largely trapped in basins at the proximal margin, as the locus of deformation shifts here, in response to the sediment load.

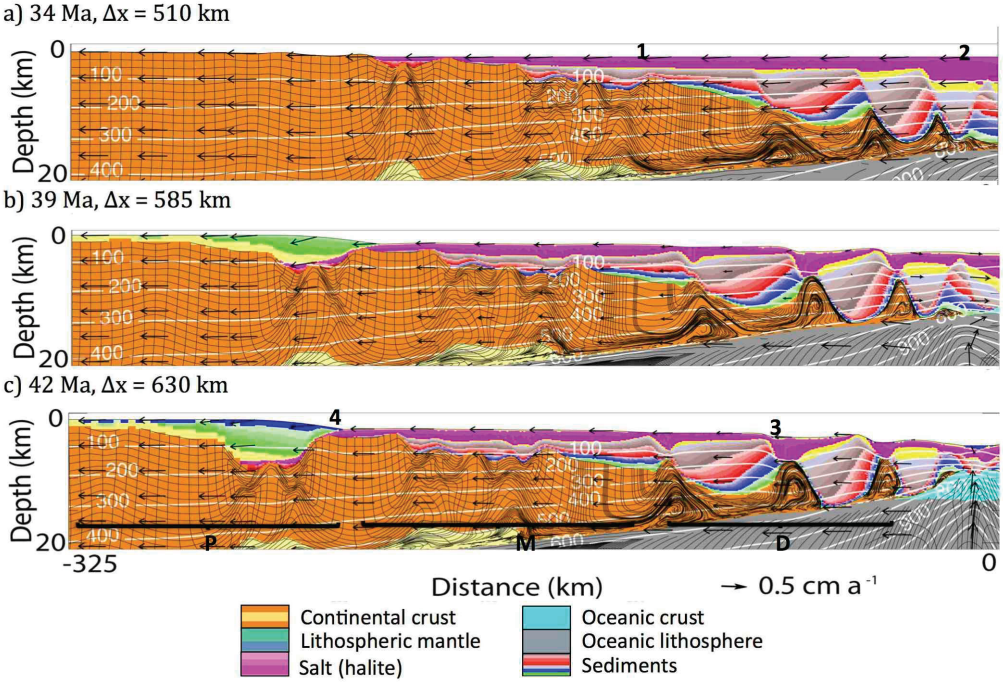

Figure 4.9 L: Model 3-LS, late syn-rift salt followed by sediment progradation. Panels a-c show successive times in model evolution. Salt is deposited as a thin continuous body across the conjugate margins, over previously deposited aggradating syn-rift sediments. Prograding sediments deposited later in the model evolution do not appreciably shift the locus of deformation; thinning of the crust under the salt continues. Salt forms escarpments as underlying sediments extend and thin in response to ongoing rifting.

Model 3-ES (above) and Model 3-LS (below)

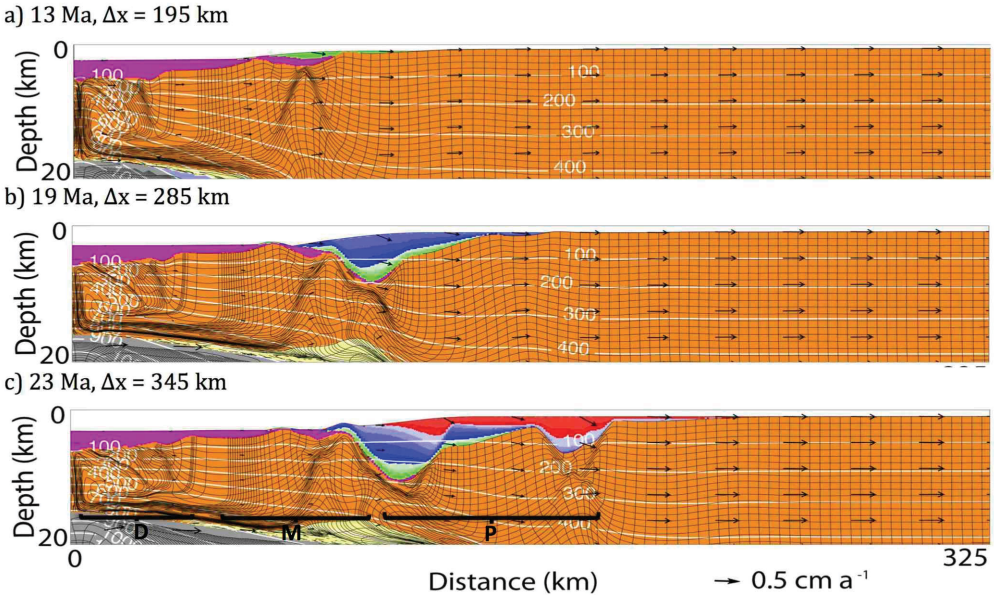

Figure 4.8 R: Model 3-ES, early syn-rift salt followed by sediment progradation. Panels a-c show successive times in model evolution. Salt is deposited onto continental crust, across the conjugate margins. Prograding sedimentat is largely trapped in basins at the proximal margin, as the locus of deformation shifts here, in response to the sediment load.

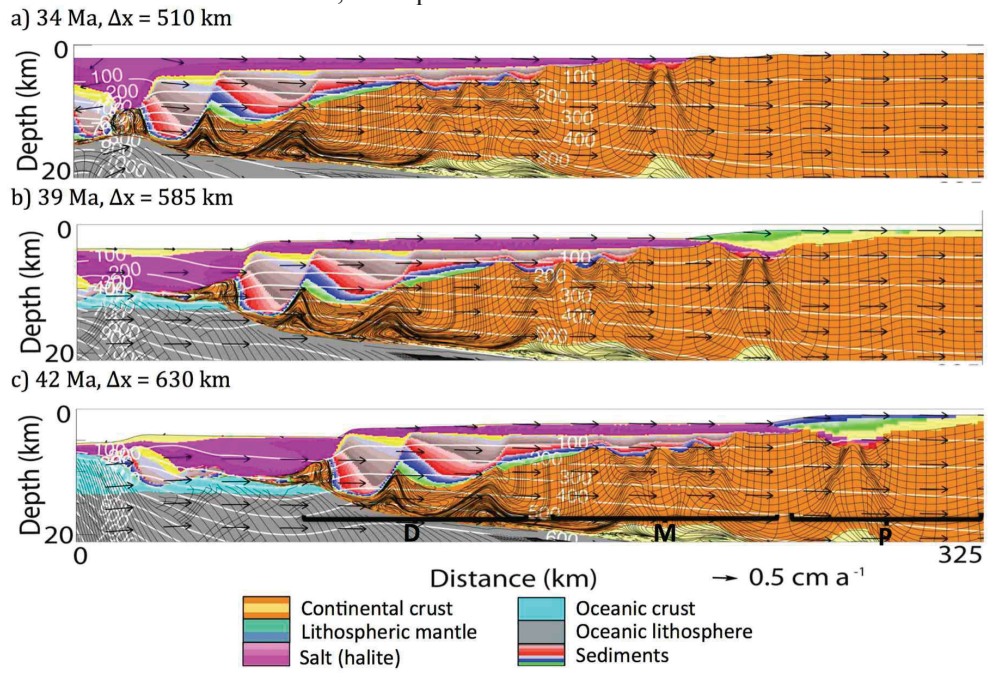

Figure 4.9 R: Model 3-LS, late syn-rift salt followed by sediment progradation. Panels a-c show successive times in model evolution. Salt is deposited as a thin continuous body across the conjugate margins, over previously deposited aggradating syn-rift sediments. Prograding sediments deposited later in the model evolution do not appreciably shift the locus of deformation; thinning of the crust under the salt continues. Salt forms escarpments as underlying sediments extend and thin in response to ongoing rifting.

4.7 Nature Example: The Nova Scotia Rifted Margin

4.7.1 Nova Scotian Margin Tectonic and Sedimentation history

The Nova Scotia Atlantic rifted margin (Fig. 4.10) formed in response to lithospheric plate separation between Africa and North America as Pangea broke apart (*Klitgord and Schouten*, 1986; *Wade and MacLean*, 1990). Rifting began in the Middle or early Late Triassic (e.g. *Wade et al*., 1995; *Olsen*, 1997), propagating from south to north, and eventually leading to the opening the Atlantic Ocean. Along the Nova Scotia margin rifting terminated in the Early Jurassic, as early as 190 Ma (*Labails et al.,* 2010; *Sibuet et al.*, 2012), or as late as 175 Ma (*Klitgord and Schouten*, 1986). Seaward dipping reflections are interpreted to indicate that the southwestern part of the Nova Scotia margin experienced volcanic (magma rich) rifting, but the absence of these reflection packages along the central and northeastern parts of the margin indicate a transition to non-volcanic (magma-poor) rifting (*Keen and Potter*, 1995; *Louden et al*., 2012). This study focuses on the central and northeastern, non-volcanic parts of the margin.

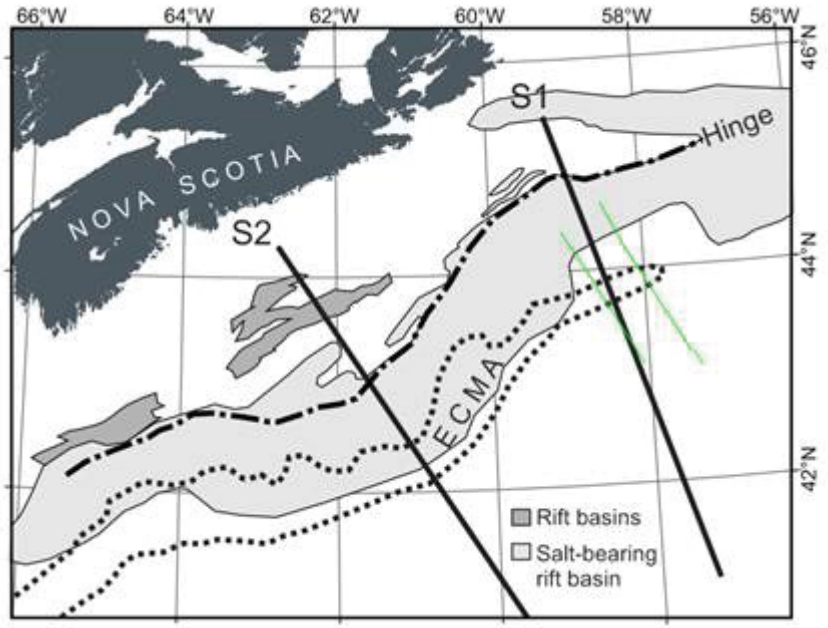

Figure 4.10: Base Map of Nova Scotia margin, showing locations of SMART I (SI) and SMART II (S2).

Continental crust beneath the continental shelf of central and northeastern Nova Scotia has a maximum thickness of approximately 36 km and thins seaward to < 5 km over distances of 255 to 315 km (*Keen and Potter* 1995; *Funck et al*. 2004; Wu *et al*, 2006). In the northeast, thinning of the crust takes place most abruptly under the modern continental shelf (*Funck et al*. 2004). Along the central margin a small degree of thinning occurs under the shelf but thinning of the continental crust occurs most abruptly under the continental slope (*Wu et al*., 2006). Placement of the seaward limit of continental crust is equivocal. For the central margin it has been placed along the East Coast Magnetic Anomaly (ECMA) at the seaward limit of the salt (*Salisbury and Keen* 1993; *Keen and Potter*, 1995) or 60 km seaward of this, outboard heavily rotated fault blocks interpreted as continental crust (*Wu et al*. 2006). For the northeastern margin the edge of continental crust has been placed along the dimmer eastern continuation of the ECMA (e.g. *Sahabi et al.* 2004; *Sibuet et al*., 2012) or more than 70 km seaward (e.g.

Keen and Potter, 1995; *Funck et al*. 2004), beneath the distal most allochthonous salt body expelled from a large-scale salt detachment system.

Crustal extension in both regions produced a series of east-west to northeast-southwest trending grabens or half grabens that step down from relatively unfaulted basement platforms (*Wade and MacLean*, 1990). The oldest dated margin sediments (stratigraphic chart Fig. 4.11) are found in these rift basins and consist of continental red clastics of the Eurydice Formation that give way both laterally (towards the rift axis) and up-section to widespread accumulations of Argo Formation salt (massive halite) deposited during intermittent latest Triassic and Early Jurassic marine incursions (*Jansa and Wade*, 1975b; *Wade and MacLean*, 1990; *Weston et al.* 2012). On the central margin, there does not appear to be any salt in the landward-most half grabens, whereas on the northeastern margin salt occupies even the most proximal rift basins. The combined thickness of the Eurydice and Argo formations is estimated to be up to several kilometers thick, but the succession has never been fully penetrated on the Nova Scotian margin (*Wade and MacLean*, 1990). Salt deposition ceased in the Early Jurassic.

The Eurydice and Argo formations are overlain unconformably by immature clastics and evaporitic dolostones of the Mohican and Iroquois formations (*Wade and MacLean*, 1990). Initial displacement of salt took place during deposition of the Mohican Formation, but the age of this unit is poorly constrained (e.g. *Weston et al*. 2012). Similarly, regardless of whether 'break-up' took place at 190 Ma (*Labails et al*., 2010; *Sibuet et al*., 2012) or 175 Ma (*Klitgord and Schouten*, 1986), recent regional

biotratigraphic studies were unable to diagnose any post-Triassic to pre-Bajocian strata (~200 to 172 Ma; *Weston et al*. 2012). Combined with the inability to correlate a distinct break-up unconformity on seismic profiles beyond the proximal parts of the rifted margin (*Wade and MacLean*, 1990), the stratigraphic position of 'break-up' is uncertain. Previous workers have placed the break-up event above the Argo Formation and below the Mohican Formation, but it is equally plausible that break-up took place in the lower part of the Mohican Formation.

The Mohican and Iroquois formations are overlain by a widespread Bathonian to Callovian limestone unit known as the Scatarie Member that is generally 200 to 300 m thick. Along the central parts of the margin, the Scatarie Member forms the base of a widespread late Middle through Late Jurassic carbonate bank (Abenaki Formation). To the northeast however, the marker forms the base of a thick succession of mixed deltaic clastics and carbonates known as the Mic Mac Formation. Both the Abenaki and Mic Mac Formations accumulated as the margin thermally subsided and are clearly post-rift stratigraphic units.

Subsequent sedimentation consisted of thick fluvial-deltaic sediments in the Early Cretaceous, followed by marine shales with limestone in the Late Cretaceous, and mudstones, sandstones, and conglomerates in the Paleogene, and Neogene (*Wade and MacLean*, 1990).

4.7.2 Model Set 4 and Comparison with Central and Northeastern Nova Scotia Margin

To guide the construction of Model set 4, and to enable comparison with the Nova Scotian margin it was necessary to restore cross sections of the Nova Scotian margin approximately to their end of syn-rift configurations. To this end, we have created roughly backstripped versions of the SMART I and SMART II cross-section interpretations of *Funck et al*. (2004) and *Wu et al.* (2006) across the northeastern and central parts of the margin, respectively (Fig. 4.12). Backstripping includes several steps. First the post-rift sediment load was removed and the section was adjusted for isostasy. The synrift sediments were then decompacted to account for the removal of the post-rift stratigraphic succession. Lastly, the thermal subsidence that occurred after rifting ended was removed. Because it is not possible to correlate a marker that precisely defines the end of rifting, we use the widespread Scatarie Member (Fig. 4.11) to approximate the end of syn-rift sedimentation in the backstripped models. This limestone unit is known to be in the early post-rift sequence so our reconstructions slightly overestimate syn-rift sedimentation.

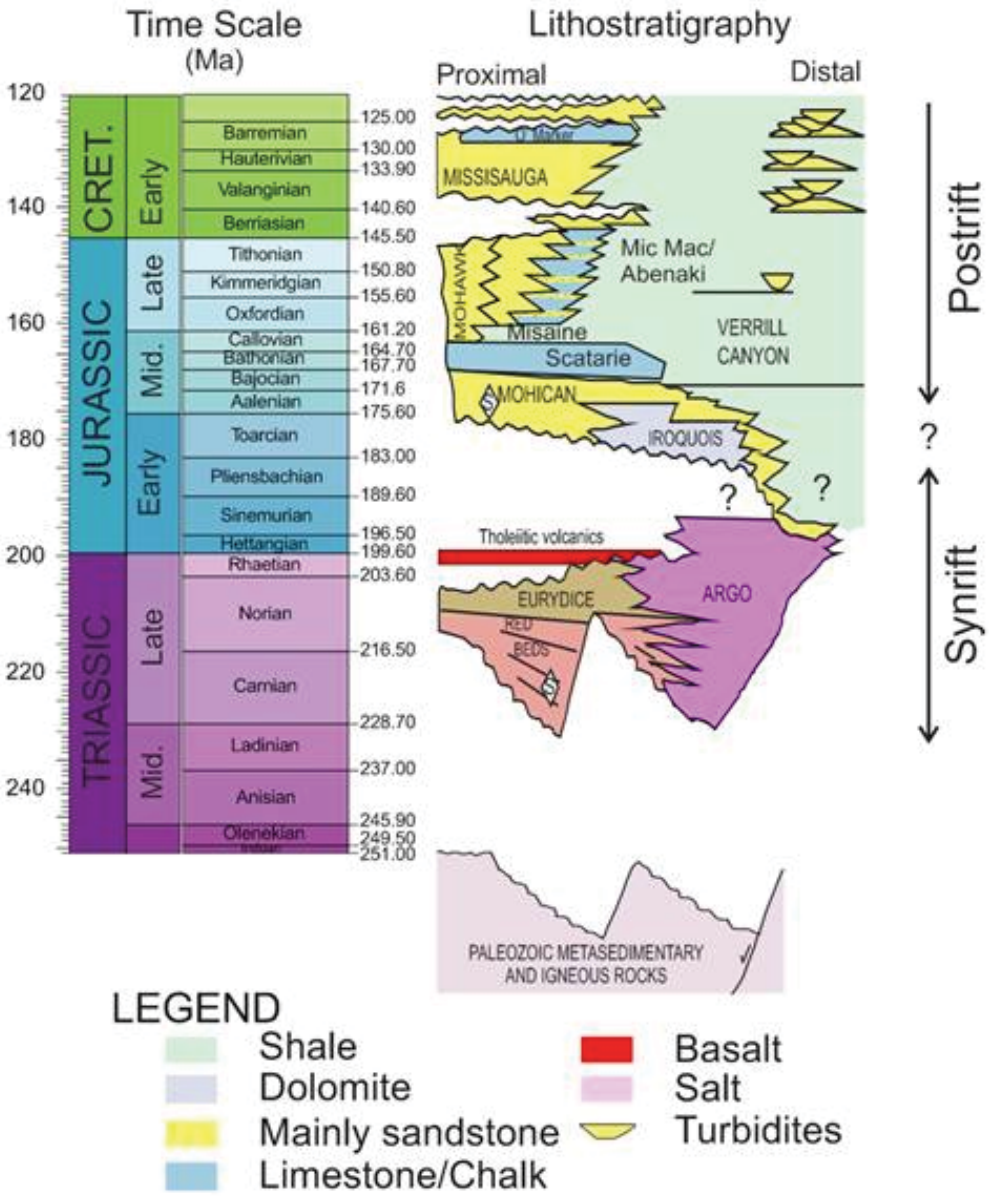

Figure 4.11: Syn-rift to early post-rift stratigraphic column, adapted from OETR (2011), with stratigraphic nomenclature from Wade and MacLean (1990, 1993). Time scale from Ogg et al. (2004).

In addition to the backstripped versions of SMART I and II velocity models, we provide line drawing type sections of Lithoprobe 88-1 (*Keen and Potter*, 1995) that is roughly

coincident with SMART II (referred to as Type Profile 2) and a new composite reflection seismic transect that roughly coincides with SMART I (referred to at Type Profile 1). (Fig. 4.12 e and b). The latter provides improved imaging of the syn-rift succession compared to the Lithoprobe 89-1 profile described by *Wade et al*. (1995) and used by *Funck et al*. (2004). Both line drawings were flattened on the J163 marker, a seismic reflection produced by the strong impedance contrast at the top of the Scatarie Member limestone or its seaward equivalent. Flattening the profiles on this horizon approximates the near end syn-rift state and artificially removes post-rift thermal subsidence and sediment loading effects, making the comparison to Model Set 4 easier.

Model Set 4 consists of two models, NSC and NSNE (Fig. 4.13), designed for comparison with the central and northeastern parts of the Nova Scotian margin, respectively. Both models have the same initial geometry and rifting velocity. We focus on syn-rift sedimentation, that is sediment deposited during the 34-35 Ma of model syn-rift time, which agrees with an interpreted syn-rift time span of 220-185 Ma for the Nova Scotian margin. Pre-salt sedimentation for Model 4-NSC consists of distributed, aggrading sediment. This was done to allow for the most laterally extensive distribution of pre-salt synrift strata possible, as observed in Type Profile 2 (Fig. 4.12). For Model 4-NSNE pre-salt sediment is also aggrading, but with more sediment deposited in the proximal basins. In both models, salt is deposited in the mid syn-rift period, between the timing of salt deposition in the early and late syn-rift salt models presented earlier in this paper. In Model 4-NSC, salt is deposited as a continuous body across the rift axis. The thickest salt accumulates where rift accommodation was greatest, nearest the rift axis.

Salt distribution is consistent with Type Profile 2 which shows salt pillows and rollers in the proximal margin passing seaward into well-developed salt diapirs, presumed to have been sourced from a thicker primary salt layer. In Model 4-NSNE, salt deposition is focused in the proximal basins, consistent with Type Profile 1 where the primary salt basin appears to be absent over the seaward reaches of the continental crust (Fig. 4.12) (*Sahabi et al*., 2004).

Post-salt sedimentation for both models is a prograding, deltaic-type wedge, initially focused at the proximal margin. The models differ in the amount of post-salt sedimentation: more for Model 4-NSNE than for Model 4-NSC. This is consistent with the significant increase in post salt sedimentation observed beneath the J163 marker in Type Profile 1 compared to Type Profile 2. The amount of sediment deposited in each model is determined by the placement of the top of the progradation profile; the profile for Model 4-NSNE is 1 km higher than that for Model 4-NSC. At each time step, all space below the top of this profile, and hence all accommodation space available in the proximal basins, is filled with sediment. In Model 4-NSNE (Fig. 4.13) there is a strong feedback between sedimentation crustal faulting and extension, leading to significant basin expansion and subsidence, and the accumulation of a thick succession of sediments in the proximal basins. Owing to the positive feedback loop, the amount of sediment deposited is much greater than the accommodation space that was initially available. This positive feedback is more muted in Model 40NSC, with only a small amount of basin expansion and subsidence, resulting in much less sediment being deposited in the proximal basins. Evidently, the higher progradation profile in Model 4-NSNE was

sufficient to trigger a strong positive feedback between sedimentation and crustal extension, whereas the lower profile in Model 4-NSC was not.

This feedback impacts the style of crustal extension in addition to the accumulation of sediments. In Model 4-NSNE deformation of the crust is localized under the deepening proximal basins, producing abrupt changes in crust thickness and more significant deformation of the mid and lower crust at this location. In contrast, in Model 4-NSNC there is no major localized crustal thinning and the final style is uniform crustal taper across the margin. There is also a correlated effect concerning the contrasting styles of margin extension. Both models have the same rate of overall extension, so that enhanced extension at the proximal margin in Model 4-NSNE must be compensated by reduced extension elsewhere. This can be seen by comparing the distal extension of Model 4-NSNE with that of Model 4-NSC (Fig 4.13 b and d); the distal crust of Model 4-NSNE is thicker and less extended than that of Model 4-NSC. This comparison demonstrates that the enhanced proximal extension was compensated by reduced distal extension. In both models, salt initially deposited at the proximal margin is stretched and thinned beneath post-salt prograding sediments and much of this salt remains in the proximal basins. Salt deposited over the mid to distal margin in Model 4-NSC experiences lateral flow and stretching.

a) SMART I, after Funk *et al.* (2004), backstripped to end of syn-rift period.

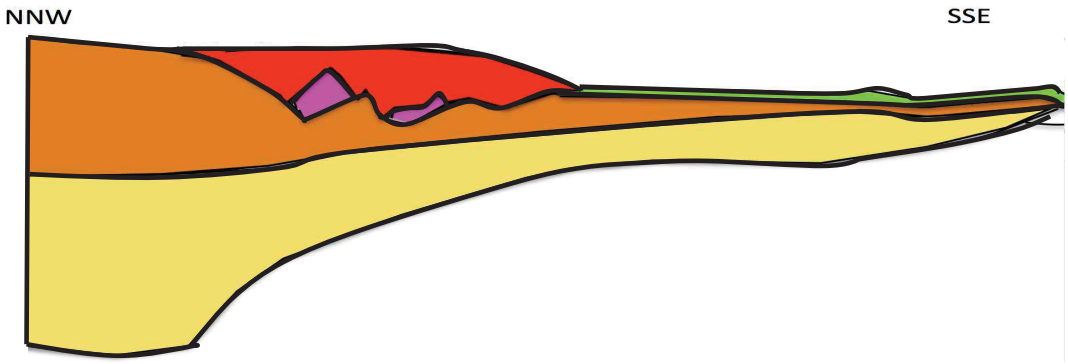

b) Northeastern NS margin, flattened on J163 marker

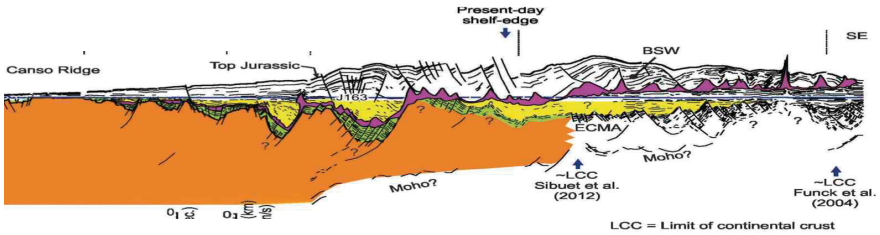

c) Model 4-NSNE, 35 Ma evolution (Δx = 525 km)

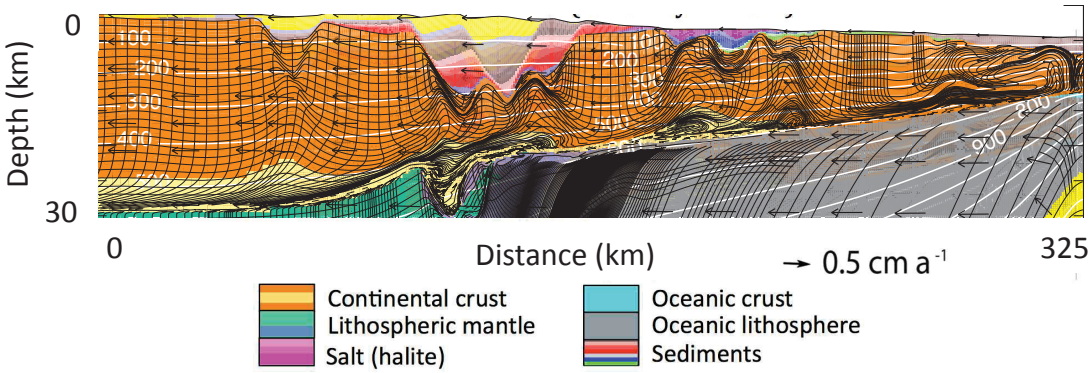

d) SMART II, after Wu *et al.* (2006), backstripped to end of syn-rift period.

e) Central NS margin, flattened on J163 marker

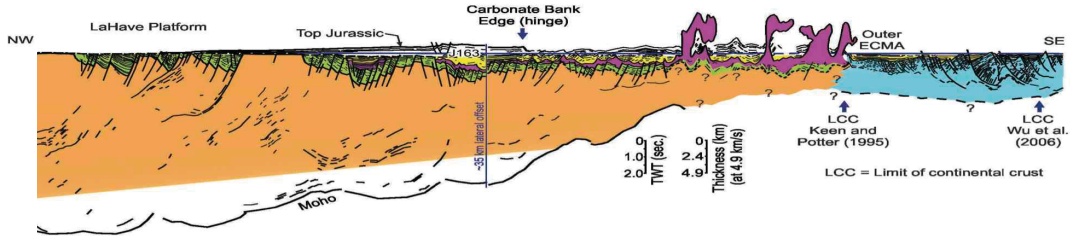

f) Model 4-NSC, 35 Ma (Δx = 525 km)

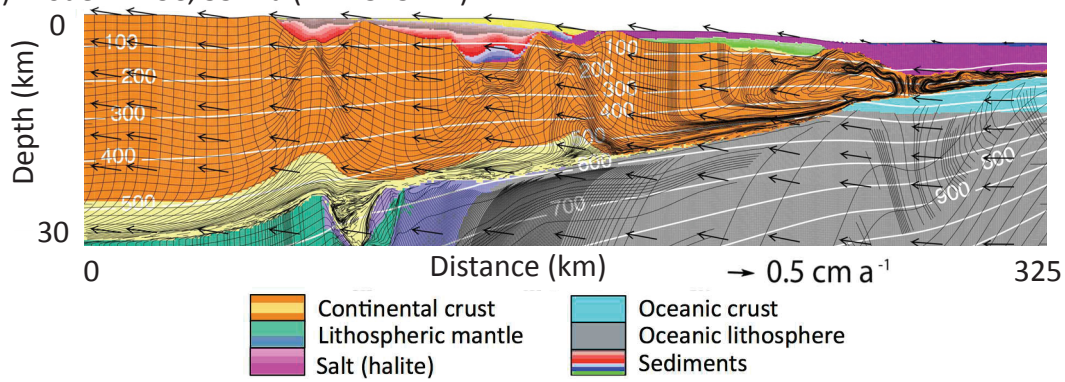

Figure 4.12: Comparison of modeling results with Nova Scotia Margin. Panels a-e show the SMART I line backstripped to roughly the end of the syn-rift period, a line drawing based on seismic data for the NE margin, flattened on approximately the end of the syn-rift strata, and our model result for the NE margin, at approximately the end of syn-rift timing. Panels d-f show the SMART II line backstripped, a line drawing informed by seismic data for the central margin, and our model for the central margin, at the end of syn-rift period.

Model NSNE (above) and Model NSC (below)

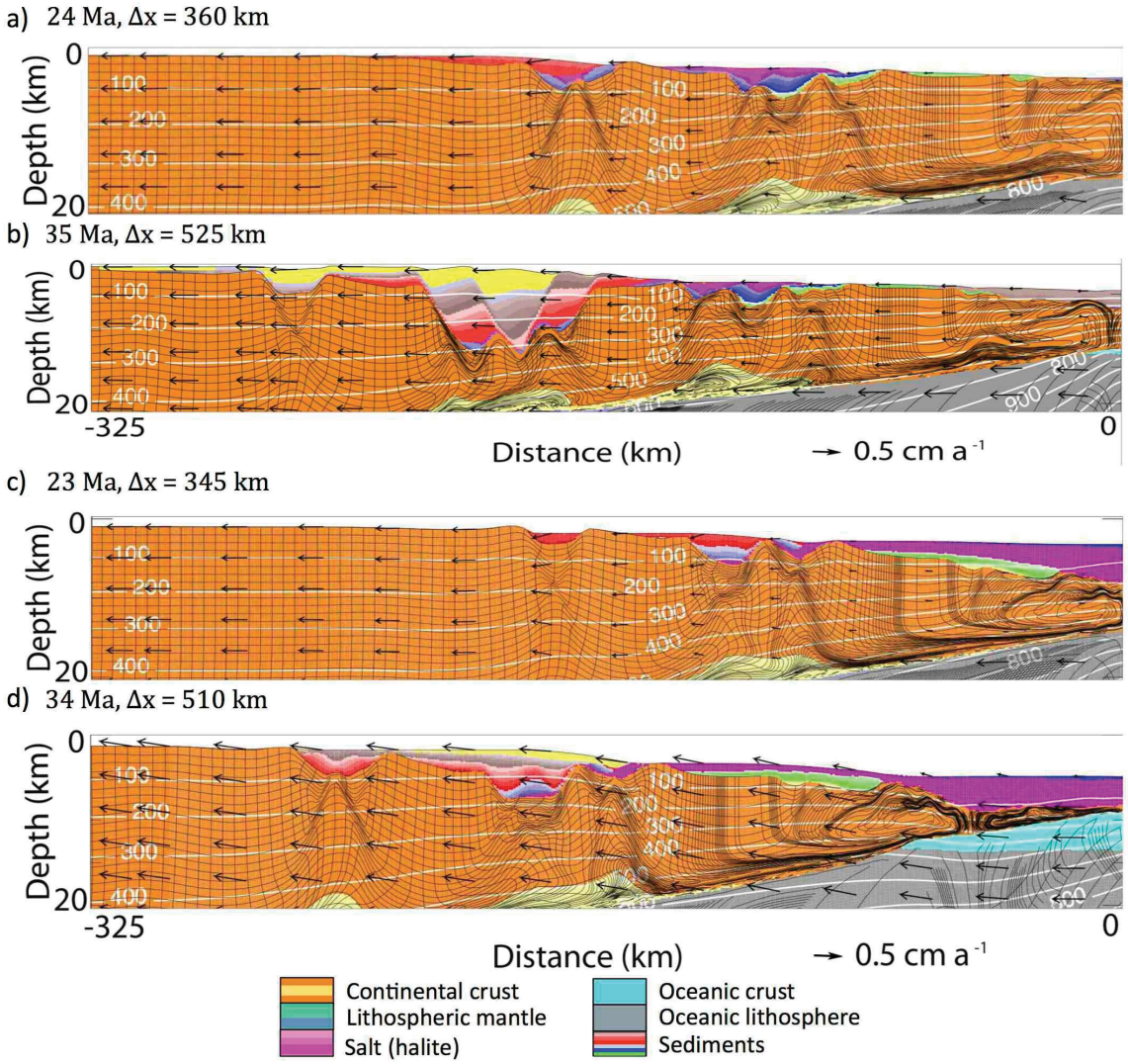

Figure 4.13: Nova Scotia margin models addressing the northeastern (NSNE) (panels a, b) and central (NSC) (c, d) margin. Model NSNE has considerable post-salt prograding sedimentation, and forms deep proximal basins. In this model, salt deposition is restricted to the proximal basins. Model NSC has moderate post-salt prograding sedimentation, and forms less deep proximal basins. Salt is deposited as a continuous body across the margin pair.

4.8 Discussion

The water loaded weak crust model considered throughout this paper produces a wide, slightly asymmetric margin pair that develops through generally distributed deformation of the upper crust, which in detail resembles boudinage with upward flow of mid- crust into the boudin necks (Fig. 4.2). Compared to our previous work on intermediate width margins with a stronger crust (*Allen and Beaumont*, 2015), this weak crust model evolves with more distributed deformation of the upper crust and less evidence for diachronous stretching, and produces a wider margin pair with more substantial deformation of the lower crust and less pronounced surface topography of the upper crust. When aggrading sediments are applied, they produce a succession of generally flat-lying sedimentary layers that young upwards at the mid margin, contrasting notably with the seaward dipping, seaward younging sedimentary successions of the intermediate crust models. In the distal margin of the weak model there is a strong interaction between sediment aggradation and crustal-scale listric normal faulting.

Some aspects of our weak crust models are similar to the Type II models of *Huismans and Beaumont* (2011, 2014), such as the separation of the continental lithosphere before the crust, producing a region of thinned continental crust underlain by hot upwelled sublithospheric mantle. The resulting conductive heating contributes to the ductile deformation of the lower crust. It should be noted that the weak crust model used in this paper is somewhat stronger than the Type II model of *Huismans and Beaumont* (2011, 2014, WQz/10 versus WQz/50). That we observe this same characteristic of decoupling

at the base of the continental crust and separation of the mantle lithosphere before the crust in our models with stronger crust is a consequence of the increased resolution of the finite element grid provided by the nested SS model. Higher resolution allows more refined definition of shear zones which correspondingly act as though they are effectively weaker. This result can be interpreted to suggest that similar results could be achieved for even stronger crust (e.g. WQz/1) given sufficiently high resolution calculations.

4.8.1 Gravitational Spreading - Channel Flow Explanation of the Interaction between Proximal Sedimentation and Margin Evolution

A major focus in this paper concerns the feedback of enhanced crustal extension in response to proximal sediment loading (c.f. Models 1, 2-P1 and 2-P2 and those for the Nova Scotia margin). As discussed earlier, the characteristics of the observed behavior are: 1) during enhanced extension the extending proximal basins develop new bounding shear zones that promote widening and deepening of these basins; 2) enhanced extension is triggered by sediment loading on the up-dip proximal margin; 3) small sediment loads or water loading alone do not cause enhanced extension; 4) enhanced extension is confined to models with weak crusts, particularly those with viscously weak mid and lower crusts. Similar characteristics have been noted for natural systems where overly deep basins (ultra-deep basins) are observed on rifted margins. This study builds on previous work, in which lower crustal flow has been invoked to explain the formation of these very deep basins in nature (e.g., *Westaway*, 1994; *Morley and Westaway*, 2006; *Westaway and Bridgland*, 2007; *Clift et al*., 2015; *Clift*, 2015).

The model characteristics described above can be explained by the stability analysis of variable thickness frictional-plastic overburden above a viscous substrate. *Gemmer et al.* (2004; 2005) provide a simple analysis of this system in the context of rifted margin salt tectonics where thicker proximal clastic sediments overly a viscous salt layer. The sediment load can result in either pressure-driven Poiseuille channel flow in the viscous salt, or failure and gravitational spreading of the overburden and salt layer as a Couette channel flow, or a combination of the these two flows (Fig. 4.14). In the Couette and combined cases the flows are accompanied by up-dip (proximal) normal faulting and extension of the overburden and down-dip (distal) thrust faulting and shortening of the overburden. When there is only Poiseuille flow faulting will may occur, but it will not result in significant extension or shortening of the overburden.

The analysis of this system can be applied at different scales and to different components of rifted margins. *Gemmer et al.* (2004, 2005) provide non-dimensional results and applied them to continental margin salt tectonics, where salt is the viscous substrate. In our case the same explanation applies at a conceptual level at the crustal scale where the mid and lower crust is the viscous substrate. There is no need to consider gravity gliding as opposed to gravity spreading because the viscous lower crust dips landward (Figs 4.5 and 6). Our problem is nevertheless made more complicated by the simultaneous syn-rift tectonic extension. It is, however, clear that the enhanced extension is driven by the sediment load and is therefore a gravity-driven component of the flow regime.

Studies of natural examples of overly deep rift basins have tended to attribute the deepening to pressure-driven Poiseuille lower crustal channel flow (c.f. references above). It is clear that our model results demonstrate the alternative, failure of the crust and ensuing Couette flow. All of the observed model characteristics (1-4 listed above) are consistent with this style of flow. In particular, the theory explains why it is triggered by sediment loading and requires a sufficiently low viscosity basal shear zone that the gravity-driven Couette flow leads to rapid finite extension of the proximal basins .

An associated question is whether equivalent crustal-scale gravitational flows develop on rifted margins during the post-rift phase when tectonic extension has ceased. The primary difference is that during syn-rift extension the frictional-plastic upper crust will be on yield or close to it owing to the tectonic rifting. This means that only minor stress increments from sediment loading can cause failure and the onset of the gravity-driven flow. In contrast, much larger sediment-loading stress increments are probably needed during the post-rift to initiate the feedback loop because the crust will no longer be close to yielding. In addition, the basal shear zone must remain viscously weak, even as the crust cools, in order that the gravitational flow will operate efficiently. We have not investigated the post-rift sediment-loading feedback for the models presented here.

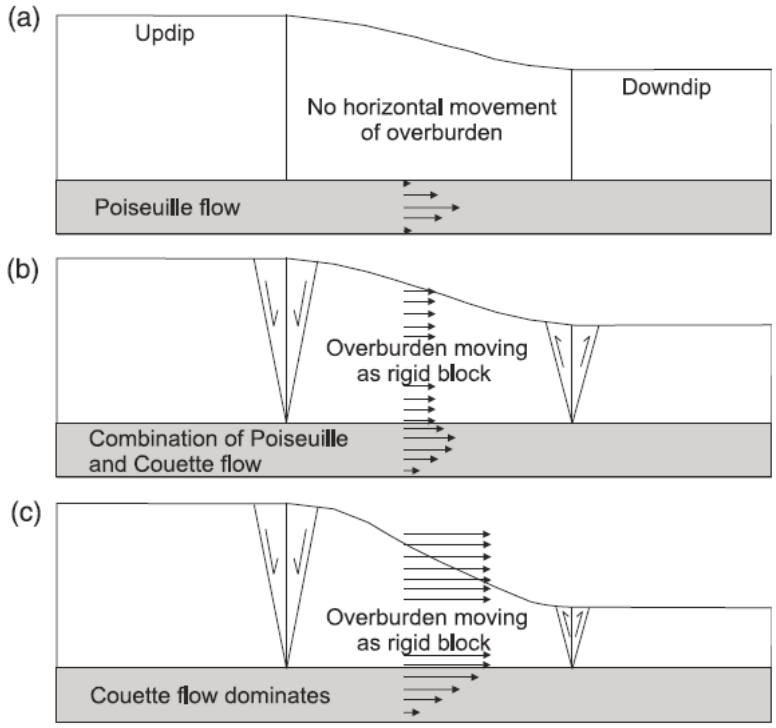

Fig. 1. Deformation styles in systems where a frictional-plastic overburden (white) of varying thickness overlies a viscous substratum (grey). (a) Stable overburden. A pressure-driven Poiseuille flow in the viscous channel dominates deformation. (b) Unstable overburden. The Couette flow-induced overburden velocities are smaller than the Poiseuille flow velocities in the viscous channel. (c) Unstable overburden. Couette flow dominates the deformation pattern.

Figure 4.14: Deformation of overburden in response to differential pressure applied to viscous substrate. From *Gemmer et al*. (2005).

Considering our natural example, the northeastern part of the Nova Scotia margin, illustrated by SMART I (Funk et al., 2004, and Figure 4.12), displays abrupt changes in crustal thickness at the proximal to mid margin, and a relatively narrow taper of the continental crust towards the distal margin, that is consistent with, but more muted than, our models of substantial sedimentation focused at proximal basins, and the associated localizing of crustal deformation at the proximal margin (Fig. 4.13b). Substantial sedimentation occurred at this part of the margin, during the syn-rift and early post-rift periods. In contrast, the central margin, exemplified by SMART II (Wu et al., 2006, and Figure 4.12), has shallow syn-rift proximal basins and a more gradual taper of crust thickness across the margin with smooth distal thinning. This style of deformation is consistent with our models with less sedimentation at the proximal margin, and a more distributed thinning of the continental crust (Fig. 4.13d). If our interpretation is correct, the lithosphere beneath the central and northeastern Nova Scotian margins may have had very similar intrinsic properties, and the difference in the present rift margin geometries may be attributable to the degree of proximal sediment loading.

4.8.2 Mid and Distal Margin Deformation

In addition to the coupling of sediment loading and crustal extension in the proximal margins, the weak crustal model shows interesting interactions between the sedimentation and tectonics for the mid and distal margins (M and D in the figures). Models with aggrading clastic sediments (Model 1-AF, Fig. 4.3a-d) and late salt deposited on aggraded sediments (Model 3-LS, Fig. 4.9L and 4.9R) show the

development of what are termed syn-rift 'sag' basins in the mid-margin. A particular characteristic of these sag basins is that the sediments are deformed in the early syn-rift but almost no deforrmation is added in the late syn-rift, as can be seen from the lack of deformation of these sediment layers. This characteristic is also observed on the mid reaches of wide, and likely weak, central South Atlantic margins, which also appear to show little late syn-rift fault-controlled deformation, suggesting that the underlying upper crust experienced minimal extension late in the syn-rift and after rifting (*Karner and Driscoll*, 1999a; *Karner et al.* 2003. *Karner and Driscoll* (1999b) and Karner *et al.* (2003) attribute this style to depth-dependent extension in which only lower crustal extension persists into the late syn-rift. *Huismans and Beaumont* (2014) explain this style of evolution for Type II wide margins by a combination of depth-dependent extension and, more importantly, diachronous extension that becomes focussed in the distal crust as rifting progresses. This behavior is also seen in Model 1-AF (Fig. 4.3a-d) and Model 3-LS (Figs 4.9R and, particularly 4.9L); parts of the distal salt are strongly disrupted by listric crustal faults but the late syn-rift mid-margin sediment and salt remain relatively undeformed. Our previous modelling involving intermediate strength crust (*Allen and Beaumont*, 2015) produced sag basins at the mid to distal margin in which sediments were faulted throughout their lateral extent, but only faults in the contemporaneous most distal margin were active at any given time. That is, the faulting is coupled to the extension such that crust located in the distal rift experiences faulting but as this part of the crust is advected away from the rift center the faulting abates. In combination, our two studies show in more detail the behavior described by *Huismans and Beaumont* (2014) and confirm the style of syn-rift sedimentary basins for Type II models they

inferred. Our model results also indicate that late syn-rift sag basin sediments in the mid margin can remain undeformed for both weak and intermediate strength crusts. Sediment at the mid to distal margin offshore northeastern Nova Scotia (Figure 4.12b) could be interpreted as a syn-rift sag basin. Applying more distributed/aggrading synrift sediments to the NE margin, as was done in some of our other models (e.g. Figs 4.3, 7, 8), would likely shift the location of sag basin deposits landward, towards the mid margin.

Not yet explained is why the mid margin sag basins in models with aggrading sedimentation remain undeformed while Model 1, which is just water loaded, shows distributed crustal deformation until final breakup (Fig. 4.2). The answer lies in the enhanced listric normal faulting beneath distal aggrading sediments seen in Models 1-AF and 1-AP (Fig. 4.3) versus Model 1 (Fig. 4.2). This focused distal faulting can be understood by considering the aggrading sediment to play the role of 'replacement' crust. Sediment deposition effectively restores the composite crust to a thickness closer to its original thickness (Fig. 4.3a-d). Given that the clastic sediment has similar frictional-plastic properties to that of the upper crust, this 'restoration' promotes a return to the initial style of crustal faulting which is focused on conjugate fault sets in the center of the rift. Addition of more aggrading sediment into the basins formed by this faulting causes the same process to persist, with more crustal-scale listric faulting of the current rift center at the distal margin (Fig 4.3a-d).

This second feedback effect of sedimentation on the crustal extension style explains the segmentation of the margin into a distal region, with focused faulting, versus a mid region where faulting has abated. This can be clearly seen from the reduced mid margin

strain rates on the crustal shears of Model 1-AF (Fig. 4.3b,d) by comparison with those of Model 1 (Fig. 4.2d), and the corresponding increase in distal strain rates in Model 1-AF (Fig. 4.3b, d). The same focused distal listric faulting leading to rotated fault blocks may also develop in the youngest hot oceanic crust if sediment is deposited on it as it develops. If this interpretation holds for natural margins, these results indicate this second feedback may be observed on wide weak rifted margins with significant, widely distributed syn-rift sedimentation. This inference appears to be consistent with observations from the wide central South Atlantic margins. This finding appears to differ from the conclusions of *Corti et al.* (2010), who showed with analogue experiments that increased sedimentation favored prolonged rifting for narrow margins thinning via brittle deformation, by prolonging movement along bounding faults. In our weak crust experiments the addition of aggrading sediments does not increase the overall duration of rifting, but does favor activity on faults at the distal margin.

4.8.3 Syn-rift Salt Tectonics

The distinctions between early and late syn-rift salt deposition for the weak crust model presented here are similar to those observed for the intermediate crust studied previously (*Allen and Beaumont*, 2015). One notable difference between syn-rift salt deposition over our weak versus intermediate strength crusts is the initial distribution of salt; the weak crust model produces a continuous salt body spanning the margin pair, for both early and late syn-rift salt deposition, whereas the intermediate strength crust model largely localized early syn-rift salt in the proximal basins. It should be noted, however, that this distinction is related to our choice of the mechanism for salt deposition. It would

certainly be possible for syn-rift salt to be focused in the proximal basins at a wide margin produced by extending weak crust if only the proximal basins experienced desiccation. *Rowan* (2015) suggests that isolated salt bodies, contained in distinct basins may be more common in the early syn-rift (syn-stretching) phase. In our models of the Nova Scotia margin, we have varied the location of salt deposition, and the amount of pre-salt sediment deposited at the proximal margin, to demonstrate a range of behavior that can be produced with this weak crust base model and mid syn-rift salt deposition. In our model NSNE we show an example of mid syn-rift salt isolated in proximal basins; this may occur if, for example, the barrier between the proximal basin and the sea has a low hydraulic conductivity, allowing evaporation to outpace refilling of the proximal basin. In our model NSC, mid syn-rift salt is deposited across the margin pair; this model is representative of the situation where all basins across the margin are relatively well connected such that evaporation proceeds at a similar pace for all seawater across the margin pair.

Some features of the Nova Scotia margin may be better modeled by a stronger crust than the one presented here. One example is lateral movement of salt out of proximal basins and towards the mid margin. This behavior of salt was captured in the intermediate crust models published previously (*Allen and Beaumont*, 2015), and is not well developed in the weak crust models here, primarily because loading by prograding sediments produces localized extension at the proximal margin, that inhibits advancement of the post-salt prograding wedge across the proximal margin.

Relatively subdued salt structures develop as rifting continues in our models, for both the early and late syn-rift salt models. This is largely due to localization of deformation at the proximal margin, discussed above, limiting advancement of the post-salt prograding sediment. This style of salt tectonics is also reflected in the development of our Nova Scotia models. In model NSC, compared with the central Nova Scotia margin, some salt remains in proximal basins, under an advancing prograding wedge (Figure 4.12, f). In our model compared with the northeastern Nova Scotia margin, interaction of prograding sediment and salt in the proximal basins is less notable than for our model NSC, as ongoing sedimentation is trapped in a more proximal area of the margin, in response to localization of extension in this area. Salt is observed in the proximal basins of at both the central and northeastern Nova Scotia margin (Figure 4.12 b, e). Deformation of salt at the mid to distal margin is more complex than is captured in our models, partly due to our focus on the syn-rift period (subsequent, post rift sedimentation would contributed to salt deformation), but also impacted by the tendency of our models to localize deformation at the proximal margin. A prograding wedge may advance more effectively towards the mid margin in the post-rift period, if the feedback between sediment load and lower crustal flow operates less efficiently at this point. The feedback between sediment load at the proximal margin and lower crustal flow does not develop for models with intermediate strength continental crust. In our previous work (*Allen and Beaumont*, 2015), the post-salt prograding wedge advances beyond the proximal margin, and interacts more substantially with syn-rift salt at the mid margin. For a prograding wedge style of post-salt sedimentation, the complexity of salt tectonic structures that develop may depend on the strength of the underlying crust, with very weak crust producing

thinned salt and salt trapped in proximal basins, and slightly stronger crust producing more diapirs and salt tongues.

While this paper focuses on syn-rift sedimentation, it is important to note that the post-rift sedimentation is notably different between the central and northeastern parts of the margin, with the northeastern margin accumulating significantly more sediment than the central margin. A substantial component of the difference in total sedimentation between the central and northeastern margins can be attributed to the post-rift period. While this paper, including models NSNE and NSC, focuses on syn-rift sedimentation, different amounts of early post-rift sedimentation would produce similar differences in deformation of the weak crust used throughout this paper.

4.9 Conclusions

This paper considers interactions between syn-rift sedimentation, margin geometry, and syn-rift salt tectonics. Finite element numerical modeling has been used to study these interactions, for a weak crust, developing a wide margin pair. Syn-rift clastic sedimentation, both distributed across the margin pair and localized at the proximal margin, has been shown to impact the style of the resultant margin. Early and late syn-rift deposition of salt yield subtle salt tectonic features, compared to previous work on margins developing from stronger crusts. Our results are discussed in the context of the Nova Scotia margin, where the northeastern and central parts of the margin are

contrasted. The following general conclusions can be drawn from the study of syn-rift sedimentation and salt tectonics for this weak crust.

1. The amount and nature of syn-rift sedimentation, distributed versus localized, impacts the style of rifting and deformation of the crust. More substantial syn-rift sedimentation has a more significant impact of crust deformation. Distributed, aggrading sedimentation produces more abrupt changes in crust thickness. Localized, prograding sedimentation can initiate a feedback between lower crustal flow and sediment accumulation at the proximal margin basins. Prograding sedimentation can also shift the locus of rifting, localizing stretching of the crust under the proximal basins.
2. The feedback between sedimentation and lower crustal flow is most efficient for a) high sediment volume and b) sediment deposition in the early to mid syn-rift period. This impacts the interaction between syn-rift salt and post-salt sedimentation; late syn-rift salt experiences more interaction with post-salt progradation than does early syn-rift salt. Prograding sediments in the early syn-rift period are largely trapped in basins at the proximal margin.
3. As seen in our previous work, the timing of salt deposition relative to rifting impacts the final distribution and deformation of salt. Compared to our previous work, salt tectonic structures developed in this analysis are subtle, owing mostly to the tendency of post-salt prograding sediment to be trapped in the proximal basins, as extension of the crust and generation of accommodation space is localized in this area.

4. Differences between the northeastern and central parts of the Nova Scotia margin, including the degree of thinning of the crust at the proximal margin, and the linked inferred amount of extension of the distal margin, as well as salt distribution, can be produced using models that differ mostly in the degree of post-salt, syn-rift sedimentation. This analysis does not consider differences in post-rift sedimentation, though a similar albeit weaker feedback between lower crustal flow and sediment loading may persist after the crust ruptures, particularly on the NE NS margin, where postrift sedimentation rates were still very high. Differences in crust strength and heterogeneity of the crust across the margin were not considered here, and would impact the structural evolution of the margin.

4.10 References

Albertz, M., C. Beaumont, J.W. Shimeld, S.J. Ings, and S. Gradmann (2010), An investigation of salt tectonic structural styles in the Scotian Basin, offshore Atlantic Canada: 1: Comparison of observations with geometrically simple numerical models, *Tectonics*, *29*, TC4017, doi:10.1029/2009TC002539.

Albertz, M., and C. Beaumont (2010), An investigation of salt tectonic structural styles in the Scotian Basin, offshore Atlantic Canada: 2. Comparison of observations with geometrically complex numerical models, Tectonics, 29, TC4018, 2010, doi:10.1029/2009TC002540.

Allen, J. and Beaumont, C. (2015). Continental Margin Syn-Rift Salt Tectonics at Intermediate Width Margins. Basin Research. 10.1111/bre.12123

Baikpour, S., G. Zulauf, A. Sebti, H. Kheirolah, and C. Dieti (2010), Analogue and geophysical modelling of the Garmsar Salt Nappe, Iran: constraints on the evolution of the Alborz Mountains, *Geophysical Journal International*, *182*(2), 599-612, doi: 10.1111/j.1365-246X.2010.04656.8.

Beaumont, C., Jamieson, R.A., Butler, J.P. and Warren, C.J. (2009) Crustal structure: A key constraint on the mechanism of ultra-high-pressure rock exhumation. *Earth and Planetary Science Letters*, 287(1-2), 116-129, doi: 10.1016/j.epsl.2009.08.001.

Bialas, R.W. and Buck, W.R. (2009) How sediment promotes narrow rifting: Application to the Gulf of California. *Tectonics*, 28, TC4014, doi:10.1029/2008TC002394 .

Brun, J.P. (1998) Narrow rifts versus wide rifts: inferences for the mechanics of rifting from laboratory experiments, *Philosophical Transactions of the Royal Society of London*, 357, 695-712, doi: 10.1098/rsta.1999.0349.

Brun, J.P., and T.P.O. Mauduit (2009), Salt rollers: Structure and kinematics from analogue modelling, *Marine and Petroleum Geology*, *26*(2), 249-258, doi: 10.1016/j.marpetgeo.2008.02.002.

Bonini, M. (2003), Detachment folding, fold amplification, and diapirism in thrust wedge experiments, *Tectonics*, *22*(6), 1065-1076, doi: 0.1029/2004JB003552.

Burchardt, S., Koyi, H. and Schmeling, H. (2011) Strain pattern within and around denser blocks sinking within Newtonian salt structures. *Journal of Structural Geology*, 33(2), 145-153, doi: 10.1016/j.jsg.2010.11.007.

Burov, E., and Cloetingh, S. (1997). Erosion and rift dynamics: new thermomechanical aspects of post-rift evolution of extensional basins. *Earth and Planetary Science Letters*, 150: 7-26.

Butler, J.P., Beaumont, C. and Jamiesson, R.A. (2014) The Alps 2: Controls on crustal subduction and (ultra) high-pressure rock exhumation in Alpine-type orogens, *Journal of Geophysical Research*.

Carter, N.L., Handin, J., Russel, J.E. and Horseman, S.T. (1993) Rheology of rock salt. *Journal of Structural Geology*, 15, 1257-1271.

Chemia, Z., Koyi, H. and Schmeling, H. (2008) Numerical modeling of rise and fall of a dense layer in salt diapirs. *Geophysical Journal International*, 172(2), 798-816, doi: 10.1111/j.1365-246X.2007.03661.x.

Chen, A., Jin, C., Lou, Z. Chen, H., Xu, S., Huang, K., and Hu, S. (2013). Salt tectonics and Basin Evolution in the Gabon Coastal Basin, West Africa. *Journal of Earth Science*, 24(6): 903-817. Doi: 10.1007/s12583-013-0383-5.

Clift, P.D., Brune, S., and Quinteros, J. (2015). Climate changes control offshore crustal structure at South China Sea continental margin. *Earth and Planetary Science Letters*. 420 : 66-72. 10.1016/j.epsl.2015.03.032.

Corti, G., Ranalli, G., Muluget, G., Agostini, A., Sani, F. and Zugu, A. (2010) Control of the rheological structure of the lithosphere on the inward migration of tectonics activity during continental rifting. *Tectonophysics*, *490*, 165-172, doi: 10.1016/j.tecto.2010.05.004.

Corti, G., Ranalli, G., Agostini, A. and Sokoutis, D. (2013) Inward migration of faulting during continental rifting: Effects of pre-existing lithospheric structure and extension rate. *Tectonophysics*. 594, 137-148, doi: 10.1016/j.tecto.2013.03.028.

Costa, E., and B.C. Vendeville (2002), Experimental insights on the geometry and kinematics of fold-and-thrust belts above weak, viscous evaporitic decollement, *Journal of Structural Geology*, *24*(11), 1729-1739, doi: 10.1016/S0191-8141(01)00169-9.

Crosby, A.G., White, N.J., Edwards, G.R.H., Thompson, M., Corfield, R., and Mackay, L. (2011). Evolution of deep-water rifted margins: Testing depth-dependent extensional models. *Tectonics*, 30: TC1004. Doi: 10.1029/2010TC002687.

Davison, I., Anderson, L., and Nuttall, P. (2012). Salt deposition, loading and gravity drainage in the Campos and Santos salt basins. Geological Society, London, Special Publications, 363: 159-174. Doi: 10.1144/SP363.8.

Del Ventisette, C., Montanari, D., Sani, F. and BonniO, M. (2004) Basin inversion and fault reactivation in laboratory experiments. *Journal of Structural Geology*, 28(11), 2067-2083, doi: 10.1016/j.jsg.2006.07.012.

Del Ventisette, C., D. Montanari, M. Bonini, and F. Sani (2005), Positive fault inversion triggering 'intrusive diapirism': an analogue modeling perspective, *Terra Nova*, *17*, 478-485, doi: 0.1111/j.1365-3121.2005.00637.x.

Fullsack, P. (1995), An arbitrary Lagrangian-Eulerian formulation for creeping flows and its application in tectonic models, *Geophysical Journal International*, *120*(1), 1-23.

Funck, T., Jackson, H.R., Louden, K.E., Dehler, S.A., and Wu., Y. (2004). Crustal structure of the northern Nova Scotia rifted continental margin (eastern Canada). Journal of Geophysical Research. 109: B09102, doi:10.1029/2004JB003008.

Ge, H.X., M.P.A. Jackson, and B.C. Vendeville (1997), Kinematics and dynamics of salt tectonics driven by progradation, *American Association of Petroleum Geologists Bulletin*, *81*(3), 398-423.

Gleason, G.C. and Tullis, J. (1995) A flow law for dislocation creep of quartz aggregates determined with the molten-salt cell. *Tectonophysics*, 247(1-4), 1-23, doi: 10.1016/0040-1951(95)00011-B.

Goteti, R., Ings, S.J. and Beaumont, C. (2012) Development of salt minibasins initiated by sedimentary topographic relief. *Earth and Planetary Science Letters*, 339, 103-116, doi: 10.1016/j.epsl.2012.04.045.

Gueydan, F., Morency, C. and Brun, J.P. (2008) Continental rifting as a function of lithosphere mantl strength. *Tectonophysic*s, 460, 83-93. doi:10.1016/j.tecto.2008.08.012.

Hudec, M.R., M.P.A Jackson, and D.D. Schultz-Ela (2009), The paradox of minibasin subsidence into salt: Clues to the evolution of crustal basins, *Geological Society of America Bulletin*, *121*(1-2), 201-221.

Huismans, R. and Beaumont, C. (2011) Depth-dependent extension, two-stage breakup and cratonic underplating at rifted margins. *Nature*, 473(7345), 74-U85, doi: 10.1038/nature09988.

Huisemans, R. and Beaumont, C. (2014) Rifted continental margins: The case for depth-dependent extension. *Earth and Planetary Science Letters,* 407, 148-162, doi:10.1016/j.eps1.2014.09.032.

Jansa, L. F., and Wade, J.A. (1975). Paleogeography and sedimentation in the Mesozoic and Cenozoic, southeastern Canada. (1975): 79-102.

Karato, S. and Wu, P. (1993) Rheology of the upper mantle – a synthesis. *Science*, 260(5109), 771-778, doi: 10.1126/science.260.5109.771.

Keen, C. E., and Potter, D. P. (1995). The transition from a volcanic to a nonvolcanic rifted margin off eastern Canada. *Tectonics* 14.2: 359-371.
Klitgord and Schouten, 1986;

Labails, C. et al. (2010). An alternative early opening scenario for the Central Atlantic Ocean. *Earth and Planetary Science Letters* 297.3 (2010): 355-368.

Lavier, L.L. and Manatschal, G. (2006) A mechanism to thin the continental lithosphere at magma-poor margins. *Nature,* 440(7082,: 324-328, doi: 10.1038/nature04608.

Lister, G.S., Etheridge, M.A. and Symonds, P.A. (1986) Detachment faulting and the evolution of passive continental margins. *Geology*, 14(3), 246-250, doi: 10.1130/0091-7613(1986)14.

Lister, G.S., Etherdige, M.A. and Symonds, P.A., (1991) Detachment models for the formation of passive continental margins. *Tectonics*, 10(5), 1038-1064, doi: 10.1029/90TC01007.

Longoni, M., Malossi, A.C.I. and Villa, A. (2010) A robust and efficient conservative technique for simulating three-dimensional sedimentary basin dynamics. *Computers & Fluids*, 39(10), 1964-1976, doi: 10.1016/j.compfluid.2010.06.028.

Louden, K., Wu, Y., and Tari, G. (2012). Systematic variations in basement morphology and rifting geometry along the Nova Scotia and Morocco conjugate margins. *Geological Society, London, Special Publications*. 369: 267-287. Doi: 10.1144/SP369.9.

Mackwell, S., Zimmerman, M. and Kohlstedt, D. (1998) High-temperature deformation of dry diabase with application to tectonics on Venus. *Journal of Geophysical. Research-Solid Earth*, 103, 975–984.

McKenzie, D. (1978) Some remarks on the development of sedimentary basins. *Earth and Planetary Science Letters*, 40, 25-32, doi: 10.1016/0012-821X(78)90071-7.

Morley, C.K., and Westaway, R. 2006. Subsidence in the super-deep Pattani and Malay basins of Southeast Asia: a coupled model incorporating lower-crustal flow in response to post-rift sediment loading. Basin Research. 18, 51-84.

Nagel, T.J. and Buck, W.R. (2004) Symmetric alternative to asymmetric rifting models. *Geology*. 32(11), 937-940, doi: 10.1130/G20785.1.

Olsen, P.E. (1997). Stratigraphic record of the early Mesozoid breakup of Pangea in the Laurasia-Gondwana rift system. *Annual Review Earth and Planetary Science*, 25: 337-401.

Rowan, M.G. (2014) Passive-margin salt basins: hyperextension, evaporite deposition, and salt tectonics. *Basin Research*, *2*6, 154-182, doi: 10.1111/bre.12043.

Sahabi, M., Aslanian, D., and Olivet, J.L. (2004). A new starting point for the history of the central Atlantic. *Comptes Rendus Geoscience,* 336.12: 1041-1052.

Schubert, G., Turcotte, D. and Olson, P. (2001) *Mantle convection in the Earth and planets,* Cambridge University Press.

Sibuet, J.C., Rouzo, S., and Srivastava, S. (2012). Plate tectonic reconstructions and paleogeographic maps of the central and north Atlantic oceans. *Canadian Journal of Earth Sciences*, 49: 1395-1415.

Sun, Z., Stock, J., Jian, Z., McIntosh, K., Alvarez-Zarikian, C.A., and Klaus, A. (2016). *Expedition 367/368 Scientific Prospectus: South China Sea Rifted Margin.* International Ocean Discovery Program. http://dx.doi.org/10.14379/iodp.sp.367368.2016.

Tirel, C., Brun, J.P. and Sokoutis, D. (2006) Extension of thickened and hot lithospheres: Inferences from laboratory modeling. *Tectonics,* 25, TC1005, doi:10.1029/2005TC001804.

Unternehr, P., Peron-Pinvidic, G., Manatschal, G., and Suttra, E. (2010). Hyper-extended crust in the South Atlantic: in search of a model. *Petroleum Geoscience* 16.3: 207-215. Doi: 10.1144/1354-079309-904.

van Avendonk, H.J.A., Lavier, L.L., Shillington, D.J. and Manatschal, G. (2009) Extension of continental crust at the margin of the eastern Grand Banks, Newfoundland. *Tectonophysics*, 468, 131-148, doi:10.1016/j.tecto.2008.05.030.

van Keken, P.E., C.J. Spiers, A.P., van den Berg, and E.J. Muyzert, E.J. (1993), The effective viscosityof rocksalt: implementation of steady-state creep laws in numerical models of salt diapirism. *Tectonophysics, 225*, 457-476.

von Nicolai, C., Scheck-Wenderoth, M., Warsitzka, M., Schodt, N., and Andersen, J. (2013). The deep structure of the South Atlantic Kwanza Basin—Insights from 3D structural and gravimetric modelling. *Tectonophysics* 604: 139-152. Doi: 10.1016/j.tecto.2013.06.016.

Wu, Y., Louden, K.E., Funck, T., Jackson, H.R., and Dehler, S.A. (2006). Crustal structure of the central Nova Scotia margin off Eastern Canada. *Geophysical Journal International*. 166: 878-906.

Wade, J. A., and MacLean, B.C. (1990). The geology of the southeastern margin of Canada. *Geology of the continental margin of eastern Canada: Geological Survey of Canada, Geology of Canada* 2: 167-238.

Wade, J.A., MacLean, B.C., and Williams, G.L. (1995). Mesozoic and Cenozoic stratigraphy, eastern Scotian Shelf: new interpretations. *Canadian Journal of Earth Sciences*, 32: 1462-1473.

Warren, J.K. (2010) Evaporites through time: Tectonic, climatic and eustatic controls in marine and nonmarine deposits. *Earth-Science Reviews,* 98, 217–268, doi: 10.1016/j.earscirev.2009.11.004.

Wernicke, B. (1985) Low-angle normal faults in the basin and range province – nappe tectonics in an extending orogen. *Nature*, 291(5817), 645-648, doi: 10.1038/291645a0.

Wernicke, B. (1981) Uniform-sense normal simple shear of the continental lithosphere, *Canadian Journal of Earth Sciences*, 22(1), 108-125, doi: 10.1139/e85-009.

Westaway, R., and Bridgland, D. 2007. Late Cenazoic uplift of southern Italy deduced from fluvial and marine sediments: Coupling between surface processes and lower-crustal flow. Quaternary International. 175. 86-124.

Weston, J.F., MacRae, R.A., Ascoli, P., Cooper, M.K.E., Fensome, R.A., Shaw, D., and Williams, G.L. (2012). A revised biostratigraphic and well-log sequence-stratigraphic framework for the Scotian Margin, offshore eastern Canada. *Canadian Journal of Earth Sciences*, 49: 1417-1462.

Chapter 5: Salt minibasin formation through uneven sedimentation: A fully 3D numerical modeling approach

Janice Allen, David Whipp, Christopher Beaumont

5.1 Preface

This chapter is based on an ongoing project to augment existing 3D numerical modeling software to suit the study of salt tectonics. A paper is planned based on this work, but will require further work beyond what is presented here; the results in this chapter are preliminary. Janice Allen contributed to writing additions to the software, with appreciable supervision from Dave Whipp and Chris Beaumont (Dave and Chris also contributed software development beyond Janice's efforts). Design of the models in this chapter was a coordinated effort among the co-authors. Janice ran the models in this chapter, wrote the text, and produced the figures. Dave Whipp and Chris Beaumont provided supervision and mentoring in all aspects of this work.

5.2 Abstract

Salt tectonics plays an important role in the evolution of many rifted margins, and has been studied extensively using data from natural examples and comparison with numerical and physical analogue modeling methods. While numerical modeling has captured many of the physical processes important to the study of salt tectonics, most numerical analyses have been limited to two dimensions. Salt tectonics is inherently three-dimensional, with considerable variation in the deformation of salt observed along strike at rifted margins. This chapter presents the methodology for and preliminary results of a fully 3D numerical modeling analysis of salt minibasin formation through uneven sedimentation (low amplitude regional mounding on kilometer and larger horizontal scales). This analysis builds on similar studies of 2D numerical models, by comparing fully 3D and 2D-equivalent versions of a given model geometry. The majority of this work uses a confined minibasin design, where the width of the minibasin is equal to the width of the model. This design approximates the case where adjacent minibasins form simultaneously, that is the boundaries of the model have mirror symmetry. A few unconfined models, where the model domain is larger than the minibasin forming, are also included. A realistic sedimentary frictional plastic overburden is used, incorporating simple methods of sediment compaction and its effect on density. Preliminary results show notable differences in the evolution of fully 3D models of minibasin formation, compared to similar models with a 2D-equivalent geometry. The models in this chapter illustrate the potential usefulness of this type of analysis, but are preliminary. Development of the 3D modeling software used in this

study is ongoing, and further work is needed to present a robust analysis of minibasin formation using the approach presented here. For example, compaction velocity is applied generally correctly, but in detail is not entirely consistent with expectations. The work included in this chapter highlights the progress made towards a realistic fully 3D numerical treatment of salt tectonics, and emphasizes the value of this approach.

5.3 Introduction

Salt, and more generally evaporites, contribute to the structural evolution of many developing and established rifted continental margins and other sedimentary basins, including the Red Sea, the Mediterranean Sea, and the margins of the south Atlantic Ocean (e.g. Hudec and Jackson, 2007). Understanding the controls on the deposition and deformation of salt is relevant to studying the evolution of sedimentary basins and rifted margins, in particular, and has applications to petroleum systems and evaporite mineral resources. Previous numerical modeling studies of salt tectonics at rifted margins have largely been restricted to two-dimensional analyses. This work uses a fully three-dimensional numerical modeling approach to illustrate the differences in evolution between fully 3D and 2D-equivalent versions of simple salt tectonic systems.

The deposition and deformation of salt (salt tectonics) has been studied using direct interpretation of data from natural systems, particularly seismic data and field mapping. In addition, conceptual (e.g. Rowan, 2014) and analytical approaches (e.g. Gemmer et al., 2005), as well as numerical (e.g. Chemia et al., 2008; Albertz et al., 2010; Albertz and

Beaumont, 2010; Longoni et al., 2010; Burchardt, et al., 2011; Goteti et al., 2012) and physical analogue (e.g., Costa and Vendeville, 2002; Del Vintisette et al., 2005; Bonini, 2003; Ge et al., 1997; Baikpour et al., 2010; McClay et al., 2003) models have been employed to gain more insight into the mechanics and physics of salt tectonics. Numerical modeling has been applied to problems such as the impact of basement geometry and post-salt sedimentation on the development of 2D salt structures (Albertz et al., 2010; Albertz and Beaumont, 2010), the impact of layered halite on salt deformation (Albertz and Ings, 2012), the influence of underlying crustal tectonics (e.g. Fort and Brun, 2012), initiation of minibasins through uneven sedimentation (e.g. Toniolo et al., 2006, Goteti et al., 2012), and the role of timing of salt deposition relative to rifting, on the distribution and deformation of salt at rifted continental margins (Allen and Beaumont, 2015). Previous numerical modeling efforts have, however, largely been restricted to two dimensions. Physical analogue models have also been used to study the deformation of salt under a variety of loading conditions (e.g., Costa and Vendeville, 2002; Del Ventisette et al., 2005, 2006; Bonini, 2003; Ge et al., 1997; Baikpour et al., 2010; Brun and Mauduit, 2009) such as the evolution of diapirs in response to uneven sediment loading. Physical analogue models have the advantage of simulating the fully three-dimensional evolution of the salt tectonic system, but it is often difficult to find appropriately scaled materials to represent salt and clastic sediments (e.g. Allen and Beaumont, 2012, Brun and Fort, 2011; Warsitzka et al., 2011).

Few previous studies have used 3D numerical modeling to study salt tectonics, and these analyses generally included a simplified treatment of sedimentary overburden. Ismael-

Zadeh et al., (2004), approximating sedimentary overburden as a viscous material, studied the formation of diapirs and salt walls, arising from an initially flat interface between salt and overlying sediment. Koupriantchik et al. (2005) used a 3D finite difference model to study the development of an individual diapir, with an emphasis on the stress field produced, and the impact on the mechanical properties of the surrounding rock. In some cases, preliminary studies of salt tectonics using a 3D numerical modeling approach have included a more broad description of new developments in numerical modeling, highlighting the need for advancement in modeling software, to accurately study salt tectonics (e.g. Longoni et al., 2011; Longoni et al., 2010; Massimi et al., 2007). Forward and reverse modeling of 3D viscous Rayleigh-Taylor instabilities has been investigated by Kaus and Podladchikov (2001), who found that the resultant structures tended to be linear or three-dimensional, depending on the amplitude of the initial perturbation. Fernandez and Kaus (2014) used 3D numerical modeling to show that pre-existing salt diapirs can localize folding in salt tectonic systems. One facet of the study of salt tectonics generally not captured by previous 3D numerical modeling studies, is a realistic treatment of sedimentary overburden.

This study builds on the work of Goteti et al. (2012), who demonstrated using 2D numerical models that uneven sedimentation can drive minibasin formation. Following the description of Hudec et al. (2009) of mounding (accumulation of an uneven, lobate sediment mass) as a means of minibasin formation, Goteti et al. (2012) made a quantitative study of the ranges and wavelengths of sinusoidal perturbations of the upper sediment surface that would produce successful minibasin. As described in Goteti et al.,

minibasin formation through uneven sedimentation (mounding) occurs in two phases. In Phase 1, the sediment lens is thin and floats in isostatic balance on top of the salt. During Phase 1, a convex up surface of the minibasin must be maintained to continue minibasin development. In Phase 2, sufficient sediment has accumulated to drive ongoing sediment sinking into the salt without a convex up sediment surface. Phase 2 is initiated when the average density of the sediment at the centre of the lens is greater than the salt density. As noted by Goteti et al. (2012), successful minibasin formation by mounding requires that that an uneven, convex up sediment surface geometry be maintained throughout Phase 1. Once the average sediment density exceeds salt density, the sediment surface may continue to be convex up, or may assume a flat geometry, and minibasin development (sediment sinking into salt) will continue. Goteti et al. (2012) also note that in a salt layer of infinite thickness, longer wavelength sediment mounds subside faster than those with shorter wavelengths. When a finite thickness salt layer in considered, the advantage of longer wavelengths is offset by viscous forces generated from interaction with the base of the salt layer, resulting in an optimal wavelength at which a sediment lens will sink most quickly into the underlying salt (Cathles, 1975). At the optimal wavelength, the duration of Phase 1 is minimized. Goteti et al. (2012) suggest that the optimal wavelength is roughly 3-12 times the salt layer thickness. Goteti et al. further explore the required duration of uneven sedimentation (persistence time) necessary to initiate Phase 2. In the experiments presented here, a concave up sediment surface is maintained throughout the model evolution. This work explores different wavelengths and ranges of a sinusoidal perturbation of the sediment surface.

This paper presents a fully 3D study of minibasin formation through uneven sedimentation, incorporating frictional plastic sediments with compacting density. An accurate, if simple, treatment of compacting sediment density with depth is critical for this study; average sediment density has a direct impact on the minibasin formation through mounding. A single, non-compacting density does not accurately capture the changing differential pressure resulting from uneven sediment accumulation. Strength of the overburden is also dependent on pore fluid pressure. These features allow for a more accurate modeling of salt tectonics developing in a submarine setting, and represent an advancement on previous work.

The models in this paper consider the development of salt diapirs, walls and minibasins, in response to uneven sedimentation. These models focus on deformation after salt deposition has ceased. The geometry of original salt bodies and the style of subsequent sedimentation has purposely been kept simple, with the main intent to demonstrate the capabilities of this version of the finite element software DOUAR for calculations necessary for modeling salt-tectonics.

5.4 Methods

5.4.1 Model Design

This work focuses on the development of minibasins through uneven sedimentation, in confined settings. Following Goteti et al. (2012) we drive minibasin formation through aggrading sedimentation with a perturbed upper surface, following a sinusoidal geometry (Figure 5.1). The aim of this work is to contrast the evolution of fully 3D models of confined minibasin development with 2D-equivalent models of the same design. In this way, the importance of capturing the 3D nature of salt deformation, even in this very simple system, can be demonstrated.

Also in the same manner as Goteti et al., we define confined minibasins as those where the wavelength of perturbation of the sediment surface is equal to the planform dimension of the model domain (Figure 5.1). These models can be thought of as one part of a larger system, where other minibasins would be forming beside the one shown in Figure 5.1. In other words, the confined minibasins models in this work (Model Sets 1 and 2) address the development of a single minibasin and associated partial diapirs with regard to adjacent confined minibasins undergoing identical development. The term 'confined' is used because all material is retained within the domain of the single minibasin and adjacent partial diapirs.

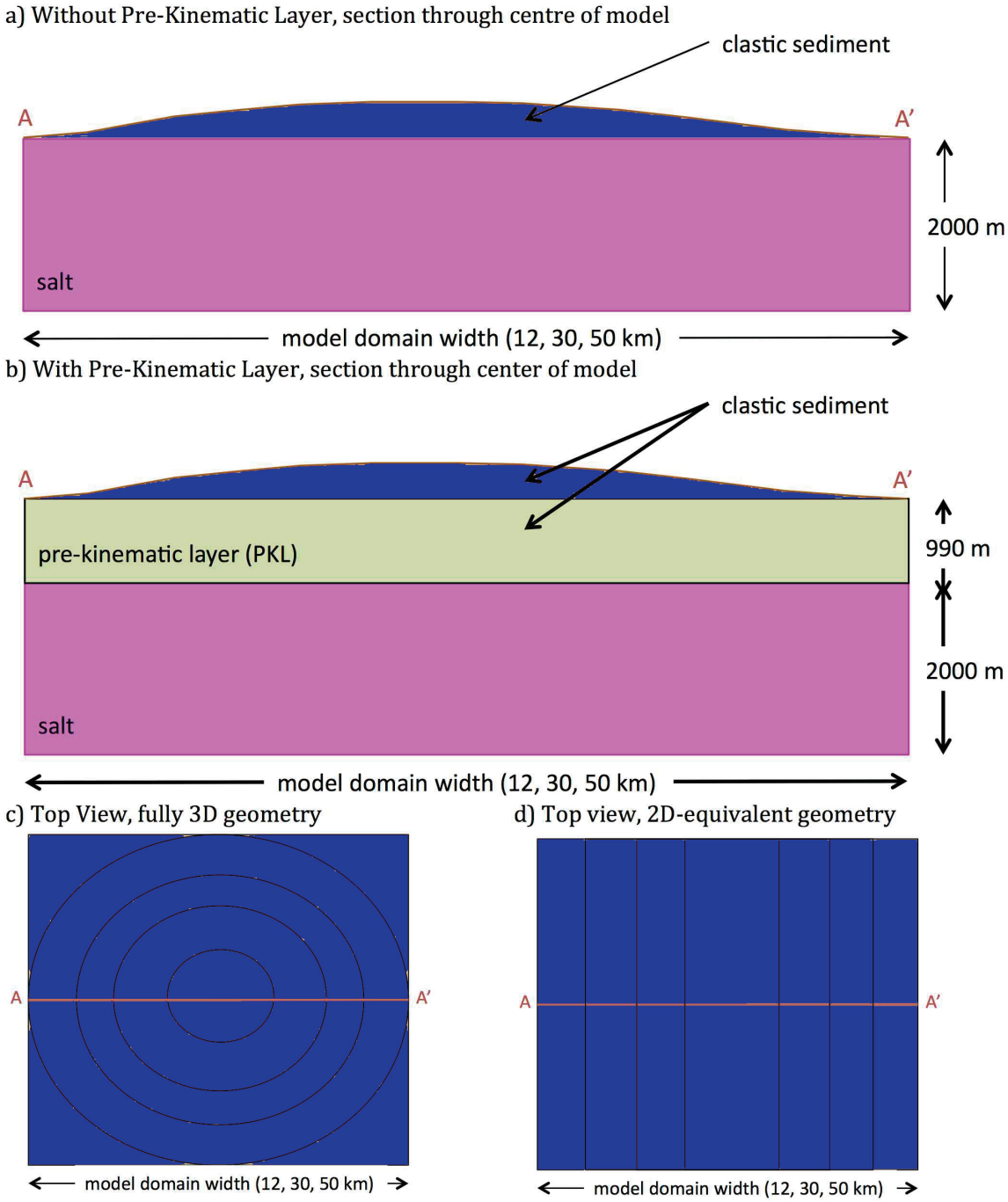

Figure 5.1: Model initial geometry. Panels a and b show sections through the centre of the model domain, for confined minibasin geometry without and with a Pre-Kinematic Layer. Panels c and d are top views of the model surface, for fully 3D and 2D-equivalent model geometries.

These confined minibasin models have an initially uniform horizontal 2 km thick salt layer, which in some cases is overlain by an initially uniform layer of compacted frictional-plastic clastic sediments (termed a pre-kinematic layer, or PKL, following Goteti et al. 2012, because this layer of sediment is deposited before uneven sedimentation begins). Deformation is initiated by uneven aggrading sedimentation, with the same top surface geometry (with sinusoidal perturbation) as the original model design. This sedimentation is maintained throughout the model evolution. That is, the rate of upward movement of the aggradation profile is the same everywhere across the model, and the sinusoidal geometry of the upper surface of the sediment is maintained. Wavelengths of perturbation, also equal to the dimensions of the base of the model, of 12, 30, and 50 km are considered. These values span the wavelengths considered by Goteti et al. (2012), chosen because they fall near the predicted optimal wavelength for rapid sinking into the underlying salt, and are considered to represent a range of naturally realistic scales for minibasin formation. For each wavelength, fully 3D and 2D-equivalent versions of the model were computed (Figure 5.1). In the fully 3D models, sinusoidal perturbation of the top surface was applied in both x and y directions, creating a radially symmetric geometry. The 2D-equivalent model geometry has a sinusoidal perturbation of the top surface only in the x direction; the geometry of the top surface does not vary in the y direction. Model Sets 1 and 2 consist of confined minibasin models without and with a Pre-Kinematic Layer. For all models in Model Sets 1 and 2, the range (crest to trough) of the sinusoidal perturbation of the sediment surface was 60 m. Model Set 3 considers different aggradation rates, and Model Set 4 explores a larger range of the

sinusoid. Model Set 5 consists of simple unconfined model geometries, where the model domain (60 km) is larger than the uneven sediment lens (30 km).

Model Set 2, with PKL, has the same confined geometry as Model Set 1, but has in the initial configuration a sediment layer of uniform thickness overlying the salt layer. Uneven sediment load is applied above this PKL in the same manner as for the models without a PKL, and the total sediment load acts on the salt. The PKL thickness was chosen so that the sediment density at the base of the PKL was equal to the salt density. The additional sediment load required to induce a Rayleigh-Taylor instability (when the average density of the sediment column is greater than the density of the underlying salt) is thereby reduced. In the models presented here, uneven sediment surface geometry is maintained throughout the model evolution. Future work will address the persistence time, the duration of uneven sedimentation, required to initiate minibasin formation.

In all models the sides of the model have a free slip boundary conditions (except for the corners, where only vertical motion is free slip), and the base of the model has a no slip boundary condition. Side boundary velocities normal to the model boundaries are set to 0; that is, no material may enter or exit the model through these faces. All models are non-dimensional and are computed on a unit cube DOUAR model domain (with or without rescaling (flattening) in the vertical, z direction – see supplementary material) . The non-dimensional scaling is explained in the Supplementary Material. However, to make the results more accessible we display and discuss the models in terms of natural physical sizes. The width of the model domain and horizontal resolution for Model Sets 1 and 2 varies; see Table 1.

Table 5.1: Model Design, Confined Minibasins Models

Model Sets 1,2: Confined minibasins with and without pre-kinematic layer			
Model Width	12 km	30 km	50 km
Time step length	30,000 a	30,000 a	30,000 a
Horizonal resolution	188 or 94 m	469 or 234 m	781 or 391 m
Vertical resolution	94 or 47 m	94 or 47 m	94 or 47 m
Sinusoid wavelength	12 km	30 km	50 km
Sinusoid amplitude	60 m	60 m	60 m
Aggradation rate	250 m/Ma	250 m/Ma	250 m/Ma
Salt layer thickness	2000 m	2000 m	2000 m
Model Set 2: Confined minibasins with pre-kinematic layer			
PKL thickness	990 m	990 m	990 m

Table 5.2: Material Properties

Material	***Clastic Sediments***	***Salt (halite)***
Density	Variable, compacts	2150 kg/m^3
Grain density	2500 kg/m^3	NA
Pore fluid density	1000 kg/m^3	NA
Surface porosity	0.4	NA
Compaction coefficient	7.0*10^{-4} m^{-1}	NA
Cohesion	0.1 MPa	NA
Viscosity	NA	10^{18} Pa s
Angle of internal friction	30 °	NA

5.4.2 Material Properties

Deformation of frictional-plastic clastic sediments is approximated using a Drucker Prager yield criterion (Equation 1) based on the compromise cone proposed by Schweiger (1994). To approximate submarine conditions more accurately, pore fluid pressure has been taken into account in the calculation of the Drucker-Prager failure criterion. For the current study, pore fluid pressure is calculated along a vertical hydrostatic gradient relative to the surface position, and is applied to the failure criterion of frictional plastic clastic sediment. The approximation of hydrostatic pressure is considered adequate for our model designs, where the surface bathymetry is subtle.

$$\sigma_y = \frac{6C\cos\phi}{\sqrt{3}\left(3+\sin\phi\right)} - \frac{6\sin\phi}{\sqrt{3}\left(3+\sin\phi\right)}\left(P - P_f\right), \qquad (1)$$

where C is cohesion, ϕ is the angle of internal friction, P is the dynamic pressure, and P_f is the pore fluid pressure. Salt does not experience hydrostatic pressure. Materials do not strain soften in these calculations.

Salt is modeled as a linear viscous material, with viscosity 10^{18} Pa s. This simplification, which strictly applies to halite deforming by pressure solution (Carter *et al*., 1993; van Keken *et al*., 1993), is a reasonable starting point for our first models of salt tectonics in 3D. More complicated salt rheologies, encompassing a range of evaporite behavior, will be considered in future work.

All materials are incompressible, except in the case of sediment compaction, noted above and discussed in the Supplementary Material. The models are purely mechanical; material properties are not temperature-dependent.

Frictional plastic sediment undergoes compaction, discussed in the following section, and in the Supplementary Material. Salt does not compact.

5.4.3 Numerical Methods

This work uses the 3D finite element numerical modeling software DOUAR (Braun et al, 2008; Thieulot et al, 2008), which solves thermomechanically coupled Stoke's flow to model the deformation of both viscous and frictional-plastic materials. The software and examples of the application of DOUAR are described elsewhere (Braun et al., 2008), including a description of the non-dimensional scaling used in DOUAR. In the work presented here, output is converted to dimensional units for display. For this work, we've made additions to the software, to facilitate the study of salt tectonics. One critical development, the ability to model compacted sediment density, is described briefly below. Details about the software modifications are available in the Supplementary Material.

In DOUAR, the model domain is defined within a unit cube (with lengths scaled to a non-dimensional fraction of this cube). Resolution of the elements within the cube is

established using an octree approach, in which the cube is divided into 2^n elements along each edge, where n is the level of resolution. The user may specify n, as well as an additional vertical scaling factor that allows for the definition of elements that are thinner (i.e. have finer resolution) in the vertical direction. Most of the models in this work use n = 6 (64 by 64 elements in the x and y directions), with a vertical flattening factor of between 0.5 and 0.1. The horizontal and vertical resolution of the elements is dependent on the length scale of the model design. For a 30 km confined minibasin model, with a model edge length of 30 km, a level 6 model with vertical scaling factor of 0.2 has elements with dimensions 470 x 470 x 74 m.

5.4.3.1 Sediment Compaction

Frictional-plastic sediments in DOUAR can now undergo kinematically calculated compaction, to more accurately represent the effect of volume and density changes during compaction and the development of differential loading due to uneven accumulation of sediment over salt. As noted above, including compaction is essential for our current study. Compacted density is calculated according to an Athy curve (Table 5.2), on the assumption that compaction is the result of expulsion of pore fluids, and is averaged vertically over each finite element (See Supplementary Material). Expelling pore water leads to vertical contraction of the sediment column. This is calculated for each model time step by adding a compaction velocity, in addition to the tectonic velocity, to the nodes of elements containing compacting sediment. This added velocity reflects the change in volume associated with the expulsion of pore fluids

(Supplementary Material). Note that expelled pore fluids are considered to leave the system; they do not contribute to pore fluid pressure. Compacted sediment densities increase with additional sediment load, but are not reversed with erosion; sediment does not de-compact.

5.4.3.1 Model Geometry

In most cases, a 2D slice through the centre of one of the models presented here (at y = 0.5) has the same overall geometry as one of the 2D models presented by Goteti et al. Notable differences in the model include reduced resolution, both horizontal and vertical, compared to Goteti et al. (2012). This work includes 2D-equivalent models, in which the original geometry and sedimentation definition does not vary in the y-direction, and fully 3D models, which are symmetric in a radial, planform sense. A constant y value slice through the 2D-equivalent models has the same overall geometry as the confined minibasin models in Goteti et al. (2012), for any given y position. A slice through the fully 3D models will only match a similar Goteti et al. model for the case where y = 0.5 (or x = 0.5, if aligned with the x axis). This is because the distance from the centre to the corners of the fully 3D models is longer than the half width of a similar 2D model (Figure 5.1 c,d).

5.5 Results

This section describes a preliminary set of results produced using the adaptations added to DOUAR during the development of this project. The output is presented and described in detail, to illustrate the usefulness of models of this type in assessing the differences in development of minibasins through uneven sedimentation in 2D versus fully 3D geometries. The results presented here demonstrate much of the functionality that was added to DOUAR during this project, for example compacting sediment density with depth, incorporation of pore fluid pressure, and more options for surface geometries. These features are necessary for the study of salt tectonics, and expand the potential uses of DOUAR. Development of DOUAR for use in the study of salt tectonics is ongoing; the results presented here are subject to change with further refinement of the software.

5.5.1 Model Set 1: Confined Minibasins without Pre-Kinematic Layer

In this section fully 3D and 2D-equivalent versions of confined minibasins are compared. A pre-kinematic layer is not used. Wavelengths of 12, 30, and 50 km are considered. In each of the fully 3D models, the radial symmetry of the model geometry drives salt deformation outward from underneath the maximum sediment thickness, in all directions. In contrast, the 2D-equivalent geometry does not vary in the y direction, and so lateral salt flow is driven only in the x direction. The 2D-equivalent geometry models were designed to approximate modeling that can be achieved with a planar, 2D model.

As can be seen in Figures 5.2-5.7, the fully 3D and 2D-equivlaent versions of the confined minibasin models presented here have some notable differences in their behavior. The figures shown here display cross sections through each model, along y = 0.5. In the fully 3D models, this cross section passes through the thickest sediment, at the centre of the model. In the 2D-equivalent models, this cross section also passes through the thickest sediment, though sediment thickness at x = 0.5 does not vary in the y direction. All models in this set drive salt flow out from beneath the thickest sediment, in response to differential pressure induced by the uneven sediment load. In all cases, the fully 3D version of the models expels salt more efficiently from underneath the thickest sediment. This can be seen in the greater sediment thickness at x = 0.5 for the fully 3D models, compared to their 2D-equivalent counterparts. This observation is likely explained by noting that in the fully 3D model salt is free to flow laterally away from the thickest sediment in all directions, while in the 2D-equivalent models, lateral salt flow is only driven in the x direction. This behavior might suggest that the 3D equivalent versions of the models are more efficient at forming minibasins. However, for all wavelengths considered, the fully 3D models also accumulate sediment more readily at the edges of the model domain, impeding thickening of salt at these locations, and suppressing diapir formation. The differential pressure induced by the uneven top surface geometry is maintained throughout these model runs. All models in this set eventually accumulate sediment over the edges of the model, but this accumulation occurs more quickly in the fully 3D models. This may be due to larger area over which thickened salt is developing in the 3D models, compared to the 2D-equivalent versions.

Thickening salt over this area requires more salt flow than does thickening salt along the x=0 and x=1 edges of the 2D-equivalent models.

Success of minibasin formation, as defined by Goteti et al. (2012), is not demonstrated by the models in this section. Minibasin formation requires continued salt flow throughout the model evolution, sediment sinking at x=0.5 in these cross sections, and a lack of sediment accumulation over thickened salt at the edges of the models. In addition, Goteti et al. switched from uneven sedimentation to a flat top of sediment surface at various points in their models' evolution, and successful minibasins experienced continued sediment sinking into salt after this point. For this to happen, the average density of the sediment at the centre of the model domain needs to be greater than the density of the underlying salt. This is not achieved for the models that were run with the older version of the code. From the last panels in Figures 5.2-5.3, we can see that the density of the sediment at the base of the sedimentary succession is greater than the salt below, however the average density of the sediment in these models is still less than the density of the salt. The models that were run with the newer version of the code (Figures 5.4-5.7) show high sediment density later in the model run, and likely produce a density inversion that would drive continued minibasin subsidence in the absence of uneven sedimentation.

The output shown in Figure 5.2 and 5.3 was produced with a version of the DOUAR upgrades known to have an issue with the way compaction velocity was applied. This lead to some salt being advected out the base of the model over the course of the model run. The main consequence of this error is that the volume of salt in the model is not

consistent over time. These models are designed as a confined system, with no flow intended out of the base or sides of the model. Salt diapirs form at the edges of the model domain in response to uneven sediment loading, and because salt is not permitted to flow out of the model domain. With this restriction not correctly enforced (when salt is able to leave the base of the model), the tendency to form salt diapirs and successful minibasins is impaired. This issue has since been fixed. Figures 5.8 and 5.9 show output for 2D-equivalent and fully 3D models run with the corrected version of the code, for the model design with a 30 km model width. In these figures, output is given at time step 400, after 12 Ma model evolution. The version of the code used to generate particular output is noted in the figure captions.

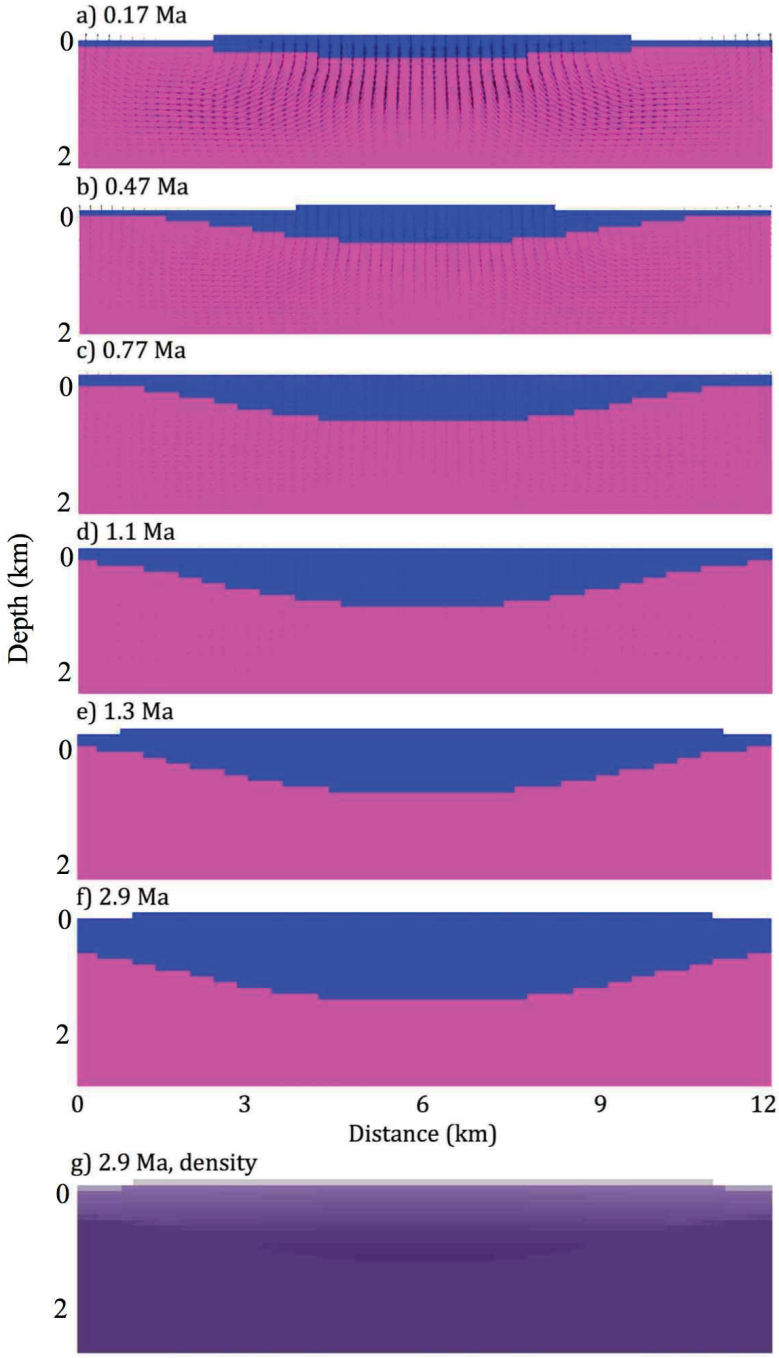

Figure 5.2: 12 km confined minibasin, fully 3D geometry, without pre-kinematic layer. Panels a through e show early model evolution, with no buildup over salt at the edges of the model. Panel f is from later model evolution, and shows accumulation of sediment over the diapirs at either edge of the model domain. Panel g shows compacted density density for the same point in model evolution. Initial model thickness is 2 km. This model was run with the older version of the software.

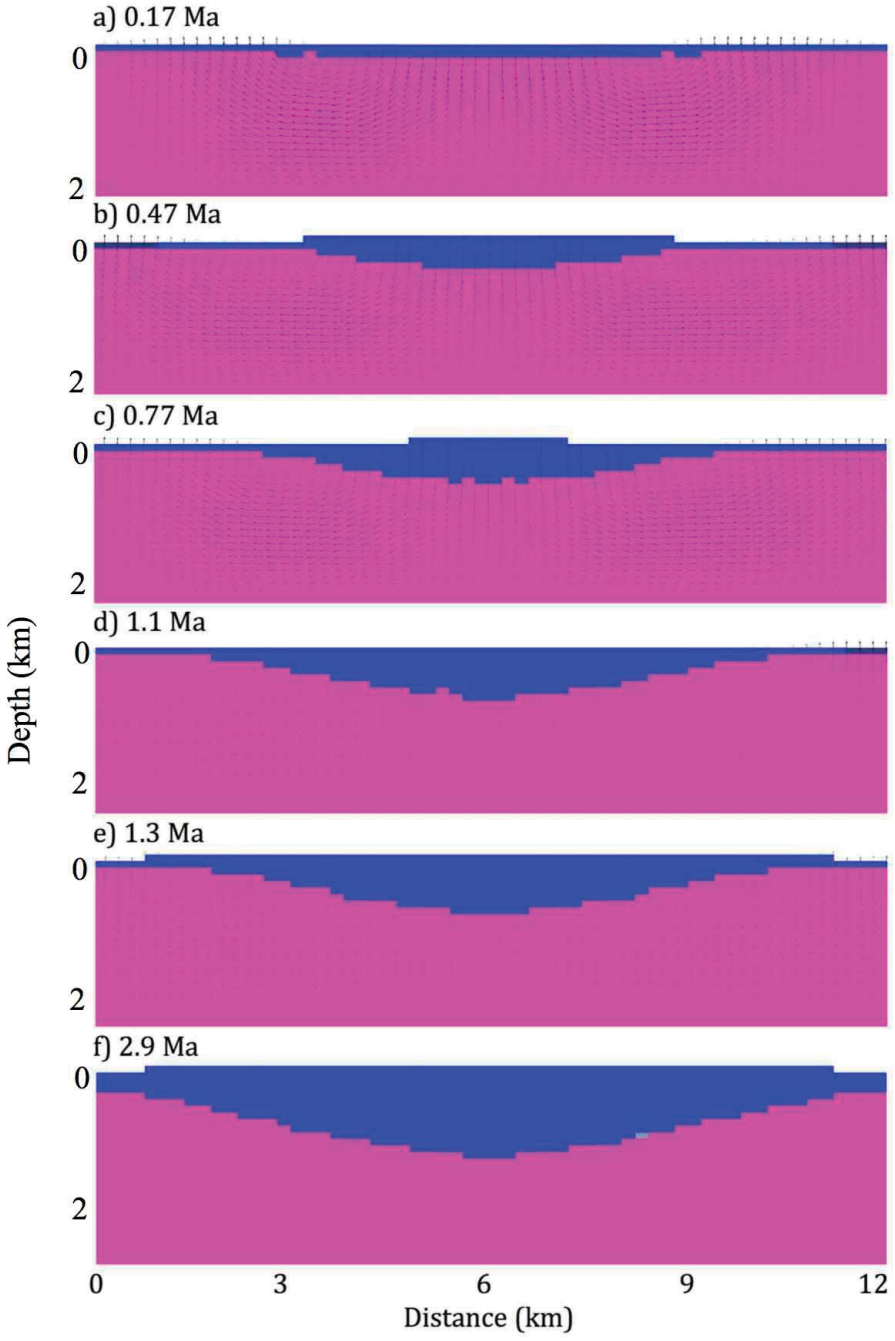
a) 0.17 Ma
b) 0.47 Ma
c) 0.77 Ma
d) 1.1 Ma
e) 1.3 Ma
f) 2.9 Ma
0
2
Depth (km)
0
3
6
9
12
Distance (km)

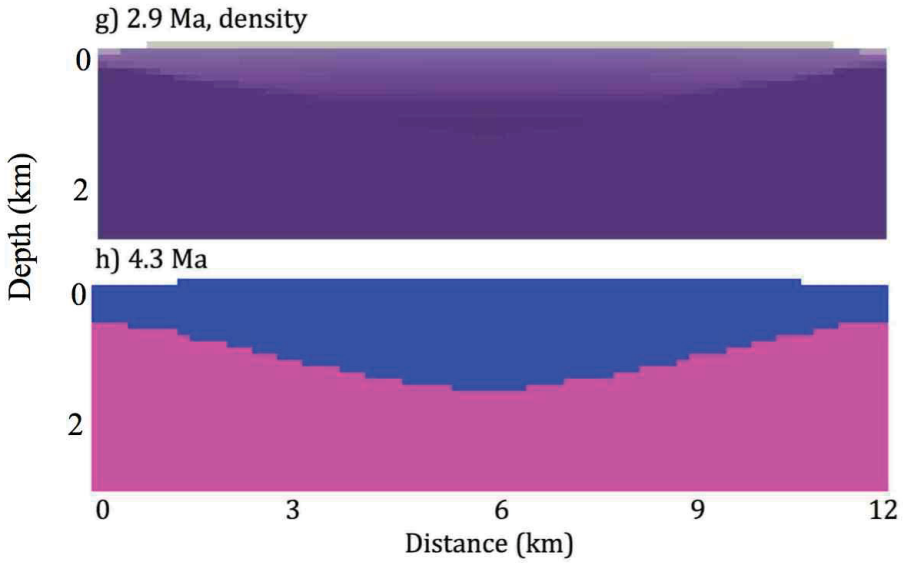

Figure 5.3: 12 km confined minibasin, 2D-equivalent geometry, without pre-kinematic layer. Panels a through e show early model evolution, with no buildup over salt at the edges of the model. Panel f is from later model evolution, and shows a small accumulation of sediment over the diapirs at either edge of the model domain. Panel g shows compacted density density for the same point in model evolution. Panel h shows later still model evolution, where build up of sediment at the edge of the model domain is more obvious. Initial model thickness is 2 km. This model was run with the older version of the software.

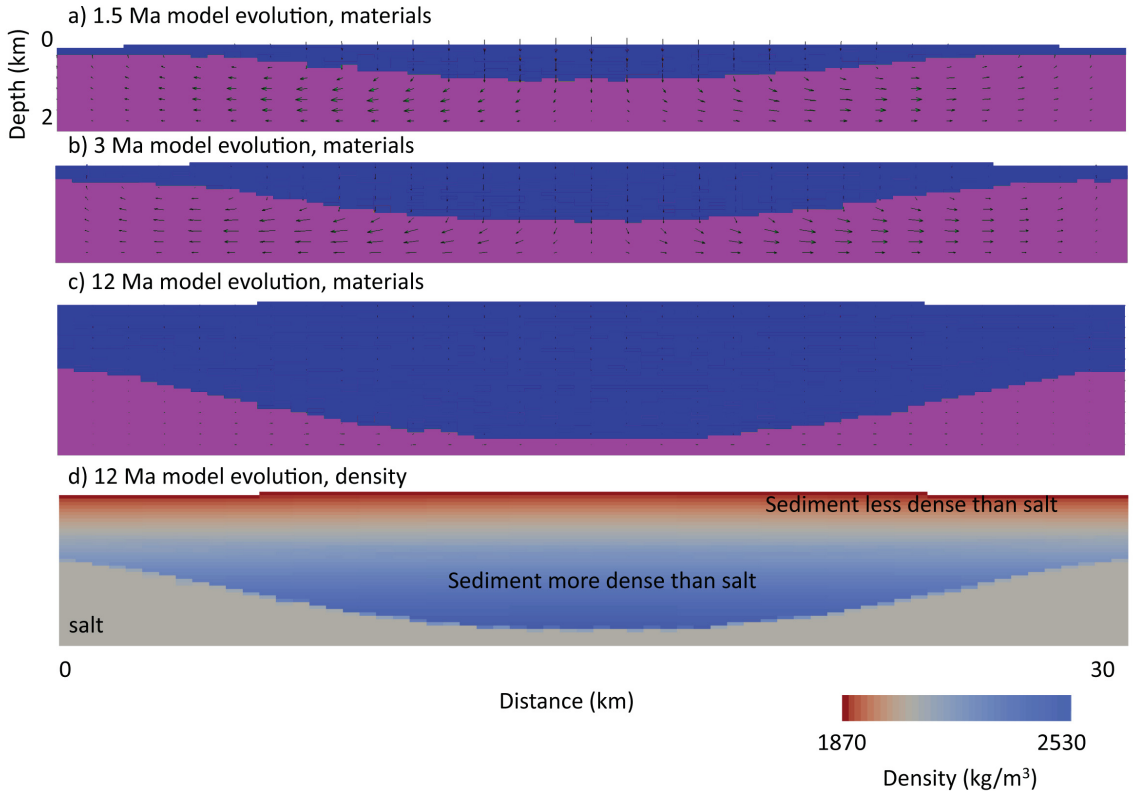

Figure 5.4: 30 km confined minibasin, fully 3D geometry, without pre-kinematic layer. Panels a through e show early model evolution, with incipient minibasin formation. Panel f is from later model evolution, and shows accumulation of sediment over the diapirs at either edge of the model domain. Panel g shows compacted density density for the same point in model evolution. Initial model thickness is 2 km. This model was run with the new version of the software.

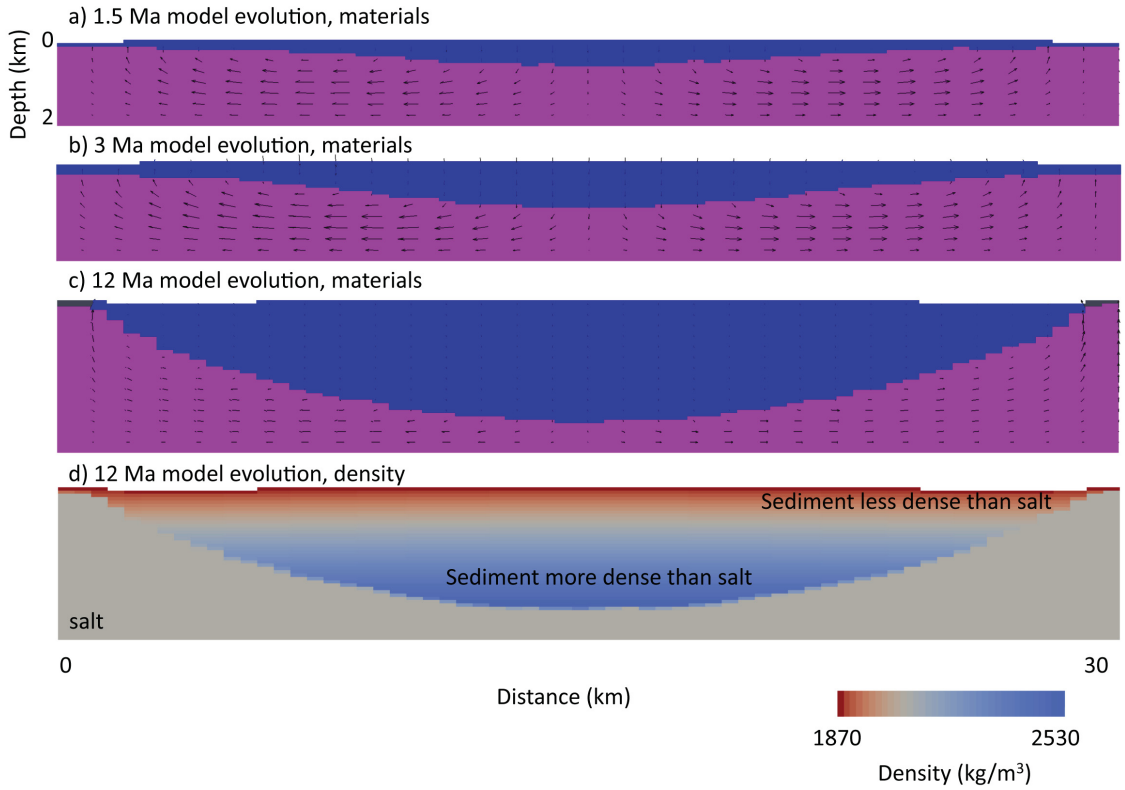

Figure 5.5: 30 km confined minibasin, 2D-equivalent geometry, without pre-kinematic layer. Panels a through e show early model evolution. Sediment sinks into salt more slowly than for the fully 3D model shown in Figure 5.4. Panel f shows later model evolution; sediment accumulation over the diapirs at the edge of the model domain is less pronounced than for the fully 3D model (Figure 5.4). Panel g shows compacted density density for the same point in model evolution. Initial model thickness is 2 km. This model was run with the new version of the software.

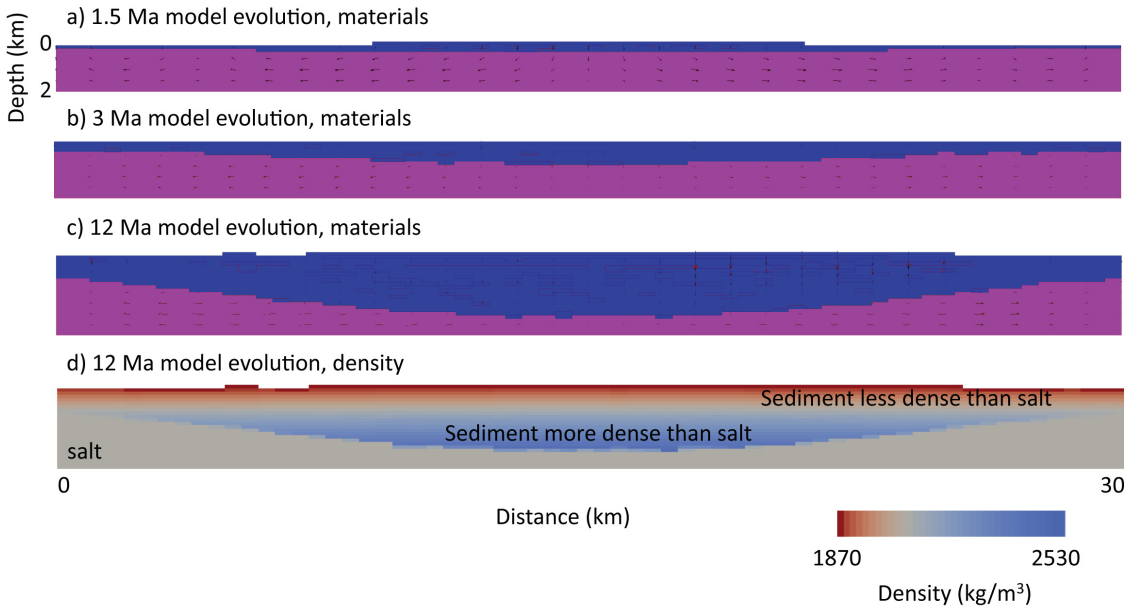

Figure 5.6: 50 km confined minibasin, fully 3D geometry, without pre-kinematic layer. Panels a through e show early model evolution, with no buildup over salt at the edges of the model. Panel f is from later model evolution, and shows significant accumulation of sediment across the model domain, including over the diapirs at either edge of the model. Panel g shows compacted density for the same point in model evolution. Initial model thickness is 2 km. This model was run with the new version of the software.

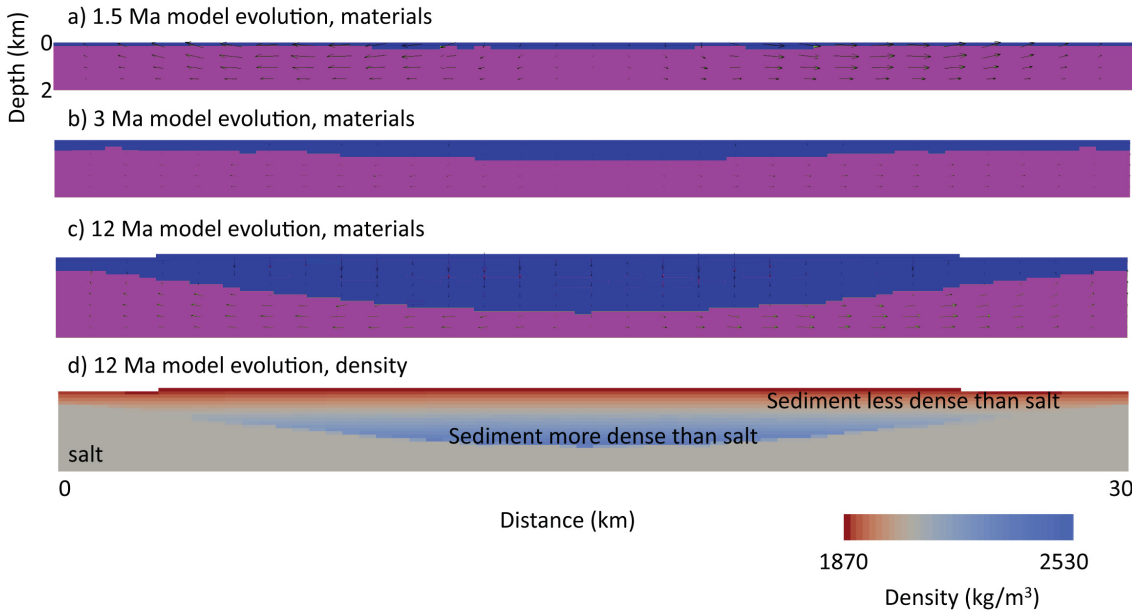

Figure 5.7: 50 km confined minibasin, 2D-equivalent geometry, without pre-kinematic layer. Panels a through e show early model evolution, with no buildup over salt at the edges of the model. Panel f is from later model evolution, and shows significant accumulation of sediment across the model domain, inlcuding over the diapirs at either edge of the model. Panel g shows compacted density density for the same point in model evolution. Initial model thickness is 2 km. This model was run with the new version of the software.

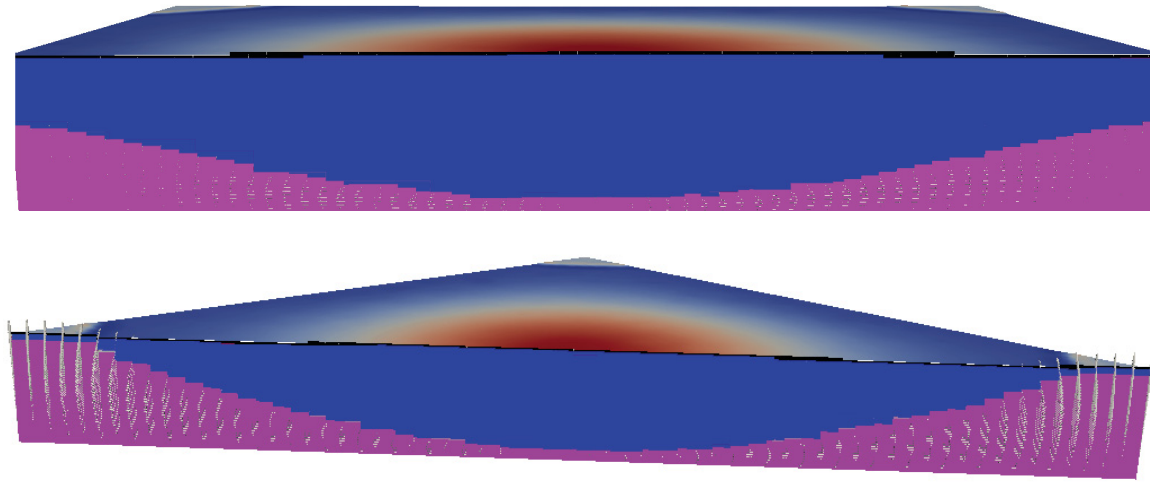

Figure 5.8: Confined minibasin, fully 3D, 30 km model width, with correction to compaction velocity. In this model run, with the correction in place, salt does not escape through the base of the model. The top panel shows the model sliced along the place y=0.5; the bottom panel shows a slice through x=y. Both slices are shown at 12 Ma model evolution.

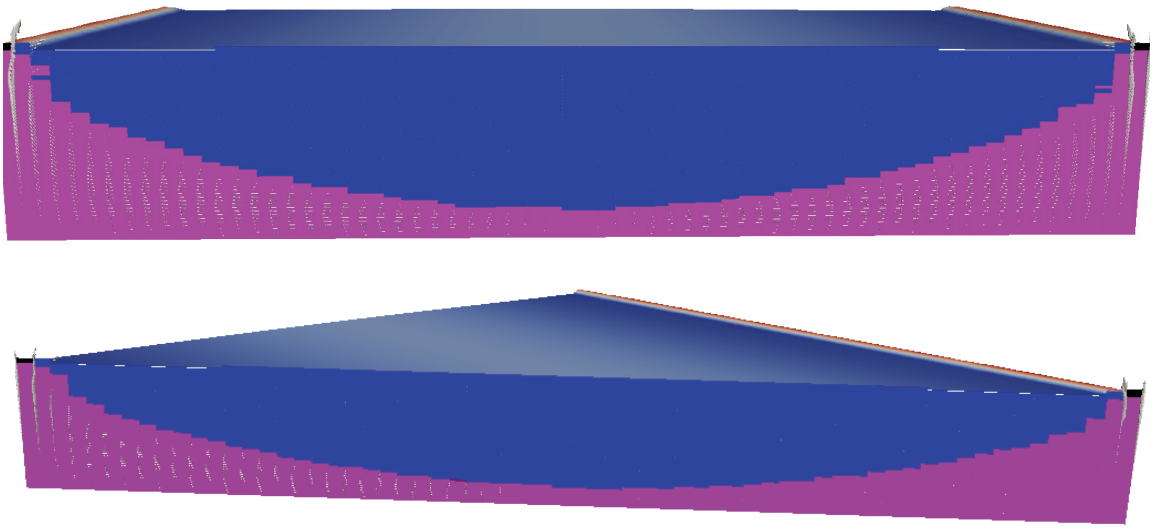

Figure 5.9: Confined minibasin, 2D-equivalent, 30 km model width, with correction to compaction velocity. In this model run, with the correction in place, salt does not escape through the base of the model. The top panel shows the model sliced along the place y=0.5; the bottom panel shows a slice through x=y. Both slices are shown at 12 Ma model evolution.

5.5.2 Model Set 2: Confined Minibasins with Pre-Kinematic Layer

In this section, results from models with a PKL are compared with results from comparable models without a PKL. These models were run with the older version of the software. The Pre-Kinematic Layer increases the density of the sediment throughout the sediment thickness, and brings the average sediment density closer to that of salt at the start of the model run. Figure 5.11 shows cross sections from the models at 1.3 Ma evolution for fully 3D and a 2D-equivalent 30 km models with a PKL. Panels from the same point in model evolution, from 30 km models without a PKL are also shown. Compared to the models without PKL, the models with a PKL accumulate sediment at the edges of the model much more quickly. By 1.3 Ma, the models with a PKL have accumulated a thick layer of sediment across the model domain, over the PKL.

For the model pair with 30 km wavelength, 2D-equivalent and fully 3D versions, in the presence of a pre-kinematic layer, the 2D-equivalent model more effectively drives salt flow from underneath the centre of the model, indicated by the thinner salt and thicker sediment at the centre of the cross section, compared to the fully 3D model with PKL (Figure 5.11). While the fully 3D model is free to expel salt in all directions, it also must deform a larger area of the PKL than does the 2D-equivalent model (in the corners of the model), to drive salt thickening at the model edges. The pre-kinematic layer favors development of a density inversion by increasing the average density of the sediment, and thus facilitates lateral flow of salt. However it also increases the strength of the (thickened) sediment at the edges of the model, which inhibits diapir formation.

The average sediment densities for 30 km confined minibasin models with and without pre-kinematic layers, for both the fully 3D and the 2D-equivalent models, is shown for 1.3 Ma model evolution in Table 3. Of the four models considered here, only the 2D-equivalent model with PKL achieves an average sediment density greater than that of salt (2200 kg/m^3). This density inversion could drive further minibasin subsidence in the absence of continued uneven sedimentation, however, by the time this is achieved, the model has accumulated a thick succession of sediment at the model edges, which impedes thickening of salt at these locations. To be comparable across the various model designs (some of which have not been re-run with the newer code), these results are from models run with the previous version of the code, including the error of salt exiting the base of the model. Because sediment density greatly exceeds salt density in the lower part of the sediment column for models run with the newer version of the code (Figures 5.4-5.7), it is likely that a successful density inversion would form in these models.

Table 5.3 Average Sediment Density by Model

Model Description	**Average Sediment Density at 1.3 Ma (kg/m^3)**
No PKL, fully 3D	2011
No PKL, 2D-equivalent	1821
With PKL, fully 3D	2145
With PKL, 2D-equivalent	**2231**

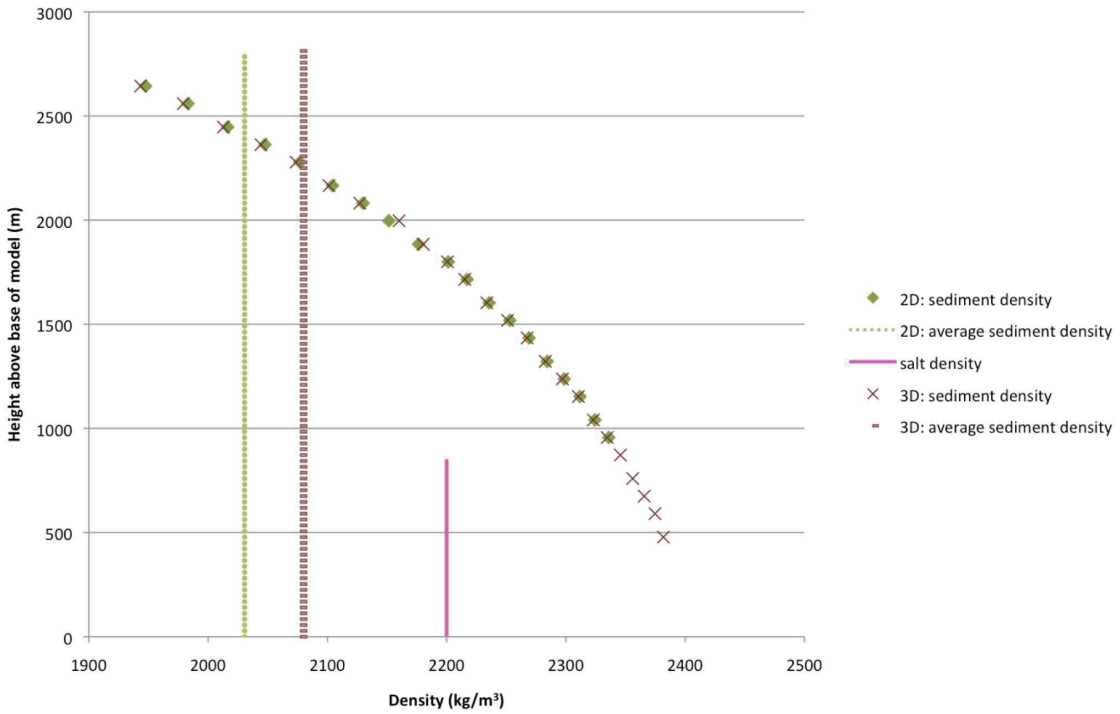

Figure 5.10: Density profile and average density of sediment for fully 3D and 2D-equivalent 30 km models without pre-kinematic layer, at 2.9 Ma model evolution, at the centre of the model domain. In the fully 3D model sediment extends further towards the base of the model. Sediment density at the top of salt is greater than salt density, but average sediment density for both the fully 3D and the 2D-equivalent models is less than the density of salt.

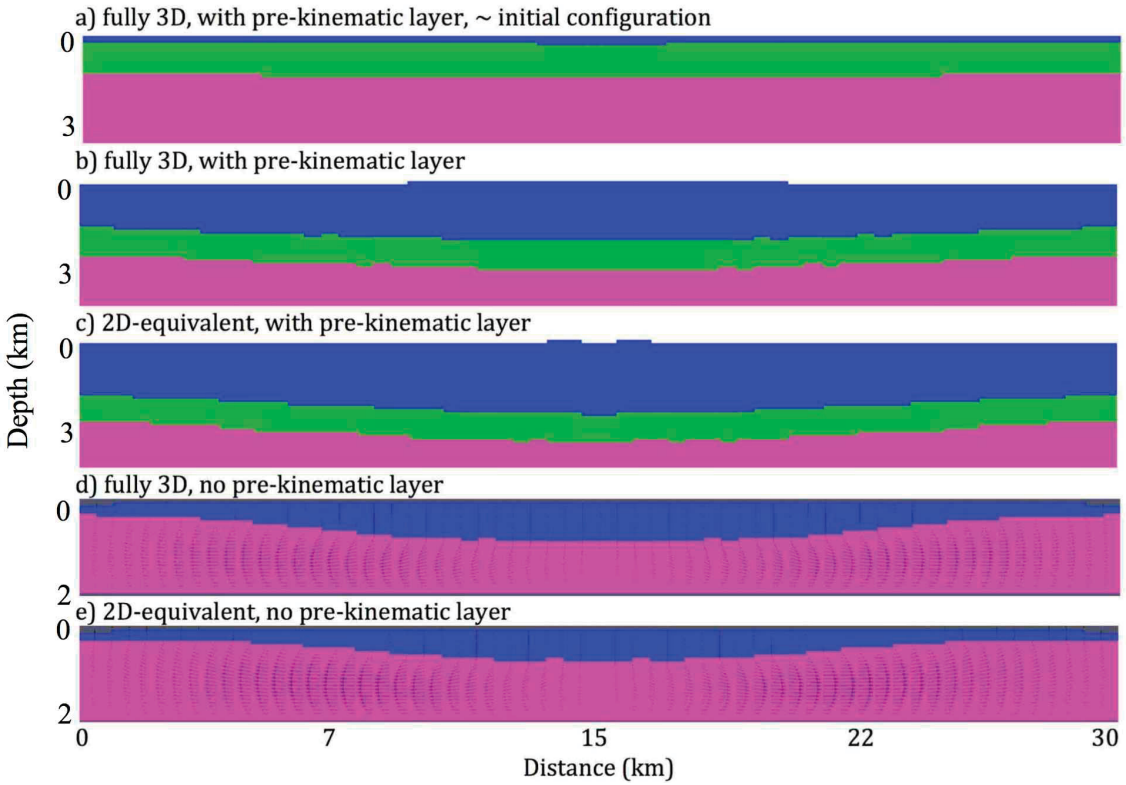

Figure 5.11: 30 km confined minibasin model with pre-kinematic layer. Panel a) shows the fully 3D model at approximately the initial configuration; the 2D-quivalent models appears similar in cross section at this point in the model evolution. Panels b) and c) show the fully 3D and 2D-equivalent models at 1.3 Ma evolution. The 2D-equivalent model expels more salt from under the thickest sediment, and both models accumulate thick sediment over the PKL, across the model domain. Panels d) and e) show the 30 km models without PKL at the same point in evolution. Compared to the models without PKL, the models with PKL accumulate sediment over the edges of the model much more quickly. In the models without PKL, sediment deposition is largely restricted to the centre of the model domain at this point in the model evolution. Sections are through y = 0.5. Velocity scale is the same for all panels. Initial model thickness is 2 km. These models were run with the older version of the software.

5.5.3 Impact of Variations in Aggradation Rate

For the 30 km confined minibasin model with no PKL, the aggradation rate was varied from 250 m/Ma (as in the results shown above) to 50 m/Ma, to assess the impact of aggradation rate on the tendency towards minibasin formation. Figure 5.12 shows the evolution of models with aggradation rates of 250, 125, and 50 m/Ma. Reducing aggradation rate has two main effects on the model evolution. First, salt is expelled more slowly from beneath the centre of the model. Second, the tendency for sediment to accumulate over the edges of the model is reduced. At a slower aggradation rate (50 m/Ma), this second effect leads to minibasins that are more likely to be successful, that is, to continue to sink sediment into salt. Note that these models apply uneven sedimentation throughout the model evolution. They show that reducing aggradation rate mitigates the suppression of minibasin formation by accumulation of sediment at the model edges. This effect is seen for both the fully 3D and the 2D-eqivalent versions of the model. These models were run with the older version of the software.

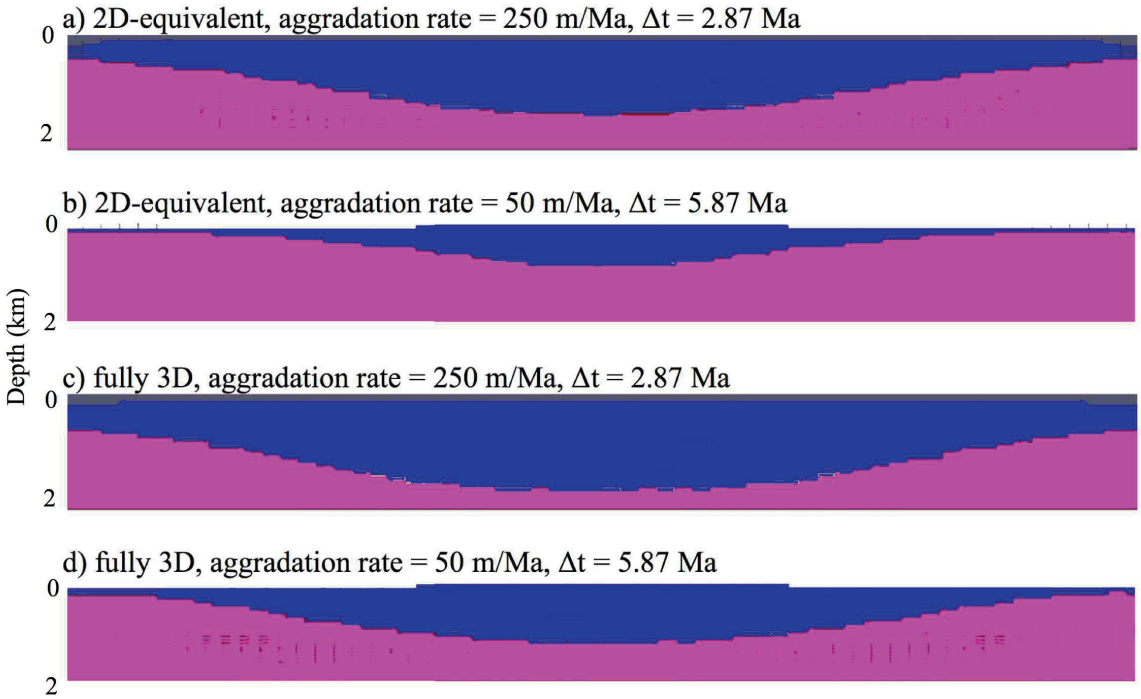

Figure 5.12: Impact of reducing aggrdation rate. 30 km confined minibasin, 2D-equivalent (a and b) and fully 3D (c and d) versions, without pre-kinematic layer, with aggradation rate 250 m/Ma (a and c) and 50 m/Ma (b and d). For the faster aggradation rate models (a and c) panels are shown at 2.87 Ma model evolution; for the slower aggradation rate models (b and d) panels are shown at 5.87 Ma. The models with slower aggradation rate expel salt from beneath the centre of the model more slowly, and show no tendency towards accumulating sediment over the edges of the model. At both the faster and the slower aggradation rates, the fully 3D models are more efficient at expelling salt and accumulating sediment in the minibasin, compared to the 2D-equivalent models. At the faster aggradation rate, the fully 3D model accumulates sediment at the edges of the model more quickly than the 2D-equivalent model. At the slower aggradation rate, neither model accumulates sediment over the edges of the model. Velocity vectors are the same for the 2D-equivalent (a and b) and fully 3D (c and d) versions. Horizontal dimension is 30 km; original salt thickness is 2 km. Images are cross sections along y=0.5. These models were run with the older version of the software.

5.6 Discussion

This work demonstrates the importance of studying salt tectonics using fully 3D approaches, by comparing the evolution of fully 3D and 2D-equivalent versions of models of minibasin formation through uneven sedimentation. By producing otherwise comparable model pairs, that vary only in their geometry in the out-of-plane direction, we can comment on the effect of including the third dimension, for the simple salt tectonics problems considered here. While a few issues (described below) remain that must be addressed before this analysis could be considered final, the work presented here demonstrates the potential of fully 3D numerical modeling of salt tectonics, to address the inherently three-dimensional nature of salt deformation.

Previous 2D numerical modeling studies of minibasin formation have shown that uneven sedimentation alone can drive minibasin formation. The duration required of uneven sedimentation, for successful minibasins to form, depends on the wavelength of the perturbation of the overburden material (Goteti et al., 2012). We find that fully 3D minibasins forming in response to uneven sedimentation develop thicker sediment accumulations within the basin, in a given period of time, but displace a smaller total volume of salt, and so accumulate sediment over the edges of the minibasin more readily, compared to their 2D equivalents. For the models run with the older version of the code (eg. Figures 5.2, 5.3) we did not observe successful minibasin development, that is, transition to Phase 2, with continued sinking of sediment into salt after uneven sediment load is no longer applied. In these models, the average density of sediment overlying the salt did not exceed that of the underlying salt, so transition to Phase 2 did not occur. Salt

expulsion from beneath the thickest sediment at the centre of the model did not outpace sediment accumulation across the top of the salt. Sediment accumulation at the edges of the model suppressed growth of the partial diapirs here, and reduced the rate of lateral salt flow. Consequently, sediment sinking at the centre of the model occurred at a reduced rate, and the average sediment density in the lens increased more slowly. In the models run with the newer version of the code (Figures 5.4-5.7) sediment sinking into salt occurs more effectively, and sediment appears to reach a higher average density. These models more closely resemble the results of Goteti et al. (2012).

It is important to note that Goteti et al. (2012) used a different numerical modeling software, Sopale (Fullsack et al., 1995). While DOUAR and Sopale capture many of the same physical properties of salt and sedimentary overburden, there are differences in how the two pieces of software operate. Our work should not be considered directly comparable with the 2D models of Goteti et al. (2012).

5.6.1 Decreasing Aggradation Rate

Compared to the 2D models of Goteti et al. (2012), the confined minibasin models presented here develop more slowly. Reducing aggradation rate produces models that behave more similarly to those of Goteti et al. (2012). This difference between the evolution of Goteti et al.'s 2D models and the 2D-equivalent models presented here deserves further investigation. A slower aggradation rate may lead to slower

accumulation of sediment at the edges of the model, and as such may facilitate vertical salt movement and diapir formation at these locations.

5.6.2 Models Combining Progradation and Aggradation

To explore interaction between prograding deltas and minibasin formation, we designed and ran a small number of larger scale models that combine aggradation and progradation. These models are potentially quite informative, in that they allow investigation of minibasin formation through uneven sedimentation in the context of a more complex setting. In these models, the full domain spans 150 x 150 km, and includes a progradation of a wedge of deltaic sediment over a field of minibasins forming through uneven sedimentation. The progradation front applies a uni-directional lateral driving force in the positive x-direction while the uneven aggradation drives lateral salt flow in both the positive and negative x-directions. Near the edge of the prograding wedge, these forces compete, under the sediment wedge the progradation-driven salt flow dominates, and far from the progradation front aggradation supplies the dominant force driving salt flow. Note that a linear progradation front was used in these early models, but we have incorporated the ability to generate a more realistic, lobate progradation profile (see supplementary material for this chapter). With this type of model, we can investigate combinations of aggradation and progradation that produces successful minibasins. Both confined and unconfined minibasin geometries can be incorporated into this type of model design.

Figure 5.13 shows the early evolution of one such model, with a linear progradation front and a field of uneven aggrading sedimentation in which each lobe is a sinusoidal perturbation with wavelength of 30 km and range of 100 m. From the top view, it can be seen that surface perturbations associated with uneven sedimentation are more prominent far from the progradation front. This is partly because the base level for the aggradation profile is flat, and is overprinted by the sloping progradation profile in the left part of the model. Also, lateral salt expulsion from beneath the prograding sediment wedge produces thickened salt around and under the minibasins nearest to the progradation front.

The results shown here are for 0.3 Ma model evolution. This type of model, which requires high resolution both vertically and horizontally, runs quite slowly in its present form. To produce useful results we would likely need to capture at least 3 Ma of evolution. Future work will extend these early results to either a) finding a means to improve run efficiency for this type of model or b) accepting long run times and allocate more time to completing these models.

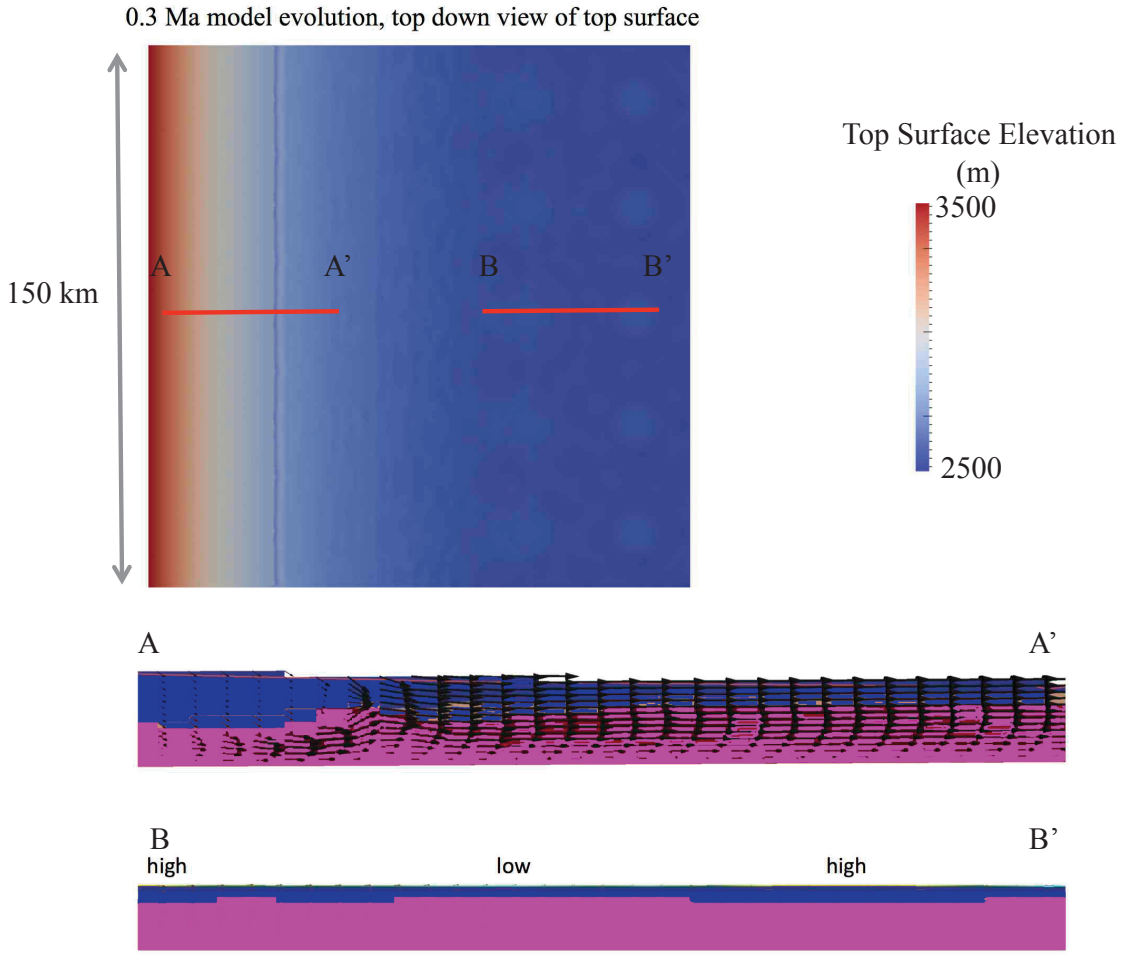

Figure 5.13: View of top surface (above) and section along y=0p5 (below). In top surface view, the edge of the progradation front is visible on the left hand side of the model domain, and 'egg carton' minibasins can be seen on the right hand side of the model. In the sections, you can see sediment sinking into salt and lateral expulsion of salt near the x = 0 edge of the model. Near the x = 1 edge of the model salt movement is much slower. Some sinking of sediment into salt can be seen, with slightly thickened sediment at high points in the egg carton surface. The legend in this panel is for the top surface position, scaled to show the range of the minibasin sinusoid. This model was run with the older version of the software.

5.6.3 Future Work

The models in this paper do not include water load. Where the upper surface of the model (the seabed) has only low angle variations from horizontal, water load will have only a minimal impact on the development of minibasins and diapirs or salt walls. A flat seabed would experience no differential pressure due to water load. The confined minibasin models in this paper have only slight slopes to the seabed, and as such we consider the omission of water load to have a negligible impact on their evolution.

This analysis considers one type of sedimentary overburden, the shale characterized by Jackson and Talbot (1986). As Goteti et al (2012) showed, the time required to successfully develop minibasins through uneven sedimentation varies with overburden type. A more thorough future analysis should consider a range of sedimentary overburden types.

5.7 Conclusions

For the simple confined minibasin models included in the study, we draw the following conclusions:

1. Correctly modeling compacting sediment density directly impacts the development of minibasin formation through uneven sedimentation. A non-compacting sedimentary overburden leads to faster minibasin formation without a

pre-kinematic layer, and slower minibasin formation with a pre-kinematic layer, compared to models with corrected, compacting sediment density.

2. Compared to 2D-equivalent models, fully 3D models of minibasin formation through uneven sedimentation, without a pre-kinematic layer, develop thicker sediment at the basin centre, and accumulate sediment more quickly over the diapirs on either side of the minibasin.
3. The addition of a pre-kinematic layer does not, for the 30 km confined minibasin included here, facilitate minibasin formation. For the 30 km models included here, when a pre-kinematic layer is included, the 2D-equivalent model expels salt more efficiently from beneath the thickest sediment than does the comparable fully 3D models.
4. As expected, for the confined minibasin models with no pre-kinematic layer, decreasing the aggradation rate produces more efficient salt expulsion and more rapid sinking of sediment into salt.
5. The modifications made to DOUAR, to facilitate the study of salt tectonics, require further revision, before reliable results can be obtained.

5.8 Supplementary Material

5.8.1 Modifications to the DOUAR Code

This section outlines the modifications made to the DOUAR 3D numerical modeling software for the purpose of 3D salt tectonic modeling in the current project, together with justification for each set of changes. Particular attention is given to changes needed to study features peculiar to salt tectonics systems, such as high rates of deformation, large strains and significant total deformation, unique surface geometries used to model different types of sedimentation, and the importance of sediment compaction and the evolving density of the clastic sediments.

5.8.2 DOUAR Software

The modeling software DOUAR was introduced prior to this work. DOUAR is an Eulerian finite element code with brick elements that do not change in shape throughout the evolution of an experiment. The number and dimension of Eulerian elements is based on subdivisions of a unit cube Divisions of the cube are based on an octree system, in which the number of elements along one edge of the cube is 2^n, where n is the octree level. There is also the option in DOUAR to use a vertical scaling (flattening factor), which produces elements that have a square base but a vertical thickness reduced by the vertical scaling. This is useful for increasing the number of elements contained in a thin (shallow vertically) model design. Numerical calculations in DOUAR use non-dimensional values, and all inputs (material properties, lengths, time scales) must be

scaled from their dimensional equivalents. The length of the unit cube, for example, scales to 1 in non-dimensional DOUAR units. Non-dimensional scaling of time and material properties depends on the particular values used. Two general scaling options can be used: a kinematic scaling option, if a characteristic velocity drives deformation; or a dynamic scaling if deformation is driven by buoyancy and/or differential pressure. A cloud of Lagrangian particles tracks strain, and is advected with the velocity solution. In previous versions of DOUAR, material advection was tracked using surfaces, which are interfaces between different types of materials. Material properties were identified with the surfaces; space below each surface was designated as a particular material. These surfaces were advected according to the velocity solution. In this work, we've modified DOUAR so that material advection can be tracked using the cloud of Lagrangian particles. In this case, individual particles have an associated material property that they retain throughout the model evolution.

5.8.3 Surface Removal

Previous versions of DOUAR tracked material advection using surfaces. These tended to become highly deformed and entangled over the evolution of some models. This also led to problems with surface refinement. An alternative approach is to track the material properties on the cloud of particles; in this case, surfaces within the model can be replaced by inferred interfaces between different Lagrangian particle types. Although this is less accurate than advection of the intact surface it overcomes the tangling. The top surface of the model, however, must be retained. Elements cut by the top surface have

mixed properties, between the material specified above and below the surface cutting the element. The process by which these averaged properties are assigned is called 'divFEM'. Retained surfaces are advected with the velocity solution, and in this way, movement of material was recorded.

When modeling a system with high strain, surfaces tracking the interface between two materials can become highly distorted even when the surface geometry is dynamically refined. Surfaces are defined by a grid of points connected in a triangular mesh. As this mesh is distorted, the sides of triangles between points on the surface become stretched, and new points are injected. If too many additional points need to be injected, to maintain the grid, refining the surface shape becomes unwieldy. In addition, if multiple surfaces originally defined in close proximity to one another deform substantially they may become entangled. Refining surfaces that become highly distorted, or are located very close to another surface can cause DOUAR to terminate with an refinement error. Problems in salt tectonics involve high strain and complex deformation of the interface between salt and the overlying sediment, and as such are likely to create both of these types of problems with surface refinement.

To reduce the number of surfaces that must be tracked, we have opted to track material deformation on the cloud of Langrangian particles. Instead of tracking interfaces between material types using surfaces, the cloud of Lagrangian particles carries with it material identification. Each particle has an associated material number, linked to mechanical properties for that material. Material properties of an element are determined

by querying the material number(s) of the cloud particles within the element at each time step; the material type with the largest number of particles is assigned to the element (majority rule). Other options for deriving elemental material numbers from the material numbers tracked on the cloud may be added in the future. In the case of a tie, the material number of the element from the previous time step is assigned to the element at the current time step. This approach allows the number of surfaces retained throughout the model run to be reduced, and hence minimizes the requirement of surface refinement, and reduces instances where surface distortion or entanglement impede model performance.

For each surface, the user must now indicate if the surface is to be removed after the initial definition of material properties on the cloud particles. In this way, surfaces other than the free surface may be removed after the initial material assignment. For surfaces that are retained, the user can specify whether these surfaces will be used to assign material properties and override material assignment based on the cloud particles. If so, these surfaces are used to determine the material number of particles injected into elements cut by each surface.

As a model evolves, it is sometimes necessary to inject new particles, to maintain a well-populated, dense cloud of particles that fills the model domain. This happens, for example, as sedimentation elevates the top surface of the model, creating a region (between the previous and current top surface positions) without cloud particles. Injected particles are assigned the material number of the element into which they are injected,

unless the host element is cut by a retained surface. Particles injected into elements cut by a retained surface (or more than one surface) are assigned a material number based on their position relative to an approximation of the position of a surface dividing material types within an element known as the level set function of the surface (Braun et al., 2008). The level set function is a planar approximation of the surface geometry within the element. A modification of this, intended to differentiate particles of the same material (sediment) that were deposited recently from those deposited longer ago, occurs when stratigraphy is used (see notes below).

5.8.4 Compacting Sediments

Calculation of the deformation of frictional plastic material, including sediments, with Drucker-Prager or Mohr-Coulomb failure criteria is included in previous versions of the DOUAR code (Braun et al., 2008). This capability did not, however, extend to modeling compaction of sediment. In the study of salt tectonics, compaction of sediments is critical. Salt (halite) has a density between that of most types of uncompacted and compacted sediment. As sediment accumulates over salt and compacts under the weight of overlying material, the sedimentary overburden, initially less dense than salt, becomes more dense than salt, creating a density inversion. Capturing this process is critical to correctly modeling salt tectonics systems. We have added the ability to calculate vertical kinematic sediment compaction according to a simple exponential user-defined Athy-type density versus depth curve. Our implementation of compaction consists of two

parts: Calculation of a compacted density profile with depth, and determination of corresponding kinematic compaction velocities.

The Athy (1930) formulation of sediment compaction describes how sediment density increases with depth by assuming that sediment comprises solid grains and pore fluid when deposited. As the sediment is buried it compacts by expelling water, such that its density $\rho(z)$ versus depth (z) is given by equation (1).

$$\rho = \rho_{grain} - \left(\rho_{grain} - \rho_{fluid}\right)\eta_s e^{-cz} \tag{1}$$

Where ρ is the compacted density, ρ_{grain} and ρ_{fluid} are the grain density and pore fluid density, η_s is the surface porosity, c is the compaction coefficient, and z is depth. In the implementation of DOUAR, the inputs ρ_{grain}, η_s, and c are specified by the user. In our study, we have taken values from previous work, where they were determined empirically for various sedimentary rock types (e.g.Nelson, 1991; Jackson and Talbot, 1986; Schmoker and Halley, 1982). In the present study, we focus on one sediment type, shale, using the compaction parameters given by Jackson and Talbot (1986). Pore fluid density, ρ_{fluid}, was taken as the density of water. This approach is only an averaged approximation of observed density vs depth observations, but is a useful approximation for our application where we need to calculate the integrated weight of sediment versus depth, which will be much smoother than the density vs depth distribution.

The density profile with depth for compactible sediments in DOUAR follows the Athy curve calculated from the inputs of grain density, pore fluid density, surface porosity, and compaction coefficient (Equation 1). The calculation of compacted density is performed at several points along a vertical string (a new structure we have called density strings) passing through the centre of a vertical stack of elements. The number of calculation points within each element can be specified; we have used 9 points per element. This produces a satifactory density profile with depth. Elemental compacted density is determined by averaging the densities at each point along the vertical string, within the element. Compaction density is first calculated at a specified higher resolution than the vertical dimension of the element, then is averaged to obtain a compacted elemental density. This provides a more accurate density profile with depth than would be obtained if compaction density was initially calculated at the whole element level. For each material type, the user must specify whether the material is compactible, and if so, must supply the inputs for the Athy curve (*Athy*, 1930).

The material number is used to determine whether or not a material compacts, and if so, which compaction inputs are used. The material number (and hence material properties) at each point on the density string can be determined either using the level set functions, or by using the cloud particles in a given element. When compacted densities are calculated at the start of the model run, the level set functions for all surfaces are used. Thereafter, the level set function of the free surface is used to determine the elevation of the free surface for a given column of elements and the cloud particles are used for all points below the free surface to determine the material number. In elements that contain

more than one material type, the element is divided into slices, stacked vertically, where each slice represents one material type. The thickness of each slice is proportionate to the percentage of cloud particles with that material number in the element, and the stacking of the slices is determined by the average vertical position of cloud particles of that material type. This is done within the calculation of compaction density only, and is used to assign an average density to the element. Note that the material type of the element is still defined by the majority rule of the material numbers on the cloud particles. Elements that are cut by a surface use divFEM to determine elemental density; the density calculated by divFEM overwrites the compacted elemental density.

Figure S1 shows compaction density versus depth, output for two depth profiles at different positions in a model with a prograding sediment wedge over a rectangular salt body. The model configuration is shown schematically in the figure, as are the locations of the two depth profiles. One profile passes through a stack of elements entirely within the sediment, while the other profile passes through sediment overlying salt. Elemental density is taken from the model output, at the elemental level. The curve labeled 'Athy curve' shows the calculated compaction density for sediments, as a function of depth below the sediment surface, calculated according to Equation 1. Note that this curve is only valid within the sediment. The top of salt position and the salt density are indicated, for the profile passing through salt. Good agreement is seen between the calculated sediment density and the output elemental sediment density.

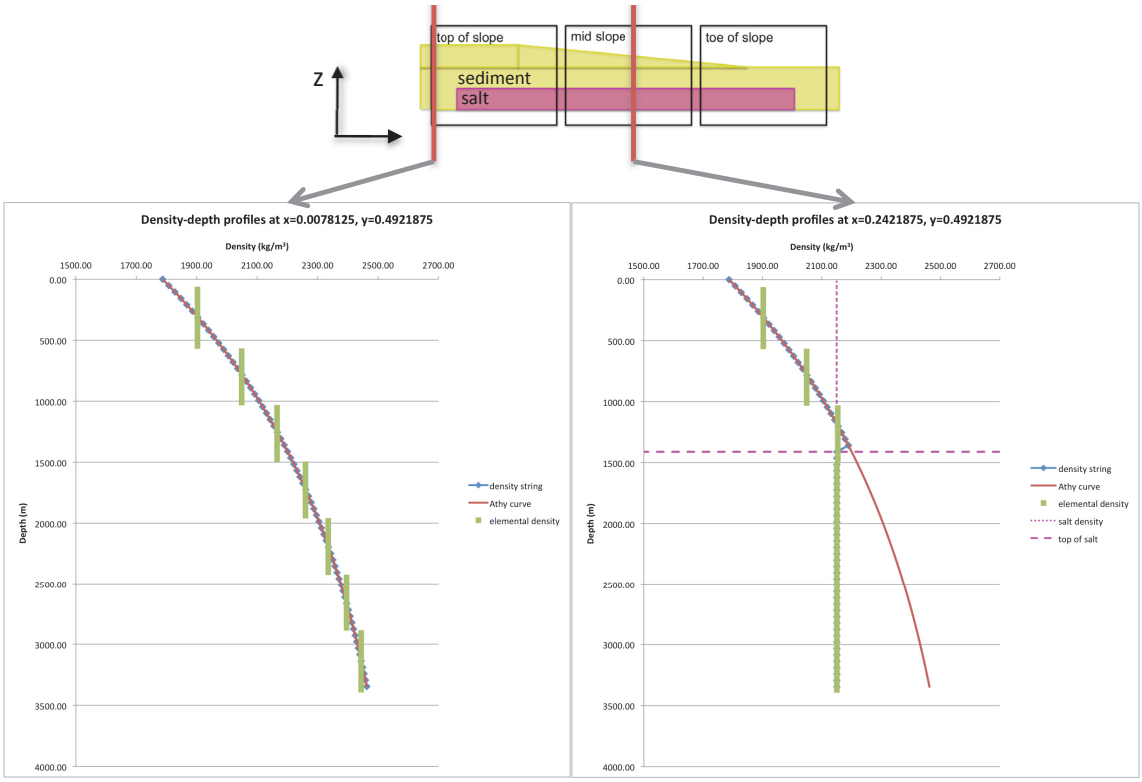

Figure 5.S1: Predicted and observed compacted sediment density.

As sediment compacts, pore fluids are expelled, and the volume of a given sample of sediment contracts. To account for this, a compaction velocity, $v_{comp,}$ is applied to the top nodes of each element that experiences compaction. It is assumed that compaction occurs entirely in the vertical direction. This velocity is calculated as the vertical displacement necessary to account for the change in volume associated with the expulsion of pore fluids for this position and time step(Equation 2), divided by the time step length. Both the current density with depth profile and the profile from the previous grid iteration are stored for each density string. For a given position on a string, the difference in porosity between the current and previous grid iteration is determined from the compacted densities (Equation 3). Compaction velocity is calculated at the same

points along the density string, and summed from the bottom to the top of each density string. The compaction velocity calculation is thus

$$v_{comp} = L\left(\frac{\eta - \eta_p}{dt}\right) \tag{2}$$

$$\eta = \frac{\rho + \rho_{grain}}{\rho_{grain} - \rho_{fluid}} \tag{3}$$

where L is the length increment between vertical positions on the density string, η and η_p are current and previous porosity at this position on the density string, dt is the time step length (or half time step length, for the mid point calculation), ρ is the compacted density at this depth, and ρ_{grain}, and ρ_{fluid} are the grain density and pore fluid density for the compacting material. Compaction velocity acts vertically, and is applied in conjunction with the velocities from the mechanical solution.

Sediments do not de-compact. That is, if erosion occurs, compacted sediment density does not decrease according to the new, more shallow burial depth. If erosion is followed by subsequent sedimentation, total burial depth is used to calculate compacted sediment density. For each density string, the current density profile with depth is compared against the profile from the previous grid iteration to determine whether sedimentation or erosion has occurred. Densities on the string are updated to match the current Athy curve only in cases where the current density is greater than the previous density.

Figure S2 is a schematic depiction of how compacted density changes when a) sedimentation is applied, or b) erosion occurs. Both panels show density profiles with depth, for two times in model evolution. As sediment is added, the density-depth profile adjusts to compact densities to account for the new surface position. When sediment is removed during erosion, compacted densities do not adjust (the sediment does not de-compact).

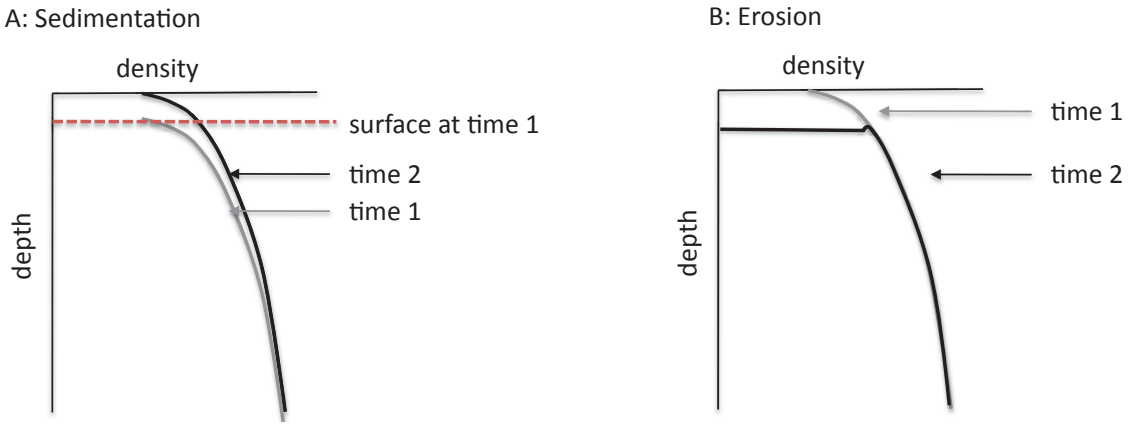

Figure 5.S2: Schematic density profiles with depth showing that compacted density increases in response to sedimentation, but does not decrease in response to erosion.

Figures 5.S3 and 5.S4 demonstrate the importance of correctly applying compaction to accumulating sediment. Two scenarios are shown, for a confined minibasin model with and without a pre-kinematic layer (PKL). A confined minibasins model is one in which sediment accumulates over salt, with the top of the sediment surface perturbed following a sinusoidal pattern in both the lateral (x and y) directions, and the wavelength of the sinusoid equal to the horizontal length dimension of the model. In models without a pre-kinematic layer, sediment accumulation starts at the top of salt surface. When a pre-kinematic layer is used, a layer of uniform thickness sediment overlies salt at the beginning of the model; the layer thickness is such that sediment density at the base of

the layer is equal to the density of the underlying salt. For a model without a PKL, non-compacting sediment drives salt deformation more quickly than in the corresponding model with correctly compacting sediment. Where a PKL is used, non-compacting sediment leads to slower salt deformation than in a model with corrected, compacting sediment. In the study of minibasins development it is critical to correctly address the rate of salt deformation and the tendency of sediment to sink into underlying salt. It is therefore crucial to include compacting sediment density in the current experiments.

Compaction is initiated at the beginning of a new model run such that the specified geometry is applied with fully compacted sediment at the start of the first time step. That is, the initial geometry is retained, compacted densities are applied to compacting sediments, but compaction velocities are not applied in the initial model set up.

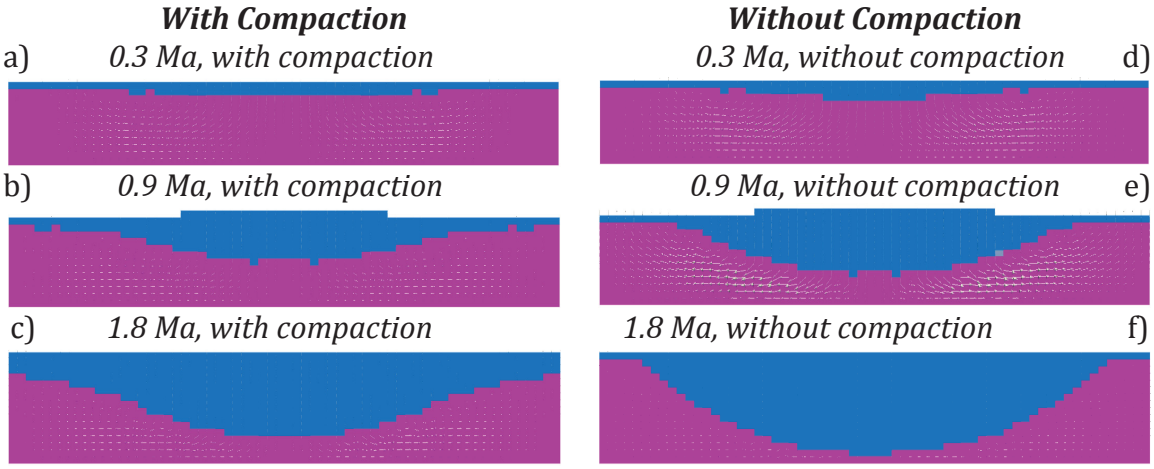

Figure 5.S3: Impact of correctly modeling compacting sedimentary overburden density for minibasin development without a pre-kinematic layer. Successive panels show model evolution for cases with and without compacting sediment density. View is a section through the centre of the model, parallel to one side of the model domain. Non-compacting sediments produce too quick salt deformation without a PK. Salt is magenta, aggrading sediment is blue. Vertical exaggeration ~ 6:1.

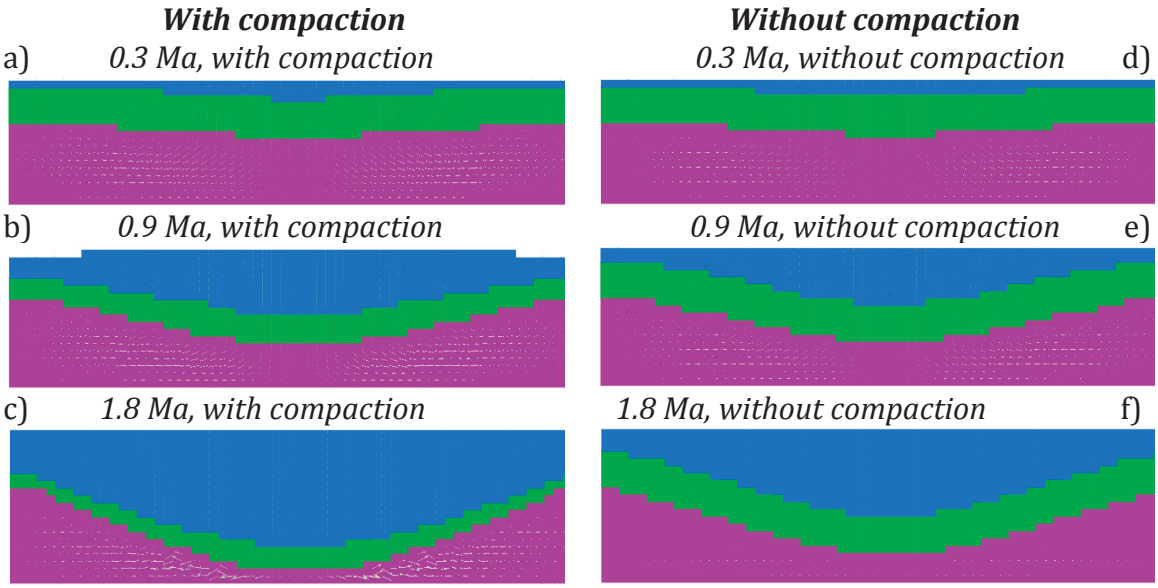

Figure 5.S4: Impact of correctly modeling compacting sedimentary overburden density for minibasin development and with a pre-kinematic layer. Successive panels show model evolution for cases with and without compacting sediment density. View is a section through the centre of the model, parallel to one side of the model domain. Non-compacting sediments produce too slow salt deformation with a PKL Salt is magenta, aggrading sediment is blue, and PKL is green. Vertical exaggeration ~ 6:1.

5.8.5 Stratigraphy

It is now possible to specify different colouring for the sedimentary material deposited at different intervals, facilitating improved visualization of models with sedimentation. These materials may have the same properties, but have different material numbers, allowing them to be coloured differently when plotting the model output. Particles injected near the model's surface, as sedimentation is applied, are assigned different material numbers as the model evolves; in this way, younger sediment can be coloured differently from older sediment, and internal deformation of sediments can be more easily shown. The number of such materials is specified in the input file, along with the activation time of each material.

Stratigraphy tracking is accomplished by retaining a second surface, which tracks the free surface with a one time step lag. Particles injected between the free surface and this second surface (the stratigraphy surface) are assigned a material number based on the activiation time for the series of colours assigned with each stratigraphy time interval. This is implemented by initially assigning new cloud particles a material number based on the level set functions, for particles injected between the free surface and the stratigraphy surface, and then subsequently updating the material number of the injected particles based on the stored activation times of the stratigraphy materials.

Particles injected below the stratigraphy surface are assigned the material of the element into which they are injected. In the future, this may be adjusted, so that injected cloud particles are assigned the material number of the nearest neighboring cloud particle at the time of injection.

Stratigraphy has been tested and worked as designed, but does not distinguish sediments of different depositional ages as clearly as could be hoped. For the current version of this manuscript, stratigraphy has not been used. For the final version of this paper, adjustments to stratigraphy may be necessary.

5.8.6 Initial Particle Injection – Distribution

Particle injection at the initial set up of the model can now be done according to an evenly-spaced grid. Users specify the maximum and minimum number of particles as

before. Optional new inputs include the number of particles to be injected in the x, y, and z directions, and whether there will be a particle injected at the centre of the element. Particles injected as the model evolves follow previous methods for distribution within an element. This is an improvement on the previous approach, which positioned new particles so as to be far away from particles previously injected into an element. This approach tended to position particles towards the corners of elements, with few particles in the middle of elements.

5.8.7 Sedimentation Options and Associated Surface Geometries

Several new sedimentation options were added to the DOUAR code. Sedimentation is applied after the mechanical solution has been calculated and before compaction and isostasy are applied, both at the mid point solution and at the end of the time step. A defined sedimentation bathymetry is advected with a specified velocity, and at each grid iteration all empty space beneath the profile is filled with sediment. Sedimentation is accomplished by repositioning the top surface of the model (and the stratigraphy surface, if applicable), to the current position of the sedimentation bathymetry. Where the existing model surface is above the sedimentation bathymetry, as a result of movement due to processes other than sedimentation, such as deformation of the model or isostasy, it is not adjusted and material is not removed.

A number of sedimentation geometries are now possible (see Figure S5), including: a flat aggradation surface, a 3D sinusoidally perturbed aggradation surface, a 2D-equivalent

sinusoidally perturbed aggradation surface, a linear progradation profile with half Gaussian in the x direction, and a progradation profile with half Gaussian in the x direction and full Gaussian in the y direction. When using aggradation geometries, a vertical aggradation velocity is also specified, which determines how quickly the surface is moved upward. When using progradation geometries, a progradation velocity in the x direction is specified, and dictates how quickly the profile is moved in the x direction. Aggradation and progradation profiles can be combined, as in the 'Progradation with 3D aggradation' example in Figure S5. Parameters defining the geometry options (wavelength for sinusoidal perturbations, Gaussian half width, etc.) are specified in the input file.

Corresponding surface geometries were also developed, so that the initial model geometry can be set to match sedimentation geometries. This removes the need for significant deformation of the free surface (and stratigraphy surface, if there is one) when sedimentation is first applied. Previously, the geometry of the model at the beginning of the run would have had a flat top surface or a simple linear progradation profile geometry. The top surface would then have been deformed to the sedimentation geometry specified during the first time step. Developing matching geometries for the initial configuration of the model produces a more smooth application of sedimentation.

Figure S5 shows top views of some of the sedimentation and surface type options added. For the case of a progradation profile that varies in both the x and y directions, the sediment surfaces profiles in x and y are also shown.

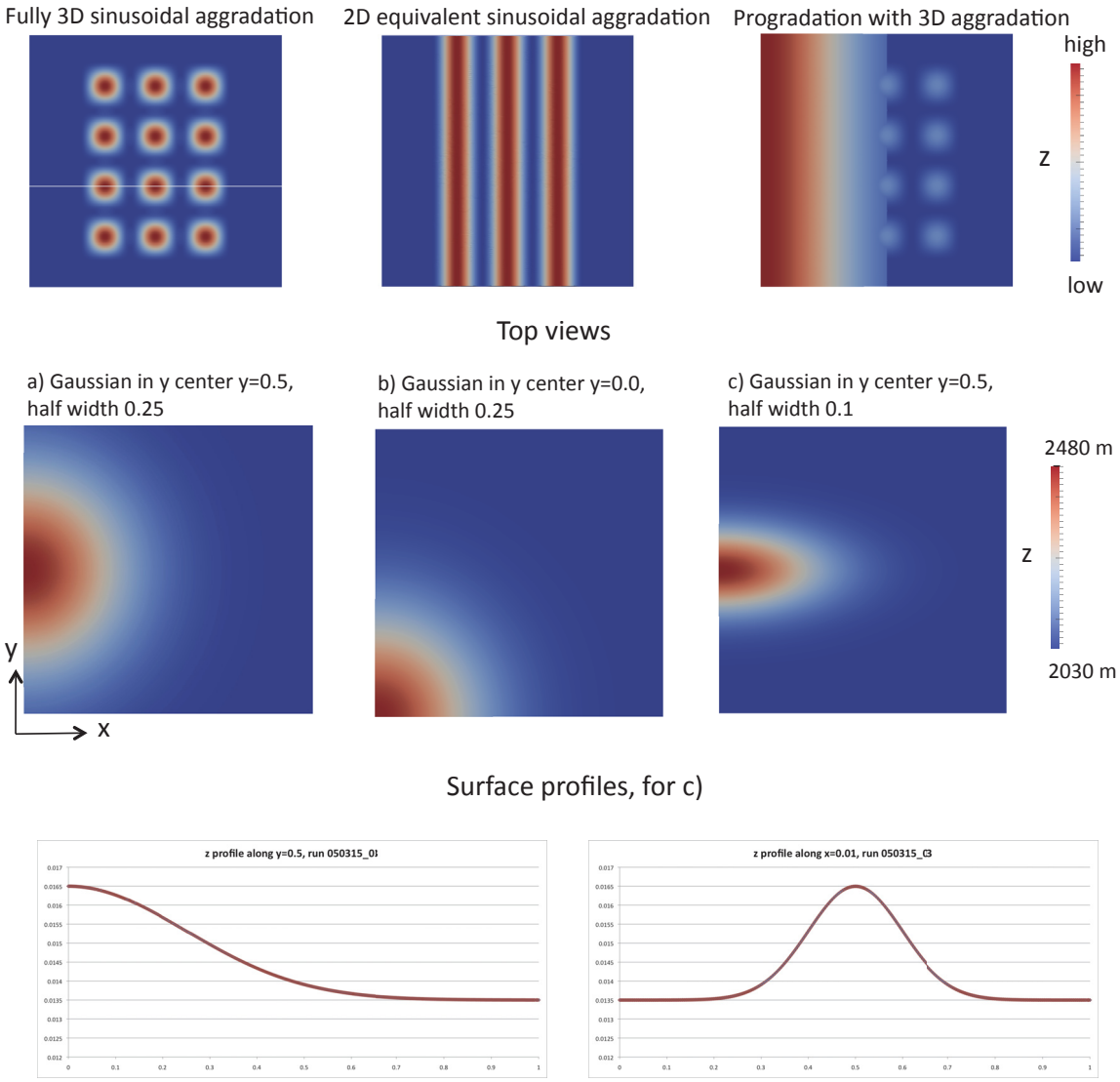

Figure 5.S5: New sedimentation and surface geometry options. Top view of a few of the new options are shown. Profiles in x and y are shown for one the progradation profile options. While relatively simple additions to the code, these new sedimentation options add considerable functionality when studying salt tectonics.

5.8.8 Submarine Conditions

Capturing the complete physical development of a submarine environment would involve accounting for both water load and pore fluid pressure. This version of DOUAR incorporates hydrostatic pore fluid pressure, which is used to reduce the (compromise cone) Drucker Prager yield stress, according to Equation 4.

$$\sigma_y = \frac{6C\cos\phi}{\sqrt{3}\left(3+\sin\phi\right)} - \frac{6\sin\phi}{\sqrt{3}\left(3+\sin\phi\right)}\left(P - P_f\right) \tag{4}$$

Where σ_y is the effective yield stress, P is the dynamic pressure, P_f is the hydrostatic pressure of the pore fluids, C is cohesion of the sediments, and ϕ is the angle of internal friction.

Hydrostatic pore fluid pressure is calculated relative to the position of the upper surface. For each element, the depth of the element's centre beneath the upper surface position is determined, and the corresponding hydrostatic pressure is calculated. This pressure is passed to the yield stress calculation, where it is used in conjunction with the dynamic pressure to calculate the modified yield criterion according to Equation 4. For each material, the user specifies whether pore fluid pressure will be used in the yield stress calculation. So while hydrostatic pressure is calculated throughout the model domain, it is applied as pore fluid pressure only for those materials where this is specified. This method calculates an approximation of hydrostatic pressure, which is only strictly correct

for a flat upper surface. However, for geometries in which the upper surface has a minimal bathymetry, this approximation is acceptable.

Figure S6 shows dynamic pressure and observed and predicted hydrostatic pressure as a function of depth, for a confined minibasin model. The depth profiles are along a vertical line at x=y=0.5, at the centre of the model domain. Dynamic pressure and observed hydrostatic pressure are taken from the model output. Predicted hydrostatic pressure, P_h, is calculated according to $P_h=\rho*g*h$ where ρ is the pore fluid density, h is the depth below the sediment surface, and g is the acceleration due to gravity. There is reasonable agreement between predicted and observed hydrostatic pressure, though there is a slight difference in the slope of the two profiles.

Figure 5.S7 shows the predicted and observed yield stress for the same model run with and without pore fluid pressure used in the yield stress calculation. Observed hydrostatic pressure and dynamic pressure are also shown. The profiles here are all taken through a vertical column of elements in the model, with depth measured below the sediment surface. Observed yield stress is taken directly from the model output. Predicted yield stress is calculated according to the Drucker-Prager yield criterion given in Equation 4. Cohesion and internal angle of friction were taken from the values specified for the sediments in this model, and dynamic and hydrostatic pressure were taken from the model output. Reasonable agreement is seen between the predicted and observed values of yield stress, suggesting that pore fluid pressure is being appropriately applied to reduce

yield stress in the sediments. Note that while hydrostatic pressure is calculated in the part of the model domain occupied by salt, pore fluid pressure is not applied here.

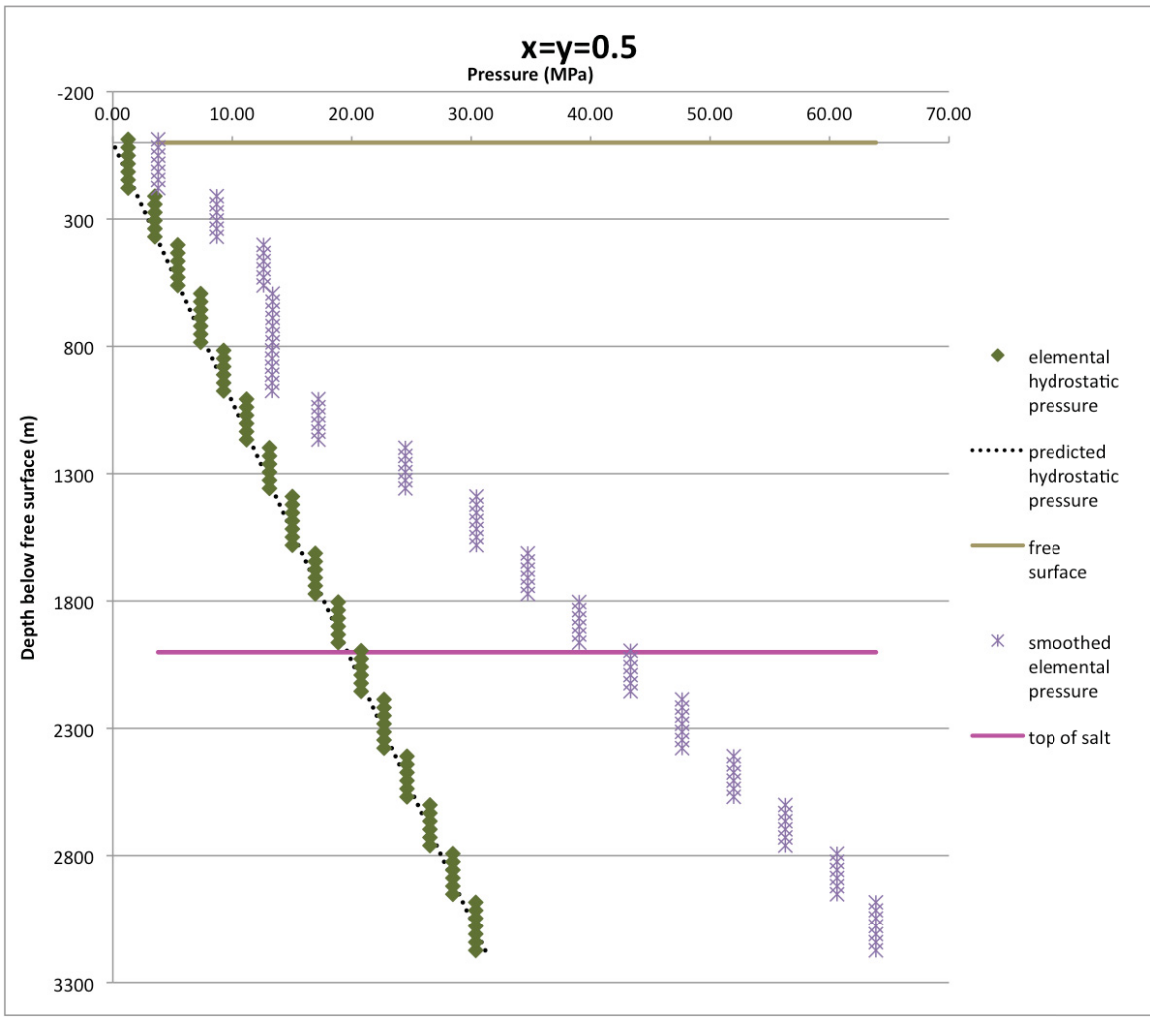

Figure 5.S6: testing the calculation of hydrostatic pressure, P_h, against predicted values calculated using $P_h=\rho*g*h$ where ρ is the pore fluid density, h is the depth below the sediment surface, and g is the acceleration due to gravity.

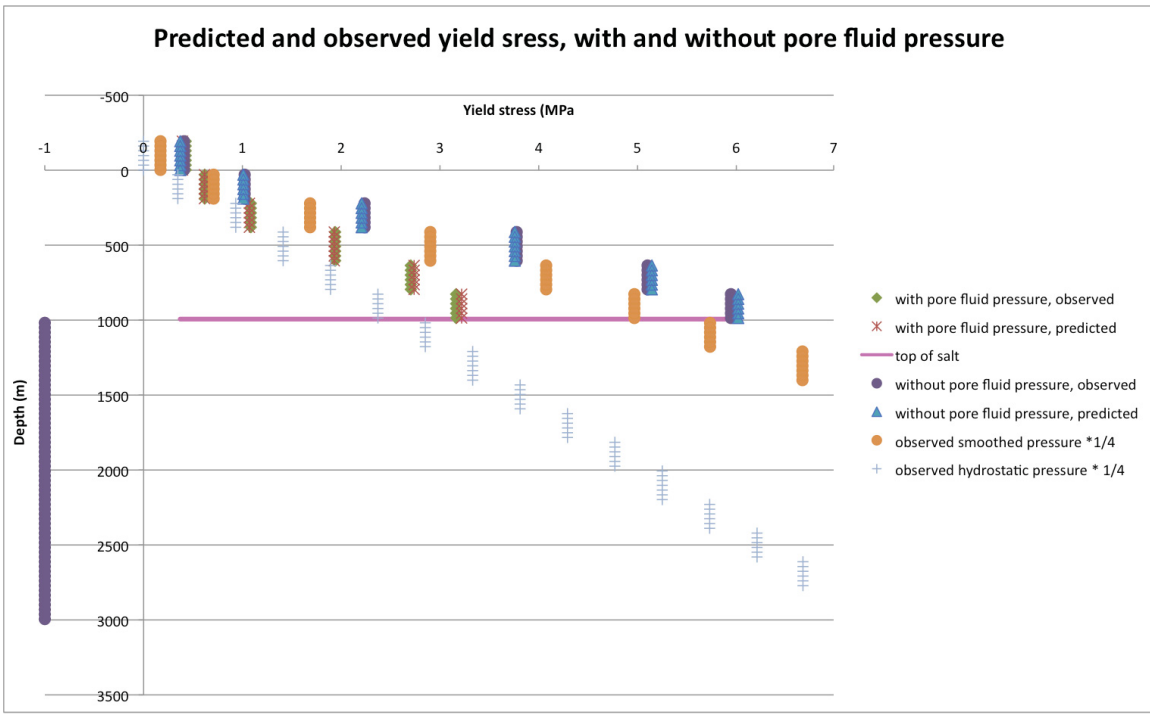

Figure 5.S7: testing implementation of pore fluid pressure, to reduce yield stress.

Water load is not incorporated in this version of DOUAR. There does not exist a means for the additional load of the water to be born by both the grains and the pore fluids, As such, applying the water load would add an unrealistic stress to the sediment. This is particularly problematic near the model surface, where sediment strength is small. Not including water load leads to errors in lateral variations in pressure, however, this effect is small where bathymetry of the sediment surface is smooth.

5.9 References

Albertz, M. & Beaumont, C. (2010) An investigation of salt tectonic structural styles in the Scotian Basin, offshore Atlantic Canada: 2. Comparison of observations with geometrically complex numerical models. *Tectonics*, 29, TC4018, doi: 10.1029/2009TC002540.

Albertz, Markus, and Steven J. Ings. "Some consequences of mechanical stratification in basin-scale numerical models of passive-margin salt tectonics." *Geological Society, London, Special Publications* 363.1 (2012): 303-330.

Albertz, M., C. Beaumont, J.W. Shimeld, S.J. Ings, and S. Gradmann (2010), An investigation of salt tectonic structural styles in the Scotian Basin, offshore Atlantic Canada: 1: Comparison of observations with geometrically simple numerical models, *Tectonics*, *29*, TC4017, doi:10.1029/2009TC002539.

Baikpour, S., G. Zulauf, A. Sebti, H. Kheirolah, and C. Dieti (2010), Analogue and geophysical modelling of the Garmsar Salt Nappe, Iran: constraints on the evolution of the Alborz Mountains, *Geophysical Journal International*, *182*(2), 599-612, doi: 10.1111/j.1365-246X.2010.04656.8.

Bonini, M. (2003), Detachment folding, fold amplification, and diapirism in thrust wedge experiments, *Tectonics*, *22*(6), 1065-1076, doi: 0.1029/2004JB003552.
Brun, J.P., and T.P.O. Mauduit (2009), Salt rollers: Structure and kinematics from analogue modelling, *Marine and Petroleum Geology*, *26*(2), 249-258, doi: 10.1016/j.marpetgeo.2008.02.002.

Braun, J.P., Thieulot, C., Fullsack, P., DeKool, M., Beaumont, C., and Huismans, R. (2008). DOUAR: A new three-dimensional creeping flow numerical model for the solution of geological problems. *Physics of the Earth and Planetary Interiors,* 171(1): 76-91. doi:10.1016/j.pepi.2008.05.003

Brun, J.P., and X. Fort (2011), Salt tectonics at passive margins: Geology versus models, *Marine and Petroleum Geology*, *28*, 1123-1145, doi: 0.1016/j.marpetgeo.2011.03.004.

Burchardt, S., Koyi, H. and Schmeling, H. (2011) Strain pattern within and around denser blocks sinking within Newtonian salt structures. *Journal of Structural Geology*, 33(2), 145-153, doi: 10.1016/j.jsg.2010.11.007.

Cathles, L.M, 1975. The viscosity of the Earth's mantle. Princeton Univ. Press. Princeton, N.J. 386 pp.

Chemia, Z., Koyi, H. and Schmeling, H. (2008) Numerical modeling of rise and fall of a dense layer in salt diapirs. *Geophysical Journal International*, 172(2), 798-816, doi: 10.1111/j.1365- 246X.2007.03661.x.

Costa, E., and B.C. Vendeville (2002), Experimental insights on the geometry and kinematics of fold-and-thrust belts above weak, viscous evaporitic decollement, *Journal of Structural Geology*, *24*(11), 1729-1739, doi: 10.1016/S0191-8141(01)00169-9.

Del Ventisette, C., D. Montanari, M. Bonini, and F. Sani (2005), Positive fault inversion triggering 'intrusive diapirism': an analogue modeling perspective, *Terra Nova*, *17*, 478-485, doi: 0.1111/j.1365-3121.2005.00637.x.

Fernandez, N., and Kaus, B. J.P. (2014). Influence of pre-existing salt diapirs on 3D folding patterns. *Tectonophysics*, 637: 354-369. doi:10.1016/j.tecto.2014.10.021.

Fort, X., and J. P. Brun. "Kinematics of regional salt flow in the northern Gulf of Mexico." *Geological Society, London, Special Publications,* 363.1 (2012): 265-287.

Fullsack, P. (1995), An arbitrary Lagrangian-Eulerian formulation for creeping flows and its application in tectonic models, *Geophysical Journal International*, *120*(1), 1-23.

Ge, H.X., M.P.A. Jackson, and B.C. Vendeville (1997), Kinematics and dynamics of salt tectonics driven by progradation, *American Association of Petroleum Geologists Bulletin*, *81*(3), 398-423.

Gemmer, L., Beaumont, C., and Ings, S.J., 2005. Dynamic modeling of passive margin salt tectonics: effects of water loading, sediment properties, and sedimentation patterns. Basin Research, 17, 383-402.

Goteti, Rajesh, Steven J. Ings, and Christopher Beaumont. 2012. "Development of salt minibasins initiated by sedimentary topographic relief." Earth and Planetary Science Letters 339: 103-116.

Goteti, R., Beaumont, C. and Ings, S.J. (2013) Factors controlling early stage salt tectonics at rifted continental margins and their thermal consequences. *Journal of Geophysical Research – Solid Earth*, 118(6), 3190-3220, doi: 10.1002/jgrb.50201.

Hudec, M.R., Jackson, M.P.A., and Schultz-Ela, D.D. (2009). The paradox of minibasin subsidence into salt: clues to the evolution of crustal basins. Geol Soc. Am. Bull. 121, 201-221.

Hudec, Michael R., and Martin PA Jackson. "Terra infirma: understanding salt tectonics." *Earth-Science Reviews* 82.1 (2007): 1-28.

Ismail-Zadeh, Alik, et al. "Three-dimensional forward and backward modelling of diapirism: numerical approach and its applicability to the evolution of salt structures in the Pricaspian basin." *Tectonophysics* 387.1 (2004): 81-103.

Kaus, B.J.P., and Podladchikov, Y.Y. (2001). Forward and reverse modeling of the three-dimensional viscous Rayleigh-Taylor instability. *Geophysical Research Letters*, 28(6): 1095-1098. Doi: 10.1029/2000GL011789.

Longoni, Matteo, A. Cristiano I. Malossi, and Andrea Villa. "A robust and efficient conservative technique for simulating three-dimensional sedimentary basins dynamics." *Computers & Fluids* 39.10 (2010): 1964-1976.

Longoni, Matteo, et al. "An ALE-based numerical technique for modeling sedimentary basin evolution featuring layer deformations and faults." *Journal of Computational Physics* 230.8 (2011): 3230-3248.

Massimi, P., Quarteroni, A., Saleri, F., and Scrofani, G. (2007). Modeling of salt tectonics. *Computer methods in applied mechanics and engineering*, *197*(1), 281-293.

McClay, K., T. Dooley, and G. Zamora (2003), Analogue models of delta systems above ductile substrates, in, *Subsurface Sediment Mobilization*, *Geological Society Special Publication*, *216*, edited by P. Van Rensbergen, R.R. Hillis, A.J. Maltman, and C.K.Morley, 411-428, doi: 10.1144/GSL.SP.2003.216.01.27.

Schweiger, H. (1994), On the use of drucker-prager failure criteria for earth pressure problems, Comput. Geotech., 16(3), 223–246, doi:10.1016/
0266-352X(94)90003-5.

Warsitzka, M., Kley, J., Jahne, F., and N. Kukowski (IN PRESS), Salt diapirism driven by differential loading – some insights from analogue modelling, *Tectonophysics*, doi: 10.1016/j.tecto.2011.11.018.

Chapter 6: Discussion

This thesis consists of four independent projects, related through their connection to the study of salt tectonics at rifted continental margins. Each of the projects presented here makes a new contribution to our understanding of the development or study of salt tectonics. This work spans different settings and scales, from individual minibasins, as small as 12 km across, to rifted continental margin pairs, extending over 500 km. Some models mimic physical analogue experiments, but most are designed to approximate natural settings. In most cases the model design has been chosen with an intentional simplicity, to highlight general patterns of physical behavior. Some models have been designed to represent the more nuanced elements of actual natural settings (for example, layered evaporite in the central Red Sea). In all cases there is an emphasis on the processes responsible for the development of salt tectonics, more so than highlighting resultant structures. All four projects in this thesis use numerical modeling experiments, with the last project showing potential in a new direction, presenting fully 3D models of salt and sedimentary overburden.

The following section places each of the four projects comprising this thesis in the context of previous and ongoing research, and discusses the major contributions of each study to the field of salt tectonics research. Limitations and the current work and possibilities for future research are also noted. This section is intended to augment the discussion sections of each of the individual papers.

6.1 Paper 1: Density Scaling in Physical Analogue Models of Salt Tectonics

This paper contributes to an ongoing discussion within the community of physical analogue modelers, on the importance of density scaling of the materials used to model salt and sedimentary rock. It's been known for some time that these materials are generally not scaled correctly to nature, however, this discrepancy is usually considered inconsequential. Often, little or no explanation is given justifying authors' choice to downplay the importance of density scaling in physical analogue models of salt tectonics. This paper directly answers the question of how important these errors in density scaling are, using a simple model design meant to mimic a physical analogue apparatus.

The results of this paper show that substantially different styles of salt tectonic deformation develop in response to prograding, deltaic type sediment over a salt body of initially uniform thickness, for models with correct density scaling vs comparable models with density scaling typical of physical analogue experiments. The same initial configuration was used in models with and without the corrections to density scaling. The model design has a flat base, representing the table-top type apparatus commonly used in physical analogue experiments. Salt is linear viscous, and sediment is frictional-plastic.

While the models of this paper capture many of the key features typical of physical analogue experiments studying salt tectonics, some aspects of the physical experiments were not incorporated. For example, prograding sediments were applied continuously (or rather, at each time step) in these numerical experiments, while in physical analogue experiments, prograding sediment is applied in discrete stages. This will result in a

different loading pattern between the two types of experiment. In the models of this paper, the differential pressure under the sediment wedge gradually advances seaward, with the sediment profile tending to expel salt laterally, out from under the toe of the sediment wedge. In physical analogue experiments, the progradation profile is often effectively advanced a considerable distance instantaneously, abruptly repositioning the slope of the progradation front, and with it the differential pressure driving lateral salt flow. This may lead to more salt being trapped under the prograding wedge, and possibly to the development of complex salt tectonic structures in the landward part of the model, as a consequence. This difference could be addressed with numerical models like the ones in this paper, but with the progradation profile advanced in stages, with sedimentation ceasing between each episode of advancement. The most obvious aspect of physical analogue experiments not captured by the models of this paper is their three-dimensional nature. The models in this paper are 2D, and as such do not allow for out-of-plane salt flow. It is therefore impossible to distinguish between 2D features and their 3D equivalents, for example salt diapirs vs salt walls, when describing the results of this paper and comparing them against physical analogue studies. Additionally, development of minibasins may proceed more slowly in these models than it would in fully 3D equivalent experiments, because salt flow from underneath sinking sediment is limited to the plane of the model. Equivalent, fully 3D numerical models would more accurately represent this aspect of minibasins development, and provide a more direct comparison with physical analogue experiments.

This paper was the first attempt to directly assess the impact and importance of density scaling errors in the materials used to model salt and sedimentary rocks in physical analogue studies of salt tectonics. Future work on this subject could include 2D and/or 3D experiments, designed to incorporate more subtle aspects of physical analogue experiments, such as advancement of the progradation profile in discrete steps. A range of model designs could also be included, to ascertain the importance of this density scaling error for different types of physical experiments, for example, undulating, uneven sediment loading, rather than a prograding, deltaic type sediment front. Ideally, comparable physical analogue experiments would also be conducted, using materials with and without the corrections to density scaling suggested in this paper. These physical experiments would provide a direct link between the analytical work and numerical modeling presented in this paper, and the world of physical analogue modeling, and may increase the impact of the findings of this paper in the physical analogue modeling community.

6.2 Paper 2: Syn-rift salt tectonics at intermediate width margins

This project explores the impact of timing of salt deposition relative to rifting on the distribution and deformation of salt, for a rifted continental margin pair of moderate width. Prior to this work, only a handful of studies had considered the interaction between rifting and sedimentation, as it relates to salt tectonics. Considerable effort had been directed towards understanding the processes of rifting (e.g. Gueydan *et al*., 2008; Nagel and Buck, 2004; Lavier and Manatschal, 2006; Van Avendonk *et al*., 2009;

Huismans and Beaumont, 2011), and separately towards unraveling the key controls on the development of salt tectonics (e.g. Chemia *et al*., 2008; Albertz *et al*., 2010; Albertz and Beaumont, 2010; Longoni *et al*., 2010; Burchardt*, et al*., 2011; Goteti *et al.*, 2012; Ge *et al*., 1997; Hudec and Jackson, 2007; Hudec *et al*., 2009; Warren*,* 2010; Warren*,* 2006). One previous study directly considered the question of how timing of salt deposition relative to rifting impacts the style of salt tectonics that develops (Rowan, 2014). Rowan (2014) used a series of conceptual models, supported by compiled data from natural examples, to explore the differences in salt tectonic styles observed for salt deposition in the pre-rift, and early, mid, and late syn-rift periods (which he terms syn-stretching, syn-thinning, and syn-exhumation phases of rifting). Allen and Beaumont (2015) is the first time that numerical modeling has been used to show how different distributions and styles of deformation of salt can develop as a direct consequence of timing of salt deposition relative to rifting. Salt tectonics and rifting evolution are directly linked in this work; salt basin geometry develops as a direct consequence of stretching and thinning of the lithosphere, and salt deformation is driven both by subsequent sedimentation and by changes in the salt geometry driving by underlying crustal rifting. The same general model design is used in all experiments in this paper; differences in distribution and style of deformation of salt result solely from the timing of salt deposition relative to rifting and the nature of pre-and post-salt sedimentation. This paper complements the work of Rowan (2014), with an alternate approach to studying syn-rift salt tectonics.

Additional complexities could be added to the work presented in Chapter 3, to capture a range of scenarios observed in nature. Variations included three phases of salt deposition, early, mid, and late syn-rift salt, and two salt viscosities (10^{18} and 10^{19} Pa s). Some facets of the work that could be extended include: alternate continental crust and/or lithosphere rheologies (see Chapter 4), pre-rift salt deposition, layered or non-linear viscous salt, and multiple episodes of salt deposition. The three periods of syn-rift salt deposition were chosen to show contrasting examples of salt tectonic styles and salt distribution. Intermediate or blended cases, with salt deposition between two of the phases presented here, are certainly likely in nature. A more extensive study of this subject could consider a larger range of windows of salt deposition. Multiple episodes of salt deposition can also occur during rifting and continental breakup. This paper could be extended to consider models with multiple, discrete episodes of salt deposition. Finally, in nature salt is typically layered; a more thorough consideration of syn-rift salt tectonics could include the deposition of layered evaporite, with viscosities representing different types of evaporite. The linear viscous rheology used in this paper is thought to be a good representation of halite. Layered salt has been modeled previously, for experiments with pre-defined salt basin geometries and initial salt configuration (Albertz and Ings, 2012), and has been shown to impact the style of deformation of salt. Allen and Beaumont (2015) makes some consideration of layered salt in the central Red Sea example, where non-halite evaporites are modeled as frictional-plastic materials. A more extensive study of syn-rift salt tectonics could include layered salt in models exploring the range of timing of salt deposition relative to rifting, as well as the effect of multiple phases of rifting.

6.3 Paper 3: Sedimentation and syn-rift salt tectonics at wide rifted margins

This paper focuses on wide rifted margins, generated from weak continental crust, and explores the interactions between sedimentation, salt tectonics, and ongoing rifting. This paper extends the previous analysis of syn-rift salt tectonics and intermediate width margins (Chapter 3), to consider another crustal rheology (weak crust) and resultant margin type (wide margins). In addition, this paper delves more deeply than the second paper into the impact of sedimentation on the evolution of rifting. The weak continental crust used in the models of this paper is more susceptible to flow in response to sediment loading, and so deforms more significantly in response to sedimentation. Both distributed, aggrading and localized, prograding, deltaic-type sedimentation are considered, and their impacts on the style of deformation of the margin are explored. Two windows of salt deposition, early and late syn-rift salt, are explored. The distribution of salt and interaction of salt with ongoing sedimentation were found to differ notably, compared to the intermediate crust model used in Paper 2, highlighting the need to explore weak crust, wide margin experiments separately.

This paper considered a range of sedimentation scenarios, in examining the impact of sedimentation on development of a wide rifted margin pair. The development of deep sedimentary basins through localized, prograding sediment showed general agreement with previous work in this area (e.g. Morley and Westaway, 2006; Clift et al., 2015). A new perspective on this phenomenon, contributed here, is a dramatic difference in the

tendency of these deep basins to form, or not form, in response to different amounts of sediment deposition, for the same weak crust model. This work showed that for the same weak crust, substantial sedimentation produces deep basins while minimal sedimentation does not. Further work could explore this threshold in greater detail. This paper also briefly explored deep basin formation in models with strong and intermediate crust strengths, and found that deep sedimentary basins of this type tend not to form for stronger crusts. This work could be extended to fine tune the crust strengths used in the included models, and more fully explore the range of crust strengths over which deep sedimentary basins tend to form through flow in the lower crust (and the degree to which they form for different weak crust models). Distributed, aggrading sediment was also shown to impact development of the margin pair for the weak crust base model used in this paper, producing more abrupt changes in crustal thickness across the margin. Two different durations of aggrading sedimentation were used to show that this effect is most pronounced when aggrading sediment continues throughout rifting. The amount of sediment deposited in this part of the analysis was substantial; these models are thought of as end member cases. This work could be extended to include different amount of aggrading sediment deposition throughout the rifting process.

6.4 Project 4: 3D minibasins formation through uneven sedimentation

The final project in this thesis uses fully 3D numerical modeling software to study minibasins formation through uneven sedimentation. The preliminary results presented here demonstrate the potential of this study, and indicate the potential for a notable

advancement on previous numerical modeling of salt tectonics. The vast majority of numerical modeling studies of salt tectonics have been two-dimensional, which captures many important features of the deformation of salt and surrounding sediment, but is obviously limited to a two-dimensional viewpoint. Salt tectonics is highly three-dimensional, with significant out-of plane variation observed in nature. A few studies (e.g. Ismael-Zadeh et al., 2004; Koupriantchik et al., 2005; Longoni et al., 2011; Longoni et al., 2010; Massimi et al., 2007; Fernandez and Kaus, 2014; Kaus and Podladchikov, 2001) have modeled salt deformation using 3D numerical software. These have generally made a set of simplifications that detract from the realistic physical evolution of the system, including: sediments and sedimentary rock modeled as viscous material, and a uniform sediment density not compacting with depth. The results presented in this thesis are preliminary, and will be fine-tuned for publication.

These results presented here could be enhanced in several ways, in addition to the code modifications discussed in Chapter 5. Most of the models included in this chapter have a confined minibasin geometry, meaning that the wavelength of sediment deformation used to drive minibasin formation is the same as the spatial dimensions of the model. That is to say, the entire model space is taken up with one minibasin. Goteti et al. (2012), in their study using 2D models, found that minibasin development differed when an unconfined geometry was used. This type of geometry differs in that the model domain is larger than the dimensions of the minibasin, and salt is free to flow further away from the area of uneven sedimentation. A continuation of the present study would include a more complete study of the bahviour of minibasin that are unconfined. Among the

additions to the software DOUAR is the ability to combine progradation and aggradation styles of sedimentation. Further work on this study would include models where prograding and aggrading sediment apply competing pressures that drive salt deformation in combination.

Given the differences observed for the evolution of 2D-equivalent versus fully 3D models, it is worth considering whether the results of the first paper, examining the impacts of density scaling in physical analogue models, may differ if a fully 3D modeling approach were used to study this problem. The 2D models used in the first paper are meant to represent 2D-equivalent physical analogue models. To ascertain whether the same difference in structural evolution persists in a fully 3D model, the models from the first paper could be considered in a fully 3D approach. This would determine the difference between salt wall and diapir formation, in response to different density scaling options. This point should be revisited when final results of the 3D modeling analysis have been presented.

6.5 Synthesis

The four projects within this thesis relate to the development or study of salt tectonics at rifted continental margins. The second and third projects make this connection directly, using a large model domain that encompasses the entire rifted margin pair, and follows the evolving rifted margin from the onset of rifting through continental breakup. The first and fourth projects focus on a smaller scale, studying a single salt basin, in the case

of the first paper, or individual salt tectonic structures, in the fourth project. These smaller scale studies effective zoom in on a particular area of what would be a larger rifted continental margin.

The second and third projects allow for a comparison of the development of salt tectonics in the context of ongoing rifting of stronger and weaker continental crust. In these models, the size, location, and evolving geometry of salt basins derive directly from the dynamics of the rifting system, as they would in nature. The geometry of basins available for salt deposition is notably different between the second and third projects, which use stronger and weaker continental crust in the model design. The intermediate strength crust of the second project deforms primarily through movement along distinct shear zones that penetrate most or all of the way through the crust. This style of deformation leads to more distinct, separate, and deeper basins. The weaker crust of the third project thins mostly via distributed deformation, and produces basins that are wider, shallower (though this may be influenced by sedimentation), and more connected. These differences in style of deformation of the crust and resultant distinct geometries of basins impact the initial geometry of salt and its mobility as rifting continues. Lateral movement of salt may be impeded by basement steps at the edges of basins; in this sense weaker crusts allow for more free flow of salt across the margin, as weak crust produces less pronounced basement steps. On the other hand, stronger crust produces a more sharply tapered (narrower) margin which may facilitate salt flow by gravity gliding, where the basement has a steeper slope than is generally seen in the models with weaker crust. In the case of a stronger crust (such as the intermediate strength crust of the second project),

the initial thickness of salt and the total volume of salt deposited may also respond to ongoing deformation of the crust, in that the additional load of salt deposited into the proximal basins will drive basin subsidence via movement along the basin bounding faults. This process is less pronounced for the weaker crust models of the third paper, because crust deformation is less localized. In this case, flow of the mid to lower crust and formation of deep basins may depend on a pressure gradient induced by deposited sediments; salt is deposited with a generally flat upper surface and does not produce such a pressure gradient.

The distribution and style of deformation of salt varied with both the timing of salt deposition relative to rifting and the style of deformation of the underlying crust (deriving in these studies from the crust strength). Figure 6.1 summarizes the trends in salt distribution and deformation in response to these two factors. Wide salt bodies of approximately uniform thickness, extending across the mid to distal margin, are more likely to form when salt is deposited later in the syn-rift period, or at margins formed from weaker crust. Late syn-rift deposition and weak crust also favour deposition of salt as an initially continuous body extending across the margin pair. Thick salt bodies in general, and particularly at the proximal margin, are more likely to form over stronger crusts (which produce deeper basins), and in the early syn-rift period. The later point is especially true for the intermediate strength crust models, in which extension at the proximal margin occurs primarily in the early syn-rift; with reduced deformation of the proximal margin in the mid to late syn-rift time, accommodation space for salt deposition is not generated in these models. Although not shown in the models presented here,

conceivably weak crusts could support deposition of thick salt in proximal margin basins in the late syn-rift period, if previous sedimentation has initiated a feedback loop driving deep basin formation. Seaward flow of salt under gravity gliding and gravity spreading (when sedimentation facilitates this) are more likely for salt deposited over intermediate strength crusts, for two reasons. First, the intermediate strength crust produces basement with a more pronounced slope and second, prograding sediment interacts with the weak crust in a feedback loop that focuses deformation at the proximal margin and stalls forward movement of the sedimentation front (hence the ability for the sedimentation to provide a driving force for salt flow is impeded). For this same reason, some specific types of internal deformation of the salt, those that rely on either steep basement slopes or loading by prograding post-salt sediment, are seen in the models with intermediate strength crust and not in those with weak crust. Examples include flow of older salt over younger salt at the mid margin, and rotated flow within thick salt bodies. Stretching and thinning of salt bodies at the mid to distal margin occurs effectively in the models with weak crust, and in the intermediate strength crust model with late syn-rift salt deposition. This type of salt deformation relies on deposition of salt as a continuous body across the margin pair, so that the salt experiences tension in response to the ongoing rifting process. Salt escarpments form in all models where a wide body of salt overlies crust and sediment that experience localized deformation; this can be seem for the late syn-rift cases of both the intermediate strength crust and the weak crust model designs.

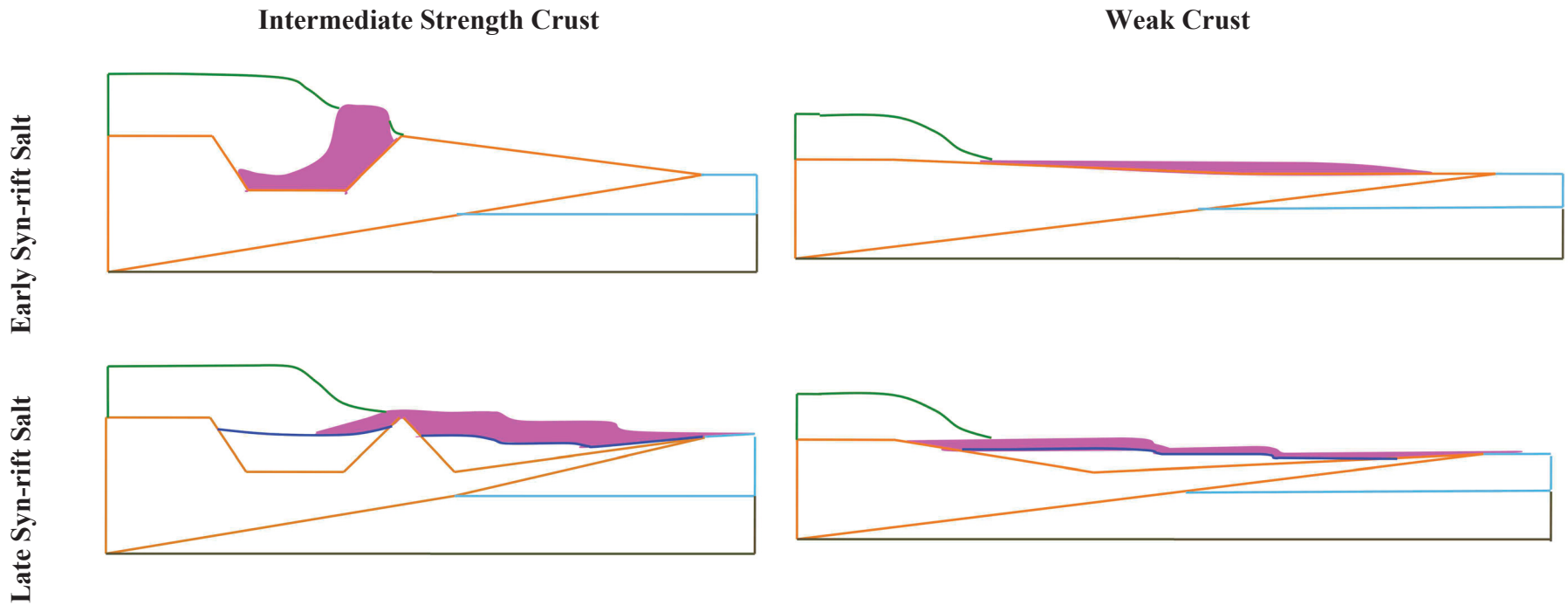

Figure 6.1: Schematic diagram showing trends in salt distribution and deformation for early vs late syn-rift salt deposition and intermediate vs weak crust strength.

The research in the four projects of this thesis takes advantage of current and cutting edge numerical modeling capabilities. The first three projects use 2D numerical modeling software, while the fourth project branches to fully 3D modeling. The second and third projects use a nested approach, which allows high resolution visualization of salt movement while capturing the physical system of the entire rifting margin. The models in the first project are intentionally of a simpler design, with a pre-defined salt basin geometry, flat base of the model, and no allowance for isostasy; this approach facilitates comparison of these models with physical analogue experiments. The fourth project focuses on single minibasins, which allows each model to capture the development of an individual minibasin with reasonable spatial resolution. The move to the fully 3D numerical modeling of salt tectonics is new, particularly with the physically realistic characterization of clastic sedimentary overburden presented in this project. As such, the capacity to produce models with fine resolution, both in time and in space, is still evolving. Fully 3D models with relatively small overall spatial and temporal dimensions, such as the single minibasins models in this thesis, make a useful contribution, using the capacity of current hardware and software.

6.6 References

Albertz, M. and Beaumont, C. (2010) An investigation of salt tectonic structural styles in the Scotian Basin, offshore Atlantic Canada: 2. Comparison of observations with geometrically complex numerical models. *Tectonics*, 29, TC4018, doi: 10.1029/2009TC002540.

Albertz, M., Beaumont, C., Shimeld, J.W., Iings, S.J. and Gradmann, S. (2010) An investigation of salt tectonic structural styles in the Scotian Basin, offshore Atlantic Canada: 1: Comparison of observations with geometrically simple numerical models. *Tectonics*, 29, TC4017, doi:10.1029/2009TC002539.

Albertz, M., and Ings, S.J. (2012). Some consequences of mechanical stratification in basin-scale numerical models of passive-margin salt tectonics. *Geological Society, London, Special Publications*, 363, p303-330. Doi: 10.1144/SP363.14.

Burchardt, S., Koyi, H. and Schmeling, H. (2011) Strain pattern within and around denser blocks sinking within Newtonian salt structures. *Journal of Structural Geology*, 33(2), 145-153, doi: 10.1016/j.jsg.2010.11.007.

Chemmia, Z., Koyi, H. and Schmeling, H. (2008) Numerical modeling of rise and fall of a dense layer in salt diapirs. *Geophysical Journal International*, 172(2), 798-816, doi: 10.1111/j.1365-246X.2007.03661.x.

Clift, P.D., Brune, S., and Quinteros, J. (2015). Climate changes control offshore crustal structure at South China Sea continental margin. Earth and Planetary Science Letters, 420, 66-72. Doi: 10.1016/j.2015.03.0320012-821x

Fernandez, N., and Kaus, B. J.P. (2014). Influence of pre-existing salt diapirs on 3D folding patterns. *Tectonophysics*, 637: 354-369. doi:10.1016/j.tecto.2014.10.021.

Ge, H.X., Jackson, M.P.A. and Vendeville, B.C. (1997) Kinematics and dynamics of salt tectonics driven by progradation. *American Association of Petroleum Geologists Bulletin*, 81(3), 398-423.

Goteti, R., Ings, S.J. and Beaumont, C. (2012) Development of salt minibasins initiated by sedimentary topographic relief. *Earth and Planetary Science Letters*, 339, 103-116, doi: 10.1016/j.epsl.2012.04.045.

Gueydan, F., Morency, C. and Brun, J.P. (2008) Continental rifting as a function of lithosphere mantl strength. *Tectonophysic*s, 460, 83-93. doi:10.1016/j.tecto.2008.08.012.

Hudec, M.R. and Jackson, M.P.A. (2007). Terra Infirma: Understanding salt tectonics, *Earth Science Reviews*, 82(1-2), 1-28, doi 10.1016/j.earscirev.2007.01.001.

Hudec, M.R., Jackson, M.P.A. and Schultz-Ela, D.D. (2009) The paradox of minibasin subsidence into salt: Clues to the evolution of crustal basins. *Geological Society of America Bulletin, 121*(1-2), 201-221, doi: 10.1130/B26275.1.

Huismans, R. and Beaumont, C. (2011) Depth-dependent extension, two-stage breakup and cratonic underplating at rifted margins. *Nature*, 473(7345), 74-U85, doi: 10.1038/nature09988.

Ismail-Zadeh, Alik, et al. (2004). Three-dimensional forward and backward modelling of diapirism: numerical approach and its applicability to the evolution of salt structures in the Pricaspian basin. *Tectonophysics,* 387.1, 81-103.

Kaus, B.J.P., and Podladchikov, Y.Y. (2001). Forward and reverse modeling of the three-dimensional viscous Rayleigh-Taylor instability. *Geophysical Research Letters*, 28(6): 1095-1098. Doi: 10.1029/2000GL011789.

Koupriantchik, D., Hunt, S.P., Boult, P.J., and Meyers, A.G. (2005). Geomechanical modeling of salt diapirs: 3D salt structure from the Officer Basin, South Asutralia. *Munson TJ, Ambrose GJ. Proceedings of the Central Australian Basins Symposium (CABS), Alice Springs, Northern Territory*. Vol. 1618.

Lavier, L.L. and Manatschal, G. (2006) A mechanism to thin the continental lithosphere at magma-poor margins. *Nature,* 440(7082,: 324-328, doi: 10.1038/nature04608.

Longoni, M., Malossi, A.C.I. and Villa, A. (2010) A robust and efficient conservative technique for simulating three-dimensional sedimentary basin dynamics. *Computers & Fluids*, 39(10), 1964-1976, doi: 10.1016/j.compfluid.2010.06.028.

Longoni, Matteo, et al. (2011). An ALE-based numerical technique for modeling sedimentary basin evolution featuring layer deformations and faults." *Journal of Computational Physics* 230.8, 3230-3248.

Massimi, P., Quarteroni, A., Saleri, F., and Scrofani, G. (2007). Modeling of salt tectonics. *Computer methods in applied mechanics and engineering*, *197*(1), 281-293.

Morley, C.K., and Westaway, R. (2006). Subsidence in the super-deep Pattani and Malay basin of Southeast Asia: a coupled model incorporating lower-crustal flow in response to post-rift sediment loading. *Basin Research*, 18, 51-84. Doi: 10.1111/j.1365-2117.2006.00285.x

Nagel, T.J. and Buck, W.R. (2004) Symmetric alternative to asymmetric rifting models. *Geology*. 32(11), 937-940, doi: 10.1130/G20785.1.

Rowan, M.G. (2014). Passive-margin salt basins: hyperextension, evaporite deposition, and salt tectonics. *Basin Research*, *2*6, 154-182, doi: 10.1111/bre.12043.

Van Avendonk, H.J.A., Lavier, L.L., Sshillingston, D.J. and Manatschal, G. (2009) Extension of continental crust at the margin of the eastern Grand Banks, Newfoundland. *Tectonophysics*, 468, 131-148, doi:10.1016/j.tecto.2008.05.030.

Warren, J.K. (2010) Evaporites through time: Tectonic, climatic and eustatic controls in marine and nonmarine deposits. *Earth-Science Reviews,* 98, 217–268, doi: 10.1016/j.earscirev.2009.11.004.

Warren, J. K. (2006) Evaporites: Sediments, Resources and Hydrocarbons. Springer, Berlin.

References

Adam, J., Ge, Z. and Sanchez, M. (2012a) Salt-structural styles and kinematic evolution of the Jequitinhonha deepwater fold belt, central Brazil passive margin. *Marine and Petroleum Geology*, 37, 101-120, doi: 10.1016/j.marpetgeo.2012.04.010.

Adam, J., Ge, Z. and Sanchez, M. (2012b) Post-rift salt tectonic evolution and key control factors of the Jequitinhonha deepwater fold belt, central Brazil passive margin: Insights from scaled physical experiments. *Marine and Petroleum Geology*, 37, 70-100, doi: 10.1016/j.marpetgeo.2012.06.008.

Albertz, M. and Beaumont, C. (2010) An investigation of salt tectonic structural styles in the Scotian Basin, offshore Atlantic Canada: 2. Comparison of observations with geometrically complex numerical models. *Tectonics*, 29, TC4018, doi: 10.1029/2009TC002540.

Albertz, M., Beaumont, C., Shimeld, J.W., Iings, S.J. & Gradmann, S. (2010) An investigation of salt tectonic structural styles in the Scotian Basin, offshore Atlantic Canada: 1: Comparison of observations with geometrically simple numerical models. *Tectonics*, 29, TC4017, doi:10.1029/2009TC002539.

Albertz, M., and Ings, S.J. (2012). Some consequences of mechanical stratification in basin-scale numerical models of passive-margin salt tectonics. *Geological Society, London, Special Publications*, 363, p303-330. Doi: 10.1144/SP363.14.

Allen, J. and Beaumont, C. (2015). Continental Margin Syn-Rift Salt Tectonics at Intermediate Width Margins. Basin Research. 10.1111/bre.12123

Athy, L.F. (1930), Density, porosity, and compaction of sedimentary rocks, *American Association of Petroleum Geologists Bulletin*, *14*, 1-22.

Augustin, N., Devey, C.W., Van Der Zwan, F.M., Feldens, P., Tominaga, M., Bantan, R.A., and Kwasnitschka T. (2014) The rifting to spreading transition in the Red Sea. *Earth and Planetary Science Letters*, 395, 217-230. doi: 10.1016/j.epsl.2014.03.047.

Baikpour, S., G. Zulauf, A. Sebti, H. Kheirolah, and C. Dieti (2010), Analogue and geophysical modelling of the Garmsar Salt Nappe, Iran: constraints on the evolution of the Alborz Mountains, *Geophysical Journal International*, *182*(2), 599-612, doi: 10.1111/j.1365-246X.2010.04656.8.

Baldwin, B., and C.O. Bulter (1985), Compaction curves, *American Association of Petroleum Geologist Bulletin, 69*, 622-623.

Beaumont, C. and Ings, S.J. (2012) Effect of depleted continental lithosphere counterflow and inherited crustal weakness on rifting of the continental lithosphere:

General results. *Journal of Geophysical Research – Solid Earth*, 177, B08407, doi: 10.1029/2012JB009203.

Beaumont, C., Jamieson, R.A., Butler, J.P. & Warren, C.J. (2009) Crustal structure: A key constraint on the mechanism of ultra-high-pressure rock exhumation. *Earth and Planetary Science Letters*, 287(1-2), 116-129, doi: 10.1016/j.epsl.2009.08.001.

Beaumont, C., Nguyen, M.H., Jamieson R.A. & Ellis, S. (2006) Channel flow, ductile extrusion and exhumation on continental collision zones. *Geological Society Special Publication*. 268, 91-145, doi: 0.1144/GSL.SP.2006.268.01.05.

Bialas, R.W. and Buck, W.R. (2009) How sediment promotes narrow rifting: Application to the Gulf of California. *Tectonics*, 28, TC4014, doi:10.1029/2008TC002394 .

Bialas, R.W., Funiciello, F., and C. Faccanna (2011), Subduction and exhumation of continental crust: insights from laboratory models, *Geophysical Journal International, 184*, 43-64, doi: 10.1111/j.1365-246X.2010.04824.x.

Bonini, M. (2003), Detachment folding, fold amplification, and diapirism in thrust wedge experiments, *Tectonics*, *22*(6), 1065-1076, doi: 0.1029/2004JB003552.

Bonatti, E. (1985) Punctiform initiation of seafloor spreading in the Red-Sea during transition from a continental to an oceanic rift. *Nature*, 316(6023), 33-37, doi: 10.1038/316033a0.

Bosworth, W., Huchon, P. and McClay, K. (2005) The Red Sea and Gulf of Aden basins. *Journal of African Earth Sciences*, 43(1-3), 334-378, doi: 10.1016/j.jafrearsci.2005.07.020.

Braun, J.P., Thieulot, C., Fullsack, P., DeKool, M., Beaumont, C., and Huismans, R. (2008). DOUAR: A new three-dimensional creeping flow numerical model for the solution of geological problems. *Physics of the Earth and Planetary Interiors,* 171(1): 76-91. doi:10.1016/j.pepi.2008.05.003

Braun, J. and Beaumont, C. (1989) Dynamical models of the role of crustal shear zones in asymmetric continental extension. *Earth and Planetary Science Letters*, 93(3-4), 405-423, doi: 10.1016/0012-821X(89)90039-3.

Brun, J.P., and X. Fort (2011), Salt tectonics at passive margins: Geology versus models, *Marine and Petroleum Geology*, *28*, 1123-1145, doi: 0.1016/j.marpetgeo.2011.03.004.

Brun, J.P., and X. Fort (2004), Compressional salt tectonics (Angolan margin), *Tectonophysics*, *382*, 129-150, doi: 10.1016/j.tecto.2003.11.014.

Brun, J.P., and T.P.O. Mauduit (2009), Salt rollers: Structure and kinematics from analogue modelling, *Marine and Petroleum Geology*, *26*(2), 249-258, doi: 10.1016/j.marpetgeo.2008.02.002.

Brun, J.P. (1998) Narrow rifts versus wide rifts: inferences for the mechanics of rifting from laboratory experiments, *Philosophical Transactions of the Royal Society of London*, 357, 695-712, doi: 10.1098/rsta.1999.0349.

Buck, W. R. (1991) Modes of continental lithospheric extension, J. *Geophysical Research*, 96(B12), 20,161–20,178.

Buck, W. R., (1993) Effect of lithospheric thickness on the formation of high- and low-angle normal faults. *Geology*, 21, 933–936, doi: 10.1130/0091-7613(1993)021.

Buck, W.R., Lavier, L.L. and oliakov, A.N.B. (1999) How to make a rift wide. *Philosophical Transactions of the Royal Society of London*, 357, 671-693. doi: 10.1098/rsta.1999.0348.

Burchardt, S., Koyi, H. and Schmeling, H. (2011) Strain pattern within and around denser blocks sinking within Newtonian salt structures. *Journal of Structural Geology*, 33(2), 145-153, doi: 10.1016/j.jsg.2010.11.007.

Burov, E., and Cloetingh, S. (1997). Erosion and rift dynamics: new thermomechanical aspects of post-rift evolution of extensional basins. *Earth and Planetary Science Letters*, 150: 7-26.

Butler, J.P., Beaumont, C. and Jamiesson, R.A. (2014) The Alps 2: Controls on crustal subduction and (ultra) high-pressure rock exhumation in Alpine-type orogens, *Journal of Geophysical Research*.

Carter, N.L., Handin, J., Russel, J.E. and Horseman, S.T. (1993) Rheology of rock salt. *Journal of Structural Geology*, 15, 1257-1271.

Cathles, L.M, 1975. The viscosity of the Earth's mantle. Princeton Univ. Press. Princeton, N.J. 386 pp.

Chen, A., Jin, C., Lou, Z. Chen, H., Xu, S., Huang, K., and Hu, S. (2013). Salt tectonics and Basin Evolution in the Gabon Coastal Basin, West Africa. *Journal of Earth Science*, 24(6): 903-817. Doi: 10.1007/s12583-013-0383-5.

Chemmia, Z., Koyi, H. and Schmeling, H. (2008) Numerical modeling of rise and fall of a dense layer in salt diapirs. *Geophysical Journal International*, 172(2), 798-816, doi: 10.1111/j.1365-246X.2007.03661.x.

Chenin, P. and Beaumont, C. (2013) Influence of offset weak zones in the development of rift basins: activation and abandonment during continental extension and breakup. *Journal of Geophysical Research*, 118(4), 1698-1720, doi 10.1002/jgrb.50138.

Choi, E., Buck, W.R., Lavier, L.L. and Petersen, K.D. (2013) Using core complex geometry to constrain fault strength. *Geophysical Research Letters*, 40*(*15), 3863 – 3867, doi: 10.1002/grl.50732.

Chu, D.Z. and Gordon, R.G. (1998) Current plate motions across the Red Sea. *Geophysical Journal International*, 135(2), 313-328, doi: 10.1046/j.1365-246X.1998.00658.x.

Clift, P.D., Brune, S., and Quinteros, J. (2015). Climate changes control offshore crustal structure at South China Sea continental margin. Earth and Planetary Science Letters, 420, 66-72. Doi: 10.1016/j.2015.03.0320012-821x

Cobbold, P.R., and L. Castro (1999), Fluid pressure and effective stress in sandbox models, *Tectonophysics*, *301*, 1-19, doi: 10.1016/S0040-1951(98)00215-7.

Cohen, H.A., and K. McClay (1996), Sedimentation and shale tectonics of the northwestern Niger Delta front, *Marine and Petroleum Geology*, *13*(3), 313-328, doi: 10.1016/0264-8172(95)00067-4.

Cochran, J.R. (1983) A model for the development of the Red Sea. *American Association of Petroleum Geologists Bulletin,* 67, 41-69.

Cochran, J.R. and Martinez, F. (1988) Evidence from the northern Red-Sea on the transition from continental to oceanic rifting. *Tectonophysics*, 153(1-4), 25-53, doi: 10.1016/0040-1951(88)90006-6.

Corti, G., Ranalli, G., Muluget, G., Agostini, A., Sani, F. and Zugu, A. (2010) Control of the rheological structure of the lithosphere on the inward migration of tectonics activity during continental rifting. *Tectonophysics*, *490*, 165-172, doi: 10.1016/j.tecto.2010.05.004.

Corti, G., Ranalli, G., Agostini, A. and Sokoutis, D. (2013) Inward migration of faulting during continental rifting: Effects of pre-existing lithospheric structure and extension rate. *Tectonophysics*. 594, 137-148, doi: 10.1016/j.tecto.2013.03.028.

Costa, E., and B.C. Vendeville (2002), Experimental insights on the geometry and kinematics of fold-and-thrust belts above weak, viscous evaporitic decollement, *Journal of Structural Geology*, *24*(11), 1729-1739, doi: 10.1016/S0191-8141(01)00169-9.

Crosby, A.G., White, N.J., Edwards, G.R.H., Thompson, M., Corfield, R., and Mackay, L. (2011). Evolution of deep-water rifted margins: Testing depth-dependent extensional models. *Tectonics*, 30: TC1004. Doi: 10.1029/2010TC002687.

Davison, I., Anderson, L., and Nuttall, P. (2012). Salt deposition, loading and gravity drainage in the Campos and Santos salt basins. Geological Society, London, Special Publications, 363: 159-174. Doi: 10.1144/SP363.8.

Del Ventisette, C., D. Montanari, M. Bonini, and F. Sani (2005), Positive fault inversion triggering 'intrusive diapirism': an analogue modeling perspective, *Terra Nova*, *17*, 478-485, doi: 0.1111/j.1365-3121.2005.00637.x.

Del Ventisette, C., Montanari, D., Sani, F. and BonniO, M. (2004) Basin inversion and fault reactivation in laboratory experiments. *Journal of Structural Geology*, 28(11), 2067-2083, doi: 10.1016/j.jsg.2006.07.012.

Dooley, T.P., M.P.A. Jackson, and M.R. Hudec (2007), Initiation and growth of salt-based thrust belts on passive margins: results from physical models, *Basin Research*, *19*(1), 165-177, doi: 0.1111/j.1365-2117.2007.00317.x.

Dooley, T.P., M.P.A. Jackson, and M.R. Hudec (2009), Inflation and deflation of deeply buried salt stocks during lateral shortening, *Journal of Structural Geology*, *31*, 582-600, doi: 10.1016/j.jsg.2009.03.013.

Ebinger, C., Ayele, A., Keir, D., Rowland, J., Yirgu, G., Wright, T., Belachew, M. and Hamlings, I. (2010) Length and timescales of rift faulting and magma intrusion: The Afar rifting cycle from 2005 to present. *Annual Reviews of Earth and Planetary Science,* 38, 439–66, doi:10.1146/annurev-earth-040809-152333.

Fernandez, N., and Kaus, B. J.P. (2014). Influence of pre-existing salt diapirs on 3D folding patterns. *Tectonophysics*, 637: 354-369. doi:10.1016/j.tecto.2014.10.021.

Fort, X. and Brun, J.P. (2012) Kinematics of regional salt flow in the northern Gulf of Mexico. *Geological Society, London, Special Publications,* 363, 265-287, doi: 10.1144/SP363.12.

Fullsack, P. (1995), An arbitrary Lagrangian-Eulerian formulation for creeping flows and its application in tectonic models, *Geophysical Journal International*, *120*(1), 1-23.

Funck, T., Jackson, H.R., Louden, K.E., Dehler, S.A., and Wu., Y. (2004). Crustal structure of the northern Nova Scotia rifted continental margin (eastern Canada). Journal of Geophysical Research. 109: B09102, doi:10.1029/2004JB003008.

Fullsack, P. (1995), An arbitrary Lagrangian-Eulerian formulation for creeping flows and its application in tectonic models, *Geophysical Journal International*, *120*(1), 1-23.

Gawthorpe, R.L., Sharp, I., Underhill, J.R. and Gupta, S. (1997) Linked sequence stratigraphic and structural evolution of propagating normal faults. *Geology*, 25(9), 795-798, doi: 10.1130/0091-7613(1997)025.

Ge, H.X., Jackson, M.P.A. and Vendeville, B.C. (1997) Kinematics and dynamics of salt tectonics driven by progradation. *American Association of Petroleum Geologists Bulletin*, 81(3), 398-423.

Gemmer, L., C. Beaumont, and S.J. Ings (2005), Dynamic modelling of passive margin salt tectonics: effects of water loading, sediment properties and sedimentation patterns, *Basin Research*, *17*, 383-402.

Gemmer, L., S.J. Ings, S. Medvedev, and C. Beaumont (2004), Salt tectonics driven by differential sediment loading: stability analysis and finite-element experiments, *Basin Research*, *16*, 188-218, doi: 10.1111/j.1365-2117.2004.00229.x.

Gleason, G.C. and Tullis, J. (1995) A flow law for dislocation creep of quartz aggregates determined with the molten-salt cell. *Tectonophysics*, 247(1-4), 1-23, doi: 10.1016/0040-1951(95)00011-B.

Goteti, R., Ings, S.J. and Beaumont, C. (2012) Development of salt minibasins initiated by sedimentary topographic relief. *Earth and Planetary Science Letters*, 339, 103-116, doi: 10.1016/j.epsl.2012.04.045.

Goteti, R., Beaumont, C. and Ings, S.J. (2013) Factors controlling early stage salt tectonics at rifted continental margins and their thermal consequences. *Journal of Geophysical Research – Solid Earth*, 118(6), 3190-3220, doi: 10.1002/jgrb.50201.

Gueydan, F., Morency, C. and Brun, J.P. (2008) Continental rifting as a function of lithosphere mantl strength. *Tectonophysic*s, 460, 83-93. doi:10.1016/j.tecto.2008.08.012.

Haq, B.U., Hardenbol, J. & Vail, P.R. (1987) Chronology of fluctuating sea levels since the Triassic. *Science*, 235(4793), 1156-1167, doi: 10.1126/science.235.4793.1156.

Hempton, M.R. (1987) Constraints on Arabian plate motion and extensional history of the Red-Sea. *Tectonics*, 6(6), 687-&, doi: 10.1029/TC006i006p00687.

Hofmann, C., Courillot, V., Feraud, G., Rochette, P., Yirgu, G., Ketefo, E. and Pik, R. (1997) Timing of the Ethiopian flood basalt event and implications for plume birth and global change. *Nature*, 389(6653), 838-841.

Hopper, J.R. and Buck, W.R. (1996) The effect of lower crustal flow on continental extension and passive margin formation. *Journal of Geophysical Research*, 101(B9), 175-194, doi: 0.1029/96JB01644.

Hopper, J.R. and Buck, W.R. (1998) Styles of extensional decoupling. *Geology*, 26(8), 699-702, doi: 10.1130/0091-7613(1998)026.

Hudec, M.R. and Jackson, M.P.A. (2007). Terra Infirma: Understanding salt tectonics, *Earth Science Reviews*, 82(1-2), 1-28, doi 10.1016/j.earscirev.2007.01.001.

Hudec, M.R., Jackson, M.P.A. and Schultz-Ela, D.D. (2009) The paradox of minibasin subsidence into salt: Clues to the evolution of crustal basins. *Geological Society of America Bulletin, 121*(1-2), 201-221, doi: 10.1130/B26275.1.

Hughes, G.W. and Beydoun, Z.R. (1992) the Red-Sea Fule of Aden – biostratigraphy, lithostratigraphy and paleoenvironments. *Journal of Petroleum Geology*, 15(2), 135-156, doi: 10.1111/j.1747-5457.1992.tb00959.x.

Hughes, G.W. and Filatoff, J. (1995) New biostratigraphic constraints on Saudi Arabian Red Sea pre- and syn- rift sequences. In: *Middle East Petroleum Geosciences, Geo '94 vol. 2* (Ed. by Al-Husseini, M.I.), pp 517-528. Gulf PetroLink, Bahrain.

Huismans, R. and Beaumont, C. (2014) Rifted continental margins: The case for depth-dependent extension. *Earth and Planetary Science Letters,* 407, 148-162, doi:10.1016/j.eps1.2014.09.032.

Huismans, R. and Beaumont, C. (2011) Depth-dependent extension, two-stage breakup and cratonic underplating at rifted margins. *Nature*, 473(7345), 74-U85, doi: 10.1038/nature09988.

Hsuimans, R. and Beaumont, C. (2008) Complex rifted continental margins explained by dynamical models of depth-dependent lithospheric extension. *Geology*, 36(2), 163-166, doi: 10.1130/G24231A.1.

Huismans, R. and Beaumont, C. (2005) Effect of plastic-viscous layering and strain softening on mode selection during lithospheric extension. *Journal of Geophysical Research – Solid Earth*, 110(B2), B02406, doi: 10.1029/2004JB003114.

Ismail-Zadeh, Alik, et al. (2004). Three-dimensional forward and backward modelling of diapirism: numerical approach and its applicability to the evolution of salt structures in the Pricaspian basin. *Tectonophysics,* 387.1, 81-103.

Izzeldin, A.Y. (1987) Seismic, gravity and magnetic surveys in the central part of the Red Sea: Their interpretation and implications for the structure and evolution of the Red Sea. *Tectonophysics,* 143, 269-306.

Jammes, S., Manatschal, G. and Lavier, L. (2010) Interaction between prerift salt and detachment faulting in hyperextended rift systems: The example of the Parentis and Mauleon basins (Bay of Biscay and western Pyrenees). *American Association of Petroleum Geologists Bulleti*n, 94(7), 957-975, doi: 10.1306/12090909116.

Jansa, L. F., and Wade, J.A. (1975). Paleogeography and sedimentation in the Mesozoic and Cenozoic, southeastern Canada. (1975): 79-102.

Karner, G.D. and Driscoli, N.W. (1999) Tectonic and stratigraphic development of the West African and eastern Brazilian Margins: insights from quatitative basin modeling. In: *The Oil & Gas Habitats of the South Atlantic* (Ed. by Cameron, N.R., Bate, R.H. & Clure, V.S), Geological Society, London, Special Publications, 153, 11-40.

Karner, G.C. and Gamboa, L.A.P. (2007) Timing and origin of the South Atlantic pre-salt sag basins and their capping evaporites. *Geological Society, London, Special Publications*, 285, 15-35. Doi: 10.1144/SP285.2.

Karato, S. and Wu, P. (1993) Rheology of the upper mantle – a synthesis. *Science*, 260(5109), 771-778, doi: 10.1126/science.260.5109.771.

Kaus, B.J.P., and Podladchikov, Y.Y. (2001). Forward and reverse modeling of the three-dimensional viscous Rayleigh-Taylor instability. *Geophysical Research Letters*, 28(6): 1095-1098. Doi: 10.1029/2000GL011789.

Keken, P.E., Spiers, C.T., Van Den Berg, A.P. and MUYZERT, E.J. (1993) The effective viscosity of rocksalt: implementation of steady-state creep laws in numerical models of salt diapirism. *Tectonophysics*, 225, 457-476.

Keen, C. E., and Potter, D. P. (1995). The transition from a volcanic to a nonvolcanic rifted margin off eastern Canada. *Tectonics* 14.2: 359-371.

Kuo, A.C.M. (1999), *Polymer Data Handbook*, Oxford University Press, p. 57-73.

Koupriantchik, D., Hunt, S.P., Boult, P.J., and Meyers, A.G. (2005). Geomechanical modeling of salt diapirs: 3D salt structure from the Officer Basin, South Asutralia. *Munson TJ, Ambrose GJ. Proceedings of the Central Australian Basins Symposium (CABS), Alice Springs, Northern Territory*. Vol. 1618.

Krezsek, C., Adam, J., and D. Grujic (2007), Mechanics of fault and expulsion rollover systems developed on passive margins detached on salt: insights from analogue modelling and optical strain monitoring, *Geological Society, London, Special Publications, 292*: 103-121, doi: 10.1144/SP292.6.

Labails, C. et al. (2010). An alternative early opening scenario for the Central Atlantic Ocean. *Earth and Planetary Science Letters* 297.3 (2010): 355-368.

Lavier, L. L., Buck, W.R. and Poliakov, A.N.B. (1999) Self-consistent rolling- hinge model for the evolution of large-offset low-angle normal faults. *Geology*, 27, 1127–1130, doi: 10.1130/0091-7613(1999)027.

Lavier, L. L. and Buck, W.R. (2002) Half graben versus large-offset low-angle normal fault: Importance of keeping cool during normal faulting. *Journal of Geophysical Research*, 107(B6), 2122, doi:10.1029/2001JB000513.

Lavier, L.L. and Manatschal, G. (2006) A mechanism to thin the continental lithosphere at magma-poor margins. *Nature,* 440(7082,: 324-328, doi: 10.1038/nature04608.

Ligi, M., Bonatti, E., Bortoluzzi, G., CiprianiI, A., Cocchi, L., Tontini, F.C., Carminate, E., Ottolini, L. and Schettino, A. (2012) Birth of an ocean in the Red Sea: Initial pangs. *Geochemistry Geophysics Geosystems*, 13, Q08009, doi: 10.1029/2012GC004155.

Lister, G.S., Etheridge, M.A. and Symonds, P.A. (1986) Detachment faulting and the evolution of passive continental margins. *Geology*, 14(3), 246-250, doi: 10.1130/0091-7613(1986)14.

Lister, G.S., Etherdige, M.A. and Symonds, P.A., (1991) Detachment models for the formation of passive continental margins. *Tectonics*, 10(5), 1038-1064, doi: 10.1029/90TC01007.

Longoni, M., Malossi, A.C.I. and Villa, A. (2010) A robust and efficient conservative technique for simulating three-dimensional sedimentary basin dynamics. *Computers & Fluids*, 39(10), 1964-1976, doi: 10.1016/j.compfluid.2010.06.028.

Longoni, Matteo, et al. (2011). An ALE-based numerical technique for modeling sedimentary basin evolution featuring layer deformations and faults." *Journal of Computational Physics* 230.8, 3230-3248.

Lohrmann, J., N. Kukowski, J. Adam, and O. Oncken (2003), The impact of analogue material properties on the geometry, kinematics, and dynamics of convergent sand wedges, *Journal of Structural Geology*, *25*, 1691–1711, doi: 10.1016/S0191-8141(03)00005-1.

Loncke, L., B.C. Vendeville, V. Gaullier, and J. Mascle (2010), Respective contributions of tectonics and gravity-driven processes on the structural pattern in the Eastern Nile deep-sea fan: insights from physical experiments, *Basin Research*, *22*(5), 765-782, doi: 10.1111/j.1365-2117.2009.00436.x.

Louden, K., Wu, Y., and Tari, G. (2012). Systematic variations in basement morphology and rifting geometry along the Nova Scotia and Morocco conjugate margins. *Geological Society, London, Special Publications*. 369: 267-287. Doi: 10.1144/SP369.9.

Mackwell, S., Zimmerman, M. and Kohlstedt, D. (1998) High-temperature deformation of dry diabase with application to tectonics on Venus. *Journal of Geophysical. Research-Solid Earth*, 103, 975–984.

Maillard, A., V. Gaullier, B.C. Vendeville, and F. Odonne (2003), Influence of differential compaction above basement steps on salt tectonics in the Ligurian-Provencal Basin, northwest Mediterranean, *Marine and Petroleum Geology*, *20*(1), 13-27, doi: 10.1016/S0264-8172(03)00022-9.

Marone, C. (2003), Laboratory-derived friction laws and their application to seismic faulting, *Annual Review Earth and Planetary Science Letters*, *26*, 643-696, doi: 10.1146/annurev.earth.26.1.643.

Marues, F.O. (2008), Thrust initiation and propagation during shortening of a 2-layer model lithosphere, *Journal of Structural Geology, 30*(1), 29-38, doi: 10.1016/jsg.2007.09.005.

Massimi, P., Quarteroni, A., Saleri, F., and Scrofani, G. (2007). Modeling of salt tectonics. *Computer methods in applied mechanics and engineering*, *197*(1), 281-293.

McClay, K., T. Dooley, and G. Zamora (2003), Analogue models of delta systems above ductile substrates, in, *Subsurface Sediment Mobilization*, *Geological Society Special Publication*, *216*, edited by P. Van Rensbergen, R.R. Hillis, A.J. Maltman, and C.K.Morley, 411-428, doi: 10.1144/GSL.SP.2003.216.01.27.

McKenzie, D. (1978) Some remarks on the development of sedimentary basins. *Earth and Planetary Science Letters*, 40, 25-32, doi: 10.1016/0012-821X(78)90071-7.

Mitchell, N.C., Ligi, M., Ferrante, V., Bonatti, E. and Rutter, E. (2010) Submarine salt flows in the central Red Sea. *Geological Society of America Bulletin*, 122(5-6), 701-713, doi: 10.1130/B26518.1.

Morley, C.K., and Westaway, R. (2006). Subsidence in the super-deep Pattani and Malay basin of Southeast Asia: a coupled model incorporating lower-crustal flow in response to post-rift sediment loading. *Basin Research*, 18, 51-84. Doi: 10.1111/j.1365-2117.2006.00285.x

Mourgues, R. and P.R. Cobbold (2006), Sandbox experiments on gravitational sliding and gliding in the presence of fluid overpressures, *Journal of Structural Geology*, *28*, 887-901, doi: 10.1016/j.jsg.2005.12.013.

Nagel, T.J. and Buck, W.R. (2004) Symmetric alternative to asymmetric rifting models. *Geology*. 32(11), 937-940, doi: 10.1130/G20785.1.

Nagel, T.J. and Buck, W.R. (2007) Control of rheological stratification on rifting geometry: a symmetric model resolving the upper plate paradox. *International Journal of Earth Sciences*, 96, 1047-1057, doi: 10.1007/s00531-007-0195-x.

Omar, G.I., Steckler, M.S., Buck, W.R. and Kohn, B.P. (1989) Fission-track analysis of basement apatites at the western margin of the Gulf-of-Suez rift, Egypt – evidence for synchroneity of uplift and subsidence. *Earth and Planetary Science Letters*, 94(3-4), 316-328, doi: 10.1016/0012-821X(89)90149-0.

Olsen, P.E. (1997). Stratigraphic record of the early Mesozoid breakup of Pangea in the Laurasia-Gondwana rift system. *Annual Review Earth and Planetary Science*, 25: 337-401.

Orszag-Sperber, F., Hardwood, G., Kendall, A. and Purser, B.H. (1998) A Review of the evaporites of the Red Sea – Gulf of Suez rift. In: *Sedimentation and Tectonics of Rift Basins: Red Sea – Gulf of Aden* (Ed. by Purser, B.H. & Bosence, D.W.J.). Chapman & Hall, London. 409-426.

Peron-Pinvidic, G. and Manatschal, G. (2009) The final rifting evolution at deep magma-poor passive margins from IberiaeNewfoundland: a new point of view. *International Journal of Earth Sciences*, 98, 1581-1597, doi: 10.1007/s00531-008-0337-9.

Peron-Pinvidic, G., Manatschal, G. and Osmundsen, P.T. (2013) Structural comparison of archetypal Atlantic rifted margins: A review of observations and concepts. *Marine and Petroleum Geology*, 43, 21-47, doi: 10.1016/j.marpetgeo.2013.02.002.

Press, W.H., B.P. Flannery, S.A. Teukolsky, and W.T. Vetterling (1986), *Numerical Recipes*, Cambridge Univeristy Press, Cambridge.

Rossi, D., and F. Storti (2003), New artificial granular materials for analogue laboratory experiments: aluminum and siliceous microspheres, *Journal of Structural Geology, 25*(11), 1893-1899, doi: 10.1016/S0191-8141(03)00041-5.

Rowan, M.G. (2014) Passive-margin salt basins: hyperextension, evaporite deposition, and salt tectonics. *Basin Research*, *2*6, 154-182, doi: 10.1111/bre.12043.

Rowan, M.G., and B.C. Vendeville (2006), Foldbelts with early salt withdrawal and diapirism: Physical models and examples from the northern Gulf of Mexico and the Flinders Ranges, Australia, *Marine and Petroleum Geology*, *23*(9-10), 871-891, doi: 10.1016/j.marpetgeo.2006.08.003.

Richardson, M. and Arthur, M.A. (1988) The Gulf of Suez-Northern Red-Sea neogene rift – a quantitative basin analysis. *Marine and Petroleum Geology*, 5(3), 247-270, doi: 10.1016/0264-8172(88)90005-0.

Sahabi, M., Aslanian, D., and Olivet, J.L. (2004). A new starting point for the history of the central Atlantic. *Comptes Rendus Geoscience,* 336.12: 1041-1052.

Schubert, G., Turcotte, D. and Olson, P. (2001) *Mantle convection in the Earth and planets,* Cambridge University Press.

Schultz-Ela, D.D., M.P.A. Jackson and B.C. Vendeville (1993), Mechanics of salt diapirism, *Tectonophysics, 228*, 275-312.

Schweiger, H. (1994), On the use of drucker-prager failure criteria for earth pressure problems, Comput. Geotech., 16(3), 223–246, doi:10.1016/
0266-352X(94)90003-5.

Sclater, J.G., and P.A.F. Christie (1980), Continental stretching: An explanation of the post-mid-Cretaceous subsidence of the central North Sea basin, *Journal of Geophysical Research*, *85*, 3711-3739, doi: 10.1029/JB085iB07p03711.

Scott, R.W. and Govean, F.M. (1985) Early depositional history of a rift basin – Miocene in Western Sinai. *Palaeogeography Palaeolimatology Palaeoecology*, 52(1-2), 143-158, doi: 10.1016/0031-0182(85)90035-5.

Searle, R.C. and Ross, D.A. (1975) Geophysical study of Red-Sea axial trough between 20.5degrees and 22degrees N. *Geophysical Journal of the Royal Astronomical Society*, 43(2), 555-572, doi: 10.1111/j.1365-246X.1975.tb00647.x.

Sibuet, J.C., Rouzo, S., and Srivastava, S. (2012). Plate tectonic reconstructions and paleogeographic maps of the central and north Atlantic oceans. *Canadian Journal of Earth Sciences*, 49: 1395-1415.

Sokoutis, D., Corti, G., Bonini, M., Brun, J.P., Cloetingh, S., Maudiot, T. and Manetti, P. (2007) Modelling the extension of heterogeneous hot lithosphere. *Tectonophyics*, 444, 63-79, doi:10.1016/j.tecto.2007.08.012.

Storti, F., Soto Marin, R., Rossetti, F., and A.M. Casas Sainz (2007), Evolution of experimental thrust wedges accreted from along-strike tapered, silicone-floored multilayers, *Journal of the Geological Society*, *164*(1), 73-86, doi: 10.1144/0016-76492005-186.

Tirel, C., Brun, J.P. and Sokoutis, D. (2006) Extension of thickened and hot lithospheres: Inferences from laboratory modeling. *Tectonics,* 25, TC1005, doi:10.1029/2005TC001804.

Unternehr, P., Peron-Pinvidic, G., Manatschal, G., and Suttra, E. (2010). Hyper-extended crust in the South Atlantic: in search of a model. *Petroleum Geoscience* 16.3: 207-215. Doi: 10.1144/1354-079309-904.

van Avendonk, H.J.A., Lavier, L.L., Sshillingston, D.J. and Manatschal, G. (2009) Extension of continental crust at the margin of the eastern Grand Banks, Newfoundland. *Tectonophysics*, 468, 131-148, doi:10.1016/j.tecto.2008.05.030.

van Keken, P.E., C.J. Spiers, A.P., van den Berg, and E.J. Muyzert, E.J. (1993), The effective viscosityof rocksalt: implementation of steady-state creep laws in numerical models of salt diapirism. *Tectonophysics, 225*, 457-476.

von Nicolai, C., Scheck-Wenderoth, M., Warsitzka, M., Schodt, N., and Andersen, J. (2013). The deep structure of the South Atlantic Kwanza Basin—Insights from 3D structural and gravimetric modelling. *Tectonophysics* 604: 139-152. Doi: 10.1016/j.tecto.2013.06.016.

Velde, B. (1996), Compaction trends of clay-rich deep sea sediment, *Marine Geology*, *133*, 193-201, doi: 10.1016/0025-3227(96)00020-5.

Vendeville, B. (2005), Salt tectonics driven by progradation: Part I - Mechanics and kinematics, *American Association of Petroleum Geologists Bulletin*, *89*(8), 1071-1079, doi: 10.1306/03310503063.

Vendeville, B., and P.R. Cobbold (1987), Synsedimentary gravitational sliding and listric normal growth faults – insights from scaled physical models, *Comptes Rendus de L Academeie Des Sciences Serie II*, *305*(16), 1313-1319.

Wade, J. A., and MacLean, B.C. (1990). The geology of the southeastern margin of Canada. *Geology of the continental margin of eastern Canada: Geological Survey of Canada, Geology of Canada* 2: 167-238.

Wade, J.A., MacLean, B.C., and Williams, G.L. (1995). Mesozoic and Cenozoic stratigraphy, eastern Scotian Shelf: new interpretations. *Canadian Journal of Earth Sciences*, 32: 1462-1473.

Warren, J.K. (2010) Evaporites through time: Tectonic, climatic and eustatic controls in marine and nonmarine deposits. *Earth-Science Reviews,* 98, 217–268, doi: 10.1016/j.earscirev.2009.11.004.

Warren, J. K. (2006) Evaporites: Sediments, Resources and Hydrocarbons. Springer, Berlin.

Warsitzka, M., Kley, J., Jahne, F., and N. Kukowski (IN PRESS), Salt diapirism driven by differential loading – some insights from analogue modelling, *Tectonophysics*, doi: 10.1016/j.tecto.2011.11.018

Weijermars, R. H., and H. Schmeling (1986), Scaling of Newtonian and non-Newtonian fluid-dynamics without inertia for quantitative modeling of rock flow due to gravity (including the concept of rheological similarity), *Physics of the Earth and Planetary Interiors*, *43*(4), 316-330, doi: 10.1016/0031-9201(86)90021-X.

Weijermars, R., M.P.A. Jackson, and B. Vendeville (1993), Rheological and tectonic modeling of salt provinces, *Tectonophysics*, *217*, 143-174, doi: 10.1016/0040-1951(93)90208-2.

Wernicke, B. (1985) Low-angle normal faults in the basin and range province – nappe tectonics in an extending orogen. *Nature*, 291(5817), 645-648, doi: 10.1038/291645a0.

Wernicke, B. (1981) Uniform-sense normal simple shear of the continental lithosphere, *Canadian Journal of Earth Sciences*, 22(1), 108-125, doi: 10.1139/e85-009.

Westaway, R., and Bridgland, D. 2007. Late Cenazoic uplift of southern Italy deduced from fluvial and marine sediments: Coupling between surface processes and lower-crustal flow. Quaternary International. 175. 86-124.

Weston, J.F., MacRae, R.A., Ascoli, P., Cooper, M.K.E., Fensome, R.A., Shaw, D., and Williams, G.L. (2012). A revised biostratigraphic and well-log sequence-stratigraphic framework for the Scotian Margin, offshore eastern Canada. *Canadian Journal of Earth Sciences*, 49: 1417-1462.

Winn, R.D., Crevello, P.D. and Bosworth, W. (2001) Lower Miocene Nukhul formation, Gebel el Zeit, Egypt: Model for structural control on early synrift strata and reservoirs, Gulf of Suez. *American Association of Petroleum Geologists Bulletin*, 85(10), 1871-1890.

Wu, Y., Louden, K.E., Funck, T., Jackson, H.R., and Dehler, S.A. (2006). Crustal structure of the central Nova Scotia margin off Eastern Canada. *Geophysical Journal International*. 166: 878-906.

Appendix A: Copyright Agreement Forms

JOHN WILEY AND SONS LICENSE
TERMS AND CONDITIONS

Aug 31, 2016

This Agreement between Janice Allen ("You") and John Wiley and Sons ("John Wiley and Sons") consists of your license details and the terms and conditions provided by John Wiley and Sons and Copyright Clearance Center.

License Number	3939460020195
License date	Aug 31, 2016
Licensed Content Publisher	John Wiley and Sons
Licensed Content Publication	Journal of Geophysical Research: Solid Earth
Licensed Content Title	Impact of inconsistent density scaling on physical analogue models of continental margin scale salt tectonics
Licensed Content Author	Janice Allen,Christopher Beaumont
Licensed Content Date	Aug 16, 2012
Licensed Content Pages	1
Type of use	Dissertation/Thesis
Requestor type	Author of this Wiley article
Format	Print and electronic
Portion	Full article
Will you be translating?	No
Title of your thesis / dissertation	Numerical Modelling of Salt Tectonics at Rifted Continental Margins
Expected completion date	Aug 2016
Expected size (number of pages)	310
Requestor Location	Janice Allen 34 Sheep River Crescent Okotoks, AB T1S1R3 Canada Attn: Janice Allen
Publisher Tax ID	EU826007151
Billing Type	Invoice
Billing Address	Janice Allen 34 Sheep River Crescent Okotoks, AB T1S1R3 Canada Attn: Janice Allen
Total	0.00 CAD
Terms and Conditions	

their respective licensors, and your interest therein is only that of having possession of and the right to reproduce the Wiley Materials pursuant to Section 2 herein during the continuance of this Agreement. You agree that you own no right, title or interest in or to the Wiley Materials or any of the intellectual property rights therein. You shall have no rights hereunder other than the license as provided for above in Section 2. No right, license or interest to any trademark, trade name, service mark or other branding ("Marks") of WILEY or its licensors is granted hereunder, and you agree that you shall not assert any such right, license or interest with respect thereto

- NEITHER WILEY NOR ITS LICENSORS MAKES ANY WARRANTY OR REPRESENTATION OF ANY KIND TO YOU OR ANY THIRD PARTY, EXPRESS, IMPLIED OR STATUTORY, WITH RESPECT TO THE MATERIALS OR THE ACCURACY OF ANY INFORMATION CONTAINED IN THE MATERIALS, INCLUDING, WITHOUT LIMITATION, ANY IMPLIED WARRANTY OF MERCHANTABILITY, ACCURACY, SATISFACTORY QUALITY, FITNESS FOR A PARTICULAR PURPOSE, USABILITY, INTEGRATION OR NON-INFRINGEMENT AND ALL SUCH WARRANTIES ARE HEREBY EXCLUDED BY WILEY AND ITS LICENSORS AND WAIVED BY YOU.

- WILEY shall have the right to terminate this Agreement immediately upon breach of this Agreement by you.

- You shall indemnify, defend and hold harmless WILEY, its Licensors and their respective directors, officers, agents and employees, from and against any actual or threatened claims, demands, causes of action or proceedings arising from any breach of this Agreement by you.

- IN NO EVENT SHALL WILEY OR ITS LICENSORS BE LIABLE TO YOU OR ANY OTHER PARTY OR ANY OTHER PERSON OR ENTITY FOR ANY SPECIAL, CONSEQUENTIAL, INCIDENTAL, INDIRECT, EXEMPLARY OR PUNITIVE DAMAGES, HOWEVER CAUSED, ARISING OUT OF OR IN CONNECTION WITH THE DOWNLOADING, PROVISIONING, VIEWING OR USE OF THE MATERIALS REGARDLESS OF THE FORM OF ACTION, WHETHER FOR BREACH OF CONTRACT, BREACH OF WARRANTY, TORT, NEGLIGENCE, INFRINGEMENT OR OTHERWISE (INCLUDING, WITHOUT LIMITATION, DAMAGES BASED ON LOSS OF PROFITS, DATA, FILES, USE, BUSINESS OPPORTUNITY OR CLAIMS OF THIRD PARTIES), AND WHETHER OR NOT THE PARTY HAS BEEN ADVISED OF THE POSSIBILITY OF SUCH DAMAGES. THIS LIMITATION SHALL APPLY NOTWITHSTANDING ANY FAILURE OF ESSENTIAL PURPOSE OF ANY LIMITED REMEDY PROVIDED HEREIN.

- Should any provision of this Agreement be held by a court of competent jurisdiction to be illegal, invalid, or unenforceable, that provision shall be deemed amended to achieve as nearly as possible the same economic effect as the original provision, and the legality, validity and enforceability of the remaining provisions of this Agreement shall not be affected or impaired thereby.

- The failure of either party to enforce any term or condition of this Agreement shall not constitute a waiver of either party's right to enforce each and every term and condition of this Agreement. No breach under this agreement shall be deemed waived or excused by either party unless such waiver or consent is in writing signed by the party granting such waiver or consent. The waiver by or consent of a party to a breach of any provision of this Agreement shall not operate or be construed as a waiver of or consent to any other or subsequent breach by such other party.

- This Agreement may not be assigned (including by operation of law or otherwise) by you without WILEY's prior written consent.

- Any fee required for this permission shall be non-refundable after thirty (30) days from receipt by the CCC.

- These terms and conditions together with CCC's Billing and Payment terms and conditions (which are incorporated herein) form the entire agreement between you and WILEY concerning this licensing transaction and (in the absence of fraud) supersedes all prior agreements and representations of the parties, oral or written. This Agreement may not be amended except in writing signed by both parties. This Agreement shall be binding upon and inure to the benefit of the parties' successors, legal representatives, and authorized assigns.

- In the event of any conflict between your obligations established by these terms and conditions and those established by CCC's Billing and Payment terms and conditions, these terms and conditions shall prevail.

- WILEY expressly reserves all rights not specifically granted in the combination of (i) the license details provided by you and accepted in the course of this licensing transaction, (ii) these terms and conditions and (iii) CCC's Billing and Payment terms and conditions.

- This Agreement will be void if the Type of Use, Format, Circulation, or Requestor Type was misrepresented during the licensing process.

- This Agreement shall be governed by and construed in accordance with the laws of the State of New York, USA, without regards to such state's conflict of law rules. Any legal action, suit or proceeding arising out of or relating to these Terms and Conditions or the breach thereof shall be instituted in a court of competent jurisdiction in New York County in the State of New York in the United States of America and each party hereby consents and submits to the personal jurisdiction of such court, waives any objection to venue in such court and consents to service of process by registered or certified mail, return receipt requested, at the last known address of such party.

WILEY OPEN ACCESS TERMS AND CONDITIONS

Wiley Publishes Open Access Articles in fully Open Access Journals and in Subscription journals offering Online Open. Although most of the fully Open Access journals publish open access articles under the terms of the Creative Commons Attribution (CC BY) License

only, the subscription journals and a few of the Open Access Journals offer a choice of Creative Commons Licenses. The license type is clearly identified on the article.

The Creative Commons Attribution License

The Creative Commons Attribution License (CC-BY) allows users to copy, distribute and transmit an article, adapt the article and make commercial use of the article. The CC-BY license permits commercial and non-

Creative Commons Attribution Non-Commercial License

The Creative Commons Attribution Non-Commercial (CC-BY-NC)License permits use, distribution and reproduction in any medium, provided the original work is properly cited and is not used for commercial purposes.(see below)

Creative Commons Attribution-Non-Commercial-NoDerivs License

The Creative Commons Attribution Non-Commercial-NoDerivs License (CC-BY-NC-ND) permits use, distribution and reproduction in any medium, provided the original work is properly cited, is not used for commercial purposes and no modifications or adaptations are made. (see below)

Use by commercial "for-profit" organizations

Use of Wiley Open Access articles for commercial, promotional, or marketing purposes requires further explicit permission from Wiley and will be subject to a fee.

Further details can be found on Wiley Online Library

http://olabout.wiley.com/WileyCDA/Section/id-410895.html

Other Terms and Conditions:

v1.10 Last updated September 2015

Questions? customercare@copyright.com or +1-855-239-3415 (toll free in the US) or +1-978-646-2777.

JOHN WILEY AND SONS LICENSE TERMS AND CONDITIONS

Aug 31, 2016

This Agreement between Janice Allen ("You") and John Wiley and Sons ("John Wiley and Sons") consists of your license details and the terms and conditions provided by John Wiley and Sons and Copyright Clearance Center.

License Number	3939460285636
License date	Aug 31, 2016
Licensed Content Publisher	John Wiley and Sons
Licensed Content Publication	Basin Research
Licensed Content Title	Continental margin syn-rift salt tectonics at intermediate width margins
Licensed Content Author	Janice Allen,Christopher Beaumont
Licensed Content Date	May 29, 2015
Licensed Content Pages	1
Type of use	Dissertation/Thesis
Requestor type	Author of this Wiley article
Format	Print and electronic
Portion	Full article
Will you be translating?	No
Title of your thesis / dissertation	Numerical Modelling of Salt Tectonics at Rifted Continental Margins
Expected completion date	Aug 2016
Expected size (number of pages)	310
Requestor Location	Janice Allen 34 Sheep River Crescent Okotoks, AB T1S1R3 Canada Attn: Janice Allen
Publisher Tax ID	EU826007151
Billing Type	Invoice
Billing Address	Janice Allen 34 Sheep River Crescent Okotoks, AB T1S1R3 Canada Attn: Janice Allen
Total	0.00 CAD
Terms and Conditions	

their respective licensors, and your interest therein is only that of having possession of and the right to reproduce the Wiley Materials pursuant to Section 2 herein during the continuance of this Agreement. You agree that you own no right, title or interest in or to the Wiley Materials or any of the intellectual property rights therein. You shall have no rights hereunder other than the license as provided for above in Section 2. No right, license or interest to any trademark, trade name, service mark or other branding ("Marks") of WILEY or its licensors is granted hereunder, and you agree that you shall not assert any such right, license or interest with respect thereto

- NEITHER WILEY NOR ITS LICENSORS MAKES ANY WARRANTY OR REPRESENTATION OF ANY KIND TO YOU OR ANY THIRD PARTY, EXPRESS, IMPLIED OR STATUTORY, WITH RESPECT TO THE MATERIALS OR THE ACCURACY OF ANY INFORMATION CONTAINED IN THE MATERIALS, INCLUDING, WITHOUT LIMITATION, ANY IMPLIED WARRANTY OF MERCHANTABILITY, ACCURACY, SATISFACTORY QUALITY, FITNESS FOR A PARTICULAR PURPOSE, USABILITY, INTEGRATION OR NON-INFRINGEMENT AND ALL SUCH WARRANTIES ARE HEREBY EXCLUDED BY WILEY AND ITS LICENSORS AND WAIVED BY YOU.

- WILEY shall have the right to terminate this Agreement immediately upon breach of this Agreement by you.

- You shall indemnify, defend and hold harmless WILEY, its Licensors and their respective directors, officers, agents and employees, from and against any actual or threatened claims, demands, causes of action or proceedings arising from any breach of this Agreement by you.

- IN NO EVENT SHALL WILEY OR ITS LICENSORS BE LIABLE TO YOU OR ANY OTHER PARTY OR ANY OTHER PERSON OR ENTITY FOR ANY SPECIAL, CONSEQUENTIAL, INCIDENTAL, INDIRECT, EXEMPLARY OR PUNITIVE DAMAGES, HOWEVER CAUSED, ARISING OUT OF OR IN CONNECTION WITH THE DOWNLOADING, PROVISIONING, VIEWING OR USE OF THE MATERIALS REGARDLESS OF THE FORM OF ACTION, WHETHER FOR BREACH OF CONTRACT, BREACH OF WARRANTY, TORT, NEGLIGENCE, INFRINGEMENT OR OTHERWISE (INCLUDING, WITHOUT LIMITATION, DAMAGES BASED ON LOSS OF PROFITS, DATA, FILES, USE, BUSINESS OPPORTUNITY OR CLAIMS OF THIRD PARTIES), AND WHETHER OR NOT THE PARTY HAS BEEN ADVISED OF THE POSSIBILITY OF SUCH DAMAGES. THIS LIMITATION SHALL APPLY NOTWITHSTANDING ANY FAILURE OF ESSENTIAL PURPOSE OF ANY LIMITED REMEDY PROVIDED HEREIN.

- Should any provision of this Agreement be held by a court of competent jurisdiction to be illegal, invalid, or unenforceable, that provision shall be deemed amended to achieve as nearly as possible the same economic effect as the original provision, and the legality, validity and enforceability of the remaining provisions of this Agreement shall not be affected or impaired thereby.

- The failure of either party to enforce any term or condition of this Agreement shall not constitute a waiver of either party's right to enforce each and every term and condition of this Agreement. No breach under this agreement shall be deemed waived or excused by either party unless such waiver or consent is in writing signed by the party granting such waiver or consent. The waiver by or consent of a party to a breach of any provision of this Agreement shall not operate or be construed as a waiver of or consent to any other or subsequent breach by such other party.

- This Agreement may not be assigned (including by operation of law or otherwise) by you without WILEY's prior written consent.

- Any fee required for this permission shall be non-refundable after thirty (30) days from receipt by the CCC.

- These terms and conditions together with CCC's Billing and Payment terms and conditions (which are incorporated herein) form the entire agreement between you and WILEY concerning this licensing transaction and (in the absence of fraud) supersedes all prior agreements and representations of the parties, oral or written. This Agreement may not be amended except in writing signed by both parties. This Agreement shall be binding upon and inure to the benefit of the parties' successors, legal representatives, and authorized assigns.

- In the event of any conflict between your obligations established by these terms and conditions and those established by CCC's Billing and Payment terms and conditions, these terms and conditions shall prevail.

- WILEY expressly reserves all rights not specifically granted in the combination of (i) the license details provided by you and accepted in the course of this licensing transaction, (ii) these terms and conditions and (iii) CCC's Billing and Payment terms and conditions.

- This Agreement will be void if the Type of Use, Format, Circulation, or Requestor Type was misrepresented during the licensing process.

- This Agreement shall be governed by and construed in accordance with the laws of the State of New York, USA, without regards to such state's conflict of law rules. Any legal action, suit or proceeding arising out of or relating to these Terms and Conditions or the breach thereof shall be instituted in a court of competent jurisdiction in New York County in the State of New York in the United States of America and each party hereby consents and submits to the personal jurisdiction of such court, waives any objection to venue in such court and consents to service of process by registered or certified mail, return receipt requested, at the last known address of such party.

WILEY OPEN ACCESS TERMS AND CONDITIONS

Wiley Publishes Open Access Articles in fully Open Access Journals and in Subscription journals offering Online Open. Although most of the fully Open Access journals publish open access articles under the terms of the Creative Commons Attribution (CC BY) License

only, the subscription journals and a few of the Open Access Journals offer a choice of Creative Commons Licenses. The license type is clearly identified on the article.

The Creative Commons Attribution License

The Creative Commons Attribution License (CC-BY) allows users to copy, distribute and transmit an article, adapt the article and make commercial use of the article. The CC-BY license permits commercial and non-

Creative Commons Attribution Non-Commercial License

The Creative Commons Attribution Non-Commercial (CC-BY-NC)License permits use, distribution and reproduction in any medium, provided the original work is properly cited and is not used for commercial purposes.(see below)

Creative Commons Attribution-Non-Commercial-NoDerivs License

The Creative Commons Attribution Non-Commercial-NoDerivs License (CC-BY-NC-ND) permits use, distribution and reproduction in any medium, provided the original work is properly cited, is not used for commercial purposes and no modifications or adaptations are made. (see below)

Use by commercial "for-profit" organizations

Use of Wiley Open Access articles for commercial, promotional, or marketing purposes requires further explicit permission from Wiley and will be subject to a fee.

Further details can be found on Wiley Online Library

http://olabout.wiley.com/WileyCDA/Section/id-410895.html

Other Terms and Conditions:

v1.10 Last updated September 2015

Questions? customercare@copyright.com or +1-855-239-3415 (toll free in the US) or +1-978-646-2777.